

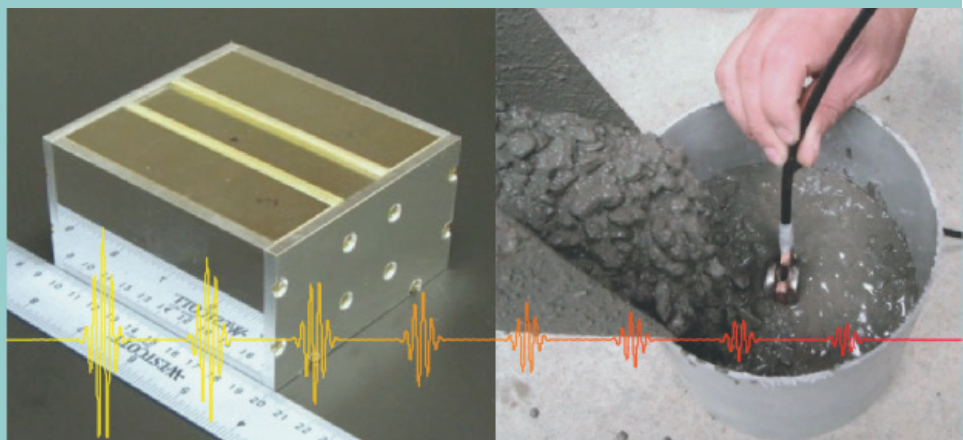


Magnetic Resonance Sensors

Edited by

Robert H. Morris and Michael I. Newton

Printed Edition of the Special Issue Published in *Sensors*



www.mdpi.com/journal/sensors

Robert H. Morris and Michael I. Newton (Eds.)

Magnetic Resonance Sensors



This book is a reprint of the Special Issue that appeared in the online, open access journal, *Sensors* (ISSN 1424-8220) from 2013–2014 (available at: http://www.mdpi.com/journal/sensors/special_issues/mrs).

Guest Editors

Robert H. Morris
Michael I. Newton

Physics and Maths
Nottingham Trent University
Clifton Lane
Nottingham, NG11 8NS
UK

Editorial Office

MDPI AG
Klybeckstrasse 64
Basel, Switzerland

Publisher

Shu-Kun Lin

Managing Editor

Limei Huang

1. Edition 2015

MDPI • Basel • Beijing • Wuhan • Barcelona

ISBN 978-3-906980-98-0 (Hbk)

ISBN 978-3-906980-99-7 (PDF)

Articles in this volume are Open Access and distributed under the Creative Commons Attribution license (CC BY), which allows users to download, copy and build upon published articles even for commercial purposes, as long as the author and publisher are properly credited, which ensures maximum dissemination and a wider impact of our publications. The book taken as a whole is © 2015 MDPI, Basel, Switzerland, distributed under the terms and conditions of the Creative Commons by Attribution (CC BY-NC-ND) license (<http://creativecommons.org/licenses/by-nc-nd/4.0/>).

Table of Contents

List of Contributors.....	VI
---------------------------	----

Preface.....	IX
--------------	----

Robert H. Morris and Michael I. Newton (Eds.)

Editorial: Magnetic Resonance SensorsApplication Specific Magnetic Resonance Sensors

Application Specific Magnetic Resonance Sensors

Floriberto Díaz-Díaz, Prisciliano F. de J. Cano-Barrita, Bruce J. Balcom, Sergio E. Solís-Nájera and Alfredo O. Rodríguez

Embedded NMR Sensor to Monitor Compressive Strength Development and Pore Size Distribution in Hydrating Concrete

Reprinted from: *Sensors* **2013**, *13*(12), 15985–15999 5

<http://www.mdpi.com/1424-8220/13/12/15985>

Pan Guo, Wei He and Juan C. García-Naranjo

Degradation of Phosphate Ester Hydraulic Fluid in Power Station Turbines Investigated by a Three-Magnet Unilateral Magnet Array

Reprinted from: *Sensors* **2014**, *14*(4), 6797–6805..... 20

<http://www.mdpi.com/1424-8220/14/4/6797>

Zheng Xu, Robert H. Morris, Martin Bencsik and Michael I. Newton

Detection of Virgin Olive Oil Adulteration Using Low Field Unilateral NMR

Reprinted from: *Sensors* **2014**, *14*(2), 2028–2035..... 29

<http://www.mdpi.com/1424-8220/14/2/2028>

Michael D. Pinter, Tod Harter, Michael J. McCarthy and Matthew P. Augustine

Towards Using NMR to Screen for Spoiled Tomatoes Stored in 1,000 L, Aseptically Sealed, Metal-Lined Totes

Reprinted from: *Sensors* **2014**, *14*(3), 4167–4176..... 37

<http://www.mdpi.com/1424-8220/14/3/4167>

Aktham Asfour, Kosai Raouf and Jean-Paul Yonnet

Software Defined Radio (SDR) and Direct Digital Synthesizer (DDS) for NMR/MRI
Instruments at Low-Field

Reprinted from: *Sensors* **2013**, *13*(12), 16245–16262 46
<http://www.mdpi.com/1424-8220/13/12/16245>

MRI Compatible Sensors

Fabrizio Taffoni, Domenico Formica, Paola Saccomandi, Giovanni Di Pino and Emiliano Schena

Optical Fiber-Based MR-Compatible Sensors for Medical Applications: An Overview

Reprinted from: *Sensors* **2013**, *13*(10), 14105–14120 64
<http://www.mdpi.com/1424-8220/13/10/14105>

Martyn N.J. Paley, Janet E. Morris, Debbie Jarvis and Paul D. Griffiths

Fetal Electrocardiogram (fECG) Gated MRI

Reprinted from: *Sensors* **2013**, *13*(9), 11271–11279 80
<http://www.mdpi.com/1424-8220/13/9/11271>

Robert Mark Wellard, Jean-Philippe Ravasio, Samuel Guesne, Christopher Bell, Adekunle Oloyede, Greg Tevelen, James M. Pope and Konstantin I. Momot

Simultaneous Magnetic Resonance Imaging and Consolidation Measurement of Articular
Cartilage

Reprinted from: *Sensors* **2014**, *14*(5), 7940–7958 89
<http://www.mdpi.com/1424-8220/14/5/7940>

Extrinsic Contrast

Dina V. Hingorani, Sandra I. Gonzalez, Jessica F. Li and Mark D. Pagel

Sensing Lanthanide Metal Content in Biological Tissues with Magnetic Resonance
Spectroscopy

Reprinted from: *Sensors* **2013**, *13*(10), 13732–13743 108
<http://www.mdpi.com/1424-8220/13/10/13732>

Philip A. Barber

Magnetic Resonance Imaging of Ischemia Viability Thresholds and the Neurovascular Unit

Reprinted from: *Sensors* **2013**, *13*(6), 6981–7003 121
<http://www.mdpi.com/1424-8220/13/6/6981>

Sebastian Meier, Pernille R. Jensen, Magnus Karlsson and Mathilde H. Lerche

Hyperpolarized NMR Probes for Biological Assays

Reprinted from: *Sensors* **2014**, *14*(1), 1576–1597..... 145

<http://www.mdpi.com/1424-8220/14/1/1576>

MRI Optimisation

Fabio Baselice, Giampaolo Ferraioli, Alessandro Grassia and Vito Pascazio

Optimal Configuration for Relaxation Times Estimation in Complex Spin Echo Imaging

Reprinted from: *Sensors* **2014**, *14*(2), 2182–2198..... 168

<http://www.mdpi.com/1424-8220/14/2/2182>

Angshul Majumdar, Kunal Narayan Chaudhury and Rabab Ward

Calibrationless Parallel Magnetic Resonance Imaging: A Joint Sparsity Model

Reprinted from: *Sensors* **2013**, *13*(12), 16714–16735 186

<http://www.mdpi.com/1424-8220/13/12/16714>

List of Contributors

Aktham Asfour: Grenoble Electrical Engineering Lab (G2E-Lab), BP 46, Saint Martin d'Hères 38402, France.

Matthew P. Augustine: Department of Chemistry, University of California, One Shields Avenue, Davis, CA 95616, USA.

Bruce J. Balcom: MRI Centre, Department of Physics, University of New Brunswick, Fredericton, NB E3B 5A3, Canada.

Philip A. Barber: Departments of Clinical Neurosciences, University of Calgary, 3330 Hospital Drive NW, Calgary, ALB T2N 4N1, Canada; Departments of Radiology, University of Calgary, 3330 Hospital Drive NW, Calgary, ALB T2N 4N1, Canada; Hotchkiss Brain Institute, University of Calgary, 3330 Hospital Drive NW, Calgary, ALB T2N 4N1, Canada

Fabio Baselice: Dipartimento di Ingegneria, Università degli Studi di Napoli Parthenope, Napoli 80143, Italy.

Christopher Bell: Discipline of Biomedical Engineering and Medical Physics, Queensland University of Technology/2 George St., Brisbane 4001, Australia.

Martin Bencsik: School of Science and Technology, Nottingham Trent University, Clifton Lane, Nottingham, NG11 8NS, UK.

Prisciliano F. de J. Cano-Barrita: Instituto Politécnico Nacional-CIIDIR Unidad Oaxaca, Hornos No. 1003, Sta. Cruz Xoxocotlán, Oaxaca 71230, Mexico.

Kunal Narayan Chaudhury: Program in Applied and Computational Mathematics (PACM), Princeton University, Princeton, NJ 08544, USA.

Giovanni Di Pino: Unit of Biomedical Robotics and Biomicrosystems, Center for Integrated Research, Università Campus Bio-Medico di Roma, Via Álvaro del Portillo, 21, Rome 00128, Italy; Institute of Neurology, Campus Bio-Medico University, and Fondazione Alberto Sordi-Research Institute for Ageing, Center for Integrated Research, Università Campus Bio-Medico di Roma, Via Álvaro del Portillo, 200, Rome 00128, Italy.

Floriberto Díaz-Díaz: Instituto Politécnico Nacional-CIIDIR Unidad Oaxaca, Hornos No. 1003, Sta. Cruz Xoxocotlán, Oaxaca 71230, Mexico.

Giampaolo Ferraioli: Dipartimento di Scienze e Tecnologie, Università degli Studi di Napoli Parthenope, Napoli 80143, Italy.

Domenico Formica: Unit of Biomedical Robotics and Biomicrosystems, Center for Integrated Research, Università Campus Bio-Medico di Roma, Via Álvaro del Portillo, 21, Rome 00128, Italy.

Juan C. García-Naranjo: Centre of Medical Biophysics, Universidad de Oriente, Patricio Lumumba S/N, Santiago de Cuba 90500, Cuba.

Sandra I. Gonzalez: Department of Biomedical Engineering, University of Arizona, Tucson, AZ 85721, USA.

Alessandro Grassia: Dipartimento di Ingegneria, Università degli Studi di Napoli Parthenope, Napoli 80143, Italy.

Paul D. Griffiths: Academic Radiology, Department of Cardiovascular Science, University of Sheffield, Sheffield S10 2JF, UK.

Samuel Guesne: National Instruments France, 2 rue Hennape, 92735 Nanterre Cédex, France.

Pan Guo: State Key Laboratory of Power Transmission Equipment & System Security and New Technology, Chongqing University, Chongqing 400044, China; MRI Centre, Department of Physics, P.O. Box 4400, University of New Brunswick, Fredericton, NB E3B 5A3, Canada.

Tod Harter: The Morning Star Packing Company, Woodland, CA 95695, USA.

Wei He: State Key Laboratory of Power Transmission Equipment & System Security and New Technology, Chongqing University, Chongqing 400044, China.

Dina V. Hingorani: Department of Chemistry and Biochemistry, University of Arizona, Tucson, AZ 85721, USA; University of Arizona Cancer Center, Tucson, AZ 85724-5013, USA.

Debbie Jarvis: Academic Radiology, Department of Cardiovascular Science, University of Sheffield, Sheffield S10 2JF, UK.

Pernille R. Jensen: Albeda Research, Gamle Carlsberg Vej 10, 1799 Copenhagen V, Denmark.

Magnus Karlsson: Albeda Research, Gamle Carlsberg Vej 10, 1799 Copenhagen V, Denmark.

Mathilde H. Lerche: Albeda Research, Gamle Carlsberg Vej 10, 1799 Copenhagen V, Denmark.

Jessica F. Li: University of Arizona Cancer Center, Tucson, AZ 85724-5013, USA.

Angshul Majumdar: Department of Electrical and Computer Engineering, University of British Columbia, Vancouver, BC V6T 1Z4, Canada.

Michael J. McCarthy: Department of Food Science and Technology, University of California, One Shields Avenue, Davis, CA 95616, USA.

Sebastian Meier: Carlsberg Laboratory, Gamle Carlsberg Vej 10, 1799 Copenhagen V, Denmark.

Konstantin I. Momot: Discipline of Biomedical Engineering and Medical Physics, Queensland University of Technology/2 George St., Brisbane 4001, Australia.

Janet E. Morris: Academic Radiology, Department of Cardiovascular Science, University of Sheffield, Sheffield S10 2JF, UK.

Robert H. Morris: School of Science and Technology, Nottingham Trent University, Clifton Lane, Nottingham, NG11 8NS, UK.

Michael I. Newton: School of Science and Technology, Nottingham Trent University, Clifton Lane, Nottingham, NG11 8NS, UK.

Adekunle Oloyede: Discipline of Biomedical Engineering and Medical Physics, Queensland University of Technology/2 George St., Brisbane 4001, Australia.

Mark D. Pagel: Department of Chemistry and Biochemistry, University of Arizona, Tucson, AZ 85721, USA; University of Arizona Cancer Center, Tucson, AZ 85724-5013, USA; Department of Biomedical Engineering, University of Arizona, Tucson, AZ 85721, USA; Department of Medical Imaging, University of Arizona, Tucson, AZ 85721, USA.

Martyn N.J. Paley: Academic Radiology, Department of Cardiovascular Science, University of Sheffield, Sheffield S10 2JF, UK.

Vito Pascazio: Dipartimento di Ingegneria, Università degli Studi di Napoli Parthenope, Napoli 80143, Italy.

Michael D. Pinter: Department of Chemistry, University of California, One Shields Avenue, Davis, CA 95616, USA.

James M. Pope: Discipline of Biomedical Engineering and Medical Physics, Queensland University of Technology/2 George St., Brisbane 4001, Australia.

Kosai Raouf: Laboratoire d'Acoustique de l'Université du Maine, Rue Aristote, Le Mans Cedex 09 72085, France.

Jean-Philippe Ravasio: SonoSite France Sarl, 19, avenue de Norvege, Parc d'activite les Fjords, Immeuble le Vega, 91140 Villebon sur Yvette, France.

Alfredo O. Rodríguez: Departamento de Ingeniería Eléctrica, Universidad Autónoma Metropolitana Iztapalapa, Mexico Distrito Federal 09340, Mexico.

Paola Saccomandi: Unit of Measurements and Biomedical Instrumentation, Center for Integrated Research, Università Campus Bio-Medico di Roma, Via Álvaro del Portillo, 21, Rome 00128, Italy.

Emiliano Schena: Unit of Measurements and Biomedical Instrumentation, Center for Integrated Research, Università Campus Bio-Medico di Roma, Via Álvaro del Portillo, 21, Rome 00128, Italy.

Sergio E. Solís-Nájera: Facultad de Ciencias, Universidad Nacional Autónoma de México, Mexico Distrito Federal 04510, Mexico.

Fabrizio Taffoni: Unit of Biomedical Robotics and Biomicrosystems, Center for Integrated Research, Università Campus Bio-Medico di Roma, Via Álvaro del Portillo, 21, Rome 00128, Italy.

Greg Tevelen: Science and Engineering Faculty, Queensland University of Technology/2 George St., Brisbane 4001, Australia.

Rabab Ward: Department of Electrical and Computer Engineering, University of British Columbia, Vancouver, BC V6T 1Z4, Canada.

Robert Mark Wellard: Discipline of Chemistry, Physics and Mechanical Engineering, Queensland University of Technology/2 George St., Brisbane 4001, Australia.

Zheng Xu: State Key Laboratory of Power Transmission Equipment & System Security and New Technology, Chongqing University, 174 Shazhengjie, Shapingba, Chongqing 400044, China.

Jean-Paul Yonnet: Grenoble Electrical Engineering Lab (G2E-Lab), BP 46, Saint Martin d'Hères 38402, France.

Preface

Magnetic Resonance finds countless applications, from spectroscopy to imaging, routinely in almost all research and medical institutions across the globe. It is also becoming more frequently used for specific applications in which the whole instrument and system is designed for a dedicated application. With beginnings in borehole logging for the petrochemical industry Magnetic Resonance sensors have been applied to fields as varied as: online process monitoring for food manufacture and medical point of care diagnostics. This great diversity is seeing exciting developments in magnetic resonance sensing technology published in application specific journals where they are often not seen by the wider sensor community. It is clear that there is enormous interest in magnetic resonance sensors which represents a significant growth area. This book aims to bring together a number of such applications into a single publication which would act as a current state of the art in this field.

The editors of this edition have a keen interest in broadening the applications of these sensors and have included here a very brief introduction and background to magnetic resonance sensors for those readers who may be interested in reading this issue but have little background in this area.

In a typical magnetic resonance set-up, not used for imaging, there are two key components, the first must supply a magnetic field and is typically a permanent or electro-magnet. The second is responsible for stimulating the system and collecting the resultant signal which is commonly known as an RF coil. These can both take many forms depending on the desired purpose of the final sensor. For example a human imaging system typically operates a 1.5 T magnetic field generated by spools of liquid Helium cooled superconducting wire. Such a design provides a very large, very homogeneous field ideal for imaging but which is clearly not useful for embedded measurements.

A challenge is presented by MR systems with regard to the electronics which are needed to generate and collect these signals. This is predominantly due to the short time durations of the pulses and signals (on the order of microseconds) and the large difference between the power of the pulses transmitted and those received which may be as different as 1000W and 1 μ W respectively. Modern digital electronics have somewhat simplified the former of these problems but the latter is often still dealt with using a passive device known as a duplexer which automatically blanks off a highly sensitive small signal radio frequency amplifier in the presence of high power transmitted signals using a set of diodes.

The volume of the region interrogated by the RF coil and magnet is known as the sensitive volume and is important to optimize as too small a volume may provide an unrepresentative analysis of the overall system whilst too large a volume is difficult to achieve in a cost effective manner. Similarly, on sensors where only a small volume is examined, a large portion of this volume will be in contact with the surface of the sensor itself which may introduce edge effects. Computer simulations can go some of the way towards the selecting a geometry with an optimized sensitive volume, however the nuances of the construction itself and subtle differences in the magnets used for permanent magnet sensors will lead to differences from the computer model in probes constructed for specific applications.

The underlying principles which underpin Magnetic Resonance exploit a quantum property known as spin. Certain nuclei such as ^1H , ^3He and ^{23}Na , when placed in a magnetic field (B_0) will experience alignment with the given field. Once aligned with this field, radio frequency (RF) energy of the correct frequency can be used to manipulate the direction of the magnetic moment of the nuclei. The spins are said to be resonant in such a magnetic field, hence the name Magnetic Resonance, and if not aligned to the field will rotate, or precess around it. The nuclei can be considered as individual tiny bar magnets so the precession of these spins will induce an EMF in a nearby conductor. The resulting signal will decay as the spins return to their equilibrium state, aligned along the magnetic field. The time constant of this relaxation is known as Spin-Lattice Relaxation or T_1 and is characteristic of the properties of the system under investigation.

An alternative measure of the properties of the system is given by spin-spin or T_2^* relaxation which is caused by interactions between the resonant nuclei themselves. For the most-part, with inhomogeneous fields, the value of T_2^* is so short that it cannot be measured. In these circumstances, it is possible to repeatedly, and rapidly stimulate the sample to reproduce the signal a known time later. This can be repeated a number of times, although with each repeat, the signal will have reduced intensity. This reduced intensity will present with an exponential envelope with a time constant T_2^{eff} . The value of T_2^{eff} is dependent on the field inhomogeneity, diffusion of the sample and the intrinsic T_2 value of the sample. With variation of the experimental parameters, any one of these dependent factors can be determined. Relaxation parameters for spins of the same nuclei under different conditions will not be the same. For example spins in a water molecules making up a substance such as a biofilm will behave differently to free water even though the molecule itself remains unchanged.

A number of commercially available MR systems, such as the NMR MOUSE® provide a very useful, small scale system for MR measurements in a laboratory setting for a fraction of the cost of a superconducting system such as a human imager. Even these systems are sometimes too expensive for embedded measurements in samples but they have opened up a field of their own, allowing exploration of previously unmeasured samples.

The final critical consideration is the signal-to-noise ratio (SNR) of the sensor while scanning. Measurements made with inhomogeneous fields, make measurements on diffusive samples such as water is more technically challenging than in a homogeneous field found in high field imaging systems. While SNR can be improved by multiple repeat experiments (often on the order of 128 for unilateral or bespoke systems), given spectrometer noise, as well as certain types of modulated noise from external sources, it is possible that a functional MR sensor might be unable to detect at all as the signal may never meaningfully exceed the noise. The wealth of literature, coupled with computer simulations (which are useful as larger sensitive volume should lead to a superior signal intensity when all other factors are the same), can provide an indication of the designs that should yield the best signal intensity but as with the other considerations a true gauge of the achievable SNR can only be achieved through prototype construction and testing.

There are a large number of works which deal in far greater detail with the background and underlying principles of magnetic resonance to which the reader is directed should they wish to investigate this interesting area of science in greater detail.

Robert H. Morris and Michael I. Newton
Guest Editors

Magnetic Resonance Sensors

Robert H. Morris and Michael I. Newton

Magnetic Resonance finds countless applications, from spectroscopy to imaging, routinely in almost all research and medical institutions across the globe. It is also becoming more frequently used for specific applications in which the whole instrument and system is designed for a dedicated application. With beginnings in borehole logging for the petro-chemical industry Magnetic Resonance sensors have been applied to fields as varied as online process monitoring for food manufacture and medical point of care diagnostics. This great diversity is seeing exciting developments in magnetic resonance sensing technology published in application specific journals where they are often not seen by the wider sensor community. It is clear that there is enormous interest in magnetic resonance sensors which represents a significant growth area. The aim of this special edition of *Sensors* was to address the wide distribution of relevant articles by providing a forum to disseminate cutting edge research in this field in a single open source publication.

Reprinted from *Sensors*. Cite as: Morris, R.H.; Newton, M.I. Magnetic Resonance Sensors. *Sensors* **2014**, *14*, 21722–21725.

Summary of the Special Issue

Of particular importance to this community is the use of small, low field instruments, the development of which has been made possible by the steady progress in permanent magnet technology. In our first two contributions we have examples of *in-situ* monitoring using such sensors: Firstly for assessing compressive strength and pore size distribution in concrete [1] where the results indicated that the sensor is capable of detecting changes in water content in fresh cement pastes and porosity refinement caused by cement hydration in hardened materials, even if they are prepared with a low water/cement ratio; Secondly to assess the degradation of hydraulic fluid in power station turbines [2]. Here, a three-magnet unilateral NMR sensor array was used in two different power stations for assessing aging of the turbine oils used. Their results showed that components of the longitudinal and transverse relaxation times shortened as the fluids aged providing a useful tool for monitoring hydraulic fluids in turbines. These two articles highlight the trend in magnetic resonance sensors towards offering sensor applications which are distinct from imaging or spectroscopy but which provide valuable information to the operator. Magnetic resonance also offers the opportunity to non-destructively monitor materials in sealed containers such as food and drink products. The next two articles report on important aspects of this branch of sensor technology: The detection of adulteration of olive oil is reported in [3] using a unilateral NMR MOUSE and applying a 2-dimensional inverse Laplace transformation. The adulteration of extra virgin olive oil with different percentages of sunflower oil or red palm oil are shown to be quantitatively different using the transverse relaxation and self-diffusion coefficients of the bulk sample. In [4] it was found that spoilage in tomato paste test samples leads to longer spin lattice relaxation times and that it is possible to use a unilateral instrument through a standard non-ferrous, metal-lined bulk storage container to

collect these signals non-invasively. Crucial for the widening the applications of magnetic resonance sensors is the availability of low cost, low power console electronics which is discussed in [5] where the authors demonstrate a proof-of-concept MR console system which is fully digital and constructed using off the shelf equipment wherever possible. The authors present such a system based on a Direct Digital Synthesizer (DDS) used to produce the pulses, a Software Defined Radio (SDR) do digitally collect and process the resultant NMR signal and a Digital Signal Processor (DSP) as the central processing unit.

A second aspect of the papers presented in this special issue is the combining of traditional MRI imaging with other sensors. A review of optical fiber sensors that are MRI compatible is presented in [6], focusing on the sensors employed for measuring physical parameters in medicine (*i.e.*, temperature, force, torque, strain, and position) including working principles and their relevant advantages and disadvantages. This may, in the future see interesting combinations with other technologies such as with gated MRI modalities like the fetal electrocardiogram triggered MRI reported in [7]. Here the authors have successfully imaged a stationary slice through a fetal heart despite the significantly higher heart rate in comparison to adult patients and the indirect connection of ECG leads. Finally in this section, in [8] an applied example of the fiber optic sensors discussed in [6] is demonstrated where the authors used a fiber-optic Fabry-Perot interferometer pressure transducer to record two transient characteristics of the consolidation of articular cartilage: the change over time of strain and the hydrostatic excess pore pressure (HEPP).

In traditional imaging, it is sometimes the case that there is no intrinsic contrast to the pathology of interest. To address this MRI contrast agents that consist of Gd(III) or other Lanthanide chelates are often used to enhance the image contrast of anatomical features. The difficulty with their use is that *ex vivo* tissue concentrations are often required. In [9] the authors present a method which uses changes in magnetic susceptibility to determine the concentration of a range of Lanthanide chelates, using NMR spectroscopy. Although presented using a high field spectrometer, this could easily be performed in the clinical setting using a bench top spectrometer system such as the Magritek Spinsolve [10] improving the efficiency at point of care. An application of such contrast agents is considered in [11] which reviews advances in our understanding of stroke pathophysiology with imaging. This article investigates the ability to image tissue viability post-stroke using MRI with and without paramagnetic contrast agents. An alternative approach to the use of a contrast agent is the application of contrast enhancement. In [12] Spin hyperpolarization is reviewed for its use in the analysis of biological assays to detect parameters within the cellular structure such as intracellular reaction progression, drug efficacy, pathway kinetics, probe uptake and export, oncogenic signaling, redox state, ion concentrations, reactive oxygen species or pH.

Our final two papers present methods to improve the way in which imaging is conducted. When setting up an MRI scan, there are numerous choices open to the operator for parameters which impact the final result. In many cases, standard settings are used which are not optimal in terms of patient scan time, image quality or contrast. This is in part due to a lack of optimization schemes which can be used to determine the optimum values for various parameters. This has been addressed in [13] where the authors present a number of recipes are presented for optimum settings in spin echo imaging modalities at 1.5 T and 3 T. Another issue which is increasingly problematic in the clinical

setting is the calibration of parallel MRI which is a technique where multiple receive coils are used to improve the signal to noise ratio. Traditionally, parallel imaging requires the use of parameter estimation or calibration prior to scanning. In [14] the authors present a new technique which requires no such calibration prior to use and yet which offers better reconstruction than alternative techniques currently available. Where implemented this will result in improved clinical images and reduced patient scan time.

To conclude, we have compiled a special issue in which we have aimed to address the disparity of publications related to magnetic resonance sensors, both from the point of view of customized probes and the sensors used with imaging or spectroscopy techniques. We would like to thank all the authors who submitted manuscripts to this Special Issue of *Sensors* for preparing such interesting and varied work and the reviewers for their careful consideration and constructive criticism during the rigorous review process.

References

1. Díaz-Díaz, F.; de J. Cano-Barrita, P.; Balcom, B.; Solís-Nájera, S.; Rodríguez, A. Embedded NMR Sensor to Monitor Compressive Strength Development and Pore Size Distribution in Hydrating Concrete. *Sensors* **2013**, *13*, 15985–15999, doi:10.3390/s131215985.
2. Guo, P.; He, W.; García-Naranjo, J. Degradation of Phosphate Ester Hydraulic Fluid in Power Station Turbines Investigated by a Three-Magnet Unilateral Magnet Array. *Sensors* **2014**, *14*, 6797–6805, doi:10.3390/s140406797.
3. Xu, Z.; Morris, R.; Bencsik, M.; Newton, M. Detection of Virgin Olive Oil Adulteration Using Low Field Unilateral NMR. *Sensors* **2014**, *14*, 2028–2035, doi:10.3390/s140202028.
4. Pinter, M.; Harter, T.; McCarthy, M.; Augustine, M. Towards Using NMR to Screen for Spoiled Tomatoes Stored in 1,000 L, Aseptically Sealed, Metal-Lined Totes. *Sensors* **2014**, *14*, 4167–4176, doi:10.3390/s140304167.
5. Asfour, A.; Raouf, K.; Yonnet, J. Software Defined Radio (SDR) and Direct Digital Synthesizer (DDS) for NMR/MRI Instruments at Low-Field. *Sensors* **2013**, *13*, 16245–16262, doi:10.3390/s131216245.
6. Taffoni, F.; Formica, D.; Saccomandi, P.; Pino, G.; Schena, E. Optical Fiber-Based MR-Compatible Sensors for Medical Applications: An Overview. *Sensors* **2013**, *13*, 14105–14120, doi:10.3390/s131014105.
7. Paley, M.; Morris, J.; Jarvis, D.; Griffiths, P. Fetal Electrocardiogram (fECG) Gated MRI. *Sensors* **2013**, *13*, 11271–11279, doi:10.3390/s130911271.
8. Wellard, R.; Ravasio, J.; Guesne, S.; Bell, C.; Oloyede, A.; Tevelen, G.; Pope, J.; Momot, K. Simultaneous Magnetic Resonance Imaging and Consolidation Measurement of Articular Cartilage. *Sensors* **2014**, *14*, 7940–7958, doi:10.3390/s140507940.
9. Hingorani, D.; Gonzalez, S.; Li, J.; Pagel, M. Sensing Lanthanide Metal Content in Biological Tissues with Magnetic Resonance Spectroscopy. *Sensors* **2013**, *13*, 13732–13743, doi:10.3390/s131013732.
10. Barber, P. Magnetic Resonance Imaging of Ischemia Viability Thresholds and the Neurovascular Unit. *Sensors* **2013**, *13*, 6981–7003, doi:10.3390/s130606981.

11. Magritek.com. Spinsolve|Magritek. Available online: <http://www.magritek.com/products/spinsolve/> (accessed 4 November 2014).
12. Meier, S.; Jensen, P.; Karlsson, M.; Lerche, M. Hyperpolarized NMR Probes for Biological Assays. *Sensors* **2014**, *14*, 1576–1597, doi:10.3390/s140101576.
13. Baselice, F.; Ferraioli, G.; Grassia, A.; Pascazio, V. Optimal Configuration for Relaxation Times Estimation in Complex Spin Echo Imaging. *Sensors* **2014**, *14*, 2182–2198, doi:10.3390/s140202182.
14. Majumdar, A.; Chaudhury, K.; Ward, R. Calibrationless Parallel Magnetic Resonance Imaging: A Joint Sparsity Model. *Sensors* **2013**, *13*, 16714–16735, doi:10.3390/s131216714.

Application Specific Magnetic Resonance Sensors

Embedded NMR Sensor to Monitor Compressive Strength Development and Pore Size Distribution in Hydrating Concrete

Floriberto Díaz-Díaz, Prisciliano F. de J. Cano-Barrita, Bruce J. Balcom, Sergio E. Solís-Nájera and Alfredo O. Rodríguez

Abstract: In cement-based materials porosity plays an important role in determining their mechanical and transport properties. This paper describes an improved low-cost embeddable miniature NMR sensor capable of non-destructively measuring evaporable water loss and porosity refinement in low and high water-to-cement ratio cement-based materials. The sensor consists of two NdFeB magnets having their North and South poles facing each other, separated by 7 mm to allow space for a Faraday cage containing a Teflon tube and an ellipsoidal RF coil. To account for magnetic field changes due to temperature variations, and/or the presence of steel rebars, or frequency variation due to sample impedance, an external tuning circuit was employed. The sensor performance was evaluated by analyzing the transverse magnetization decay obtained with a CPMG measurement from different materials, such as a polymer phantom, fresh white and grey cement pastes with different w/c ratios and concrete with low (0.30) and high (0.6) w/c ratios. The results indicated that the sensor is capable of detecting changes in water content in fresh cement pastes and porosity refinement caused by cement hydration in hardened materials, even if they are prepared with a low w/c ratio (w/c = 0.30). The short lifetime component of the transverse relaxation rate is directly proportional to the compressive strength of concrete determined by destructive testing. The r^2 (0.97) from the linear relationship observed is similar to that obtained using T_2 data from a commercial Oxford Instruments 12.9 MHz spectrometer.

Reprinted from *Sensors*. Cite as: Díaz-Díaz, F.; Cano-Barrita, P.F.d.; Balcom, B.J.; Solís-Nájera, S.E.; Rodríguez, A.O. Embedded NMR Sensor to Monitor Compressive Strength Development and Pore Size Distribution in Hydrating Concrete. *Sensors* **2013**, *13*, 15985–15999.

1. Introduction

In Portland cement concrete, porosity plays an important role in determining its mechanical and durability properties. Porosity depends on the water-to-cement ratio and the degree of hydration of the cement paste [1]. On exposure to the environment the material undergoes changes that lead to micro-cracking, increasing the permeability of concrete to water, which is a medium for transport of other aggressive species such as chloride ions and CO_2 [1]. Therefore, monitoring the moisture condition and microstructural changes in concrete are important from durability and mechanical strength points of view.

The moisture condition is normally evaluated by using relative humidity sensors that must be installed by drilling into the structural member [2]. Information obtained in this way is of limited use, unless the sorption/desorption isotherm is known for the material to determine the moisture content corresponding to a specific relative humidity. On the other hand, compressive strength of concrete is normally determined by destructive testing of cylinders cast for this purpose or by coring the structure to determine the “*in situ*” compressive strength. Traditionally, the rebound hammer and the ultrasonic pulse velocity are used to estimate the compressive strength of concrete in the field provided a calibration curve is first determined. There are however several additional factors affecting the measurements such as moisture content, type and amount of aggregates, and the presence and direction of the reinforcing steel [3].

Nuclear magnetic resonance (NMR) is a non-destructive and non-invasive technique that has been used in the laboratory to study cement-based materials [4–6]. To extend the possibilities of NMR to study these materials in the field, portable systems such as the NMR MOUSE [7,8] and the NMR MOLE [9] have been developed but the measurements are restricted to a depth of a few millimeters below the surface. Embedded miniature NMR sensors have been used to monitor changes in evaporable water and pore refinement in high water/cement ratio Portland cement mortar [10]. However, use of these sensors in materials having a low water/cement ratio (low porosity) did not provide useful NMR signal because of low signal intensity.

This paper presents an improved embedded NMR sensor capable of measuring microstructural and evaporable water changes occurring in concrete materials having high and low water/cement ratios, such as those used in the construction industry for ordinary and special applications, respectively.

2. Experimental Section

2.1. Sensor Design and Construction

Concrete is essentially a material containing hydrated Portland cement paste and aggregates (Figure 1). Since hydration of the cement paste is the process leading to changes in mechanical and transport properties of concrete, it is the part of the material that the sensor must be capable of monitoring. The sensor design considered the fact that aggregates, especially normal density coarse aggregates (>4.75 mm), may drastically reduce the amplitude of the NMR signal if they are located within the sensitive region of the sensor. These aggregates have low water absorption (less than 2%). Even if considering lightweight aggregates with much higher water absorption, the NMR signal detected would not be of interest since it does not reflect changes occurring in the cement paste caused by hydration.

Therefore, the sensor has to prevent aggregate particles from entering into its sensitive region. Several magnet arrangements were explored and the Z magnetic field component along the Y-axis (Figure 2) was measured to select those providing the highest and the most homogeneous magnetic fields [11]. The best arrangement was chosen based on the highest signal to noise ratio (SNR) obtained by measuring the transverse magnetization decay of a polymer phantom using the CPMG technique [12].

Figure 1. Piece of hydraulic concrete showing coarse aggregates (A) and mortar (B). Mortar is composed of cement paste and fine aggregates (particle size < 4.75 mm).

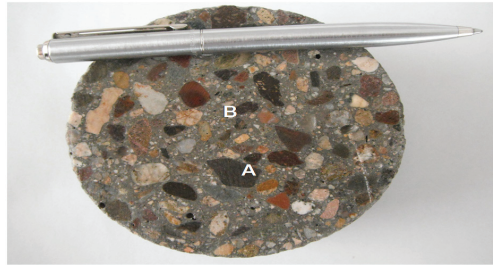
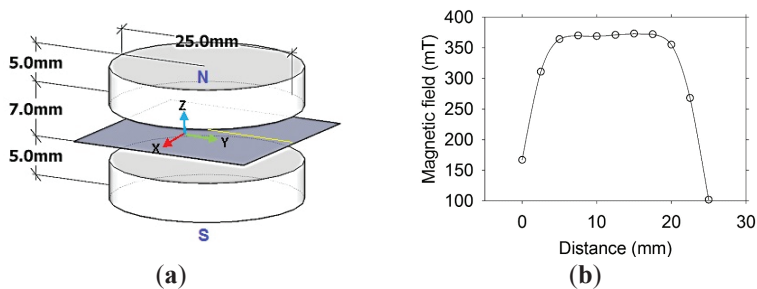


Figure 2. (a) Magnet arrangement for the sensor; (b) Measured Z magnetic field component along the Y-axis.



The magnet arrangement selected consists of two circular grade 35 NdFeB magnets, measuring 25 mm in diameter and 5 mm in thickness, with opposite poles facing (Figure 2a). This had an additional advantage of increasing the magnetic field strength and homogeneity that in turn increases sensitivity of the sensor. Figure 2b shows the magnetic field measured at the middle of the distance between the magnets. The measurement was performed by manually displacing a Gaussmeter at 2.5 mm intervals along the Y-axis. For this particular pair of magnets, the magnetic field was 0.38 T and the Larmor frequency for ^1H was 16.18 MHz.

The separation distance between the magnets was 7 mm to allow space for a Faraday cage (Figure 3) made of a phenolic printed circuit board plate, while preventing coarse aggregates from entering into the sensitive region of the sensor. The Faraday cage was used to reduce the influence of external noise on the NMR signal. During preliminary evaluation of the design, it was observed that when the sensor was introduced in the cement paste, there were changes in the tuning frequency and in the impedance of the RF coil. This was due to the influence of external impedance (fresh cement paste) over the total impedance of the RF coil, which hindered external tuning. To reduce this problem, a Teflon tube with ellipsoidal cross section measuring 11 mm in major axis, 5 mm in minor axis and 30 mm in length was used. The tube served also as a mold for the RF coil, which had 22 turns of 20 AWG copper wire. The length of the coil was 23 mm and an inductance of 2.8 μH . The length of the RG58 coaxial cable was 1.17 m ($\lambda/16$) with an effective capacitance of 110.8 pF.

Figure 3. Faraday cage (A) containing Teflon tube (B); ellipsoidal RF coil (C); and RG58 coaxial cable (D).

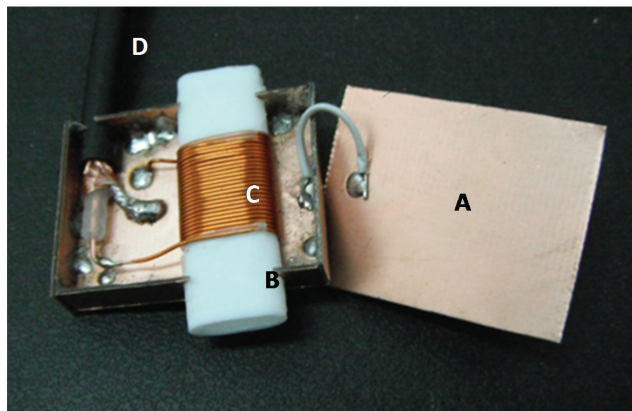
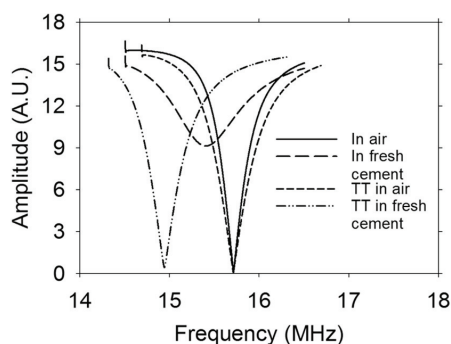


Figure 4 shows the response in frequency when the sensor without the Teflon tube is immersed in fresh cement paste. There is a change in both frequency and impedance. However, if the Teflon tube is used (could also be a glass tube) there is only a change in frequency. The effect of coupling in impedance and the change in frequency of the coil when it is embedded in the cement paste depends on the characteristics of the material, such as polarity and the dielectric constant. It is observed that the Teflon tube eliminates the impedance displacement when the sensor is embedded in the cement paste, although it does not avoid changes in frequency. This change in frequency was accommodated using the external tuning circuit described next.

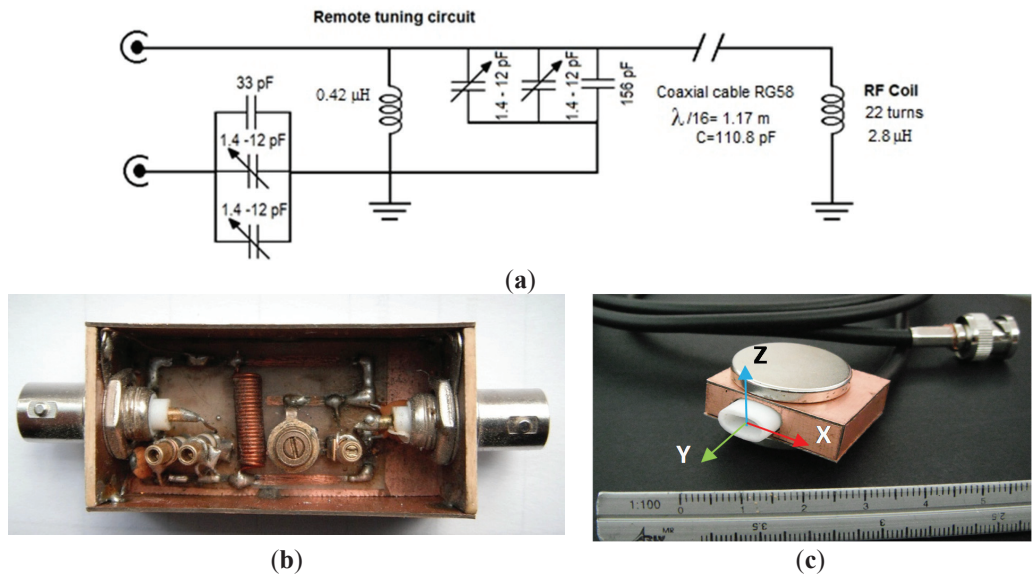
Figure 4. Frequency response of the sensor outside and inside the fresh cement paste w/c ratio = 0.60. TT means sensor with Teflon tube.



As shown in Figure 5a, the coil design does not include capacitors within the sensor; rather the tuning (16.18 MHz) was performed through a remote tuning circuit (Figure 5b). The purpose of this remote tuning circuit was to re-tune the RF coil after the sensor is embedded to accommodate frequency changes due to sample impedance, changes in temperature and/or the presence of steel rebars that influence the static magnetic field, which in turn changes the Larmor frequency. The main advantage of the external tuning circuit is the possibility of retuning the RF coil once the sensor is

embedded, compared to conventional tuning-matching circuits. The function of the additional inductance ($0.42 \mu\text{H}$) in the external tuning circuit is to adjust the resonance frequency of the RF coil. It is connected in parallel to the total inductance (coaxial cable and RF coil), therefore the equivalent inductance obtained is lower and the frequency is increased [13]. The entire sensor was covered with a layer of water resistant epoxy resin (Figure 5c).

Figure 5. (a) Circuit diagram of the sensor; (b) External tuning circuit (55 mm in length, 25 mm in width, and 20 mm in height); (c) NMR sensor constructed.



2.2. Sensor Characterization

2.2.1. NMR Measuring Technique

The CPMG technique [12] was used to obtain the transverse magnetization decay of protons from a polymer phantom and from evaporable water in fresh and hardened cement paste and concrete.

Table 1 provides the CPMG parameters used to determine the transverse magnetization decay of a polymer phantom, which possesses a bi-exponential decay with a long lifetime component of 20 ms and a short lifetime component of 4.5 ms. The SNR was obtained as the ratio of the average amplitude of the first three points of the CPMG envelope divided by the standard deviation of the last ten points where the signal has completely decayed. The coefficient of variation of the CPMG amplitude and the T_2 decay constant obtained by performing seven measurements with the same sensor and the same polymer phantom under temperature controlled conditions was less than 1%.

Table 1. CPMG parameters used to obtain the SNR for each sensor using a polymer phantom, which has a long lifetime component of 20 ms and a short lifetime component of 4.5 ms.

Sensor	Frequency (MHz)	No. of Scans	Echo Time (μ s)	No. of Echoes	Repetition Time (ms)	pw_{90° (μ s)	RF Power (Watts)	Acquisition Time (min)	SNR
S1	15.47	4,096	200	300	500	7	100	34	139
S2	15.39	4,096	200	300	500	6	100	34	173
S3	15.48	4,096	200	300	500	6	100	34	148
S4	15.17	4,096	200	300	500	6	100	34	160

Table 2 provides the CPMG parameters used for the measurements in cement pastes and concretes. These parameters were used according to the type, w/c ratio and age of the samples, so that the changes in microstructure produced by cement hydration and reflected in the relaxation times could be followed. For instance, the minimum number of scans, the maximum echo time, the maximum number of echoes, and the maximum repetition time, were used at early ages, when the T_2 relaxation times were on the order of few milliseconds.

Table 2. CPMG parameters used for the measurements in cement pastes and concretes.

Material	No. of Scans		Echo Time/ μ s		No. of Echoes		Repetition Time/ms		pw_{90°/μ s	RF power/W	Acquisition Time/min	
	Min	Max	Min	Max	Min	Max	Min	Max			Min	Max
	White cement paste	1,024	4,096	50	200	60	450	250			500	6
Grey cement paste	1,024	4,096	40	200	30	250	250	500	6	100	8.5	17.0
Concrete w/c = 0.30	4,096	8,192	36	80	30	50	250	500	6	100	34.0	34.0
Concrete w/c = 0.60	4,096	8,192	40	120	50	80	250	500	6	100	34.0	34.0

2.2.2. NMR Sensors to Characterize Fresh and Hardened Portland Cement Pastes

Ordinary and white Portland cement were used to prepare the cement pastes. White cement was used because of its lower iron content compared to grey cement (Table 3). Tap water was used to prepare the cement pastes.

Table 3. Oxide composition of the cements and fine aggregate used to prepare the cement pastes and concrete mixtures. LOI means mass loss on ignition.

Oxide (%)	Al ₂ O ₃	CaO	Fe ₂ O ₃	K ₂ O	MgO	MnO	Na ₂ O	P ₂ O ₅	SiO ₂	TiO ₂	LOI
White Portland cement	3.87	67.23	0.26	0.34	0.60	N.D.	0.08	N.D.	21.95	0.07	5.76
Ordinary Portland cement	3.69	58.70	3.97	0.31	1.58	0.10	0.18	0.09	18.75	0.17	5.44
Fine Aggregate	11.91	1.80	1.26	2.66	0.60	0.06	3.83	0.12	72.91	0.07	0.97

Seven cement pastes were prepared at w/c ratios by weight of 0.30, 0.35, 0.40, 0.45, 0.50, 0.55 and 0.60. Immediately the sensor was immersed in the fresh cement paste and the CPMG technique was used to obtain the transverse magnetization decay, which was in all cases best fit to a mono-exponential decay function to determine the NMR signal amplitude and the T_2 decay constant.

Samples from the fresh cement pastes were only taken from those having w/c ratios of 0.30, 0.40, 0.50 and 0.60. They were introduced in small plastic tubes with appropriate size to fit into the sensor and sealed to avoid ingress or loss of moisture. The transverse magnetization decay was determined in the hardened state at 1, 3, 7, 14, and 28 days of age. It was verified that the plastic tubes did not provide any NMR signal.

2.2.3. NMR Sensors Embedded in Hydraulic Concrete Cylinders

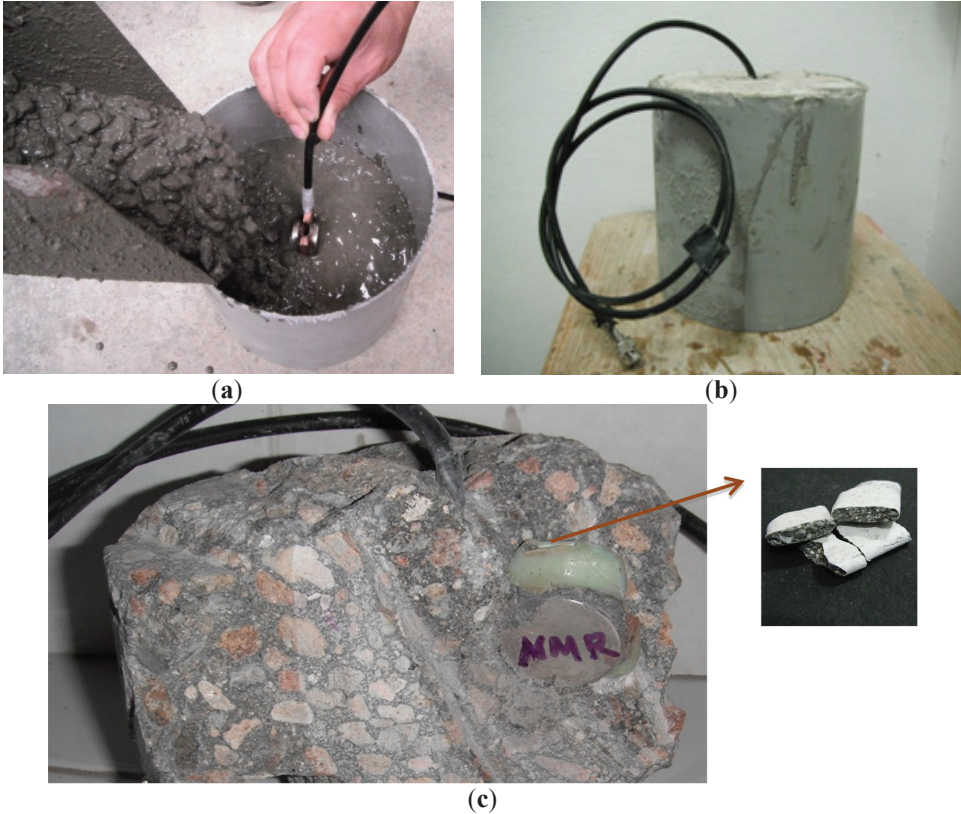
Four sensors were built to monitor changes in the transverse magnetization decay during hydration of cement in concrete. Two mixes with w/c ratios of 0.30 and 0.60 were prepared with the proportions given in Table 4. The materials used were river sand having a fineness modulus of 2.9, specific gravity of 2.65, and absorption of 1.73%. The gravel had a maximum size of $\frac{3}{4}$ inch, specific gravity of 2.68, and absorption of 1.51%. The chemical composition of the fine aggregate used is given in Table 1. Tap water was used to prepare the concrete mixtures.

Table 4. Mixture proportions used to prepare 1 m³ of concrete.

Materials	Water-to-Cement ratio, by Weight	
	w/c = 0.30	w/c = 0.60
Coarse aggregate (Kg)	948	837
Fine aggregate (Kg)	671	794
Ordinary Portland cement (Kg)	519	345
Water (Kg)	184	232
Superplasticizer (L)	4.67	-

From each concrete mixture two cylinders measuring 150 mm in diameter and 150 mm in height were cast and immediately one sensor was embedded to a half of the total height of the cylinder (Figure 6a). Before embedding the sensors in the concrete specimens, the SNR for each sensor was determined by obtaining the NMR signal from a polymer phantom. Seven specimens in triplicate measuring 100 mm in diameter and 200 mm in height were cast for compressive strength testing at 1, 3, 7, 14, 21, 28 and 56 days of age (a total of 21 cylinders). After 24 h, all the specimens were removed from the molds and stored in a moist room at 22 ± 3 °C until testing. At this time, the cylinders with the embedded sensors (Figure 6b) were non-destructively tested using a portable Magritek Kea² spectrometer to obtain the transverse magnetization decay using the CPMG technique. After each cylinder was destructively tested under compression, a sample from the center was taken for NMR measurements in an Oxford Instruments Maran DRX-HF 12/50 spectrometer (Oxford Instruments, Abingdon, UK) at 12.9 MHz, to compare the results obtained with the embedded sensors.

Figure 6. (a) Sensor embedded in fresh concrete during external vibration of the material, which made it easy to introduce cement paste and small fine aggregate particles into the sensor; (b) Sensor in a hardened concrete cylinder; (c) After breaking a hardened specimen to extract the sensor, it was observed that only cement paste and some fine aggregate particles (size < 1 mm) had penetrated into the sensor and filled the measurement volume.



2.2.4. Influence of Temperature and Reinforcing Steel Bars on Sensor Resonant Frequency

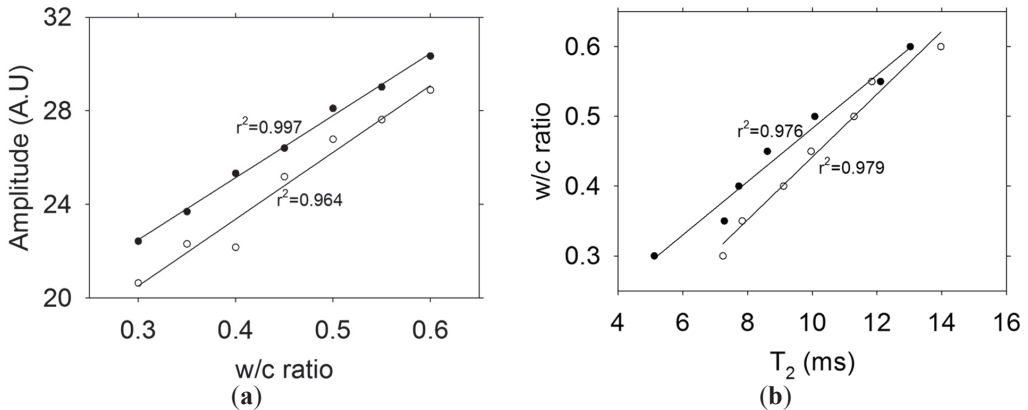
To measure the effects of temperature on sensor resonant frequency, it was located in a controlled environment at 17.5, 20 and 24 °C. In order to determine the influence of a steel rebar, the sensor was located at 0, 14 and 28 mm (using pieces of 14 mm thick plywood) from a 25.4 mm diameter steel rebar. The thickness of the plywood used to separate the sensor from the steel rebar was 14 mm. In both cases, the magnetic field changes were measured with a gaussmeter and the corresponding resonant frequency determined.

3. Results and Discussion

3.1. Fresh Cement Pastes

Figure 7a presents the relationship between the NMR signal and the water-to-cement ratio (w/c) by weight of fresh grey and white cement pastes. As expected, there is a linear relationship between the signal amplitude and the amount of water present in the cement pastes. Figure 7b shows the relationship between T_2 and the w/c ratio for the fresh cement pastes. It is observed that T_2 increases with increasing w/c ratio. This is in agreement with the fact that the w/c ratio is related to the distance between cement particles [14]. That is, in high w/c ratio pastes the cement particles are more separated than in low w/c ratio pastes. For the same w/c ratio, an enhanced relaxation produced by the higher amount of paramagnetic impurities (mainly iron) found in ordinary Portland cement (Table 1), is reflected in shorter T_2 values with respect to white cement. From these results, it is seen that both approaches (signal amplitude and T_2 values) would make it possible to determine the actual w/c ratio in fresh cement paste or concrete.

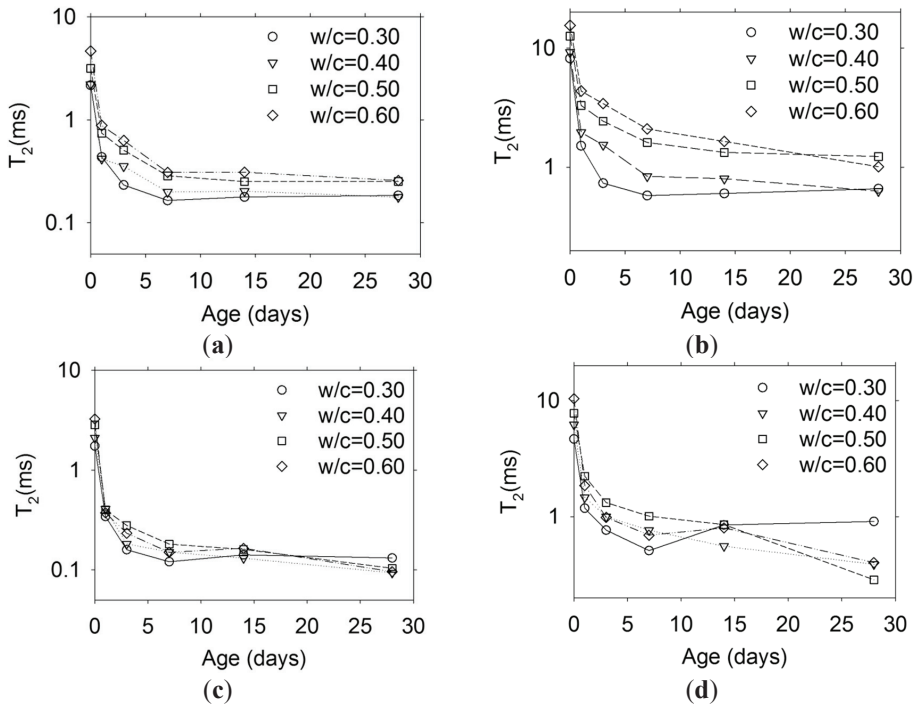
Figure 7. (a) Relationship between w/c ratio and NMR signal amplitude of cement pastes; (b) Relationship between T_2 relaxation times and w/c ratio of cement pastes. The symbols indicate: ● ordinary Portland cement, ○ white Portland cement.



3.2. Hardened Cement Pastes

Increasing hydration times cause the microstructure to change as long as there is enough water to support the hydration process [1]. Figure 8 shows the T_2 variation with hydration time for the two types of cement pastes at different w/c ratios. It is observed that the short and long lifetime components, corresponding to gel and capillary pores [15], respectively, decrease with increasing age due to pore refinement caused by cement hydration. In Figure 8d it is interesting to note an increase in the long lifetime component only for the cement paste with w/c ratio of 0.30. Since this sample was sealed, there was no external water source that could help mitigate the autogenous shrinkage occurring in low w/c ratio materials [16] and micro-cracking was developed, thus increasing the surface-to-volume ratio of the porosity.

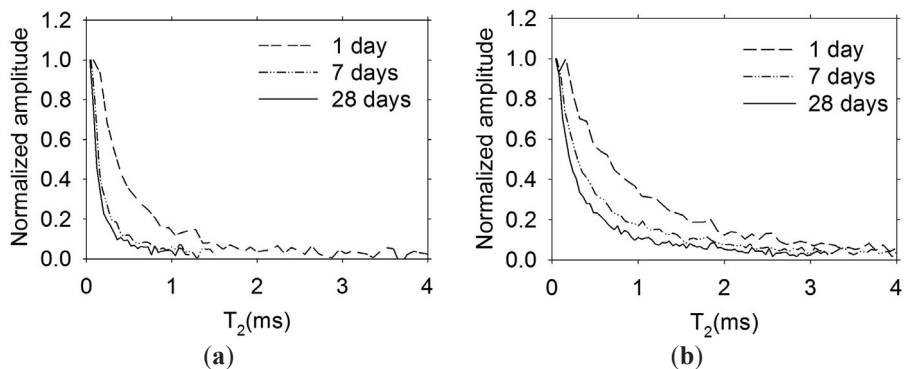
Figure 8. Evolution of the short and long lifetime components for (a) white cement-short T_2 ; (b) white cement-long T_2 ; (c) grey cement-short T_2 ; and (d) grey cement-long T_2 .



3.3. Performance of the Sensors in Hardened Hydraulic Concrete

The normalized transverse magnetization decay at 1, 7 and 28 days of age obtained with the sensors embedded in concrete are shown in Figure 9. A more rapid decay in the specimen prepared with concrete with a w/c ratio = 0.30 is observed. This is expected, since the pores are finer with respect to the higher w/c ratio concrete.

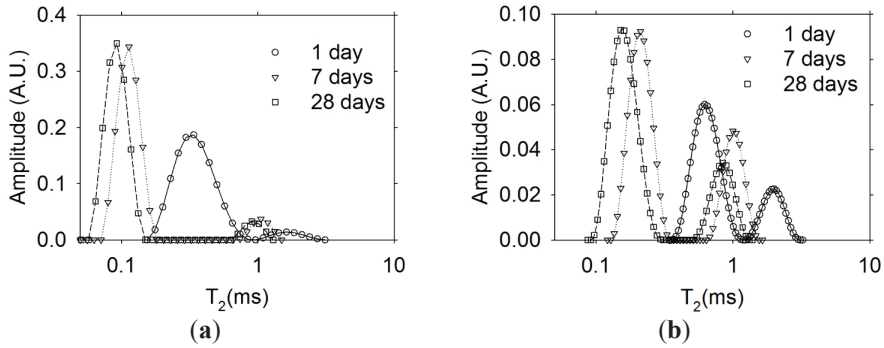
Figure 9. Normalized transverse magnetization decay measured with the embedded sensors in concrete (a) w/c ratio = 0.30 and (b) w/c = 0.60.



Comparing the SNR of the signal obtained when using the new design in concrete with w/c ratio of 0.60 (SNR = 101 for 8192 scans) to the one reported in reference [10], which was mortar with w/c ratio of 0.60 (SNR= 27.3 for 8192 scans), there is an improvement factor of about 4. This increase in sensitivity was a result of a higher magnetic field (0.38 Tesla), homogeneity and larger sensitive volume due to the nature of the magnet arrangement with respect to the unilateral design (0.24 Tesla).

Figure 10 shows the Inverse Laplace Transformation of the transverse magnetization decay data [17] shown in Figure 9. As expected, the T_2 distributions indicate that a finer porosity is obtained in the concrete with w/c ratio of 0.30 compared to the concrete with w/c ratio of 0.60 (lower T_2 values in concrete with w/c of 0.30). On the other hand, in concrete with w/c ratio of 0.30, it is only possible to resolve one peak due to the quality of the NMR signal obtained. However, in the concrete with w/c ratio of 0.60, the signal obtained was of better quality and the ILT resolves the two types of pores known in cement-based materials: capillary and gel pores [1].

Figure 10. Inverse Laplace Transformation of the transverse magnetization decay measured with the embedded sensors in concrete (a) w/c ratio = 0.30; and (b) w/c = 0.60.



The size of the gel pores in a hydrating cement paste are in the order 1 to 3 nm, whereas the size of the capillary pores depends on the w/c ratio and the degree of hydration. The size of capillary pores are in the order of 10 to 200 nm for a hydrated cement paste having a w/c ratio of 0.60, and from 10 to 90 nm for a paste with a w/c ratio of 0.30 [1]. The materials used in the present study would have gel and capillary pores sizes similar to those mentioned before.

The NMR relaxation times are sensitive to the pore structure of materials and decrease as the pore size also decreases. These times vary widely for chemically bound hydrogen, hydrogen adsorbed on the surfaces, and hydrogen in water confined in small pores. It is known that the transverse relaxation rate $1/T_2$ is proportional to the surface to volume ratio (S/V) of the pore system, as expressed by Equation (1) [18]:

$$\frac{1}{T_2} = \rho \frac{S}{V} \quad (1)$$

where ρ = T_2 surface relaxivity (T_2 relaxing strength of the pore surfaces), varies with the chemical composition of the pore surface.

It is a common practice in magnetic resonance to use T_2 as a proxy for pore size and not to convert the data to actual pore size. Figure 11 shows the transverse relaxation rate ($1/T_2$) versus compressive strength of concrete cylinders with $w/c = 0.30$. The transverse magnetization decay was better fit to a bi-exponential decay, therefore short and long lifetime components were obtained. For both sensors it is observed that the highest correlation is obtained with the short lifetime component ($r^2 \geq 0.95$). The poor correlation observed with the long lifetime component, which is related to large capillaries, might be affected by internal micro-cracking caused by significant autogenous shrinkage occurring in materials with low w/c ratio [16,18].

Figure 11. Transverse relaxation rate versus compressive strength for concrete $w/c = 0.30$ for (a) Sensor 1 and (b) Sensor 2. The symbols indicate: ● Short lifetime component, ○ Long lifetime component.

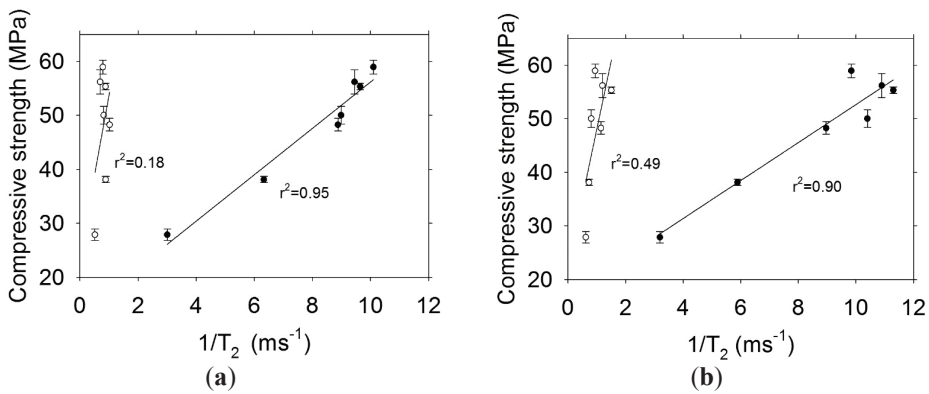


Figure 12 shows the results obtained for the relationship between the transverse relaxation rate and the compressive strength of concrete with w/c ratio = 0.60. In this case, both components (short and long lifetime) are highly correlated to mechanical strength. The highest r^2 is obtained with the short lifetime component ($r^2 > 0.97$). The effects of autogenous shrinkage in concrete with high w/c ratio are negligible [19], therefore micro-cracking should not have any significant effect on these specimens and the long lifetime component observed has information only from capillary porosity.

The correlations obtained from the T_2 measurements undertaken with the Oxford Instruments Maran DRX-HF 12/50 are shown in Figure 13. The r^2 are similar to those obtained with the sensors. Because the samples used small pieces taken from destructive testing, extensive cracking was evident by visual examination. This condition affected the long T_2 and the correlation in concrete with low and high w/c ratio had a very low r^2 .

Figure 12. Transverse relaxation rate versus compressive strength for concrete $w/c = 0.60$ for (a) Sensor 3 and (b) Sensor 4. The symbols indicate: ● Short lifetime component, ○ Long lifetime component.

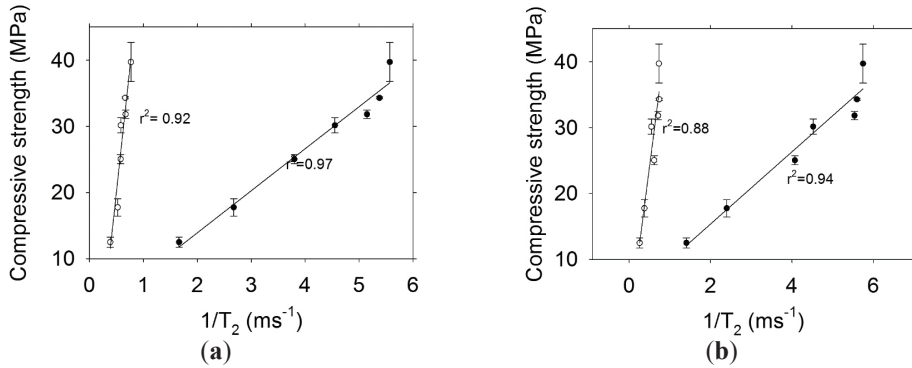
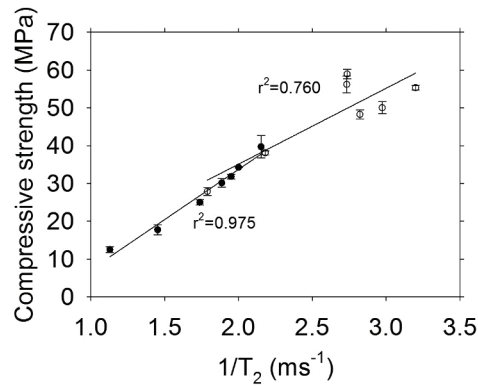


Figure 13. Transverse relaxation rate obtained with the Oxford Instruments Maran DRX-HF 12/50 system versus compressive strength. The symbols indicate: ● Concrete $w/c = 0.60$, ○ Concrete $w/c = 0.30$.



3.4. Influence of Temperature and Reinforcing Steel Bars on Sensor Resonant Frequency

Table 5 shows the frequency variation due to changes in ambient temperature or by the presence of a steel rebar.

Table 5. Effect of ambient temperature and distance to a steel rebar on the frequency of the sensor.

Temperature (°C)	Frequency (MHz)
17.5	15.967
20.0	15.900
24.0	15.883
Distance (mm)	Frequency (MHz)
≥28.0	15.883
14.0	16.133
0.0	ND

It is observed that the frequency decreases with increasing temperature while the frequency increases with reduced distance of the sensor to the steel rebar. These changes in frequency can be easily accommodated with the external tuning circuit. Based on the limited data obtained related to the influence of temperature on the sensor's magnetic field, a reasonable range of variation could be from 15 to 30 °C, which would produce changes in frequency that can be accommodated with the external tuning circuit that has a range of 1 MHz. Since the effects on frequency caused by the presence of steel bars were measured at 14 and 28 mm (one and two times the thickness of the plywood used to separate the steel from the sensor), 28 mm might be the minimum distance because the presence of the steel does not affect the magnetic field of the sensor. At shorter distances and depending on the steel bar diameter, it might create significant magnetic field gradients due to the corrugated surface of the reinforcing steel used in the construction industry. With respect to the direction, because the sensor is considered as a point sensor, it would seem to have no natural direction.

4. Conclusions

An improved miniature embeddable NMR sensor for use in cement-based materials was designed, built and characterized. Changes in frequency due to temperature variations and the presence of steel rebars can be accommodated using an external tuning circuit. The sensor was successfully used to detect water in fresh cement pastes and to monitor porosity refinement in hardened cement pastes and concretes containing ordinary materials routinely used in the construction industry. A linear relationship exists between the relaxation rate and the compressive strength of concrete mixtures at low and high w/c ratios. The results demonstrate that practical applications are possible and they will be pursued.

Acknowledgments

Prisciliano Cano acknowledges the Conacyt from Mexico for funding the project ID code CB 103763. Bruce J. Balcom thanks the Canada Chairs program for a Research Chair in MRI of materials. Solis Najera would like to thank UNAM-DGAPA for his postdoctoral stipend. Floriberto Diaz acknowledges Conacyt from Mexico for the funding provided for his MSc studies.

Conflicts of Interest

The authors declare no conflict of interest.

References

1. Mehta, P.K.; Monteiro, J.M. *Concrete, Microstructure, Properties and Materials*, 3rd ed.; McGraw Hill: New York, NY, USA, 2006; pp. 121–192.
2. ASTM F 2170-02, Standard Test Method for Determining Relative Humidity in Concrete Floor Slabs Using In-Situ Probes. Available online: <http://www.astm.org/Standards/F2170.htm> (accessed on 18 November 2013).

3. Carino, N.J. *Concrete Construction Engineering Handbook*; CRC Press: Boca Raton, FL, USA, 1997.
4. Blinc, R.; Dolinsek, J.; Lahajnar, G.; Sepe, A.; Zupancic, I.; Zumer, S.; Milia, F.; Pintar, M.M. Spin-lattice relaxation of water in cement gels. *J. Phys. Sci.* **1988**, *43*, 1026–1038.
5. Jehng, J.Y.; Sprague, D.T.; Halperin, W.P. Pore structure of hydrating cement paste by magnetic resonance relaxation analysis and freezing. *Magn. Reson. Imaging* **1996**, *14*, 785–791.
6. Apih, T.; Lahajnar, A.; Sepe, A.; Blinc, R.; Milia, F.; Cvelbar, R.; Emri, I.; Gusev, B.V.; Titova, L.A. Proton spin-lattice relaxation study of the hydration of self-stressed expansive cement. *Cem. Concr. Res.* **2001**, *31*, 263–269.
7. Blumich, B.; Blumler, P.; Eidmann, G.; Guthausen, A.; Haken, R.; Schmitz, U.; Saito, K.; Zimmer, G. The NMR-mouse: Construction, excitation, and applications—application to NMR imaging of elastomers. *Magn. Reson. Imaging* **1998**, *16*, 479–484.
8. Boguszynska, J.; Brown, M.C.A.; McDonald, P.J.; Mitchell, J.; Mulheron, M.; Tritt-Goc, J.; Verganelakis, D.A. Magnetic resonance studies of cement based materials in inhomogeneous magnetic fields. *Cem. Concr. Res.* **2005**, *35*, 2033–2040.
9. Manz, B.; Coy, A.; Dykstra, R.; Eccles, C.D.; Hunter, M.W.; Parkinson, B.J.; Callaghan, P.T. A mobile one-sided NMR sensor with a homogeneous magnetic field: The NMR-MOLE. *J. Magn. Reson.* **2006**, *183*, 25–31.
10. Cano-Barrita, P.F.J.; Marble, A.E.; Balcom, B.J.; García, J.C.; Masthikin, I.V.; Thomas, M.D.A.; Bremner, T.W. Embedded NMR sensors to monitor evaporable water loss caused by hydration and drying in Portland cement mortar. *Cem. Concr. Res.* **2009**, *39*, 324–328.
11. Díaz-Díaz, F. Sensor Miniatura de Resonancia Magnética Nuclear (NMR) de Bajo Costo Para Caracterizar de Manera no Destructiva Materiales Basados en Cemento (in Spanish). Master's Thesis, Instituto Politécnico Nacional-CIIDIR Unidad Oaxaca, Oaxaca, Mexico, January 2013.
12. Meiboom, S.; Gill, D. Modified spin–echo method for measuring nuclear relaxation times. *Rev. Sci. Instrum.* **1958**, *29*, 688–691.
13. Ludwik, R.; Bretchko, P. *RF Circuit Design Theory and Applications*; Prentice-Hall: Upper Saddle River, NJ, USA, 2000; pp. 37–130.
14. Bentz, D.; Aitcin, P.C. The hidden meaning of water-cement ratio. *Concr. Int.* **2008**, *30*, 51–54.
15. Halperin, W.P.; Jehng, J.Y.; Song, Y.Q. Application of spin-spin relaxation to measurement of surface area and pore size distributions in a hydrating cement paste. *Magn. Reson. Imaging* **1994**, *12*, 169–173.
16. Tazawa, E.; Miyazawa, S. Experimental study on mechanism autogenous shrinkage of concrete. *Cem. Concr. Res.* **1995**, *25*, 1633–1638.
17. Borgia, G.C.; Brown, R.J.S.; Fantazzini, P. Uniform-penalty inversion of multiexponential decay data. *J. Magn. Reson.* **1998**, *132*, 65–77.
18. Coates, G.; Xiao, L.; Prammer, M. *NMR Logging Principles and Applications*; Halliburton Energy Services: Houston, TX, USA, 1999; pp. 45–67.
19. Aitcin, P.C. Demystifying autogenous shrinkage. *Concr. Int.* **1999**, *21*, 54–56.

Degradation of Phosphate Ester Hydraulic Fluid in Power Station Turbines Investigated by a Three-Magnet Unilateral Magnet Array

Pan Guo, Wei He and Juan C. García-Naranjo

Abstract: A three-magnet array unilateral NMR sensor with a homogeneous sensitive spot was employed for assessing aging of the turbine oils used in two different power stations. The Carr-Purcell-Meiboom-Gill (CPMG) sequence and Inversion Recovery-prepared CPMG were employed for measuring the ^1H -NMR transverse and longitudinal relaxation times of turbine oils with different service status. Two signal components with different lifetimes were obtained by processing the transverse relaxation curves with a numeric program based on the Inverse Laplace Transformation. The long lifetime components of the transverse relaxation time $T_{2\text{eff}}$ and longitudinal relaxation time T_1 were chosen to monitor the hydraulic fluid aging. The results demonstrate that an increase of the service time of the turbine oils clearly results in a decrease of $T_{2\text{eff, long}}$ and $T_{1, long}$. This indicates that the $T_{2\text{eff, long}}$ and $T_{1, long}$ relaxation times, obtained from the unilateral magnetic resonance measurements, can be applied as indices for degradation of the hydraulic fluid in power station turbines.

Reprinted from *Sensors*. Cite as: Guo, P.; He, W.; García-Naranjo, J.C. Degradation of Phosphate Ester Hydraulic Fluid in Power Station Turbines Investigated by a Three-Magnet Unilateral Magnet Array. *Sensors* **2014**, *14*, 6797–6805.

1. Introduction

Since the discovery of their excellent anti-wear and fire resistance properties in the 1940s, the use of phosphate ester hydraulic fluids by industry has steadily increased [1,2]. In power systems, phosphate esters are used primarily as fire-resistant base-stocks in turbines for speed governing, lubricating, radiating, cleaning and vibration damping [3]. In operation at high temperatures, in the presence of oxygen, water vapor and catalytically active metals, these synthetic oils are severely stressed. These conditions may lead to a rapid degradation of their oxidation and the hydrolysis resistance, which may cause corrosion and even failure of the system [4–6]. In order to prevent change of viscosity, formation of deposits and corrosion, oil degradation must be minimized [7]. Therefore, the hydraulic system is usually equipped with a by-pass regenerating unit [3] to remove acidic substances and water, as well as solid particulate contaminants. During the aging process, the oil continuously degrades and is regenerated until it is non-renewable by accumulation of degradation products. It is very expensive (about 110,000 USD) to replace the oil in power plant turbines [8]. Consequently, a quality control measurement is needed for safe and economic operation of the power system.

With deterioration [8] of phosphate ester fire resistant oils the color deepens and precipitates are produced in severe cases. During aging, the acidity, water content, viscosity, dielectric constant, foam characteristic, and air release property, *etc.* may all change [7,9].

Traditionally phosphate ester aging was evaluated by observing color and turbidity changes [3]. This method is less rigorous, and sometimes led to major accidents and resulted in irreparable damage and significant economic losses. More recently turbine operators are required to test the appearance, acidity, resistivity and mechanical impurities of the oil at least once a week, and measure the moisture content, flash point and viscosity at least once per season [9]. Some sites even test the thermo-oxidative stability and corrosivity under simulated aging conditions, where the increase of acidity and viscosity, the formation of sludge and corrosion against various metals are controlled [7]. However, such a test program is expensive and time consuming and cannot be applied to a large number of samples in the surveillance of used oils.

NMR has been used in the past to investigate materials aging and degradation. A prominent and most practical example is the development of unilateral magnetic resonance (UMR), where the NMR experiment is carried out in the inhomogeneous field produced on one side of a portable magnet. UMR has become a powerful technique in different areas of application. New applications [10] have been developed in well-logging [11], biomedicine [12], material analysis [13] and characterization of food products [14]. Since UMR is simpler and much less expensive than traditional NMR, and produces reliable information, the development of new UMR sensors and applications should continue in the near future.

This paper presents a magnetic resonance method for phosphate ester analysis employing a three-magnet array [15,16] as a sensor. The intention of this work is to develop a rapid and simple method for estimating the degree of degradation of phosphate ester hydraulic fluids in power plant turbines. We have demonstrated that the new sensor produces reliable results and can be employed to follow the oil aging process. In the following sections, the features of the magnet and measurements on phosphate ester fire resistant oils are discussed.

2. Experimental Section

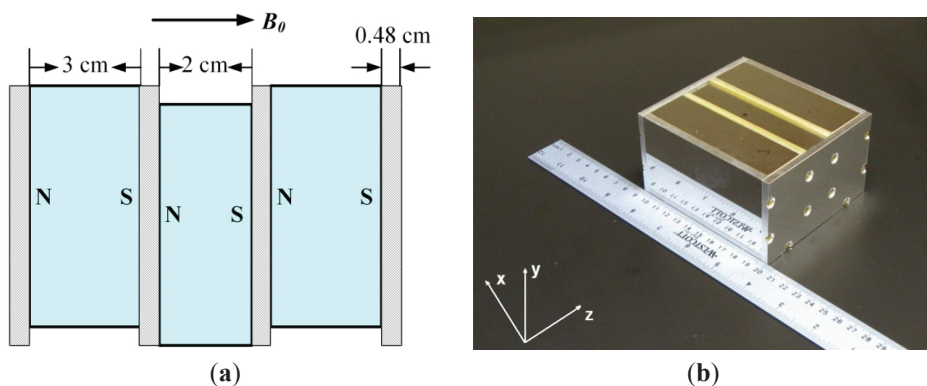
2.1. Magnet

Magnets of different types can be employed for this measurement. Closed or semi-closed magnets allow more sensitive measurements than unilateral magnets, but require of a more complicated design and adjusting process and are more sensitive to temperature variation. Unilateral magnets are in general very simple to build and can also produce reliable results.

Figure 1 shows the structure of the three-magnet array unilateral magnet developed by the UNB MRI Centre in Canada. It is a simple array of three magnet blocks with the magnetic field oriented in the same direction. A vertical displacement of the central block allows generating a homogeneous spot [15] or an extended constant gradient [16]. The design is compact and safe and the weight of the magnet array is 5 kg. The mathematical equations to describe the magnetic field distribution are relatively simple, which makes easy the simulation. It should be marked that the magnetic field homogeneity (around 1% of B_0) for the homogeneous spot design is still far away from the values employed for classic NMR experiments. The major advantages of this magnet are its simplicity and the relatively remote homogenous spot. The static magnetic field B_0 is parallel to its surface (along z axis in Figure 1) which allows employment of a very simple surface coil with good sensitivity.

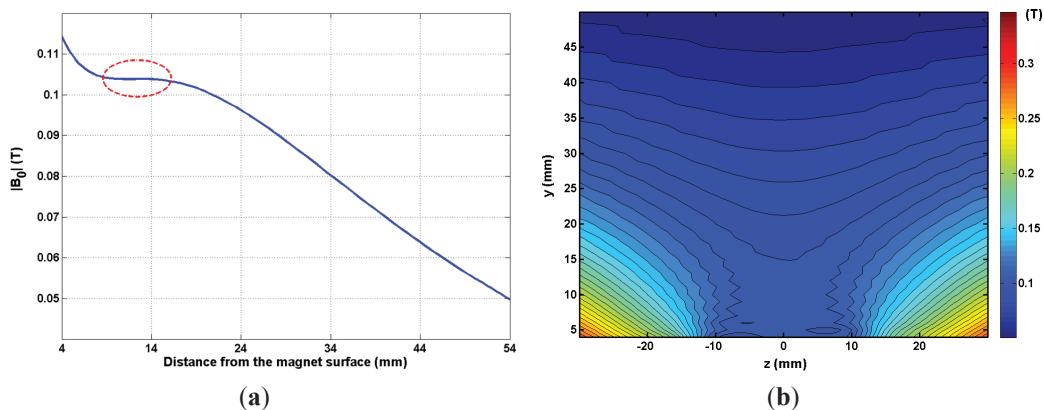
The size of the measurement spot results from the combination of B_0 distribution, bandwidth of the excitation RF pulses, bandwidth of the receiver and parameters of the surface coil like size, shape and quality factor (Q).

Figure 1. Schematic (a) and photo (b) of the three-magnet array. The centre of the upper surface of the magnet array corresponds to the position (0,0,0) in the coordinate system.



In order to adjust and characterize the magnet, magnetic field measurements were undertaken employing a three axis Hall effect magnetic field probe (Lake-Shore Cryotronics Inc., OH, USA) and a computer controlled three axis plotter (Velmex Inc., MI, USA). Figure 2a plots the magnetic field magnitude as a function of distance from the centre of the magnet. The sensitive spot of the magnet array is 8 mm to 17 mm from the magnet surface. The proton resonance frequency at this position is 4.485 MHz. Figure 2b shows a contour plot of the magnetic field along the yz plane over the magnet ($x = 0$).

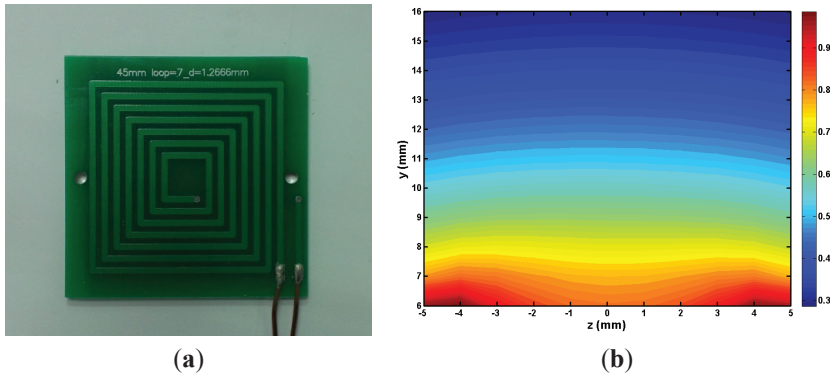
Figure 2. (a) Plot of magnetic field magnitude B_0 as a function of the distance from the centre of the magnet surface. The circled area indicates the sensitive spot position; (b) Contour plot of the magnetic field magnitude B_0 in the yz plane. The field is reasonably symmetric.



2.2. RF Coil

A square spiral RF coil, 45 mm in length with 7 turns, fabricated on a 1.2 mm thick printed circuit board (Figure 3a) was employed for the measurements since the RF field B_1 is required to be perpendicular to the static magnetic field B_0 . The lead width was 1.5 mm and the spacing 1.27 mm. The resistance and inductance of the coil were 0.41Ω and $1.439 \mu\text{H}$, respectively. The loaded quality factor (Q_L), measured with the coil placed on the magnet was 30. The RF coil was tuned 4.485 MHz, which is the proton resonance frequency at the centre of the spot. The dead time of the coil is 35 μs . The RF field above the coil, simulated employing the simulation software Maxwell 3D (Ansoft, Pittsburgh, PA, USA), is shown in Figure 3b. A 4.766 mm (3/16") fiberglass spacer was placed between the coil and the magnet to assure a better use of the homogeneous spot of the magnet and the B_1 of the coil. The distance from the RF coil upper surface to the sensitive spot is 2 mm to 11 mm.

Figure 3. (a) Photo of the RF coil; (b) The simulated result of the normalized RF field distribution in the central perpendicular plane. The B_1 field is perpendicular to the coil. $y = 6 \text{ mm}$ is the upper surface of the RF coil.



2.3. Experiment Details

Two groups of turbine phosphate ester hydraulic fluids (Table 1), in service at two different power stations, were employed for the measurements. They were housed in five cylindrical glass vessels. The dimensions (4 cm in diameter and 7 cm in length) of the glass vessels were chosen to guarantee full coverage of the measurement spot (1 cm along z axis, 1 cm along y axis and 2 cm along x axis) with the sample.

Table 1. Turbine hydraulic fluid for the measurements.

Power Station Name	State
Beilun	New
	In service
	Eliminated
Yuyao	New
	In service

All measurements were carried out with a Kea2 console (Magritek, Wellington, New Zealand), connected to a RF power amplifier (TOMCO Technologies, Stepney, Australia) at 17 ± 0.3 °C. The ^1H NMR transverse relaxation time ($T_{2\text{eff}}$) [17] and longitudinal relaxation time (T_1) were obtained with the standard Carr-Purcell-Meiboom-Gill (CPMG) sequence and T_1 Inversion Recovery with CPMG T_1 IR Add sequence, respectively. For the CPMG sequence, the 90° pulse width was $8 \mu\text{s}$, the attenuations of the 90° and 180° pulse were -18 dB and -12 dB, the echo time was $150 \mu\text{s}$, the number of echoes was 2048, the repetition time was 400 ms, and 256 scans were averaged. The total measurement time was 5 min. For the T_1 IR Add sequence, the time between the first 180° pulse and the 90° pulse was varied from 1 ms to 400 ms by log spacing with 40 steps, the number of echoes was 32, and other parameters were the same as in the CPMG sequence. The total measurement time was 3 h.

3. Results and Discussion

3.1. Transverse Relaxation Time Measurements

Once the CPMG decay from the sample (Figure 4) was obtained, an Inverse Laplace Transformation (ILT) of the CPMG data was performed with the Contin program [18]. In Figure 5 the $T_{2\text{eff}}$ distributions of two groups of turbine oils are shown. The amplitude of the short lifetime component is approximately three times less than the long component, so that the CPMG decay is dominated by the longer transverse relaxation time, $T_{2\text{eff},\text{long}}$. The measurement was repeated five times for each sample to check the reproducibility of the method. As the reproducibility of the long component is much better than the short component, only $T_{2\text{eff},\text{long}}$ will be discussed hereafter.

In Figure 5, all of the $T_{2\text{eff}}$ distribution curves have two symmetric peaks that are well separated. This behavior allows a much simpler bi-exponential fitting to be employed. In addition to more reliable results the simplicity of the bi-exponential fitting (Equation (1)) [19] makes it better option for practical measurements. Only the $T_{2\text{eff},\text{long}}$ obtained from the bi-exponential fit was chosen for display to show the contribution of the more representative component inside the oil (Table 2). The aging status of different turbine oils can be distinguished in the measured $T_{2\text{eff},\text{long}}$ and an increase in service time yields a decrease in transverse relaxation time $T_{2\text{eff},\text{long}}$. The differences in $T_{2\text{eff},\text{long}}$ are not large but they are reproducible and reliable:

$$M(t) = A_{\text{short}} \exp\left(-\frac{t}{T_{2\text{eff},\text{short}}}\right) + A_{\text{long}} \exp\left(-\frac{t}{T_{2\text{eff},\text{long}}}\right) \quad (1)$$

Figure 4. Semi-logarithmic plot of a CPMG decay from a sample of turbine hydraulic fluid.

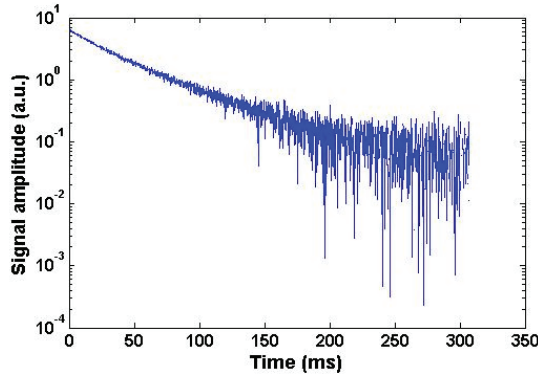


Figure 5. $T_{2\text{eff}}$ distributions from the CPMG measurement for the Beilun power station (a) and the Yuyao power station (b).

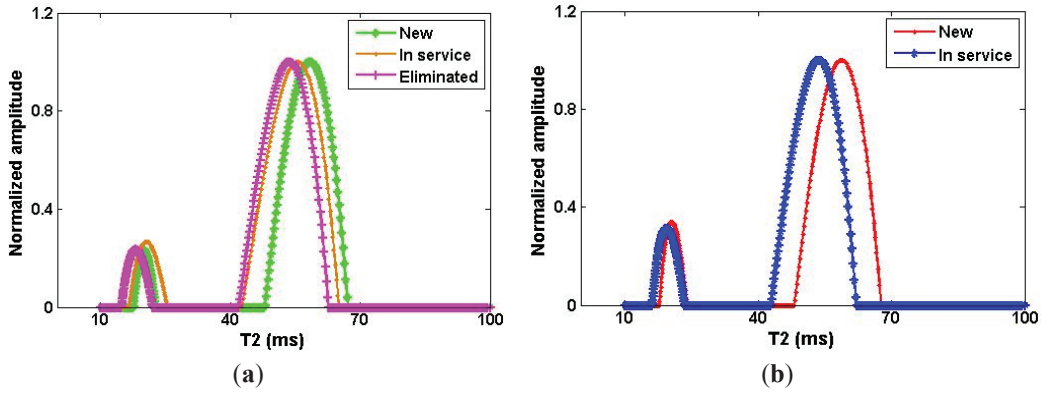


Table 2. The $T_{2\text{eff,long}}$ of different turbine oils extracted from bi-exponential fitting.

Power Station Name	Status	$T_{2\text{eff,long}}$ (ms)
Beilun	New	75.8 ± 0.9
	In service	65.8 ± 0.5
	Eliminated	61.9 ± 0.8
Yuyao	New	66.9 ± 0.7
	In service	60.8 ± 1.1

3.2. Longitudinal Relaxation Time Measurements

Since in an inhomogeneous magnetic environment it is practically impossible to obtain FID signals, inversion recovery as described by Hurliman in [20] with CPMG added, as implemented in the Prospa software (Magritek, Wellington, New Zealand) was employed as the sequence for measuring T_1 of the oils. The CPMG echo train was summed on the spectrometer before being returned to the software Prospa. The integrals of the CPMG echoes were fitted to Equation (2):

$$A = A_0 \left(a * \exp \left(-\frac{t}{T_{1,short}} \right) + b * \exp \left(-\frac{t}{T_{1,long}} \right) \right) \quad (2)$$

For clarity, only the first 30 points of the curves are shown in Figure 6. As the reproducibility of the short component was not reliable, only the long component $T_{1,long}$ was chosen to represent the longitudinal relaxation time of the turbine oils. From Table 3, an increase in the service time yields a decrease in longitudinal relaxation time.

Figure 6. T_1 decay curves of the turbine oils of the Beilun power station (a) and the Yuyao power station (b).

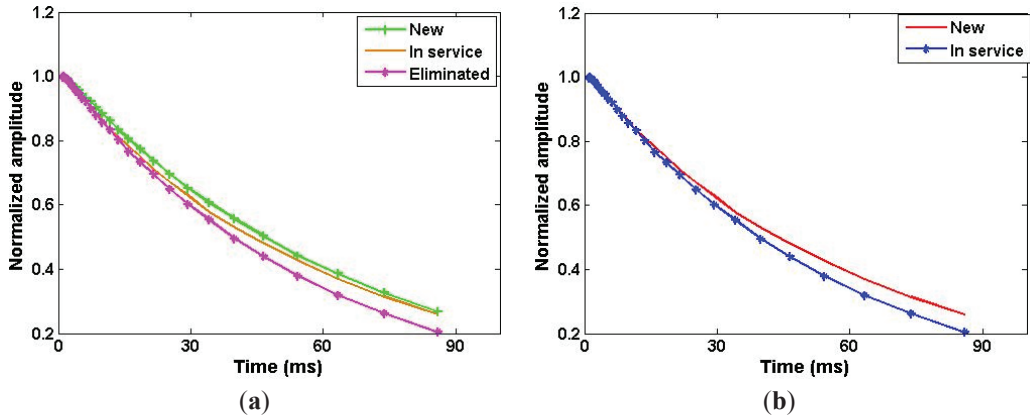


Table 3. The $T_{1,long}$ of different turbine oils extracted from the T_1 distribution curves.

Power Station Name	Status	$T_{1,long}$ (ms)
Beilun	New	73 ± 1
	In service	69.5 ± 0.7
	Eliminated	64.5 ± 0.6
Yuyao	New	62 ± 0.6
	In service	53 ± 2.0

4. Conclusions

The aging status of phosphate ester hydraulic fluids with different service times, from two different power stations, has been studied by ^1H relaxation time measurements with a three-magnet array unilateral magnet as a sensor. We demonstrate that the aging results in a decrease in $T_{2eff,long}$ and $T_{1,long}$ relaxation times. Therefore, $T_{2eff,long}$ and $T_{1,long}$ can be used as the indices of turbine oil aging. This method is simple and produces reliable results. The next step will focus on the measurements of more turbine oils to establish a statistical data base and measurements of other sample parameters, such as molecular diffusion, with unilateral magnetic resonance. We propose this method to predict when the turbine oils should be eliminated to prevent unexpected accidents in power stations.

Acknowledgments

This work was financially supported by the National Natural Science Foundation of China (No. 51107150 and 51377186). Pan Guo thanks the scholarship fund from China Scholarship Council for a visiting fellowship at UNB. We thank Bruce J. Balcom for providing the magnet. We thank the Zhejiang electric power company for supplying the turbine oils.

Author Contributions

Pan Guo built the RF probe, finished all the measurements, processed the data and wrote the paper; Wei He provided the idea of measuring turbine oils and supplied the samples; Juan C. García-Naranjo built the magnet and measured the magnetic field.

Conflicts of Interest

The authors declare no conflict of interest.

References

1. Rudnick, L.R.; Zaweski, E.F. Phosphate Esters. In *Synthetic Lubricants and High-Performance Functional Fluid*, 2nd ed.; Marino, M.P., Placek, D.G., Eds.; Marcel Dekker Inc.: New York, NY, USA, 1997; pp. 103–140.
2. Wright, J. Phosphate ester fluids-benefits and limitations. *Mach. Lubric.* **2009**, *11*, 1.
3. Liu, Y.L. The development and present situation of domestic turbine oils criteria in service. *Lubric. Oil* **2006**, *21*, 9–13.
4. Beatty, D.; Greaves, M. PAGs are rising to the top of the synthetic market. *Mach. Lubric.* **2006**, *9*, 1.
5. Sibul, B.; Crandall, L. EHC Fluid Contamination is a Major Cause of Turbine Forced Outages. Steam Turbine High Pressure System Fluid Solution. Available online: http://www.sibul.com/articles_details.php?article_id=3 (accessed on 1 November 2013).
6. Yan, B.; Lai, X.D.; Long, J.H.; Huang, X.; Hao, F. Dynamic characteristics analysis of an oil turbine. *Proc. Eng.* **2012**, *28*, 12–17.
7. Bartl, P.; Zuber, K.; Leipold, M.; Zeman, A. Quality control of used synthetic aviation turbine oils by analytical methods i. determination of the antioxidative capacity by HPLC and GC. *Fresenius' Zeitschrift für Anal. Chem.* **1983**, *314*, 25–28.
8. Zhang, X.M.; Yuan, J.; Chen, B.; Li, P.; Zhang, Y.B.; Wang, L.C. Cause of quality degradation and dehydration purification technology of phosphate ester fire-resistant oil. *Environ. Sci. Technol.* **2012**, *35*, 129–133.
9. Dong, Z.Q. The operation and maintenance for the oil used in regulating system of steam turbine. *North. Electr. Power Technol.* **2001**, *3*, 12–14.
10. Blümich, B.; Perlo, J.; Casanova, F. Mobile single-sided NMR. *Progr. Nuclear Magn. Resonance Spectrosc.* **2008**, *52*, 197–269.

11. Kleinberg, R.L.; Sezginer, A.; Griffin, D.D.; Fukuhara, M. Novel NMR apparatus for investigating an external sample. *J. Magn. Resonance* **1992**, *97*, 466–485.
12. Haken, R.; Blumich, B. Anisotropy in tendon investigated *in vivo* by a portable NMR scanner, the NMR-MOUSE. *J. Magn. Resonance* **2000**, *144*, 195–199.
13. Xu, Z.; Zhao, S.J.; Guo, P. A portable NMR sensor used for assessing the aging status of silicone rubber insulator. *Appl. Magn. Resonance* **2013**, *44*, 1405–1417.
14. Rahmatallah, S.; Li, Y.; Seton, H.C.; Gregory, J.S.; Aspden, R.M. Measurement of relaxation times in foodstuffs using a one-sided portable magnetic resonance probe. *Eur. Food Res. Technol.* **2006**, *222*, 298–301.
15. Marble, A.E.; Mastikhin, I.V.; Colpitts, B.G.; Balcom, B.J. A compact permanent magnet array with a remote homogeneous field. *J. Magn. Resonance* **2007**, *186*, 100–104.
16. Garcia-Naranjo, J.C.; Mastikhin, I.V.; Colpitts, B.G.; Balcom, B.J. A unilateral magnet with an extended constant magnetic field gradient. *J. Magn. Resonance* **2010**, *207*, 337–344.
17. Hurlimann, M.D.; Griffin, D.D. Spin dynamics of carr-purcell-meiboom-gill-like sequences in grossly inhomogeneous B₀ and B₁ fields and application to NMR well logging. *J. Magn. Resonance* **2000**, *143*, 120–135.
18. Provencher, S.W. A constrained regularization method for inverting data represented by linear algebraic or integral equations. *Commun. Comput. Phys.* **1982**, *27*, 213–227.
19. Chelcea, R.I.; Fecete, R.; Culea, E.; Demco, D.E.; Blumich, B. Distributions of transverse relaxation times for soft-solids measured in strongly inhomogeneous magnetic fields. *J. Magn. Resonance* **2009**, *196*, 178–190.
20. Hurlimann, M.D. Diffusion and relaxation effects in general stray field NMR experiments. *J. Magn. Resonance* **2001**, *148*, 367–378.

Detection of Virgin Olive Oil Adulteration Using Low Field Unilateral NMR

Zheng Xu, Robert H. Morris, Martin Bencsik and Michael I. Newton

Abstract: The detection of adulteration in edible oils is a concern in the food industry, especially for the higher priced virgin olive oils. This article presents a low field unilateral nuclear magnetic resonance (NMR) method for the detection of the adulteration of virgin olive oil that can be performed through sealed bottles providing a non-destructive screening technique. Adulterations of an extra virgin olive oil with different percentages of sunflower oil and red palm oil were measured with a commercial unilateral instrument, the profile NMR-Mouse. The NMR signal was processed using a 2-dimensional Inverse Laplace transformation to analyze the transverse relaxation and self-diffusion behaviors of different oils. The obtained results demonstrated the feasibility of detecting adulterations of olive oil with percentages of at least 10% of sunflower and red palm oils.

Reprinted from *Sensors*. Cite as: Xu, Z.; Morris, R.H.; Bencsik, M.; Newton, M.I. Detection of Virgin Olive Oil Adulteration Using Low Field Unilateral NMR. *Sensors* **2014**, *14*, 2028–2035.

1. Introduction

The detection of adulteration in high priced olive oils is a particular concern in the food industry. Virgin olive oil is simply pressed fruit without any additives and without the use of heat in the process; the best of these in terms of flavor are classified as extra virgin and must pass chemical tests in a laboratory and a sensory evaluation. The adulteration of extra virgin olive oil with other cheaper oils can lead to significant profits for the unscrupulous dealer. Laboratory-based methods have been extensively developed for the monitoring of adulteration of virgin olive oils with other edible oils [1–3]. Chromatographic methods [4] and mass spectrometry [5] have been used to study the adulteration of olive oil with hazelnut oil. Synchronous fluorescence spectroscopy was employed for quantitative determination of virgin olive oil adulteration with sunflower oil [6]. Priego Capote *et al.* developed an analytical method based on a gas chromatograph for the detection of extra virgin olive oil adulteration with four edible vegetable oils: sunflower, corn, peanut and coconut oils [7]. NMR spectroscopy was proven to be a much more effective method in the authentication of virgin olive oil based on their geographical origin [8]. For authentication purposes, several variables have been studied, including ^1H -, ^{13}C -, and ^{31}P -NMR analyses [9]. With more detailed NMR analyses, the diffusion coefficient of minor constituents of olive oil was chosen as a marker parameter [10,11]. All these methods have been employed with some success, but there are also some problems. Chromatographic methods of edible oil authentication have proved unable to detect adulterations at low concentrations [2]. Mass and NMR spectroscopy methods need large, expensive instrument, which are not suitable for screening. Fluorescence spectroscopy requires preprocessing operation to the samples and only Raman spectroscopy offers the possibility of a field portable instrument [12].

This article presents an alternative method, namely low field unilateral NMR, with the same potential as Raman for operation ‘in the field’. With this method, the transverse relaxation and

self-diffusion of different adulterated oils have been studied. The samples can be measured without any preprocessing operation and the unilateral magnet structure means that the oils need not to be taken out from their original bottles, which can remain sealed.

2. Experimental Section

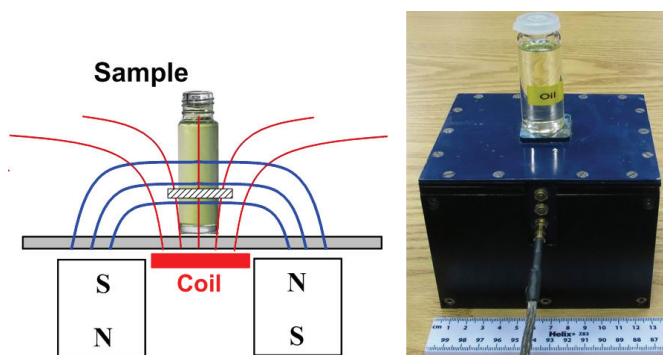
2.1. Samples

Sunflower oil (J. Sainsbury plc, Nottingham, UK) and red palm oil (Cebra Norfolk, Nottingham, UK) were used as the adulterations in the extra virgin olive oil (Napolina Ltd., Nottingham, UK). The samples were stored in the dark at room temperature until the day of analysis. Two mixtures of sunflower and extra virgin olive oils, with concentration of sunflower oil at two levels (10% and 20%), were prepared. The mixtures of sunflower and extra virgin olive oils were prepared using an Ultra-Turrax[®] (IKA, Staufen, Germany). The red palm was gently heated in warm water prior to mixing by hand with the olive oil.

2.2. Instrument

NMR signals were acquired by using a NMR portable Mouse [13] from AixNMR (Wellington, New Zealand) with a Tecmag NMR spectrometer (Houston, TX, USA). The NMR Mouse takes advantage of a unilateral permanent magnet geometry that generates a magnetic field with a uniform static gradient at a defined distance from the magnet surface (Figure 1). In the sensitive volume, the static magnetic field has a strength of 0.25 T, and the gradient of 11.38 T/m. The thickness of the sensitive volume is 100 μm . The sensitive volume is made to reside 5 mm above the coil so will probe well inside a glass container of typical wall thickness.

Figure 1. Schematic diagram of the NMR MOUSE with the sample and the selective slice shown.

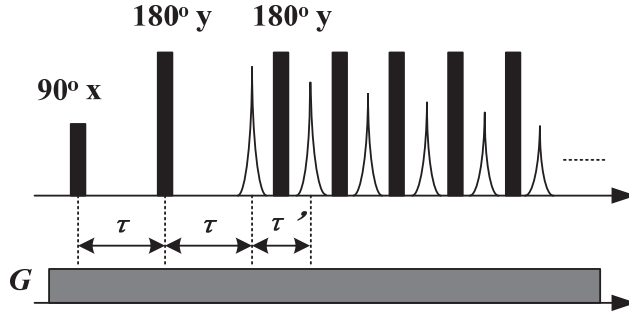


2.3. Measurement and Data Processing

To detect the transverse relaxation and self-diffusion behaviors of oils, a SGSE [14] sequence as shown in Figure 2 was employed. The pulse widths of the 90° and the 180° pulses were 8 μs . The

time interval between the 90° and the first 180° pulse (τ) was gradually increased from 120 μs to 2500 μs for diffusion encoding. The echo time of CPMG sequence (τ') was fixed at 140 μs . The symbol G in Figure 2 corresponds to the constant gradient of the static magnetic field, which was 11.38 T/m and the RF frequency was 10.64 MHz. The CPMG echoes were recorded for further processing.

Figure 2. SGSE sequence composed of a Hahn echo and a CPMG sequence.



Due to the complex constituents of the samples studied, we expect to acquire multi-exponential signals for the transverse relaxation and diffusion. The recorded CPMG decay signals related to the two dimensional probability density distribution can be expressed as:

$$M(\tau_1, \tau_2) \approx \iint k_1(T_2, \tau_1) k_2(D, \tau_2) F(T_2, D) dT_2 dD + \varepsilon(\tau_1, \tau_2) \quad (1)$$

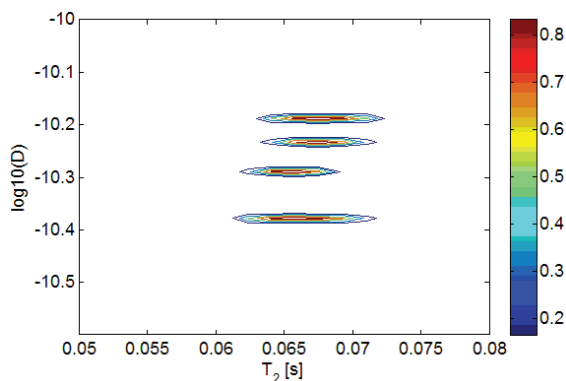
where, k_1 is the kernel function of transverse relaxation which can be expressed as $e^{-\tau_1/T_2}$; k_2 is the kernel function of diffusion which can be approximately expressed as $e^{-\frac{2}{3}\gamma^2 G^2 \tau_2^3 D}$, γ is the gyromagnetic ratio of ^1H , G is the constant gradient of the static magnetic field; $\varepsilon(\tau_1, \tau_2)$ is a noise term. $F(T_2, D)$ is the two dimensional probability density distribution of T_2 relaxation and diffusion. Although the CPMG echo train is attenuated by the diffusion, the small echo time of the CPMG sequence ($\tau' = 140 \mu\text{s}$) alleviates this effect. We also neglected the Hahn echo attenuation which is related to T_2 . We developed in Matlab a 2-dimensional Laplace Inversion according to the algorithm of Venkataraman *et al.* [15] to reconstruct $F(T_2, D)$ from the recorded CPMG decay signals.

3. Results and Discussion

3.1. Mixtures of Sunflower and Extra Virgin Olive Oils

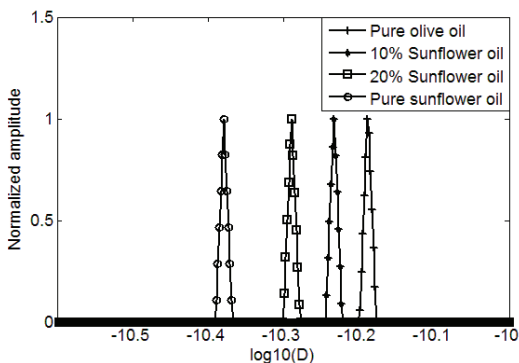
Two mixtures of sunflower and extra virgin olive oils, with sunflower concentrations at 10% and 20% by volume, pure sunflower oil and pure extra virgin olive oil, were measured. The D- T_2 distributions of the different oils are plotted in Figure 3.

Figure 3. Superimposition of D-T₂ distributions of sunflower and extra virgin olive mixed oils. From top to bottom, the peaks correspond to pure extra virgin olive oil, 10% sunflower oil, 20% sunflower oil and pure sunflower oil, respectively.



In Figure 3, we can see that the D-T₂ distribution plot of different oils separate in the vertical direction (D-axis), but overlap in the lateral direction (T₂-axis). It indicates that the adulteration of sunflower oil in the extra virgin olive oil can more readily be detected from the sample's diffusion behavior. In order to better show the differences in diffusion, the 2-dimensional D-T₂ distributions were projected to the D-axis, forming a 1-dimensional diffusion distribution, which is shown in Figure 4.

Figure 4. 1D diffusion coefficient distribution of sunflower and extra virgin olive mixed oils.



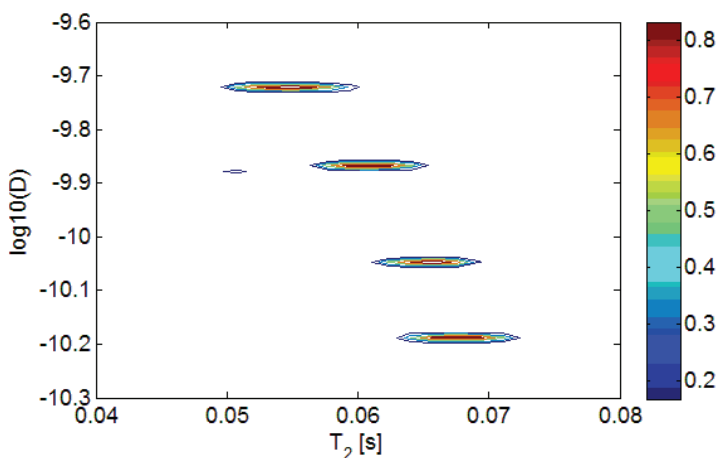
As shown in Figure 4, from right to left there are four peaks representing the pure extra virgin olive oil, 10% sunflower and 90% olive mixed oil, 20% sunflower and 80% olive mixed oil and the pure sunflower oil. The actual self-diffusion coefficients of these four oils are $6.5 \times 10^{-11} \text{ m}^2\text{s}^{-1}$, $5.9 \times 10^{-11} \text{ m}^2\text{s}^{-1}$, $5.1 \times 10^{-11} \text{ m}^2\text{s}^{-1}$ and $4.1 \times 10^{-11} \text{ m}^2\text{s}^{-1}$, respectively. Compared to the pure extra virgin olive oil, the sunflower oil mixtures have a smaller self-diffusion coefficient. The four narrow peaks in Figure 4 indicate that there are no diffusion distributions, and the diffusion has no correlation with the T₂ relaxation. The food oil we have used are not similar to petroleum oils, for example, S3 [16], which has a D-T₂ correlated distribution. The diffusion-relaxation behavior of oil is

complex, although we do not see the diffusion distribution and its correlation with relaxation, it is still possible that, for other food oils, a diffusion distribution and correlation exist.

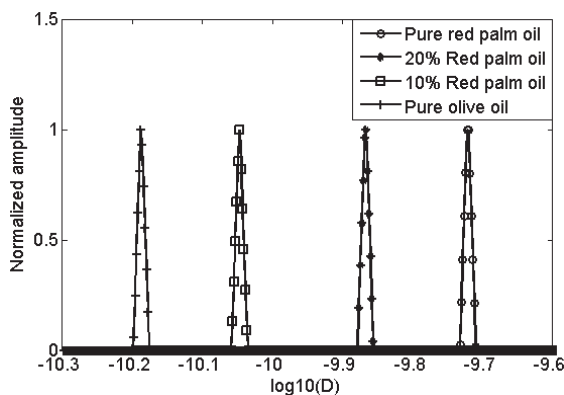
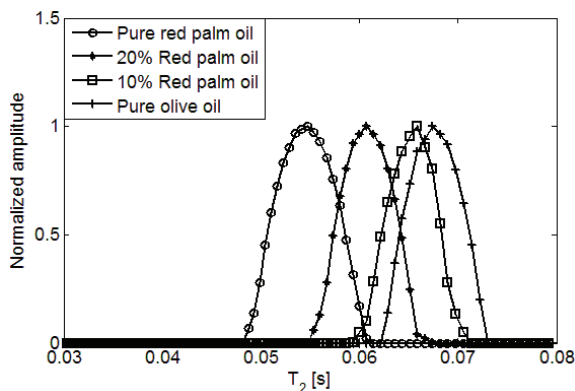
3.2. Mixtures of Red Palm and Extra Virgin Olive Oils

Two mixtures of red palm and extra virgin olive oils, with concentration of red palm oil at two levels (10% and 20%), pure red palm oil and pure extra virgin olive oil, were also measured. The D-T₂ distributions of these four different oils are plotted in Figure 5. For the red palm and extra virgin olive mixed oils, the distributions are separated not only in D-axis, but also in T₂-axis. This indicates that the adulteration of red palm oil in the extra virgin olive oil can be detected both from the diffusion and transverse relaxation behaviors. To show the differences more clearly, the 2-dimensional D-T₂ distributions were projected to the D-axis and T₂-axis, as shown in Figures 6 and 7.

Figure 5. D-T₂ distribution of red palm and extra virgin olive oil mixtures. From top to bottom, they are pure red palm oil, 10% red palm oil, 20% red palm oil and pure extra virgin olive oil, respectively.



In Figure 6, from right to left there are four peaks representing the pure red palm oil, 10% red palm and 90% olive mixed oil, 20% red palm and 80% olive mixed oil and the pure extra virgin olive oil. The self-diffusion coefficient increases as the percentage of red palm oil increases, giving $6.5 \times 10^{-11} \text{ m}^2\text{s}^{-1}$, $8.9 \times 10^{-11} \text{ m}^2\text{s}^{-1}$, $1.4 \times 10^{-11} \text{ m}^2\text{s}^{-1}$ and $1.9 \times 10^{-11} \text{ m}^2\text{s}^{-1}$, respectively. While in Figure 7, the T₂ decreases as the percentage of red palm oil increases, giving 67.5 ms, 64.1 ms, 60.8 ms and 54.9 ms, respectively. Comparing with the pure extra virgin olive oil, the red palm mixed oil has a larger self-diffusion coefficient but smaller T₂.

Figure 6. 1d diffusion coefficient distribution of red palm and extra virgin olive mixed oils.**Figure 7.** 1d T_2 distribution of red palm and extra virgin olive mixed oils.

4. Conclusions

This article demonstrates a low field unilateral NMR method to screen for the adulteration of extra virgin olive oil. With 2-dimensional Inverse Laplace transformation, the adulteration of extra virgin olive oil with different percentages of sunflower oil or red palm oil can be differentiated from the transverse relaxation and self-diffusion behaviors. The detection threshold is similar to that achieved using the much more expensive pulsed field gradient diffusion NMR measurement [10]. The narrow peaks in the diffusion distributions indicate that there is no distribution in the diffusion coefficients of our samples. It further suggests that the measurement of diffusion coefficient for the adulteration of olive oil can be sped up by just using two appropriate Hahn echo times (τ). Although the feasibility of this method has been demonstrated by these experiments, one problem was encountered. Measurements on the NMR MOUSE are temperature-sensitive because of the poor temperature coefficient of NdFeB magnets and an unstable static magnetic field influences the diffusion behavior measurement significantly. This however could be overcome using a temperature controlled environment or speeding up the measurement. Further work will concentrate of the ability of this technique to discriminate multiple additives.

Acknowledgments

Zheng Xu acknowledges financial support from the National Natural Science Foundation of China (No. 51107150 and 51377182).

Conflicts of Interest

The authors declare no conflict of interest.

References

1. Aparicio, R.; Harwood, J. *Handbook of Olive Oil*, 2nd ed.; Springer: New York, NY, USA, 2013; pp. 163–395.
2. Ellis, D.I.; Brewster, V.L.; Dunn, W.B.; Allwood, J.W.; Golovanov, A.P.; Goodacre, R. Fingerprinting food current technologies for the detection of food adulteration and contamination. *Chem. Soc. Rev.* **2012**, *41*, 5706–5727.
3. Frankel, E.N. Chemistry of Extra Virgin Olive Oil: Adulteration, Oxidative Stability, and Antioxidants. *J. Agric. Food Chem.* **2010**, *58*, 5991–6006.
4. Flores, G.; del Castillo M.L.R.; Herraiz, M.; Blanch, G.P. Study of the adulteration of olive oil with hazelnut oil by on-line coupled high performance liquid chromatographic and gas chromatographic analysis of filbertone. *Food Chem.* **2006**, *97*, 742–749.
5. Pena, F.; Cardenas, S.; Gallego, M.; Valcarcel, M. Detection of adulteration of olive oil with hazelnut oil by direct coupling of headspace and mass spectrometry. *J. Chromatogr. A* **2005**, *1027*, 215–221.
6. Poulli, K.I.; Mousdis, G.A.; Georgiou, C.A. Synchronous fluorescence spectroscopy for quantitative determination of virgin olive oil adulteration with sunflower oil. *Anal. Bioanal. Chem.* **2006**, *386*, 1571–1575.
7. Capote, F.P.; Jiménez, J.R.; Luque de Castro, M.D. Sequential (step-by-step) detection, identification and quantitation of extra virgin olive oil adulteration by chemometric treatment of chromatographic profiles. *Anal. Bioanal. Chem.* **2007**, *388*, 1859–1565.
8. Marcone, M.F.; Wang, S.A.; Albabish, W.; Nie, S.P.; Somnarain, D.; Hill, A. Diverse food-based applications of nuclear magnetic resonance (NMR) technology. *Food Res. Int.* **2013**, *51*, 729–747.
9. Alonso-Salces, R.M.; Moreno-Rojas, J.M.; Holland, M.V.; Reniero, F.; Guillou, C.; Heberger, K. Virgin olive oil authentication by multivariate analyses of ¹H NMR fingerprints and ¹³C and ²H data. *J. Agric. Food Chem.* **2010**, *58*, 5586–5596.
10. Smejkalova, D.; Piccolo, A. High-power gradient diffusion NMR spectroscopy for the rapid assessment of extra-virgin olive oil adulteration. *Food Chem.* **2010**, *118*, 153–158.
11. Altun, A.; Ok, S. NMR Analyses and Diffusion Coefficient Determination of Minor constituents of olive oil: Combined Experimental and Theoretical Studies. *J. Chem. Eng. Data* **2012**, *57*, 2619–2624.

12. Zou, M.Q.; Zhang, X.F.; Qi, X.H.; Ma, H.L.; Dong, Y.; Liu, C.W.; Guo, X.; Wang, H. Rapid Authentication of Olive Oil Adulteration by Raman Spectrometry. *J. Agric. Food Chem.* **2009**, *57*, 6001–6006.
13. Eidmann, G.; Savelsberg, R.; Blumler, P.; Blumich, B. The NMR MOUSE, a mobile universal surface explorer. *J. Magn. Reson.* **1996**, *122*, 104–109.
14. Rata, D.G.; Casanova, F.; Perlo, J.; Demco, D.E.; Blumich, B. Self-diffusion measurements by a mobile single-sided NMR sensor with improved magnetic field gradient. *J. Magn. Reson.* **2006**, *180*, 229–235.
15. Venkataramanan, L.; Song, Y.Q.; Hurlimann, M.D. Solving Fredholm integrals of the first kind with tensor product structure in 2 and 2.5 dimensions. *IEEE Trans. Sign. Process.* **2002**, *50*, 1017–1026.
16. Hurlimann, M.D.; Venkataramanan, L. Quantitative measurement of two-dimensional distribution functions of diffusion and relaxation in grossly inhomogeneous fields. *J. Magn. Reson.* **2002**, *157*, 31–42.

Towards Using NMR to Screen for Spoiled Tomatoes Stored in 1000 L, Aseptically Sealed, Metal-Lined Totes

Michael D. Pinter, Tod Harter, Michael J. McCarthy and Matthew P. Augustine

Abstract: Nuclear magnetic resonance (NMR) spectroscopy is used to track factory relevant tomato paste spoilage. It was found that spoilage in tomato paste test samples leads to longer spin lattice relaxation times T_1 using a conventional low magnetic field NMR system. The increase in T_1 value for contaminated samples over a five day room temperature exposure period prompted the work to be extended to the study of industry standard, 1000 L, non-ferrous, metal-lined totes. NMR signals and T_1 values were recovered from a large format container with a single-sided NMR sensor. The results of this work suggest that a handheld NMR device can be used to study tomato paste spoilage in factory process environments.

Reprinted from *Sensors*. Cite as: Pinter, M.D.; Harter, T.; McCarthy, M.J.; Augustine, M.P. Towards Using NMR to Screen for Spoiled Tomatoes Stored in 1000 L, Aseptically Sealed, Metal-Lined Totes. *Sensors* **2014**, *14*, 4167–4176.

1. Introduction

Globally, around 1.3 billion tons of food is wasted per year. In North America alone, approximately 175 kg·food/person is compromised at the pre-consumption stages of production [1]. In order to minimize this loss, food packaging companies are constantly seeking ways to improve packing process sanitation. In spite of these efforts, spoilage is never entirely eliminated. The direct consequence of a few spoiled containers translates into four to six figure financial losses when both the spoiled product and waste disposal are considered [1]. Bacterial contamination is a primary source of food spoilage that many industrial food processes attempt to eliminate by operating in aseptic environments [2]. Once introduced into a system, bacteria proliferate as a function of temperature and available metabolic nutrients. Technologies that provide early detection of bacterial growth can ultimately provide food companies with a competitive edge in the industry and decrease the environmental impact of waste disposal.

The tomato paste processing industry is interested in spoilage because contaminated tomato paste spoils in a matter of days. Industrial tomato paste totes or bags that comprise an inner plastic sack and a thin outer aluminum layer are designed to accommodate a 1000 L volume [3], which means that the introduction of even a small amount of contamination is costly. The tomato paste industry is interested in developing ways to detect tomato spoilage in these 1,000 L non-ferrous, metal-lined containers without violating the seal. Although early spoilage detection cannot preserve the contents of the compromised tote, it would eliminate costs associated with shipping, disposal, and frustration incurred when a tote with spoiled tomato paste arrives at its destination.

Several analytical methods that are traditionally used to measure food spoilage fail in the industrial tomato paste manufacturing domain. Laser and other optical methods that involve passing light through a sample require non-metal, transparent containers [4]. Mass spectrometry threatens tomato

paste sterility as it is an invasive process that requires the container seal to be broken for sampling [4]. Nuclear magnetic resonance (NMR), on the other hand, is a non-invasive approach that has gained traction recently in studying problems in industrial process environments [5–7]. These examples share the common theme of being modifications to the conventional NMR approach involving a sample in a non-metal container enclosed by a large magnet. In the case of tomato paste these conditions do not apply. Firstly, the container is a 1,000 L non-ferrous, metal-lined tote that cannot fit inside of a standard magnetic resonance or imaging magnet. Moreover, the tote is filled with ca. 1 metric tonne of tomato paste and cannot be moved to the sensor. The aluminum lining in these totes presents an additional problem as eddy currents are generated on the surface of the metal that attenuate the applied radio frequency (rf) magnetic field [8]. The skin depth $\delta = (2/\mu\sigma\omega)^{1/2}$, written in terms of the metal conductivity σ , the metal magnetic permeability μ , and angular frequency ω , is the distance into metal at which incident radiation is attenuated by e^{-1} [8]. Traditional NMR spectroscopy operates at Larmor frequencies $\omega_0/2\pi = \gamma B_0 > 100$ MHz yielding $\delta < 8$ μm for aluminum. This shielding prevents signals from being observed through the 75 μm thick aluminum layer incorporated into the tote material.

A useful food spoilage detector must have four essential design features. It should be noninvasive, portable, accept a variety of sample geometries, and probe both metal and non-metal containers. These features are provided by a unilateral NMR circuit, or single-sided coil, which is an NMR tank circuit with a planar inductor that can non-invasively probe a wide range of sample geometries [9]. Interfacing this coil with a light weight permanent magnet that produces a small static magnetic field ultimately leads to increased metal transparency. The decreased field strength leads to a lower Larmor frequency $\omega_0/2\pi \approx 5$ MHz that concomitantly increases the skin depth in aluminum to $\delta \approx 40$ μm thus providing access to the study of the contents of non-ferrous, metal-lined containers. In practice, a portable single sided coil and magnet system could be placed flush with a 1,000 L industrial tomato tote to non-invasively provide spoilage information about the contents. Small, portable single sided coil and magnet systems are commercially available with the most well-known example being the NMR Mobile Universal Surface Explorer, developed at RWTH-Aachen [10].

The ultimate goal of this work was to determine if NMR spectroscopy is sensitive to tomato paste spoilage and to record the NMR signal from tomato paste in industrial, non-ferrous, metal-lined 1,000 L totes. To this end, tomato paste NMR relaxation parameters were monitored in small 100 mL glass containers using a customized low magnetic field NMR spectrometer to find a measureable variable that correlates with tomato spoilage. After the spoilage dependent NMR parameter was determined in non-metal containers, it was confirmed that it can be measured using a sample in a non-ferrous, metal-lined tote using a single sided coil/magnet system. As NMR experiments in metal containers are rarely reported in the literature, effort is spent in the next section describing the $\omega_0/2\pi = 4$ MHz electromagnet based and the $\omega_0/2\pi = 5.25$ MHz single sided magnet based systems.

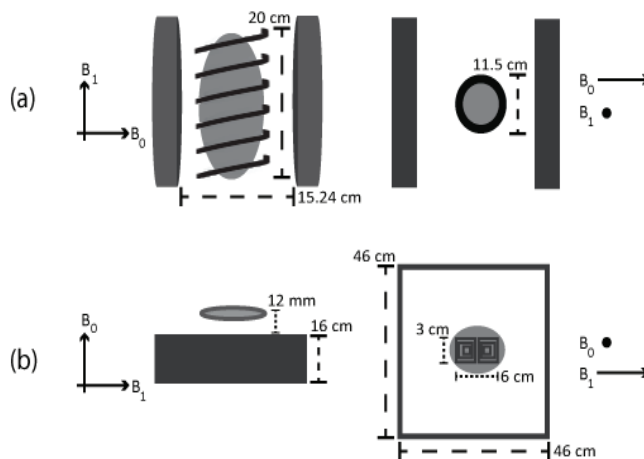
2. Materials and Methods

Commercial tomato paste was used as received from The Morning Star Company. Small format samples were prepared in a clean room by aseptically transferring fresh tomato paste into thirty

100 mL VWR media bottles. The thirty identical samples were separated into two, separate, fifteen bottle sets. The control group was set aside while the other fifteen bottles were inoculated with a mixed culture of microorganisms that were harvested from a leaking aseptic filler line at the Los Baños, CA, Morning Star Company food packing facility. Immediately after preparation, the thirty samples were cooled to $T < 5\text{ }^{\circ}\text{C}$ and stored in a refrigerator. These samples were transported from The Morning Star Company to UC Davis in a standard cooler and were stored in the laboratory refrigerator until needed. Large format samples were contained in standard 1,000 L storage totes with a $75\text{ }\mu\text{m}$ thick metal lining. These aluminum layered, plastic bags were short filled with tomato paste, stored at room temperature, and shipped from The Morning Star Company to UC Davis.

A Tecmag Redstone NMR spectrometer was used to acquire all transient NMR relaxation signals from the small format 100 mL samples. As shown in Figure 1a, the small format samples were completely enclosed by the $\omega_0/2\pi = 4\text{ MHz}$ tuned and matched, 11.5 cm diameter, 20 cm long, 11 turn variable pitch inductor situated inside of a homebuilt NMR probe. This probe was mounted inside of a $B_0 = 980\text{ G}$ SMIS electromagnet with a 15.24 cm pole face separation. A standard inversion recovery pulse sequence involving 625 W, $20\text{ }\mu\text{s}$ $\pi/2$ rf pulses and 21 non-linear sampled recovery times between 0 and 300 ms was used to recover T_1 values while a multiple π rf pulse Carr-Purcell-Meiboom-Gill (CPMG) pulse sequence with an 8 ms π rf pulse separation involving the same rf pulse power and length was used to recover T_2 values by non-linearly increasing the number of π rf pulses to 60 in 18 steps. All measurements reported for this geometry did not require signal averaging and corresponded to one transient signal per relaxation time point.

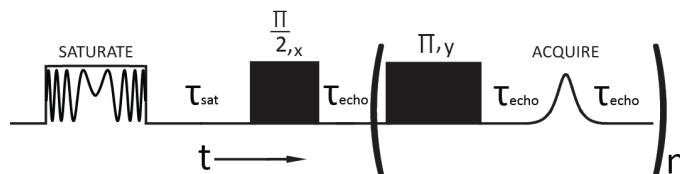
Figure 1. Diagrams comparing the conventional low field NMR instrument in (a) to the single sided instrument in (b). The primary difference between these two geometries is that applied rf interacts with the entire sample in (a) and only a fraction of the sample in (b) as shown by the shaded gray area.



In the case of the large format metal-lined totes, the Tecmag Redstone NMR spectrometer was connected to an ABQMR single sided permanent magnet system. In this case the sample was not inside of the rf coil as shown in Figure 1b and the homogeneous sample volume of the $B_0 = 1,300\text{ G}$ static

magnetic field was adjusted to be 12 mm above the surface of a flat rf coil tuned to $\omega_0/2\pi = 5.25$ MHz and designed to provide an ≈ 1 cm thick homogeneous rf excitation slice spatially coincident with the static magnetic field. The saturation recovery pulse sequence shown in Figure 2 used a 500 ms long, 25 W, ± 75 kHz frequency swept rf pulse to saturate the wide NMR line presented by the single sided magnet and a CPMG spin echo train with 3 μ s long, 625 W $\pi/2$ rf pulses, $\tau_{\text{echo}} = 1.5$ ms and $500 \mu\text{s} < \tau_{\text{sat}} < 3$ s to observe the time domain signal. The sum of the first ten echoes in the CPMG spin echo train was used to estimate the signal intensity for T_1 estimates. All measurements reported for this geometry required 30 transient signals to be averaged per relaxation time point.

Figure 2. Modified saturation recovery pulse sequence that incorporates a ± 75 kHz frequency sweep into the saturation pulse. The CPMG backend is required to observe a signal because of the large inhomogeneous static field and rf circuit ring down. The variable frequency rf pulse more efficiently saturates the magnetization in single sided mode in comparison to the conventional rf pulse train used for sample-in-the-coil geometries.



Unless otherwise specified, all reported T_1 and T_2 values correspond to an average of the exponential signal decay constant over 15 samples while the 95% confidence limit was established using the standard deviation of the same data along with the appropriate Student t factor. All data processing was accomplished using Matlab.

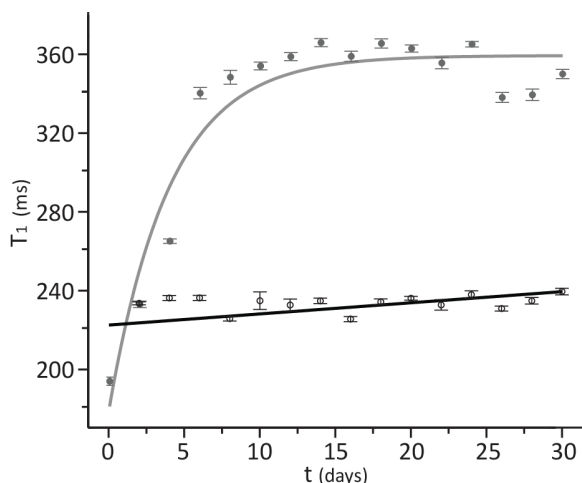
3. Results

The 980 G SMIS electromagnet was used to obtain T_1 and T_2 values for all thirty samples as a function of time at both low and room temperature. The available room temperature shims in the electromagnet were used to reduce the NMR line width for these samples in the as received glass jars to less than 100 Hz.

The low temperature measurements were accomplished on ten randomly selected sterile and unsterile samples. These samples were only removed from the low temperature storage refrigerator for $t \approx 5$ min to obtain the T_1 and T_2 values reported in Table 1. Given the heat capacity of the tomatoes and the glass container, the temperature rise during this time was less than $+3$ °C. As long as the storage temperature was maintained below 5 °C, the T_1 and T_2 values remain constant over the course of at least one month. Room temperature T_1 and T_2 measurements were accomplished on all thirty samples. The fifteen sterile and unsterile samples were separated into three separate batches. The first batch of five samples each was removed from the refrigerator and allowed to warm to room temperature over the course of an hour. The T_1 and T_2 values for these samples were monitored every two days for a thirty day period. At day fifteen of these measurements, a second batch of five samples

each was removed from the refrigerator and the measurements were repeated in parallel with the first batch. On the final day of measurements for the first batch, the third batch of five samples each was removed from the refrigerator and measurements were repeated in parallel with the second batch. Although the room temperature T_2 value was constant as a function of time for these samples as shown in Table 1, the corresponding T_1 values as shown in Figure 3 were not.

Figure 3. Comparison of sterile (open circles) to unsterile (solid circles) T_1 values as a function of room temperature exposure time. The 95% confidence intervals corresponding to averaging over 15 samples are included in the plot.

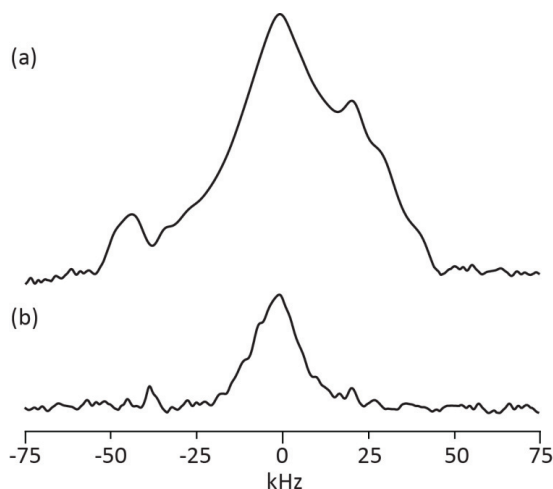


Regression of these T_1 measurements to an exponentially rising function yields the steady state spin lattice relaxation time T_1^∞ and the time constant for this increase τ , which are provided in Table 1. The lack of room temperature shims in the 1300 G single sided magnet provided a wide, inhomogeneously broadened NMR peak as shown in Figure 4a for tomato paste in a 100 mL VWR glass jar. The consequence of the metal-lined tote on this signal is demonstrated in Figure 4b for the same glass jar wrapped in the aseptic, metal-lined tote material. The ability to measure a signal from a 100 mL tomato sample wrapped with the tote material in Figure 4b prompted the recovery of the $T_1 = 226 \pm 28$ ms value for tomato paste short filled into a 1,000 L, aseptic, metal-lined tote.

Table 1. NMR Relaxation Parameters for Tomato Samples.

	$T < 5^\circ\text{C}$		$T > 25^\circ\text{C}$		
	T_1 (ms)	T_2 (ms)	T_1^∞ (ms)	τ (days)	T_2 (ms)
Sterile	217.3 ± 2.2	53.5 ± 1.4	234.8 ± 1.8	-	58.8 ± 1.0
Unsterile	199.4 ± 1.3	47.2 ± 0.9	349.0 ± 2.6	4.0 ± 1.8	57.0 ± 0.5

Figure 4. Example ^1H NMR spectra obtained with the single sided coil magnet for a 100 mL tomato paste sample without (a) and enclosed in (b) the aluminum lined tote material.



4. Discussion

The goal of this work was to determine if NMR spectroscopy could be used to identify spoiled tomato paste stored in industry standard, 1,000 L, large format, non-ferrous, metal-lined totes. There are three challenges that were met in order to accomplish this goal. Two of these, the identification of an NMR parameter that reflects tomato paste spoilage and the recovery of an NMR signal from a sample enclosed in a non-ferrous, metallic shield, were addressed using the standard NMR geometry provided by the 980 G electromagnet. Finally, the single sided system was used to measure the T_1 relaxation time for tomato paste in a short-filled, 1,000 L, non-ferrous, metal-lined tote.

In order to address the first of these challenges, a set of known sterile and unsterile tomato paste samples was studied in ideal laboratory conditions using a conventional NMR magnet that surrounds the small format samples. The results, shown in Table 1, report virtually no variability (ca. 18 ms) in the T_1 and T_2 values between the as received sterile and unsterile samples at low temperature. This result suggests that the low temperature either halts or significantly slows the bacteria mediated tomato paste spoilage. At room temperature where tomato processing, packaging, and storage occur, the relaxation times shown in Table 1 for sterile and unsterile samples are different. The ca. 115 ms difference in T_1^∞ values can be used to identify spoiled tomato paste. As shown in Figure 3, the steady state T_1^∞ value difference between sterile and unsterile samples takes ca. 5 days to develop at room temperature reflecting the rate of bacteria growth in the closed sample.

The mechanism of the relationship between bacteria mediated tomato paste spoilage and changes in T_1^∞ was not explored in detail in this work. An obvious possibility for this dependence is that the bacterial metabolism either directly or indirectly chemically changes the tomato substrate. In the direct process, bacteria directly consume the substrate, while in the indirect case, the products of bacterial metabolism react with the tomato substrate or simply dilute the mixture, decreasing the

sample viscosity. The decreased sample viscosity translates into a larger T_1^∞ value [11]. It is likely that the mechanism depends on the bacteria identity and current work involves exploring how the available NMR parameter values change with different spoilage agents. From the point of view of this work, all that matters is that the T_1^∞ value for unsterile samples measurably deviates from the sterile control set value.

Operation at a decreased magnetic field strength in comparison to standard NMR spectroscopy was motivated by the need to recover signals from samples enclosed in non-ferrous, metallic containers. Here the lower induced Larmor frequency ca. 4–5 MHz increases the penetration depth of the applied and detected radio frequency fields by about an order of magnitude in comparison to that anticipated by using typical 400–500 MHz values. As long as the effect of the non-ferrous metallic container on the tank circuit tuning and impedance matching properties have been properly compensated, the metal container can be modeled as a simple attenuator. In other words, the 4 MHz resonance frequency of the NMR tank circuit shifts to higher frequency when a non-ferrous, metallic container is studied. In the case of the plastic coated, 75 μm thick aluminum aseptic tote material, the shift is ca. 1 MHz. The addition of extra capacitance in parallel with both the tuning and matching capacitors returns the circuit resonance frequency to the original 4 MHz value. Although the circuit quality factor after this adjustment returns to the metal free value, the optimum $\pi/2$ rf pulse length is longer for the same applied rf power and the signal size is smaller. Similar efforts were necessary when the unique single sided coil/magnet system were used. The increased rf pulse length and decreased signal size can be appreciated with reference to Figure 4. Here the NMR signals for a 100 mL VWR bottle without and with the aseptic tote material are compared in Figure 4a,b, respectively. The decreased excitation bandwidth and signal-to-noise ratio in Figure 4b in comparison to Figure 4a demonstrate the attenuation effect.

The homogeneity of the applied static magnetic field in the single sided geometry is significantly less than in the standard geometry. For example, the ^1H line widths for the same 100 mL VWR sample are ca. 100 Hz and 50 kHz for the electromagnet and the single sided magnet respectively. The increased line width in the single sided geometry combined with the decreased excitation bandwidth shown in Figure 4 impacts rf pulse design. Specifically, the standard inversion recovery measurement of the T_1 relaxation time constant does not work in the single sided geometry when non-ferrous, metal containers are used because the signal cannot be completely inverted. Moreover, the inhomogeneous spectral line width is so large that the signal decays during the rf pulse ring down period preventing transient signal detection. The pulse sequence shown in Figure 2 solves both of these problems. Instead of inverting the magnetization M_0 , a swept frequency saturation pulse is used. In this way the recovery of magnetization from 0 to $+M_0$ is monitored in the saturation recovery pulse sequence instead of the usual $-M_0$ to $+M_0$ transformation used in the inversion recovery experiment. The signal damping issue is also resolved by this pulse sequence since a spin echo with a pulse delay greater than the radio frequency ring down time is used. An added benefit of the saturation recovery approach shown in Figure 2 is overall experiment time. Since the signal is recovering from a saturated state, the usual 5 T_1 waiting period between data acquisition events required for the inversion recovery pulse sequence is not necessary.

As a final test of the ability of NMR spectroscopy to study tomato paste spoilage in a large format, 1000 L, non-ferrous, metal-lined tote, the $T_1 = 226 \pm 28$ ms relaxation time constant was obtained from a factory sealed short filled tote using the single sided magnet and the pulse sequence shown in Figure 2. The order of magnitude greater error recognized in the single sided T_1 measurement in comparison to the error for the standard geometry is not problematic as the increase in T_1 in the unsterile case is four to five times greater than this uncertainty. Improvements on the single sided T_1 error can also be made by thermally stabilizing the single sided magnet. The experiments reported here operate the ABQMR system in a standard laboratory environment subject to uncontrolled temperature variations. Indeed on the basis of the room temperature electromagnet T_1 values shown in Table 1, the 226 ± 28 ms T_1 value for the short filled 1,000 L tote obtained from the single sided magnet suggests that the tomato paste in the detection volume near the tote surface is sterile and thus suitable for distribution and human consumption. Extending this NMR based local measurement to the entire contents of the 1,000 L tote is straightforward given that existing observations of spoilage are made by physically viewing the surface condition of tote stored paste. Since tomato concentrate is a liquid based product significant spoilage impacts the vast majority of the material in a tote. The concern for processors is not minor pockets of local bacteria growth but significant proliferation that impacts the bulk properties of the entire tomato concentrate and hence one or several local surface measurements is adequate to estimate spoilage.

5. Conclusions

The purpose of this work was to demonstrate that NMR spectroscopy could be used to study tomato paste spoilage in 1000 L, large format, non-ferrous, metal-lined totes. To accomplish this goal, a reduced magnetic field was used to explore the relaxation properties of sterile and unsterile samples. It was found that the increase in T_1 values for the unsterile samples could be used as a metric for spoilage and that the reduced operating frequency permitted measurement of the T_1 values for standard samples enclosed in aseptic metal-lined totes. Introduction of a single sided magnet afforded the measurement of T_1 for tomato paste in a large format tote for the first time and, coupled with the small sample T_1 metrics, can be used to non-invasively monitor tomato paste spoilage.

Two extensions of this work are being considered. The unsterile tomato paste sample set used in this study was generated from a realistic factory contamination source. One extension currently underway involves a more thorough investigation of the relationship between measured T_1 values and tomato spoilage mechanisms. Contamination sources include real in-the-field locations as well as documented bacterial strains. The second extension involves downsizing the single sided ABQMR magnet system to a hand-held NMR MOUSE device [10]. It is this portable instrument that will be useful for screening filled large format totes in a factory process environment.

Acknowledgments

Encouragement to study and theoretical support for the recovery of NMR signals from samples in non-ferrous, metal containers by Joe Broz is gratefully acknowledged. Support of this work by the California League of Food Processors is also gratefully acknowledged.

Author Contributions

Data collection and interpretation was accomplished by Michael Pinter under the supervision of Matthew Augustine and in collaboration with Michael McCarthy. Tod Harter supplied all tomato paste samples on behalf of The Morning Star Company.

Conflicts of Interest

The author declares no conflicts of interest.

References

1. Gustavsson, J.; Cederberg, C.; Sonesson, U.; van Otterdijk, R.; Meybeck, A. *Global Food Losses and Food Waste*; FAO: Rome, Italy, 2011.
2. Py, D. Process for filling a sealed receptacle under aseptic conditions. US Patent 5,641,004, 19 April 1995.
3. Scholle Packaging. Processed Fruits Bag-in-Box Packaging for Apples, Citrus Fruits, Deciduous Fruits, Tomatos and Tropical Fruits. Available online: <http://www.scholle.com/applications/processed-fruits> (accessed on 14 August 2013).
4. Skoog, D.A.; Holler, F.J.; Crouch, S.F. *Principles of Instrumental Analysis*, 6th ed.; Thomson Brooks/Cole: Belmont, CA, USA, 2007; pp. 281, 492.
5. Weekley, A.J.; Bruins, P.; Sisto, M.; Augustine, M.P. Using NMR to study full intact wine bottles. *J. Magn. Reson.* **2003**, *161*, 91–98.
6. Kim, S.M.; Chen, P.; McCarthy, M.J.; Zion, B. Fruit internal quality evaluation using on-line nuclear magnetic resonance sensors. *J. Agr. Eng. Res.* **1999**, *74*, 293–301.
7. Tzouros, N.E.; Arvanitoyannis, I.S. Agricultural Produce: Synopsis of Employed Quality Control Methods for the Authentication of Foods and Application of Chemometrics for the Classification of Foods According to Their Variety or Geographical Origin. *Crit. Rev. Food Sci. Nutr.* **2001**, *41*, 287–319.
8. Celozzi, S.; Rodolfo, A.; Lovat, G. *Electromagnetic Shielding*; John Wiley & Sons, Inc.: Hoboken, NJ, USA, 2008; pp. 65, 285.
9. Blümich, B.; Perlo, J.; Casanova, F. Mobile single-sided NMR. *Prog. Nucl. Magn. Reson. Spectrosc.* **2008**, *52*, 197–269
10. Blümich, B.; Blümmler, P.; Eidmann, G.; Guthausen, A.; Haken, R.; Schmitz, U.; Saito, K.; Zimmer, G. The NMR-mouse: Construction, excitation, and applications. *Magn. Reson. Imag.* **1998**, *16*, 479–484.
11. Poole, C.P., Jr.; Farach, H.A. Relaxation in Liquids. In *Relaxation in Magnetic Resonance*; Academic Press, Inc.: New York, NY, USA, 1971; pp. 154–196.

Software Defined Radio (SDR) and Direct Digital Synthesizer (DDS) for NMR/MRI Instruments at Low-Field

Aktham Asfour, Kosai Raof and Jean-Paul Yonnet

Abstract: A proof-of-concept of the use of a fully digital radiofrequency (RF) electronics for the design of dedicated Nuclear Magnetic Resonance (NMR) systems at low-field (0.1 T) is presented. This digital electronics is based on the use of three key elements: a Direct Digital Synthesizer (DDS) for pulse generation, a Software Defined Radio (SDR) for a digital receiving of NMR signals and a Digital Signal Processor (DSP) for system control and for the generation of the gradient signals (pulse programmer). The SDR includes a direct analog-to-digital conversion and a Digital Down Conversion (digital quadrature demodulation, decimation filtering, processing gain...). The various aspects of the concept and of the realization are addressed with some details. These include both hardware design and software considerations. One of the underlying ideas is to enable such NMR systems to “enjoy” from existing advanced technology that have been realized in other research areas, especially in telecommunication domain. Another goal is to make these systems easy to build and replicate so as to help research groups in realizing dedicated NMR desktops for a large palette of new applications. We also would like to give readers an idea of the current trends in this field. The performances of the developed electronics are discussed throughout the paper. First FID (Free Induction Decay) signals are also presented. Some development perspectives of our work in the area of low-field NMR/MRI will be finally addressed.

Reprinted from *Sensors*. Cite as: Asfour, A.; Raof, K.; Yonnet, J. Software Defined Radio (SDR) and Direct Digital Synthesizer (DDS) for NMR/MRI Instruments at Low-Field. *Sensors* **2013**, *13*, 16245–16262.

1. Introduction

The development of Nuclear Magnetic Resonance (NMR) and Magnetic Resonance Imaging (MRI) systems is still motivated by the outstanding features of this technique. Medical diagnosis and medical research as well as analytical chemical spectroscopy are the main areas that have mostly benefited from the potentials of the NMR. In these areas, high magnetic fields (up to 11 T), generally produced by superconducting magnets, are frequently used. This race to high fields is obviously justified by the high signal-to-noise ratio and the high resolution of the image and of the spectra that could be achieved.

Low-field (about 0.1 T) NMR is also well-known now. When compared to high field, low-field NMR has the main advantage of reduced system cost, size and complexity since low fields can be easily generated by electromagnets or permanent magnets. These features have allowed the technique to conquer exciting new applications, especially for situations where the bulky and prohibitively expensive high field systems cannot be used or the sample to be studied cannot be moved. The applications of low-field and mobile NMR systems could include—but are not limited to—areas such as material science, non-destructive quality control of products (food, polymers...), moisture

and porous media measurement, paper, wood and oil industries, non-destructive studies of cultural heritage (stones, old master painting, mummies...). Even biomedical applications (MRI/NMR of the tendon or skin) should benefit from mobile and low-field instruments. An excellent review of many of these promising applications of the NMR has recently been presented in [1].

Low-field NMR spectrometers are, in general, not commercially very renowned, despite the existence of some worthy and valuable commercial systems such as those from Magritek, Inc. (Aachen, Germany) for example. Nevertheless, the demand for dedicated spectrometers is still increasing. One of the difficulties associated with such systems is that it may be often necessary to perform a new hardware and software design and development to optimize the whole system for each specific application. The design of the hardware (transmitter and receiver) is crucial and it requires cautions. However, while many publications (academic courses, books, articles...) deal with the design of the radiofrequency (RF) coil itself, which obviously defines the final signal-to-noise ratio, these publications rarely address issues for the design of the transmitting and receiving electronics. This electronics is usually assumed to be a “black box”. Some groups have already worked to develop their own dedicated low- and very-low field NMR spectrometers for specific applications [2–8]. For example, we have recently proposed very low-field NMR spectrometers that allow detection of the ^1H NMR signals at 4.5 mT (about 180 kHz of Larmor frequency) without pre-polarization [2–4]. Such developments were initially motivated by their application to the measurement of the *absolute polarization* of hyperpolarized xenon (^{129}Xe). These spectrometers were based on the use of general-purpose commercial data acquisition boards (DAQ) from National Instruments (Austin, TX, USA). Based on DAQ boards, an NMR system at 0.1 T for educational purposes was also presented in [5]. Another NMR spectrometer with fully analog electronics has been proposed for the NMR of hyperpolarized helium (^3He). Other works carried out in [7,8] were focused on the realization of a digital home-built NMR spectrometer working at high field (frequencies up to 80 MHz). In these designs, the NMR system was composed of a form of combination of analog and digital circuits. Actually, analog mixers were necessary in the transmitter and/or before digitalization by the receiver. Despite the great merits and the advances achieved by these works, large spread of the low-field NMR still requires decreasing the complexity of the hardware and associated software, increasing the flexibility as well as lowering the cost of the system. A main idea is that hardware and software of the spectrometer could be easily updated for the largest number of applications and different working frequencies with minimum development time and low cost.

In our laboratory, we are currently working on the design of low-field and mobile NMR instruments for industrial applications such as the quality control of oranges, the moisture measurement in nuts or other products as well as the inside-out NMR for high resolution spectroscopy in inhomogeneous magnetic fields [9]. Our work includes the design of the full system, *i.e.*, the magnet and the spectrometer [10].

The present paper will mainly focus on a new design of the electronics for transmitting and signal receiving. It actually reports some parts of our experience in this area. This experience is presented here through the development of a fully digital RF hardware and the associated software for the NMR at 0.1 T (4.2 MHz of Larmor frequency). This electronics is based on three key elements: a Direct Digital Synthesizer (DDS) for pulse generation, a Software Defined Radio (SDR) for signal receiving

and a Digital Signal Processor (DSP) as a controller and pulse programmer. Except for the RF power amplifier and the low-noise preamplifier, the proposed system is fully digital and programmable by software. Its architecture is open so as to allow for the easy update and extension for a large number of NMR experiments and working frequencies. One of the ideas of this paper is to enable the NMR systems to “enjoy” from existing advanced technologies that have been achieved in others research areas. Actually, the main concepts of this new developed system are inspired from advanced digital signal processing techniques that are now frequently employed in telecommunication systems, especially in mobile radio and cellular base stations. The paper attempts to show that these techniques could be applied to the NMR through the realization of a proof-of-concept.

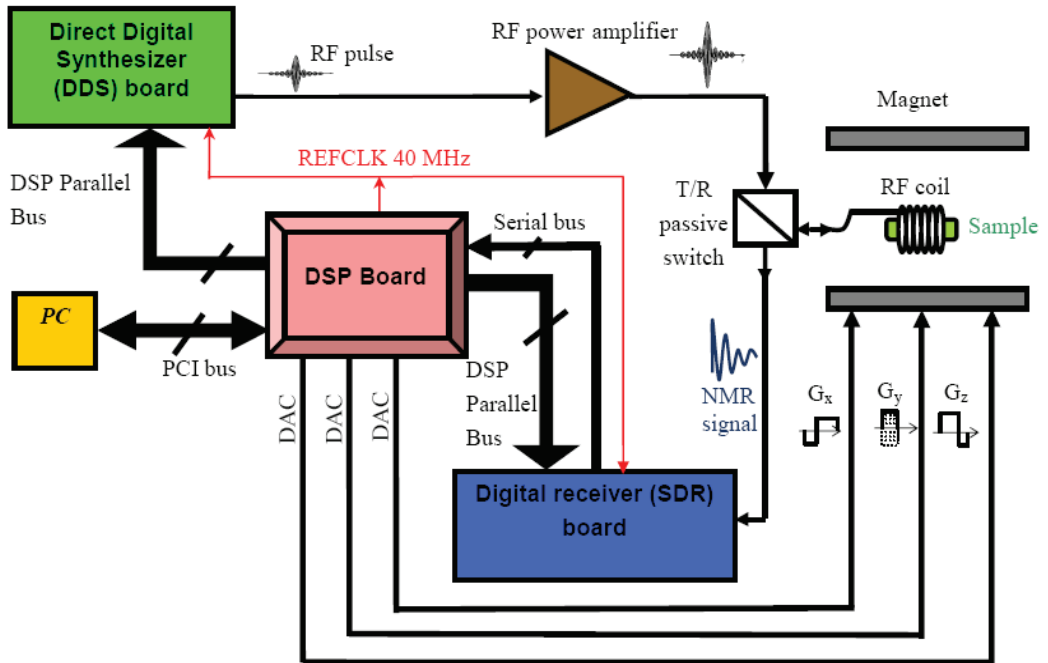
We should however note that some devices which may have similar architectures have been available from specialized manufacturers for a few years now. For example, the RedstoneTM spectrometer from Tecmag (Houston, TX, USA) has a modular design with up to 128 transmitters and 512 receivers [11]. Imaging Technology Abruzzo S.r.l (L’Aquila, Italy) proposes another console with four receiving channels [12]. Nevertheless, one goal of the paper is actually to help people to get an idea of the current trends in this area. Another goal of this paper is to try to make the NMR systems versatile and easy to replicate so as to help developers and research groups in realizing NMR spectrometers with flexibility, low cost and minimum development time. This is why we describe with some details the various aspects of the realization. While some of these aspects may seem basic for knowledgeable developers, we believe that they may be useful for those who would like to learn about the conditioning electronics and the application of telecommunication technology to NMR sensors.

In addition to the presentation of the new developed system (DSP, DDS and SDR) and the associated software, the expected performances and potentials of the system are given throughout the paper. First experimental tests of the receiver are then presented. Some issues related to the design of the RF coil and the adequate tuning and matching circuits at low-field are illustrated, together with the first Free Induction Decay (FID) for validation purposes. Development perspectives of our work in area of sensors for the low-field NMR will also be addressed.

2. Hardware Implementation

Figure 1 shows the hardware of the home-built system. The core of the design is a Digital Signal Processor (DSP) board which controls the other two elements of the electronics: the Direct Digital Synthesizer (DDS) and the Software Defined Radio (SDR) or digital receiver. These elements were designed as daughter boards of the DSP and are fully programmable by the DSP via its parallel external bus.

Figure 1. A block diagram of the DDS and SDR based NMR system at 0.1 T.



The excitation pulse is synthesized by the DDS. After amplification by a home-built RF power amplifier (about 250 W peak), this pulse is sent to the well-tuned RF coil via a transmit/receive (T/R) passive switch. At the end of the excitation pulse, the NMR signal is detected by the coil (assuming a transmit-receive coil) and transmitted, via the same T/R switch, to the digital receiver. This receiver includes an amplifier and a Software Defined Radio (SDR) for digital quadrature demodulation, decimation and filtering. The samples of the demodulated signals are then transmitted to the DSP, via a serial bus, where more signal processing could be performed if necessary.

For imaging purposes, the gradient signals are generated by the DSP board thanks to a set of three Digital-to-Analog Converters (DAC). Furthermore, the DSP, DDS and the SDR are synchronized with a same external 40 MHz reference clock (REF CLK) available on the DSP board. The key elements of this design and their main performances are addressed in the next sections.

2.1. The Digital Signal Processor (DSP) Board

The DSP was designed as PCI plug and play board. This home-built board includes mainly the processor ADSP-2106x SHARC—Super Harvard Architecture Computer—from Analog Devices (Norwood, MA, USA) [13]. The reputation of the high performance ADSP2106x processors comes mainly from their ability to perform 32-bits floating-point calculations. They are optimized for real-time digital signal processing and are widely used in applications requiring high computing speed. Compared to a conventional processor, the use of DSPs in the MRI system offers more options and flexibility in signal processing and image reconstruction in real time as well as in the time management during the sequence.

The processor has an on-chip internal memory of 4 Mbits for the temporary storage of the NMR signal samples. It has also several fast and efficient protocols for communication and data transfer with a wide variety of devices (external memory, PC, other DSP...). In particular, external parallel buses of the processor were used in our design to control and to upload the parameters of the SDR and the DDS. These chips were actually memory-mapped devices of the DSP. The high speed synchronous serial port of the DSP was used to transfer the digital data (NMR signal samples) from the digital receiver to the DSP. External channels are available to transfer data from the DSP memory to the host (PC, other DSP...).

In addition to the processor, the DSP board includes also the set of three 16-bit DACs. The level of the analog signals at the output of these DACs could be adjusted in the range ± 10 V. The residual noise output is less than 1 mV. These DACs are used for the generation of the gradient waveforms at a sampling frequency up to 2 MHz.

The DSP, which ensures the role of the pulse sequencer, is programmed in assembly language as it will be presented in Section 3. In our design, the processor is clocked at 40 MHz. This 40 MHz clock (REFCLK) is also used as a reference clock for the DDS and the SDR (Figure 1).

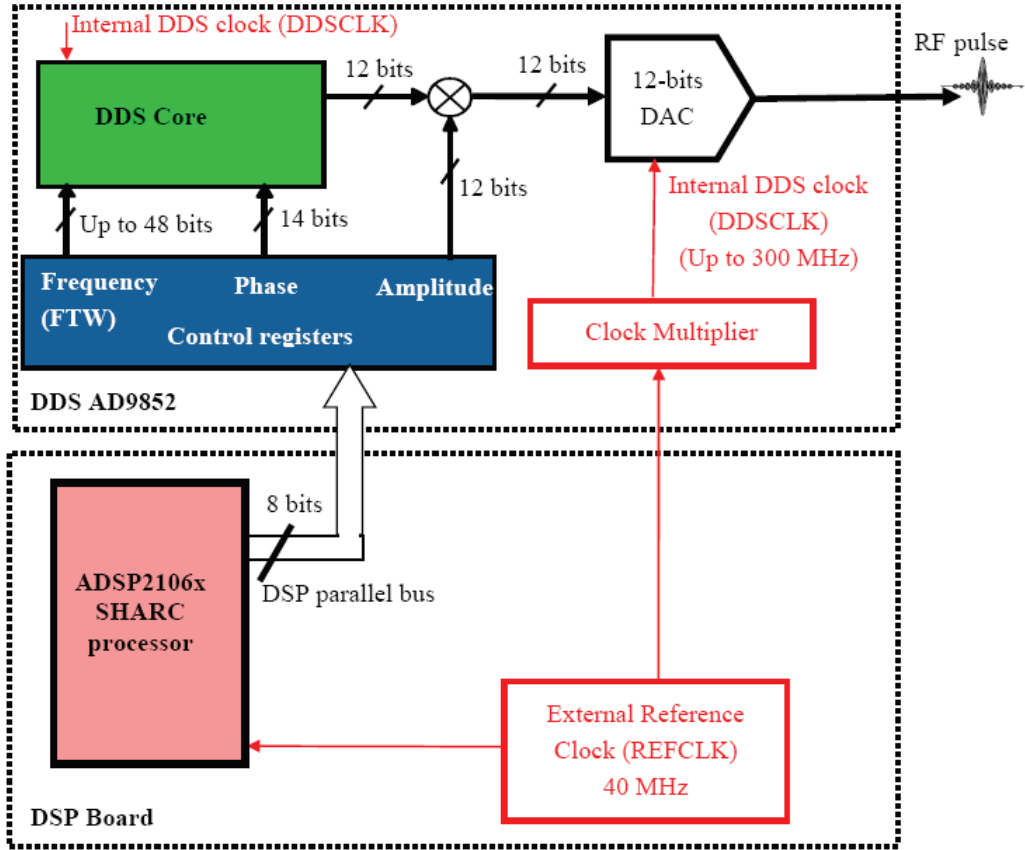
2.2. The Direct Digital Synthesizer (DDS)

The transmitter board is home-built. Its core is the DDS AD9852 from Analog Devices [14]. The DDS technology is based on the fact that one could define a sinusoid with known frequency, amplitude and phase by specifying a set of values (samples) taken at equal intervals defined by the sampling frequency. This series of values is supplied to a Digital-to-Analog Converter (DAC) that provides the analog signal. This technology is now widely used for in telecommunication systems.

Figure 2 shows a simplified diagram of the DDS AD9852 and its interface with the DSP. When referenced to an accurate clock source, the DDS, coupled with an internal high speed DAC, generates a highly stable and accurate frequency-phase-amplitude-cosine waveform. The circuit allows theoretically the generation of output signals at frequencies up to 150 MHz when it is clocked at 300 MHz.

In our design, we make use of the clock multiplier to generate an internal DDS clock (DDSCLK) from a lower frequency external reference clock (40 MHz). In addition to the fact that the whole system should be synchronized with a same clock, the use of the clock multiplier allows the developer to avoid difficulties of implementing a high frequency clock source system. We used a multiplication factor of 4 so as the final frequency of the internal clock of the DDS is 160 MHz. This frequency is also the sampling frequency of the on-chip 12-bits DAC. The value we have chosen for this frequency was actually a trade-off between the generation of cosine waveform with high resolution and spectral purity and the overheating of the chip.

Figure 2. A simplified diagram of the DDS and its interface with the DSP.



The frequency, phase and amplitude are digitally programmable by writing values in the DDS control registers through the 8-bit parallel external bus of the DSP. The desired output frequency, F , is translated to a Frequency Tuning Word (FTW) according to Equation (1):

$$FTW = 2^N \frac{F}{DDSCLK} \quad (1)$$

where N is the frequency resolution (up to 48 bits), FTW is a decimal number, DDSCLK is the frequency of the DDS clock and F expressed in Hertz.

High frequency resolution can be obtained. For example, if $DDSCLK = 160$ MHz and $N = 34$ bits, the obtained frequency resolution is about 0.009 Hz. In our implementation, this 34-bit resolution was chosen for synchronization purposes and exact match between the frequency of DDS and the demodulation frequency (frequency of the NCO) of digital receiver (see Section 2.3).

In a similar way, the output phase and amplitude can be defined digitally with resolutions up to 12-bit and 14-bit, respectively. Shaped (amplitude modulated) RF pulses are easily generated by making use of a 12-bit digital multiplier which allows user to dynamically and digitally modulate the

amplitude of the output signals. This allows generation of almost arbitrary RF pulse shape. Frequency-and phase-modulated signals can also be easily generated.

This DDS is actually a multifunction and a highly flexible device that addresses a wide range of important and required functionalities for the NMR systems. In addition to the high resolutions that could be achieved and the classical amplitude modulation, the DDS can easily satisfy more sophisticated and new emerging forms of NMR excitation such as shim-pulses (extension of the concept of uniform broadband excitation). These pulses that require phase- and amplitude- modulation of the RF pulse together with a modulation of the gradient tensor are promising excitation forms for the high resolution NMR in inhomogeneous magnetic fields [1]. Furthermore, most of the NMR techniques need that RF source of the transmitter has the agility to rapidly switch its phase, frequency and amplitude. For the used DDS, the update rate of these parameters is user programmable and could be as fast as 6 ns.

2.3. *The Software Defined Radio (SDR) for Signal Receiving*

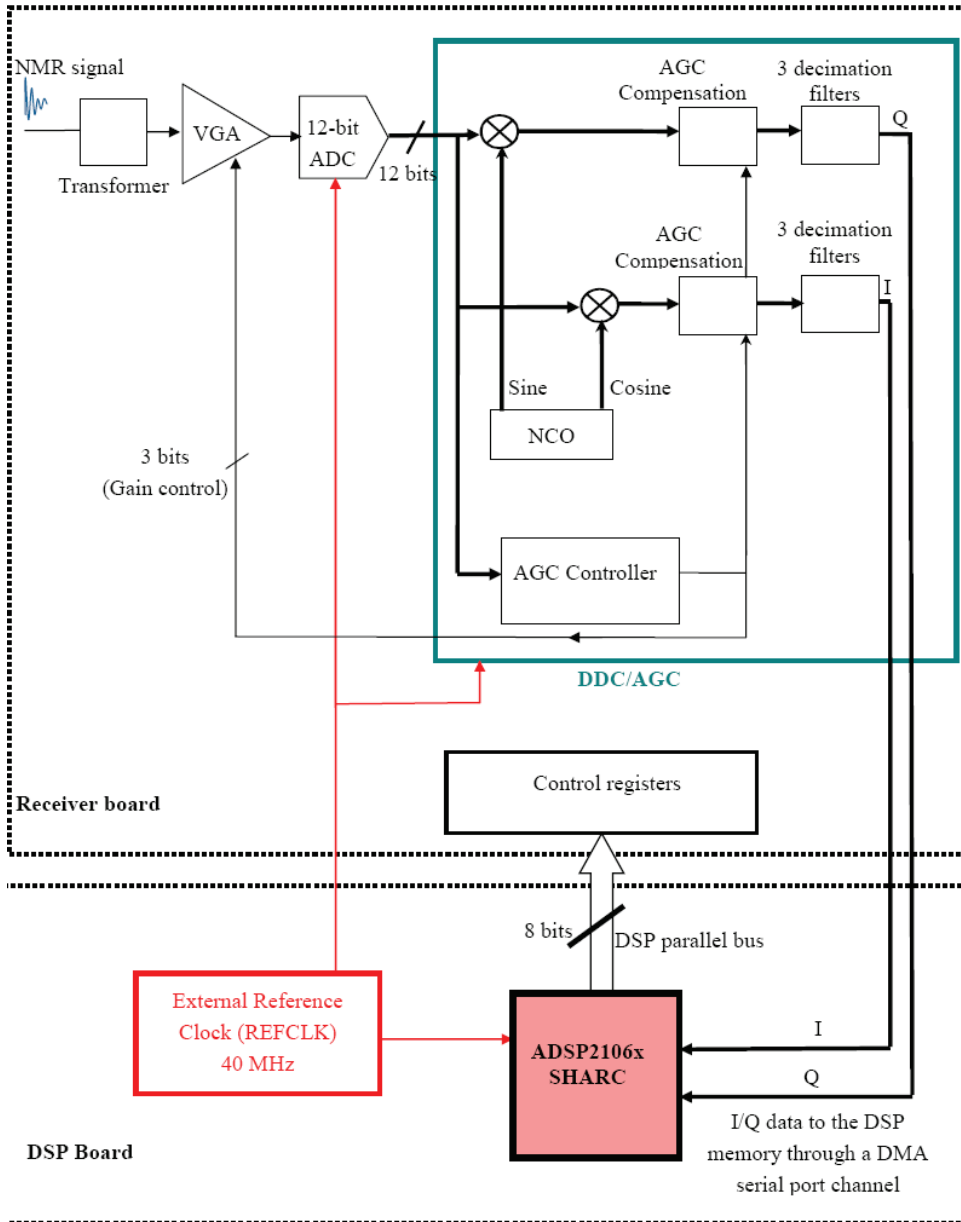
Another key element of the NMR/MRI system we built is the digital receiver. As we have mentioned in the Introduction, the architecture of the receiver is inspired from advanced digital signal processing techniques that are especially applied in mobile radio and cellular base stations. In the area of telecommunication, the set of these techniques is commonly called *Software Defined Radio (SDR)* or *digital receiving*. Its basic idea is to perform the digital-to-analog conversion as close to the receiving coil as possible. All the signal processing (quadrature demodulation, decimation, filtering) can then be realized in the digital domain. This has the advantage of noise and distortion reduction associated with analog mixing stage and better out-of-band noise rejection by the decimation and the digital filters. Moreover, the parameters of the system are fully programmable. They could be modified by the software and without changing the hardware architecture.

The receiver we built was inspired from an evaluation board of the dual Digital Down Converter Chip CLC5902 from National Semiconductor (Santa Clara, CA, USA) [15]. This evaluation board was factory designed to be programmable by the PC through the serial RS232 port, an on-board microcontroller and associated software for applications in cellular base stations, satellite receivers and digital communication.

We have re-designed this evaluation board to integrate it in our home-built NMR system (together with the DDS and the DSP boards). Hardware modifications and new software development were necessary. These modifications have allowed programming the receiver directly by the parallel port of the DSP with suitable new software and data transmission through the high speed serial port of the DSP as well as synchronization of the whole system with a same reference clock (40 MHz) for the NMR experiments. Figure 3 shows the block diagram of the architecture of one receiving channel with the DSP. The second receiving channel is identical (not shown in Figure 3) and is not currently used in our applications. Extension to more than two channels could be possible.

The receiver channel mainly consists of a Variable Gain amplifier (VGA), an Analog-to-Digital Converter (ADC) and Digital Down Converter (DDC) with an Automatic Gain Controller (AGC). It accepts intermediate frequency (IF) analog signals (NMR signals in our case) and performs a digital quadrature demodulation to obtain the final In-phase (I) and Quadrature (Q) signals.

Figure 3. Block diagram of one receiving channel and its interface with the DSP. The second receiving channel is not shown.



The channel input is coupled into the VGA by a transformer. This transformer matches the input impedance of the VGA (200 Ω) to the 50 Ω input connector and the NMR coil. The signal is then amplified by the low-noise and wideband VGA. This VGA has a digitally controlled gain range from -12 dB to +30 dB. It is also the gain control element of an Automatic Gain Control (AGC) loop.

After amplification, the signal is directly sampled by a 12-bit Analog-to-Digital Converter (ADC) clocked at 40 MHz. It is a 12-bit and wideband ADC capable of inputs as high as 300 MHz at sample rates up to 70 MHz. The sampled signal is applied to the Digital Down Converter (DDC) which integrates the AGC controller. The DDC uses a Numerically Controlled Oscillator (NCO) to generate the sine and cosine digital waveforms used by the digital mixer. The frequency and phase of the NCO are set by loading the appropriate control registers. This loading is done by the DSP. In a similar way as for DDS (Equation 1), the Frequency Tuning Word for the NCO (FTW_{NCO}) is 32-bit and is given by Equation (2):

$$FTW_{NCO} = 2^{32} \frac{F}{REFCLK} \quad (2)$$

where FTW_{NCO} is a decimal number, REFCLK is the frequency reference clock and F is the frequency expressed in Hertz. For REFCLK = 40 MHz, the obtained resolution is about 0.009 Hz.

In NMR, it is necessary to exactly match the frequencies of the NCO and the DDS. The same frequency resolution, expressed in Hertz, has to be obtained. As the NCO and DDS are clocked at different rates, it was necessary to use a 34-bit Frequency Tuning Word for the DDS. In the same way, the phases of the NCO and DDS must have the same resolution. This was straightforward to implement in our system by software. Furthermore, thanks to programming features of both NCO and DDS and the use of a unique reference clock for the whole system, the receiver remains phase locked with the transmitter. This is mandatory in NMR sequences, especially to make signal averaging possible.

The digital mixers of both channels of the DDC are followed by digital AGC compensation which is controlled by the AGC controller. This controller measures the output level of the ADC (output power measurement using an envelope detector). This measurement is used to automatically adjust the VGA gain so as the dynamic range of the input signal is expanded or compressed to fit the full scale of the ADC. By doing so, the dynamic range of the ADC is extended. This feature is particularly useful for the MRI where the signals (echoes for example) have generally very different levels. The AGC ensures optimization of the gain and the ADC dynamic range for each signal (despite the fact that the ADC may never see full scale in the case of the weak NMR signals). After digitization, it is however necessary to compensate for the compressed or expanded dynamic range. This compensation is digitally performed by the AGC loop (Figure 3). It is also possible to inhibit the AGC loop and force fixed VGA gain values. More details about the AGC operation could be found in [15].

After the digital AGC compensation, the I/Q signals are filtered by three decimation filters that achieve a low-pass filtering and low output sample rate. The first filter is a Cascaded-Integrator-Comb (CIC) with fixed coefficients. It decimates (under-samples) the input data by a programmable factor between 8 and 2048. The CIC filters are widely used in digital receivers. Their structure is very simple and their implementation requires no multipliers and only limited storage. Consequently, the computation

speed is very fast. These characteristics make them especially suitable as the first-level decimator filters for high sample rate change. The CIC output is followed by two filtering stages. The first stage is a 21-coefficients symmetric Finite Impulse Response (FIR) filter with programmable coefficients. It also decimates the input by 2 (fixed decimation factor). The second filter is also a symmetric FIR with user programmable coefficients (63 coefficients). It decimates by a factor of 2 or 4.

The operating frequency of our NMR system is 4.2 MHz (0.1 T of magnetic field). This signal will actually be over-sampled (at 40 MHz) by the ADC. An advantage of this high over-sampling rate is the potential for processing gain. Processing gain usually refers to the increase of the ADC Signal-to-Noise Ratio (SNR) and dynamic range that can be obtained by the decimation. Generally, the ADC SNR is limited by the thermal noise. For a given ADC, the noise bandwidth is normally defined as the Nyquist bandwidth (the half of the sampling frequency). For the ADC we used and for a sampling frequency of 40 MHz, this yields to an SNR of at least -65 dB relative to the full-scale (dBFS) [16]. The decimation technique that reduces the sampling frequency of the I/Q base band signal provides a much narrower final bandwidth at the output. Since the noise is spread out over the full bandwidth of the digitizer, only the noise in narrower bandwidth is retained. For example, if the final output bandwidth is 25 kHz (± 12.5 kHz) and the initial sampling frequency is 40 MHz, one can expect an ADC SNR improvement given by Equation (3):

$$\text{Processing gain} = 10 \times \log \frac{25 \text{ kHz}}{20 \text{ MHz}} = -29 \text{ dB} \quad (3)$$

The expected ADC output SNR (after the decimation filters) is then given by Equation (4)

$$\text{SNR (dBFS)} = -65 \text{ dBFS} - 29 \text{ dB} = -94 \text{ dBFS} \quad (4)$$

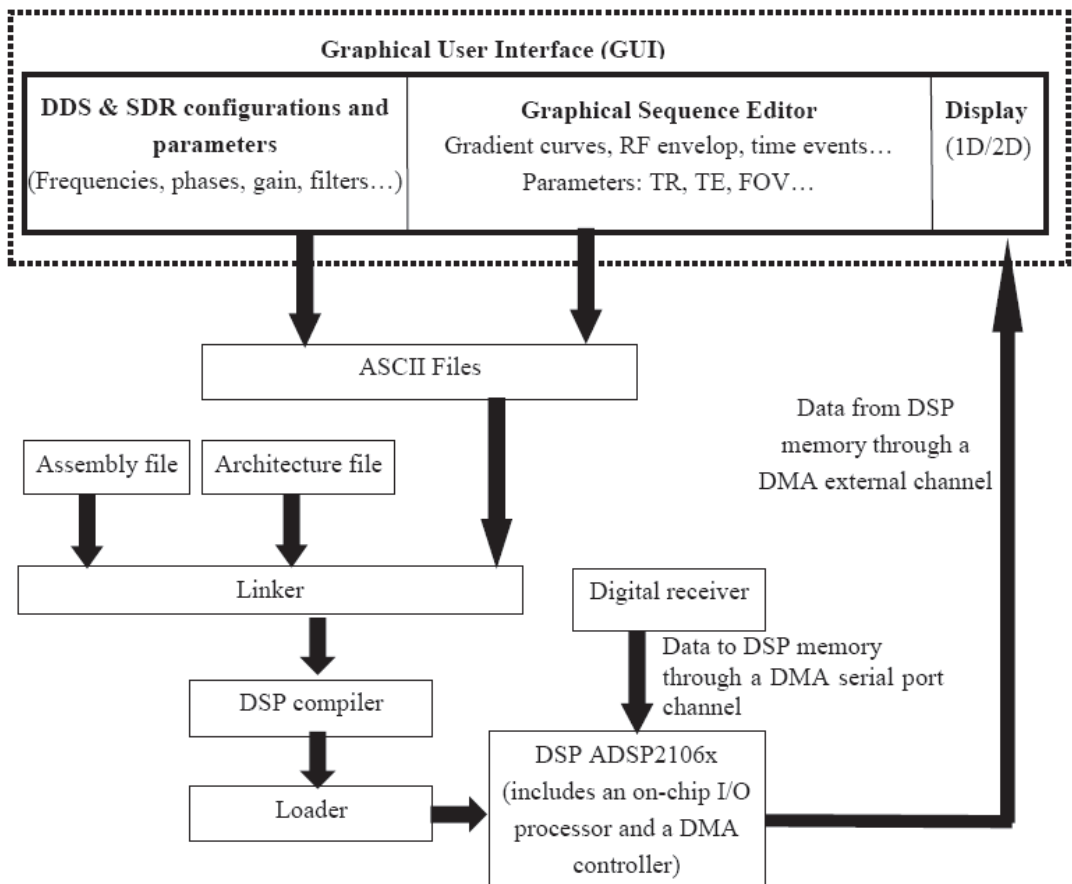
We have to mention that this SNR will not be realized in most NMR experiments. Actually, the Equation (3) does not take into account the thermal noise from the receiving coil and the preamplifier which could be more important than the other noise sources (ADC and quantization noises). The level of this thermal noise could be of several least-significant bits. One could however expect some improvement in the SNR because the well designed digital filters will be very effective in out-of-band thermal noise rejection.

3. Sequencer and Software

While the present paper is only focused on a proof-of-concept of the use of digital concepts, the software was thought to already take into account the future implementation of almost all types of NMR/MRI sequences. This software was developed using the LabWindows/CVI[®] environment and DSP assembly language [13]. Figure 4 illustrates its block diagram. The Graphical User Interface (GUI) allows user to define and edit all the configurations and parameters (frequencies, phases, filters...) of the hardware (DDS and SDR). It also enables user to draw and/or graphically edit a sequence (pulse envelop, gradient waveforms) and to define parameters such as repetition time (TR), echo time (TE) and the Field-of-View, *etc.* The use of this graphical sequence editor allows avoiding programming the gradient waveforms in text sequence editor.

Data from the GUI are stored in ASCII files. These files are then linked with the assembly and the architecture files of the DSP. The assembly compiler provides then an executable file which is loaded in the DSP RAM via the PCI bus. This assembly program or sequence program interprets all the data defined in the GUI and controls all the temporal events of the sequence and the data transfer and commands between the three boards (DSP, DDS and SDR). The use of the assembly language was adequate to optimize the memory use of the DSP and to facilitate the management of the temporal events within the sequence. In this way, the DSP ensures the role of a high performance pulse programmer (sequencer) which is able to execute each program instruction at every clock cycle with a high temporal resolution (25 ns for a clock of 40 MHz). The generation of gradient signal is achieved with 0.5 μ s of temporal resolution.

Figure 4. Block diagram of the developed software.



It is important to note that a lot of the sequence and DDS/SDR parameters could be modified in real time during the sequence execution without reloading the program in the DSP. This important functionality was naturally implemented thanks to the input/output (I/O) registers of the DSP. The

host of the DSP (the PC in our case) can directly write and/or read these registers which are continuously read by the DSP at certain interrupt services.

The management of the data transfer from the digital receiver to the DSP and from the DSP to the host PC requires some cautions. This management has been achieved relatively easily thanks to the high performances and high flexibility of the ADSP210x DSP. Actually, the architecture of this chip is composed of four main parts: a Core Processor, a Dual-Ported SRAM, an External Port and an Input/output (I/O) Processor [13]. This on-chip I/O processor is responsible for managing a Direct Access Memory (DMA) Controller. This DMA controller handles several transfer channels. Two of these channels belong to the synchronous serial ports and are used to transfer the received data from the digital receiver to the memory of the DSP (Figures 3 and 4). Once it has been setup, the DMA controller operates independently from the core processor [13]. This frees the core processor to continue with other tasks (like the generation of a next RF pulse if required in the sequence).

Acquired data could be available to the host PC immediately when a block of the data (with user-defined size) is available in the DSP memory. The used DSP has a very powerful host interface which is interfaced to the PCI bus of the PC by using a PCI target I/O accelerator bridge on the DSP board. The host can read the data as soon as they are received and at each moment independently from the core processor. This transfer between the DSP memory and the host is done, once again, by the DMA controller of the I/O processor. Actually, in addition to the serial port channels, the DMA controller manages external channels which are responsible for data transfer between the DSP memory and the external hosts via the powerful host interface.

Since the data transfer from the DSP to the host is managed by the DMA controller of the I/O processor (and not by the core processor), it could be done when the data (with user-defined size) are available. It can also be done at the end of the sequence or during its dead time. In our design, managing the moment at which one wants the data to be available to the host is a task of the sequence developer. This moment may be defined with some flexibility according to the constraints of each sequence.

The whole structure of the software is actually very flexible and open so as to allow an ease-of-use of existing sequences and low-complexity implementation of new sequences. Other required functionalities for NMR system were also implemented in the same GUI (not shown in Figure 4). These include functions for coil tuning and for active shimming.

4. Discussions and Validation

4.1. First Performances and Test of Receiver

As it was mentioned, one of the important advantages of the SDR is its completely programmable feature. This allows user to easily choose parameters such as amplifier gain, decimation factors and filters coefficients to obtain optimum performances for a given experience.

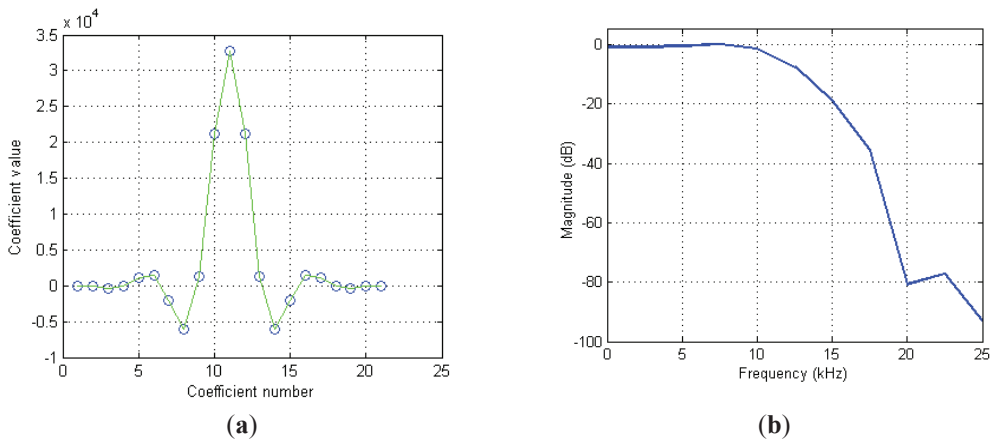
In order to test the receiver operation, we fixed the working frequency at 4.2 MHz (Larmor frequency at 0.1 T). The sample rate of the ADC was 40 MHz. The CIC decimation factor was fixed at 400. The sample rate at the output of the filter was then of 100 kHz.

The two programmable FIR filters were designed. This first one was mainly designed to compensate for a slight droop induced by the CIC filter. It improves so the flatness of the CIC

pass band. In addition, it could provide stop band assistance to the following filtering stage. Figure 5 shows an example of the impulse and frequency responses of a set of coefficients we used in our system.

The filter has a unit gain and flat pass band (only 0.01 dB ripple) over nearly the full output band pass with 70 dB of out-of-band rejection (Figure 5b). Notice also that impulse response is symmetric. Only 11 coefficients (over 21) are actually loaded in the receiver.

Figure 5. (a) The impulse response of the first programmable filter; (b) The frequency response of the same filter. The filter has a fixed decimation factor of 2. In this example, the input and the output sample rates were 100 kHz and 50 kHz, respectively.



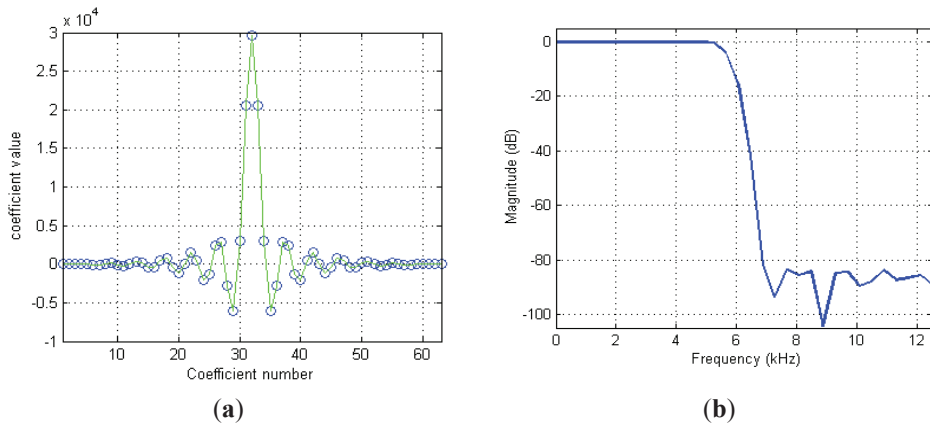
The second FIR filter is responsible for limiting the final bandwidth. It ensures also a high out-of-band noise rejection. An example of the impulse and frequency responses of this filter is shown in Figure 6. The filter has 0.03 dB of pass band ripple and about 80 dB of out-of-band rejection. The final cut-off frequency is defined mainly by this filter. In our case, it was fixed to about 5.8 kHz at -3 dB. This frequency corresponds simply to the bandwidth we have fixed for NMR signals during future image acquisition with basic spin- and gradient-echo sequences in our system. This bandwidth is naturally related to the maximum image resolution.

It is very important to note that digital decimation filters introduce actually a temporal group delay which depends on the filters order, the overall decimation factors and the system clock period.

This delay must still be present in the mind of the sequence developer and have to be taken into account, especially in situations where RF pulses and acquisition windows are very close each. Actually, in these situations, the DSP must be able to manage at the same the generation of the RF pulse and the receiving of the delayed data. In our design, this problem was solved thanks the on-chip I/O processor and the independent DMA controller offered by the ADSP2106x as it was mentioned in Section 3. Moreover, it is also very important to mention here that the filtering and decimation are done inside the digital receiver and not by the DSP. This help a lot to have an adequate distribution of the calculation power between the calculation units.

We note finally that if simultaneous RF transmission and delayed data receiving should occur, the analog noise from the transmitting section will not affect the data which are already digital. Actually, a main advantage of the direct sampling and the digital receiving is that analog noise has no more effect after the analog-to-digital converter (ADC), unless the RF, travelling by air or on the ground, is so high so as to invert digital bits. In all the cases, the layout of the whole system and grounds should be designed with cautions. In our design, separate analog and digital grounds are used for each of the DSP, DDS and SDR boards.

Figure 6. (a) The impulse response of the second programmable filter. (b) The frequency response of the same filter. The filter has a programmable decimation factor (2 or 4). In this example, the input and sample rate was 50 kHz. The decimation factor was programmed to 2. The output sample rate was 25 kHz.



Under these conditions, experimental tests have been conducted to verify some of the performances of the receiver. The VGA gain was fixed to 30 dB (the AGC loop was inhibited). First, a pure sine wave of 4.2 MHz is applied with variable amplitude from -50 dB to -130 dB to the receiver input. The observed sensitivity (the smallest observable signal) for the receiver was -120 dB and the best dynamic range for the digital full scale output was at -96 dB. Noise rejection was also evaluated by introducing a sum of 4.2 MHz sine wave and a large band noise with a zero signal-to-noise ratio. The results have shown a total rejection out-of-band noise which was beyond our measurement instrument.

We note finally that NMR spectrometer could also be used at working frequencies as high as 150 MHz (for both DDS and SDR), without any change of the hardware (except for the tuned coil) and without the use of any analog mixer as it was the case in [7].

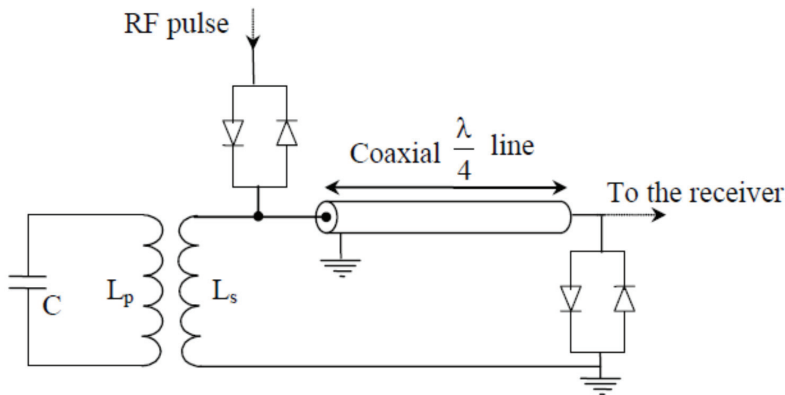
4.2. The Complete NMR System and First NMR Signals

For validation purposes, the first NMR experiments have been conducted at 0.1 T magnetic field created by a commercial electromagnet (Bouhnik S.A.S, Vélizy Villacoublay, France). The RF

coil was a home-made transmit-receive 7-turns solenoid coil of 20 mm diameter and 16 mm length. The electrical circuit of this coil is shown in Figure 7, together with the passive T/R switch.

The inductance L_p of the coil and the tuning capacitor C were about $0.7 \mu\text{H}$ and 2080 pF , respectively. No adjustable variable capacitor section was used for fine tuning the coil at this validation stage. Actually, the power supply of the used magnet allows to slightly change the value the magnetic field around 0.1 T . The working frequency of the DDS and the SDR, which is fully programmable, is then easily adjusted to fit the resonance frequency of the coil (when this is inside the magnet and loaded by the sample). In other words, we perform a tuning of the working frequency rather than a tuning of the resonance frequency of the coil. On another hand, this solution avoids the use of somewhat sized variable capacitors.

Figure 7. The electrical circuit of the coil and the matching loop L_s together with the passive T/R switch. The inductance of the coil is $L_p \approx 0.7 \mu\text{H}$ and the tuning capacitor is $C = 2,080 \text{ pF}$ ($9 \times 220 \text{ pF} + 100 \text{ pF}$ chip capacitors from ACT Corp.), L_s is the inductance of the matching loop.



The coil was matched to 50Ω using an inductive coupling between the inductance L_p of the coil and the inductance L_s of a second loop. In this design, the matching is performed for each sample by moving the loop with respect to the coil [17]. One of the advantages the inductive coupling is that the electrical balancing of the probe with respect to the electric field is automatically obtained. By doing so, the dielectric losses due to capacitive coupling between the sample and the coil are reduced [18]. These losses could not be neglected even at 4.2 MHz , especially with samples that could have a poor dielectric quality. Moreover, by using an inductive coupling, the tuning of the coil is almost unaffected by various loads (samples). Only the matching is changed. More generally, the tuning and the matching could actually be realized independently.

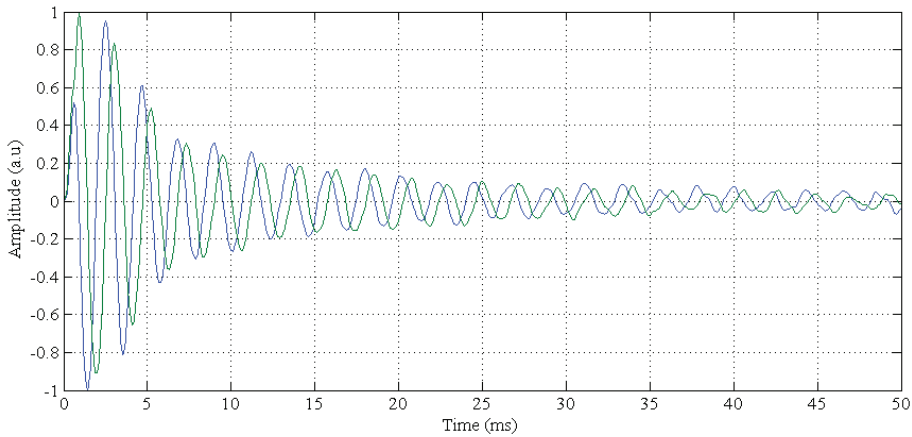
Note that the electrical balancing of the coil could be also obtained by symmetrical capacitive coupling networks. However, at 4.2 MHz the use of the inductive coupling avoids the use large values and sized capacitors (especially adjustable ones) which could be not compatible with the available space inside the magnet.

The passive switch was based on a conventional quarter-wave $\lambda/4$ transmission line approach. The use of this approach is acceptable in this validation phase. However, due to the long length of

the transmission line at such relatively low working frequencies ($\lambda/4 \approx 12$ m at 4.2 MHz), it could be more appropriate to replace this line by a lumped-elements quarter-wave phase shifter in a final system design.

First NMR signals were obtained under these conditions. The sample was a tube of about 1 cm³ of water. Figure 8 shows the I/Q base band signals of the Free Induction Decay (FID) with a small amount of off-resonance (400 Hz). The excitation was a hard 90° pulse with a width of 100 μ s. The repetition time, TR, was about 500 ms.

Figure 8. Base band I/Q signals of the free induction decay (FID) obtained with a hard 90° pulse of 100 μ s of duration and 50 ms of repetition time.



While these first results show a proof-of-concept of the use of SDF and DDS in dedicated home-built low-field NMR systems, it is however necessary to proceed well beyond this demonstration of feasibility in a future work. This work should be focalized on several directions. Firstly, it is important to qualify the SNR of the whole NMR system (including the coil and the preamplifier). The idea is to explore the different possibilities for the optimization of the performances in NMR experiments. Upon the obtained noise performances, this optimization may concern the new designs for the digital filters and the choice of another VGA with better noise performances. Secondly, the impact of the AGC operation must also be evaluated. We expect that this automatic gain control should at least contribute in the enhancement of the SNR of the NMR signals.

Other direction in our work should concern the implementation of the NMR/MRI sequences for various applications. In addition to classical spin- and gradient- echo sequences (which should also confirm the proof-of concept), the Carr-Purcell-Meiboom-Gill (CPMG) sequence will also be investigated for the application of moisture measurement of nuts. More specialized sequences for the high resolution NMR in inhomogeneous field are should be implemented in a near future. The spectrometer is easily transportable and should be suitable for use in mobile and single-sided NMR instruments.

5. Conclusions

We have presented a new electronics and associated software for low-field NMR systems. In the proposed design, we replaced as many analog components as possible with digital electronics and software. Actually, except for the RF power amplifier and the low-noise preamplifier, the whole system is digital, including a DDS for pulse generation, a SDR pour digital signal receiving and a DSP for pulse programming. The first results have validated the use of these telecommunication concepts for the NMR. The flexibility of the system should allow its use, without hardware and software modification, for large palette of NMR applications, especially for mobile and *in-situ* NMR at low-field.

Acknowledgments

The authors would like to thank Anh Tran Thien, Gabriel Malgouyard, Helmi Selmi and Vincent Petitdemaille, graduate students from the High Engineering Schools of Grenoble-INP for their very helpful contribution in the development of the DSP loader. We thank also Claude Brun from Grenoble Electrical Engineering Lab (G2ELAB) for his help in mechanical constructions.

Conflicts of Interest

The authors declare no conflict of interest.

References

1. Blumich, B.; Perlo, J.; Casanova, F. Mobile single-sided NMR. *Prog. Nucl. Magn. Reson. Spectros.* **2008**, *52*, 197–269.
2. Asfour, A. A New DAQ-Based and Versatile Low-Cost NMR Spectrometer Working at Very-Low Magnetic Field (4.5 mT): A Palette of Potential Applications. In Proceedings of the I²MTC 2008 IEEE International Instrumentation and Measurement Technology Conference, Vancouver, BC, Canada, 12–15 May 2008; pp. 697–701.
3. Asfour, A. A novel NMR instrument for the in situ monitoring of the absolute polarization of laser-polarized ¹²⁹Xe. *J. Biom. Sci. Eng.* **2010**, *3*, 1099–1107.
4. Asfour, A. Low-Field NMR/MRI Systems Using Labview and Advanced Data Acquisition Techniques. In *Practical Applications and Solutions Using LabviewTM Software*; INTECH: Rijeka, Croatia, 2011; pp. 17–40.
5. Wright, S.M.; McDougall, M.P.; Bosshard, J.C. A Desktop Imaging System for Teaching MR Engineering. In Proceedings of EMBC 2010 32nd Annual International Conference of the IEEE Engineering in Medicine and Biology Society (EMBC), Buenos Aires, Argentina, 31 August–4 September 2010; pp. 6653–6656.
6. Saam, B.T.; Conradi, M.S. Low frequency NMR polarimeter for hyperpolarized gases. *J. Magn. Reson.* **1998**, *134*, 67–71.
7. Michal, C.A.; Broughton, K.; Hansen, E. A high performance digital receiver for home-built nuclear magnetic resonance spectrometers. *Rev. Sci. Instrum.* **2002**, *73*, 453–458.

8. Li, G.; Jiang, Y.; Yuan, X.; Jiang, Y. Digital nuclear magnetic resonance spectrometer. *Rev. Sci. Instrum.* **2001**, *72*, 105101–105108.
9. Meriles, C.A.; Sakellariou, D.; Heise, H.; Moulé, A.J.; Pines, A. Approach to high-resolution *ex situ* NMR spectroscopy. *Science* **2001**, *293*, 82–85.
10. LeBec, G.; Yonnet, J.P.; Raoof, K. Coil and magnet design for nuclear magnetic resonance in inhomogeneous field. *IEEE Trans. Magn.* **2006**, *42*, 3861–3867.
11. Tecmag. Redstone™. Available online: <http://www.tecmag.com/redstone.html> (accessed on 13 November 2013).
12. Technology Abruzzo S.r.l. Available online: <http://www.imagtech.it/> (accessed on 13 November 2013).
13. Analog Devices. *ADSP-2106x SHARC® Processor User's Manual*; Analog Devices: Norwood, MA, USA, 2004.
14. Analog Devices. *AD9852 Datasheet*; Analog Devices: Norwood, MA, USA, 2002–2007.
15. National Semiconductor. *CLC5902 Datasheet*; National Semiconductor: Santa Clara, CA, USA, 2000.
16. National Semiconductor. *CLC5957 Datasheet*; National Semiconductor: Santa Clara, CA, USA, 2000.
17. Mispelter, J.; Lupu, M.; Briguet, A. *NMR Probeheads. for Biophysical and Biomedical Experiments: Theoretical Principles and Practical Guidelines*; Imperial College Press: London, UK, 2006.
18. Décorps, M.; Blondet, P.; Reutenauer, H.; Albrand, J.P.; Rémy, C. An inductively coupled, series tuned NMR probe. *J. Magn. Reson.* **1985**, *65*, 100–109.

MRI Compatible Sensors

Optical Fiber-Based MR-Compatible Sensors for Medical Applications: An Overview

Fabrizio Taffoni, Domenico Formica, Paola Saccomandi, Giovanni Di Pino and Emiliano Schena

Abstract: During last decades, Magnetic Resonance (MR)—compatible sensors based on different techniques have been developed due to growing demand for application in medicine. There are several technological solutions to design MR-compatible sensors, among them, the one based on optical fibers presents several attractive features. The high elasticity and small size allow designing miniaturized fiber optic sensors (FOS) with metrological characteristics (e.g., accuracy, sensitivity, zero drift, and frequency response) adequate for most common medical applications; the immunity from electromagnetic interference and the absence of electrical connection to the patient make FOS suitable to be used in high electromagnetic field and intrinsically safer than conventional technologies. These two features further heightened the potential role of FOS in medicine making them especially attractive for application in MRI. This paper provides an overview of MR-compatible FOS, focusing on the sensors employed for measuring physical parameters in medicine (*i.e.*, temperature, force, torque, strain, and position). The working principles of the most promising FOS are reviewed in terms of their relevant advantages and disadvantages, together with their applications in medicine.

Reprinted from *Sensors*. Cite as: Taffoni, F.; Formica, D.; Saccomandi, P.; di Pino, G.; Schena, E. Optical Fiber-Based MR-Compatible Sensors for Medical Applications: An Overview. *Sensors* **2013**, *13*, 14105–14120.

1. Introduction

Historically, the first application of optical fibers to the medical field enabled the illumination of internal organs during endoscopic procedures. During the years, the same technology has been adopted to perform other tasks, such as laser treatments, and to develop transducers for monitoring parameters of interest for both therapeutic and diagnostic purposes. Although forty years have passed since the introduction of Fiber Optic Sensors (FOS) [1] and despite some advantages of FOS with respect to other mature technologies, only during the last decade has their market grown notably, thanks to the improvement of key optical components and to the decrease of the costs [2]. Currently, FOS are exploited to monitor different chemical and physical parameters of medical interests [3,4]. These sensors are commonly grouped in two categories [5]: intrinsic sensors, where the optical fiber is, by itself, the sensing element; extrinsic sensors, where the optical fiber behaves as a medium for conveying the light, whose characteristics (e.g., intensity, frequency, phase) are modulated by the measurand. Sensors of this second class allow deploying the basic components of FOS (e.g., light

source, photodetector) away from the sensing element, in order to develop small size sensors and hybrid solutions [6].

In addition to the already well-established applications in industrial and medical fields, immunity from electromagnetic interferences, together with good metrological characteristics and small size, make FOS attractive for several applications that take place inside, or close to, the magnetic resonance scanner.

From the introduction of Magnetic Resonance Imaging (MRI), in the early seventies, its importance in clinical imaging has exceeded even the most optimistic hopes of researchers. The constant increase of examinations based on this technique and the introduction of new procedures performed under MRI-guidance in clinical practice have promoted research on new sensors to be applied in this scenario. Among the Magnetic Resonance (MR)-compatible exploitations, FOS can be useful both to improve surgical procedure outcomes and for patient monitoring. Examples of those applications range from the measurement of the temperature of patients undergoing MRI-guided hyperthermic procedures [7], to the assessment of deflection and force on needles during MRI-guided procedures [8], to the estimation of physiological parameters (e.g., heart rate and respiratory monitoring) [9]. Possible exploitations of such sensors for research protocols are innumerable.

The ASTM standard F2503 covers MR safety-related interactions concerning the use of devices inside the MR environment. The standard distinguishes between “MR safe”, “MR conditional”, and “MR unsafe”. “MR-safe” is an item that poses no known hazards in all MR environments; “MR-conditional” is an item that has been demonstrated to pose no known hazards in a specified MR environment under specified use conditions; “MR-unsafe” is an item that is known to pose hazards in all MR environments. Despite the ASTM subcommittee for the F04.15.11 MR Standards decided to withdraw the “MR compatible” term, it is still commonly used in medical and engineering practice. The differentiation between the terms “MR-safety” and “MR-compatibility” is crucial [10,11]. MR compatible indicates that a device, when used in the MR environment, is “MR safe” and has been demonstrated to neither significantly affect the quality of the diagnostic information, nor have its operations affected by the MR device.

In this light, fiber optic technology is particularly suitable to develop “MR-compatible” sensors, since its immunity from electromagnetic fields allows: (1) being safe; (2) not affecting image quality; (3) maintaining unaltered sensors’ functionalities. Furthermore, the material used to fabricate the optical fibers does not perturb magnetic fields inside the MR-scanner, which is crucial factor for the preservation of the quality of diagnostic information.

This paper provides an overview of “MR-compatible” FOS, focusing especially on sensors employed for measuring temperature, force, torque, strain, and position during several medical procedures. Throughout the paper we offer a critical review of the most promising and widespread techniques. For the sake of clarity we arranged them in three groups: (i) FOS based on fiber Bragg grating technology; (ii) intensity-based FOS; (iii) FOS based on interferometric techniques. Moreover, measuring principles, possible medical applications, advantages and weaknesses of each method are provided and discussed.

2. MR-Compatible FBG-Based Sensors

2.1. Working Principle

MR-compatible sensors based on fiber Bragg grating (FBG) technology, developed with different possible designs, allow sensing of temperature variations and strain. The introduction of the FBG in the field of thermal and mechanical measurements started with the research of Hill *et al.*, who used electromagnetic waves to locally modify the refractive index of the optical fiber core [12]. About ten years later, the study of Meltz *et al.*, promoted the diffusion of FBGs, providing the description of a more effective, holographic technique for grating formation [13]. Thanks to the characteristics of photosensitivity technology and its inherent compatibility with optical fibers, FBGs were introduced in different fields not only related to telecommunications [14], but also to the design of FOS [15]. Despite several valuable characteristics of the FBG sensors, their spread was delayed because of the high cost and the difficulties of the manufacturing, which have been overcome only during the 1990s. The last decade saw several research groups developing sensors based on FBG. The characteristics of these sensors, their fabrication process, and their applications in medicine have been already described in detail in different reviews [4,16].

The working principle of an FBG is based on radiation reflection caused by the Bragg grating: when a fiber optic, which houses an FBG, is interrogated with a polychromatic radiation, only a narrow range of wavelengths are reflected by the FBG. The central wavelength of such range, called Bragg wavelength (λ_B) can be expressed as a function of the effective refraction index of the core (η_{eff}) and of the spatial period of the grating (Λ) as follows:

$$\lambda_B = 2 \cdot \Lambda \cdot \eta_{\text{eff}} \quad (1)$$

The influence of both temperature and strain on Λ and η_{eff} allows the design of sensors for monitoring temperature and strain, and other physical parameters related to them (e.g., pressure, force, vibrations, and flow). Specific solutions for FBG-based transducers can be adopted in order to make them selectively sensitive to strain or temperature. Usually a reference FBG is added to the main sensor in order to attenuate the influence of undesired effects, thus improving the repeatability of the measurement system [17].

FBG technology allows the development of sensors with good metrological characteristics, such as good accuracy, large bandwidth, large dynamic range, and high strain and thermal sensitivity (typical values range from 0.64 pm/ $\mu\epsilon$ to 1.2 pm/ $\mu\epsilon$, and from 6.8 pm/ $^\circ\text{C}$ to 13 pm/ $^\circ\text{C}$, respectively). Moreover, this technology offers the advantages of multiplexing, because it is possible to write multiple gratings with different Bragg wavelengths on a single fiber. On the other hand, the measurement chain should adopt an expensive device to detect the wavelength of the reflected radiation (*i.e.*, an optical spectrum analyzer), in order to avoid the decrease of performances (e.g., resolution and accuracy).

2.2. Medical Applications

The main characteristics that make FBG technology particularly suitable for applications in medicine are biocompatibility, wide bandwidth, and small size. Furthermore, the immunity of fiber

optics to electromagnetic fields, and the negligible interference with the electromagnetic fields used in MRI, make this technology very attractive for developing “MR-compatible” sensors.

Some research groups have proposed FBG-based sensors for monitoring temperature in MRI, which is of main importance for different applications: for example Rao and colleagues developed a measurement chain for cardiac output estimation, with resolution of 0.2 °C and accuracy of 0.8 °C [18]. This technology is also employed to measure tissue temperature during MRI-guided hyperthermic treatments. Temperature plays indeed a crucial role during hyperthermia, and its monitoring can be useful to drive the physician in the adjustment of thermal exposure. However, the metrological performance of commonly used temperature sensors are affected by the electromagnetic fields used during the procedure to induce hyperthermia (e.g., the artifacts due to self-absorption of thermocouples [19]). To overcome this problem, Webb and coworkers proposed a measurement system with five FBGs, that allows them to perform temperature measures during hyperthermia treatment of kidney and liver in alive rabbits [20]. Similarly, other groups assessed the feasibility of using FBGs for temperature monitoring in swine pancreatic tissue undergoing hyperthermia [7,21,22]. In a subsequent study the same authors, in the attempt to improve spatial resolution, measured tissue temperature using 12 small size FBGs (1 mm length) to improve [23], and adopted an *ad hoc* designed MR-compatible polymethylmethacrylate (PMMA) mask to precisely arrange the optical applicator and the FBGs inside the tissue, as shown in Figure 1A. This technology has been also used to monitor temperature during cryosurgery of prostate [24] and liver [25], where the MRI compatibility was experimentally assessed.

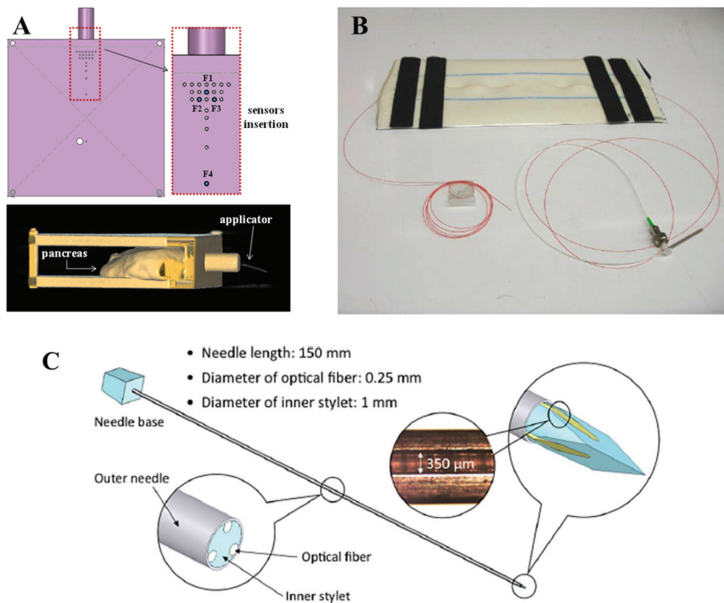
The second field of application of FBGs in MRI is the monitoring of strain and all related parameters. During the last decade, several studies focused on the monitoring of ventilatory movement and of the respiratory rate by FBG sensors [26]. More recently, Witt and Colleagues proposed for monitoring respiratory movements a system equipped with different FOS, and an FBG-based sensor to measure thorax circumference changes [27]. With a similar purpose, De Jonckheere and colleagues designed two MR-compatible sensors for recording both thoracic and abdominal movements in anesthetized patients during MRI examination. In particular, they adopted an FBG-based sensor embedded into an elastic bandage to measure thoracic movements, because of their high sensitivity to strain (*i.e.*, 1.21 pm/ $\mu\epsilon$) [28,29]. Grillet *et al.*, designed three sensors embedded into medical textiles for respiratory monitoring in MRI environment [30,31]; one of these sensors is based on FBG. A similar approach was adopted in Silva *et al.* to monitor both respiratory and heart rate (see Figure 1B [32]), and in Dziuda *et al.*, who assessed the feasibility of using FBG sensors for respiratory monitoring and heart activity inside a 1.5 T MRI scanner [9].

Recently large research efforts have been devoted to the introduction of FBG sensors in minimally invasive surgery. In this scenario the FBG sensors are useful to provide feedback information on the force applied to the tissue of the patient, in order to avoid damaging tissues during the application of surgical knots. Song and Colleagues developed a flexible and sterilizable FBG force sensor system for minimally invasive robotic surgery with resolution of 0.1 N, measurement error lower than 0.1 N and a measurement range up to 10 N [33].

Iordachita and colleagues developed a force measurement device for retinal microsurgery enabling to estimate the interaction forces at the tool tip with resolution of 0.25 mN [34].

Monfaredi *et al.*, described the design of a compact FBG sensor (15 mm of diameter and 20 mm of height) to provide force/torque feedback during robot-assisted prostate interventions. This is able to measure axial force ranging from -20 N to 20 N with 0.1 N resolution, and torque ranging from -200 N·mm to 200 N·mm with 1 N·mm resolution [35]. Park and colleagues employed three FBG sensors to detect the deflection of needles in MRI-guided procedures (Figure 1C [36,37]). In particular, they equipped a small-gauge MR-compatible needle with an FBG sensor in order to minimize the positioning error and thus procedural complications.

Figure 1. (A) FBG used to monitor temperature increase during hyperthermia. Both sensors and mask used to introduce them within the tissue are MR-compatible [23]; (B) Picture of the prototype used in [32] for respiratory and heart rate recording; (C) Prototype design with three embedded fiber Bragg grating sensors to measure needle deflection during MRI-guided interventions [37].



Finally, in Moerman *et al.*, an “MR-compatible” soft tissue indenter, equipped with an FBG force sensor, is presented with the aim of analyzing mechanical properties of skeletal muscle tissue. The sensor was calibrated up to 15 N showing a percentage difference lower than 3.1% with respect to the reference [38]. The main characteristics (*i.e.*, measurement principle, range of measurement, sensitivity, accuracy) and the medical fields of application of the FBG sensors described so far are summarized in Table 1.

Table 1. Performances and medical applications for MR-compatible FBG sensors.

Reference	Sensing Element	Measurand	Application Field	Characteristics
Rao <i>et al.</i> , 1998 [18]	FBG	Temperature	Hyperthermic treatment	Accuracy ≈ 0.8 °C, range 20 °C–60 °C, Resolution ≈ 0.2 °C
Webb <i>et al.</i> , 2000 [20]	FBG	Temperature	Hyperthermic treatment	Resolution ≈ 0.2 °C
Saccomandi <i>et al.</i> , 2012–2013 [21,22]	FBG	Temperature	Hyperthermic treatment	Range up to 80 °C
Schena <i>et al.</i> , 2013 [23]	FBG	Temperature	Hyperthermic treatment	Range 20 °C–80 °C, sensitivity ≈ 8.4 pm·°C ⁻¹
Gowardhan <i>et al.</i> , 2007 [24]	FBG	Temperature	Cryotherapy	Minimum value ≈ -60 °C
Samset <i>et al.</i> , 2005 [25]	FBG	Temperature	Cryotherapy	Range -195 °C– 100 °C
Weherle <i>et al.</i> , 2001 [26]	FBG	Inspiratory volume	Respiratory monitoring	Range 60 mL–500 mL, Frequency up to 10 Hz
Witt <i>et al.</i> , 2012 [27]	FBG	Thoracic movements	Respiratory monitoring	/
De jonckheere <i>et al.</i> , 2007 [28]	FBG	Strain	Respiratory monitoring	/
D'Angelo <i>et al.</i> , 2008 [29]	FBG	Strain	Respiratory monitoring	/
Grillet <i>et al.</i> , 2007–2008 [30,31]	FBG	Strain	Respiratory monitoring	Strain up to 41.2%, Sensitivity ≈ 0.35 nm·% ⁻¹ Accuracy ≈ 0.1 %
Silva <i>et al.</i> , 2011 [32]	FBG	Respiratory/heart rate (HR)/(RR)	Respiratory and cardiac monitoring	
Rao <i>et al.</i> , 1998 [18]	FBG	Temperature	Hyperthermic treatment	Accuracy ≈ 0.8 °C, range 20 °C–60 °C, Resolution ≈ 0.2 °C
Ioarchita <i>et al.</i> , 2009 [34]	FBG	Force	Microsurgery	Range lower than 3 mN, Resolution 0.25 mN
Dziuda <i>et al.</i> , 2013 [9]	FBG	Respiratory/heart rate (HR)/(RR)	Respiratory and cardiac monitoring	Accuracy RR: 1.2 bpm, Accuracy HR: 3.6 bpm
Song <i>et al.</i> , 2011 [33]	FBG	Force	Robotic surgery	Range up to 10 N, Resolution ≈ 0.05 N, error <0.1 N
Monfaredi <i>et al.</i> , 2013 [35]	FBG	Force/Torque	Prostatic surgery	Range -20 N– 20 N, Resolution = 0.1N, Range -200 Nmm– 200 Nmm, Resolution = 1 Nmm
Park <i>et al.</i> , 2008 [36,37]	FBG	Needle deflection	MRI-guided procedures	error in needle local curvature < 2.14 %
Moerman <i>et al.</i> , 2012 [38]	FBG	Force	Tissue mechanical properties analysis	Range up to 15 N, error < 0.043 N

3. MR-Compatible Intensity-Based and Interferometry-Based Fiber Optic Sensors

3.1. Working Principle

Different working principles based on light intensity modulation allow developing FOS for MRI applications. In this kind of sensors, the measurand modulates the intensity of light passing through the fiber. The working principles of the most widely used configurations can be grouped in three categories:

- (1) Intensity reflective FOS, where a reflector (e.g., a mirror) is placed at a known distance to the distal extremities of two optical fibers, as shown in Figure 2.

The light transported by the first fiber is reflected back by the mirror, then it is conveyed into the second fiber, which is coupled to a photodetector. In this configuration, the radiation intensity measured by the photodetector depends on the distance between the two fibers and the mirror. This configuration allows performing indirect measures since the light intensity recorded by the photodetector is related to the measurand (e.g., force, pressure, displacement, flowrate [39]) which directly acts on the mirror. Puangmali *et al.* adopted more complex configurations with the aim of improving the sensor characteristics [40].

- (2) FOS based on the light coupling between two or more fibers [41]. In these sensors, the distal tip of a fiber transporting the light is placed in front of another one or a group of them. The intensity of radiation coupled to the receiving fiber(s) decreases with the relative distance between the tips, as shown in Figure 3a–c.

FOS based on reflective and light coupling configurations are prone to unwanted drift caused by changes of input light intensity or by light lost due to fiber bending. To partially overcome these concerns, differential configurations employing two or more receiving fibers may be used (e.g., the configurations reported in Figure 3d,e). In these configurations, the outputs of two or more photodetectors are influenced in the same way by the drift. Therefore, the adequate processing of photodetectors' output allows compensating or reducing measurement errors owing to undesirable drift.

Figure 2. Sensing element of FOS based on intensity reflective principle: the output light is modulated by pressure or other physical parameters which cause a mirror displacement [4].

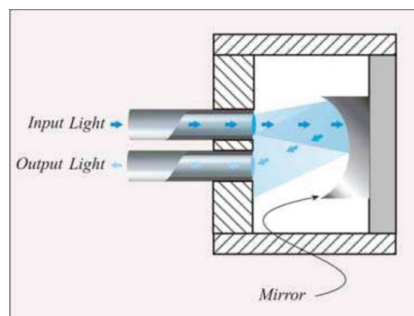
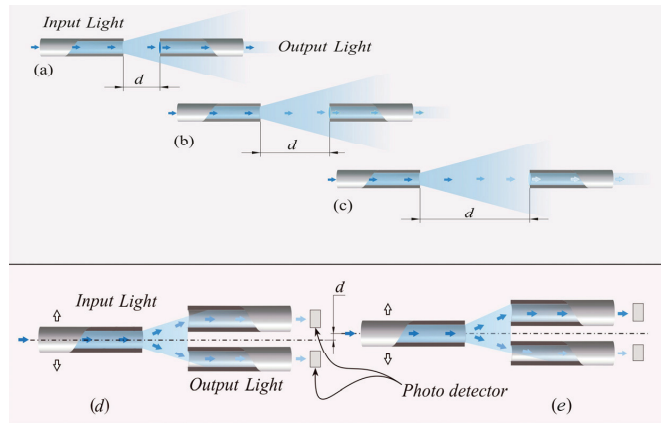


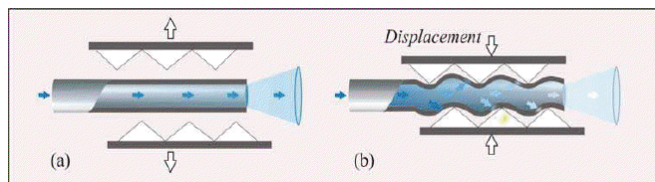
Figure 3. Design of an intensity-modulated FOS manufactured with two fibers. The intensity of the coupled radiation between the two fibers decreases with their distance d [4].



(3) Macrobending FOS: their working principle is based on the light modulation owing to fiber bending. When a light ray reaches a fiber bend, the amount of radiation lost into the cladding region increases because, beyond a critical angle, the higher-order modes hitting the cladding leak out of the fiber core. This approach can indeed be employed to measure physical parameters which cause fiber bends, such as, force, torque and pressure [42]. Usually a series of small macro bends (Figure 4) are adopted in order to increase the light leakage, aiming to improve the sensor sensitivity.

The main advantage of the intensity modulated FOS is their cheap measurement chain: differently from FBG sensors, they do not require indeed expensive devices to measure the transducer output [5].

Figure 4. Fiber optic displacement sensors based on macrobending. The radiation intensity is modulated by the displacement of a moving part: when it does not bend the fiber (a); the light intensity is maximum; on the contrary, the light intensity decreases with the bending (b) [4].



Finally, FOS can be based on interferometric techniques, such as, Sagnac, Fabry-Perot, and Michelson interferometer [43]. These approaches allow developing both intrinsic and extrinsic FOS. In the first case, the fiber is a medium to transport the radiation, which is modulated by a sensing element placed at its tip. In the second one the fiber itself represents the sensing element where interferences, modulated by the measurand, happen.

The most common interferometric configuration employed to develop FOS is based on Fabry-Perot interferometry. Its sensing principle exploits two semi-reflective mirrors, which partially transmits and partially reflects the light transported by the fiber. The electromagnetic waves, undergoing multiple reflections, constructively and destructively interact with themselves and produce fringes. The intensity of these fringes is function of the optical path, which is related to the distance between the mirrors. Therefore, these FOS can be used as secondary elements capable of measuring the parameters that change the distance between the two mirrors (such as pressure, force, torque).

3.2. Medical Applications

There are several examples of intensity based FOS employed in medicine. Tada *et al.*, described a simple intensity based 2-axis force sensor, where the force applied along two axes modulates the coupled light between one emission and four receiving fibers [44]. Polygerinos *et al.* [45] developed a three-axial force sensor based on reflective light intensity modulation. The sensor provides force feedback during MRI-guided cardiac ablation. Tan *et al.*, developed an intensity modulated and MR-compatible FOS for monitoring 3D forces during robotic MRI-guided interventions [46]. The working principle of the sensor described in this latter work is based on reflective intensity: the reflector is placed on an elastic frame structure at a distance, h , away from the transmitting and receiving fiber optics. The coupled light between the two fibers depends on the distance h , which is modulated by the applied force (Figure 5A). Gassert *et al.*, developed an “MR-compatible” robotic system equipped with a force/torque sensor and a position encoder, based on reflective intensity principle [8]. Su and colleagues developed a force/torque sensor for prostate needle placement in MRI-guided procedures [47]; the sensor is based on a spherical mirror and multiple optical fibers (Figure 5B). The light emitted from a point source is reflected by the mirror and collected by multiple optical fibers. The light intensity increases when the relative axial distance between the light source and mirror decreases. Intensity reflective FOS was also developed by Turkseven and Ueda [48] to provide force feedback in robotic applications. A similar approach was used in [49] for respiratory monitoring. The sensor measures changes of the abdominal circumference due to respiratory movements: the intensity of reflected light is modulated by the variation of the distance between the mirror and the distal part of the optical fiber, according to abdomen displacement.

Further widespread intensity-based fiber optic sensors, used in different medical applications, are based on macrobending. In Grillet *et al.*, De Jonckheere *et al.* and in Witt *et al.*, a similar approach is used to develop two macrobending sensors embedded into textiles (Figure 5C), in order to monitor respiratory abdominal movement [27,28,31]. Due to the low sensitivity compared with FBG sensors, macrobending ones are indicated for large movement monitoring. For example in respiratory monitoring, they are more appropriate for abdominal movement estimation, which are much more evident if compared with thorax excursions.

As regards interferometry-based FOS, several studies have described their use for measuring thermal and mechanical parameters of physiological interests (e.g., blood or other body compartments pressures [50–52]), but only few groups have focused their attention on MRI applications. In particular, Su *et al.*, designed and characterized a sensor for monitoring the needle

insertion force during minimally-invasive prostatic surgery [53], and assessed its MRI compatibility in a 3 Tesla system [54] (Figure 5D); Liu *et al.*, developed a FOS based on low-coherence Fabry-Perot interferometry [55] for vitreoretinal microsurgery. To sum up this section, the main characteristics (*i.e.*, measurement principle, range of measurement, sensitivity, accuracy and medical applications) of intensity- and interferometry-based MR-compatible FOS are reported in Table 2.

Figure 5. (A,B) Different configurations of intensity-based FOS tested for medical applications [46,47]; (C) FOS based on macrobending for respiratory monitoring [27,31]; (D) FOS for monitoring needle insertion force using Fabry Perot interferometry [54].

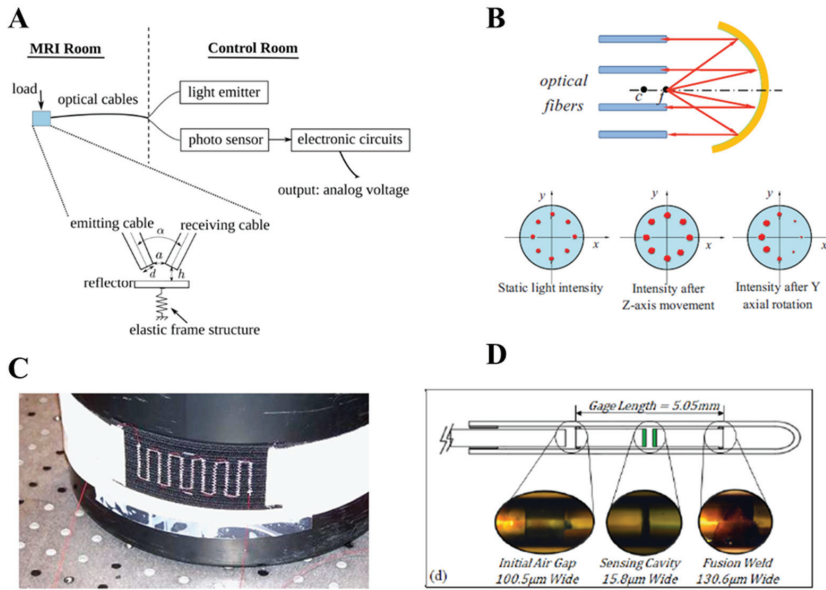


Table 2. Performances and medical applications of “MR-compatible” intensity- and interferometry-based FOS.

Reference	Sensing Element	Measurand	Application Field	Characteristics
Tada <i>et al.</i> , 2002 [44]	Intensity-based	Force	General purpose	Accuracy < 0.3 N, range up to 16 N
Polygerinos <i>et al.</i> , 2013 [45]	Intensity-based	Force	Cardiac ablation	Range up to 0.5 N, Resolution about 0.01 N,
U-Xuan Tan <i>et al.</i> , 2011 [46]	Intensity-based	Force	Robotic surgery and biopsy	Accuracy < 0.7 N, range up to 6 N
Gassert <i>et al.</i> , 2006 [8]	Intensity-based	Torque	MR-compatible robotic assistive device	Range \pm 10 Nm, resolution 0.005 Nm, sensitivity 0.66 V/Nm

Table 2. Cont.

Reference	Sensing Element	Measurand	Application Field	Characteristics
Hao Su <i>et al.</i> , 2009 [47]	Intensity-based	Force-Torque	MRI guided interventions	Range up to 10 N, sensitivity ≈ 0.2 V/N
Yoo <i>et al.</i> , 2010 [49]	Intensity-based	Abdominal movement	Respiratory monitoring	/
Turkseven <i>et al.</i> , 2011 [48]	Intensity-based	Force	Robotic surgery	/
Grillet <i>et al.</i> , 2008 [31]	Macrobending	Abdominal movement	Respiratory monitoring	Range up to 3%
De jonckheere <i>et al.</i> , 2007 [28]	Macrobending	Abdominal movement	Respiratory monitoring	/
Witt <i>et al.</i> , 2012 [27]	Macrobending	Abdominal movement	Respiratory monitoring	Linear up to 5% of elongation with sensitivity of 3 mV/%
Su Hao <i>et al.</i> , 2011 [53,54]	Interferometry-based	Force	MRI guided interventions	Range up to 9.8 N, Sensitivity 40 mV/ $\mu\epsilon$
Liu <i>et al.</i> , 2012 [55]	Interferometry-based	Force	Microsurgery	Lateral force: Range up to 6 mN Sensitivity 40 nm/mN

4. Discussion

The introduction of MRI can be considered without any reservations as the most revolutionary milestone that has characterized the last twenty years of biomedical research and practice. Just to have an idea of its social and economic implications, the Organization for Economic Co-operation and Development (OECD) health statistics declare the presence of more than 20,000 MR scanners in the OECD countries [56], and the request for high field devices (7 Tesla or even more) is increasing worldwide.

Especially thanks to its ability to investigate and discern soft tissues, MRI has become a “cannot do without tool” in medical branches as cardiology, surgery, orthopedics and neurology. Moreover, the high spatial resolution of MRI, together with the ability of this method to indirectly obtain functional parameters of the studied tissue make it fundamental for the investigation of organ functions and for imaging-guided invasive therapy.

In the just described scenario, the need for “MR-compatible” sensors able to monitor physical parameters inside the scanner, to provide real-time feedback about the status of the patient and/or the effect produced in the tissue by surgical procedures, is growing considerably.

In this paper, we reviewed the most promising principles of work adopted to design “MR-compatible” sensors based on optical fiber technology. We devoted our attention especially to transducers developed for monitoring temperature, force, torque, strain, and position; focusing particularly on their working principles, their advantages and drawbacks, and their medical applications.

Among several possible classification criteria, we grouped the “MR-compatible” sensors according to their working principle into three classes: (i) FBG sensors; (ii) intensity-based sensors; (iii) interferometry-based sensors.

“MR-compatible” sensors based on the FBG technology have been adopted for two main purposes. First, they allow the online monitoring of the key parameters during therapeutic invasive procedures, resulting in the improvement of procedure outcomes. Among the possible examples of such applications there are: (i) the measurement and control of tissue temperature during hyperthermia or cryoablation performed under MRI-guidance; (ii) the monitoring of deflection and/or force applied on needle during MRI-guided interventions. Second, FBG have been exploited for monitoring the physiological parameters of interest (e.g., respiration and heart rate). Interferometric- and intensity-based FOS have been adopted for similar applications.

Intensity-based FOS present some concerns, mainly related to unwanted drift due to light intensity changes and bending losses; on the other hand, their measurement chain does not need complex and expensive components. For this reason they are suitable for several medical applications which not have high metrological requirements e.g., respiratory rate monitoring. The use of FBG sensors allows obtaining better sensitivity and resolution, performing multipoint measurements, lastly they are unaffected by intensity changes of input light, although they require an optical spectrum analyzer which is an expensive and bulky device. Therefore, the use of FBG technology is recommended where high performance is pivotal to improve the procedure outcome (e.g., needle deflection in microsurgery).

The introduction of FOS in clinical practice [57,58] is just at the beginning. The adequate metrological characteristics for the majority of medical applications, the absence of electrical connection with the patient, the small diameter of fiber optics are overwhelming advantages compared with the conventional transducers and motivate the market growth of this technology (e.g., FISO Technologies inc. and Camino Laboratories inc. produce pressure and temperature sensors for several medical applications). Moreover the immunity from electromagnetic field makes FOS a good candidate to meet the growing demand of MR-compatible sensors. During last years, *ad hoc* designed FOS for medical application is commercially available; e.g., Micronor Inc. and Opsense Inc. produce MR-compatible FOS for displacement, temperature and pressure monitoring.

Conflicts of Interest

The authors declare no conflict of interest.

References

1. Peterson, J.I.; Vurek, G.G. 1984 Fiber-optic sensors for biomedical applications. *Science* **1984**, *13*, 123–127.
2. Devices and Technology. In *Optical Fiber Sensor Technology*; Chapman & Hall, Grattan, K.T.V., Meggitt, B.T., Eds.; Springer: London, UK, 1998.
3. Pinet, E. Medical applications: Saving lives. *Nat. Photonics*. **2008**, *2*, 150–152.
4. Silvestri, S; Schena, E. Optical-fiber measurement systems for medical applications. *Optoelectron. Devices Appl.* **2011**, 205–224.

5. Udd, E.; Spillman, W.B. *Fiber Optic Sensors*; John Wiley & Sons, Inc: Hoboken, NJ, USA, 1991.
6. Moscato, M.; Schena, E.; Saccomandi, P.; Francomano, M.; Accoto, D.; Guglielmelli, E.; Silvestri, S. A Micromachined Intensity-Modulated Fiber Optic Sensor for Strain Measurements: Working Principle and Static Calibration. In Proceedings of 34th Annual International Conference of the IEEE Engineering in Medicine and Biology Society (EMBC 2012), San Diego, CA, USA, 28 August–1 September 2012; pp. 5790–5793.
7. Saccomandi, P.; Schena, E.; Di Matteo, F. M.; Pandolfi, M.; Martino, M.; Rea, R.; Silvestri, S. Laser Interstitial Thermotherapy for Pancreatic Tumor Ablation: Theoretical Model and Experimental Validation. In Proceedings of 2011 Annual International Conference on the IEEE Engineering in Medicine and Biology Society (EMBC 2011), Boston, MA, USA, 30 August–3 September 2011; pp. 1–4.
8. Gassert, R.; Moser, R.; Burdet, E.; Bleuler, H. MRI/fMRI-Compatible robotic system with force feedback for interaction with human motion. *IEEE/ASME Trans. Mech.* **2006**, *11*, 216–224.
9. Dziuda, L.; Skibniewski, F.W.; Krej, M.; Baran, P.M. Fiber Bragg grating-based sensor for monitoring respiration and heart activity during magnetic resonance imaging examinations. *J. Biomed. Opt.* **2013**, *18*, doi:10.1117/1.JBO.18.5.057006.
10. Polygerinos, P.; Zbyszewski, D.; Schaeffter, T.; Razavi, R.; Seneviratne, L.D.; Althoefer, K. MRI-compatible fiber-optic force sensors for catheterization procedures. *IEEE Sens. J.* **2010**, *10*, 1598–1608.
11. Chinzei, K.; Bikinis, R.; Joules, F.A. MR Compatibility of Mechatronic Devices: Design Criteria. In Proceedings of Medical Image Computing and Computer-Assisted Intervention (MICCAI 1999), Cambridge, UK, 19–22 September 1999; pp. 1020–1030.
12. Hill, K.O.; Fujii, Y.; Johnson, D.C.; Kawasaki, B.S. Photosensitivity in optical fiber waveguides: Application to reflection filter fabrication. *Appl. Phys. Lett.* **1978**, *32*, 647–649.
13. Meltz, G.; Morey, W.W.; Glenn, W.H. Formation of Bragg gratings in optical fibers by a transverse holographic method. *Opt. Lett.* **1989**, *14*, 823–825.
14. Hill, K.O.; Meltz, G. Fiber Bragg grating technology fundamentals and overview. *J. Light. Technol.* **1997**, *15*, 1263–1276.
15. Kersey, A.D. A review of recent developments in fiber optic sensor technology. *Opt. Fiber Technol.* **1996**, *2*, 291–317.
16. Mishra, V.; Singh, N.; Tiwari, U.; Kapur, P. Fiber grating sensors in medicine: Current and emerging applications. *Sens. Actuators A Phys.* **2011**, *167*, 279–290.
17. Xu, M.G.; Archambault, J.L.; Reekie, L.; Dakin, J.P. Thermally-compensated bending gauge using surface mounted fiber gratings. *Int. J. Optoelectron.* **1994**, *9*, 281–283.
18. Rao, Y.J.; Webb, D.J.; Jackson, D.A.; Zhang, L.; Bennion, I. Optical in-fiber Bragg grating sensor systems for medical applications. *J. Biomed. Opt.* **1998**, *3*, 38–44.
19. Manns, F.; Milne, P.J.; Gonzalez-Cirre, X.; Denham, D.B.; Parel, J.M.; Robinson D.S. *In situ* temperature measurements with thermocouple probes during laser interstitial thermotherapy (LITT): Quantification and correction of a measurement artifact. *Lasers Surg. Med.* **1998**, *23*, 94–103.
20. Webb, D.J.; Hathaway, M.W.; Jackson, D.A. First *in vivo* trials of a fiber Bragg grating based temperature profiling system. *J. Biomed. Opt.* **2000**, *5*, 45–50.

21. Saccomandi, P.; Schena, E.; Caponero, M.A.; di Matteo, F.M.; Martino, M.; Pandolfi, M.; Silvestri, S. Theoretical analysis and experimental evaluation of laser-induced interstitial thermotherapy *in ex vivo* porcine pancreas. *IEEE Trans. Biomed. Eng.* **2012**, *59*, 2958–2964.
22. Saccomandi, P.; Schena, E.; Giurazza, F.; del Vescovo, R.; Caponero, M.A.; Mortato, L.; Panzera, F.; Cazzato, R.L.; Grasso, F.R.; di Matteo, F.M.; *et al.* Temperature monitoring and lesion volume estimation during double-applicator laser-induced thermotherapy in *ex vivo* swine pancreas: A preliminary study. *Laser. Med. Sci.* **2013**, 1–8.
23. Schena, E.; Saccomandi, P.; Giurazza, F.; Caponero, M.A.; Mortato, L.; di Matteo, F.M.; Panzera, F.; del Vescovo, R.; Zobel, B.B.; Silvestri, S. Experimental assessment of CT-based thermometry during laser ablation of porcine pancreas. *Phys. Med. Biol.* **2013**, in press.
24. Gowardhan, B.; Greene, D. Cryotherapy for the prostate: An *in vitro* and clinical study of two new developments; Advanced cryoneedles and a temperature monitoring system. *BJU Int.* **2007**, *100*, 295–302.
25. Samset, E.; Mala, T.; Ellingsen, R.; Gladhaug, I.; Søreide, O.; Fosse, E. Temperature measurement in soft tissue using a distributed fibre Bragg-grating sensor system. *Minim. Invasiv. Ther.* **2001**, *10*, 89–93.
26. Wehrle, G.; Nohama, P.; Kalinowski, H.J.; Torres, P.I.; Valente, L.C.G. A fibre optic Bragg grating strain sensor for monitoring ventilatory movements. *Meas. Sci. Technol.* **2001**, *12*, 805–809.
27. Witt, J.; Narbonneau, F.; Schukar, M.; Krebber, K.; Jonckheere, J.; Jeanne, M.; Kinet, D.; Paquet, B.; Deprè, A.; d'Angelo, L.T.; *et al.* Medical textiles with embedded fiber optic sensors for monitoring of respiratory movement. *IEEE Sens. J.* **2012**, *12*, 246–254.
28. De Jonckheere, J.; Jeanne, M.; Grillet, A.; Weber, S.; Chaud, P.; Logier, R.; Weber, J.L. OFSETH: Optical Fiber Embedded into Technical Textile for Healthcare, An Efficient Way to Monitor Patient under Magnetic Resonance Imaging. In Proceedings of 29th Annual International Conference of the IEEE Engineering in Medicine and Biology Society (EMBC 2007), Lyon, France, 23–26 August 2007; pp. 3950–3953.
29. D'Angelo, L.T.; Weber, S.; Honda, Y.; Thiel, T. A System for Respiratory Motion Detection Using Optical Fibers Embedded into Textiles. In Proceedings of 30th Annual International Conference of the IEEE Engineering in Medicine and Biology Society (EMBC 2008), Vancouver, BC, Canada, 20–25 August 2008; pp. 3694–3697.
30. Grillet, A.; Kinet, D.; Witt, J.; Schukar, M.; Krebber, K.; Pirotte, F.; Deprè, A. Optical Fibre Sensors Embedded into Medical Textiles for Monitoring of Respiratory Movements in Mri Environments. In Proceedings of Third European Workshop on Optical Fibre Sensors, Napoli, Italy, 4 July 2007; p. 66191R.
31. Grillet, A.; Kinet, D.; Witt, J.; Schukar, M.; Krebber, K.; Pirotte, F.; Deprè, A. Optical fiber sensors embedded into medical textiles for healthcare monitoring. *IEEE Sens. J.* **2008**, *8*, 1215–1222.
32. Silva, A.F.; Carmo, J.P.; Mendes, P.M.; Correia, J.H. Simultaneous cardiac and respiratory frequency measurement based on a single fiber Bragg grating sensor. *Meas. Sci. Technol.* **2011**, *22*, doi:10.1088/0957-0233/22/7/075801.

33. Song, H.; Kim, K.; Lee, J. Development of optical fiber Bragg grating force-reflection sensor system of medical application for safe minimally invasive robotic surgery. *Rev. Sci. Instrum.* **2011**, *82*, 0743011–0743019.
34. Iordachita, I.; Sun, Z.; Balicki, M.; Kang, J.U.; Phee, S.J.; Handa, J.; Gehlbach, P.; Taylor, R. A sub-millimetric, 0.25 mN resolution fully integrated fiber-optic force-sensing tool for retinal microsurgery. *Int. J. Comput. Assisted Radiol. Surg.* **2009**, *4*, 383–390.
35. Monfaredi, R.; Seifabadi, R.; Fichtinger, G.; Iordachita, I. Design of A Decoupled Mri-Compatible Force Sensor Using Fiber Bragg Grating Sensors for Robot-Assisted Prostate Interventions. In Proceedings of Medical Imaging 2013: Image-Guided Procedures, Robotic Interventions, and Modeling, Lake Buena Vista (Orlando Area), FL, USA, 9–14 February 2013; p. 867118.
36. Park, Y.L.; Elayaperumal, S.; Daniel, B.L.; Kaye, E.; Pauly, K.B.; Black, R.J.; Cutkosky, M.R. MRI-Compatible Haptics: Feasibility of Using Optical fiber Bragg Grating Strain-Sensors to Detect Deflection of Needles in An MRI Environment. In Proceedings of International Society of Magnetic Resonance in Medicine (ISMRM 2008), Toronto, ON, Canada, May 2008; p. 282.
37. Park, Y.L.; Elayaperumal, S.; Daniel, B.L.; Ryu, S.C.; Shin, M.; Savall, J.; Black, R.J.; Moslehi, B.; Cutkosky, M.R. Real-time estimation of 3-D needle shape and deflection for MRI-guided interventions. *IEEE/ASME Trans. Mech.* **2010**, *15*, 906–915.
38. Moerman, K.M.; Sprengers, A.M.J.; Nederveen, A.J.; Simms, C.K. A novel MRI compatible soft tissue indenter and fibre Bragg grating force sensor. *Med. Eng. Phys.* **2013**, *35*, 486–499.
39. Lekholm, A.; Lindström, L. Optoelectronic transducer for intravascular measurements of pressure variations. *Med. Biol. Eng.* **1969**, *7*, 333–335.
40. Puangmali, P.; Althoefer, K.; Seneviratne, L.D. Mathematical modeling of intensity-modulated bent-tip optical fiber displacement sensors. *IEEE Trans. Instrum. Meas.* **2010**, *59*, 283–291.
41. Lee, B. Review of the present status of the optical fiber sensors. *Opt. Fiber Technol.* **2003**, *9*, 57–79.
42. Lagakos, N.; Cole, J.H.; Bucaro, J.A. Microbend fiber-optic sensor. *Appl. Opt.* **1987**, *26*, 2171–2180.
43. Lee, B.H.; Kim, Y.H.; Park, K.S.; Eom, J.B.; Kim, M.J.; Rho, B.S.; Choi, H.Y. Interferometric fiber optic sensors. *Sensors* **2012**, *12*, 2467–2486.
44. Tada, M.; Sasaki, S.; Ogasawara, T. Development of An Optical 2-Axis Force Sensor Usable in Mri Environments. In Proceedings of 2002 IEEE Sensors, Orlando, FL, USA, 12–14 June 2002; pp. 984–989.
45. Polygerinos, P.; Seneviratne, L.D.; Razavi, R.; Schaeffter, T.; Althoefer, K. Triaxial catheter-tip force sensor for MRI-guided cardiac procedures. *IEEE/ASME Trans. Mechatron.* **2013**, *18*, 386–396.
46. Tan, U.X.; Yang, B.; Gullapalli, R.; Desai, J.P. Tri-axial MRI compatible fiber-optic force sensor. *IEEE Trans. Robot.* **2011**, *27*, 65–74.

47. Su, H.; Fischer, G.S. A 3-Axis Optical Force/Torque Sensor for Prostate Needle Placement in Magnetic Resonance Imaging Environments. In Proceedings of IEEE International Conference on Technologies for Practical Robot Applications (TePRA 2009), Woburn, MA, USA, 9–11 November 2009; pp. 5–9.
48. Turkseven, M.; Ueda, J. Design of An MR-Compatible Haptic Interface. In Proceedings of IEEE/RSJ International Conference on Intelligent Robots and Systems (IROS 2011), San Francisco, CA, USA, 25–30 September 2011.
49. Yoo, W.J.; Jang, K.W.; Seo, J.K.; Heo, J.Y.; Moon, J.S.; Park, J.Y.; Lee, B.S. Development of respiration sensors using plastic optical fiber for respiratory monitoring inside MRI system. *J. Opt. Soc. Korea* **2010**, *14*, 235–239.
50. Wolthuis, R.A.; Mitchell, G.L.; Saaski, E.; Hartl, J.C.; Afromowitz, M.A. Development of medical pressure and temperature sensors employing optical spectrum modulation. *IEEE Trans. Biomed. Eng.* **1991**, *38*, 974–981.
51. Chavko, M.; Koller, W.A.; Prusaczyk, W.K.; McCarron, R.M. Measurement of blast wave by a miniature fiber optic pressure transducer in the rat brain. *J. Neurosci. Meth.* **2007**, *159*, 277–281.
52. Totsu, K.; Haga, Y.; Esashi, M. Ultra-miniature fibre-optic pressure sensor using white light interferometry. *J. Micromech. Microeng.* **2005**, *15*, 71–75.
53. Su, H.; Zervas, M.; Furlong, C.; Fischer, G.S. A Miniature Mri-Compatible Fiber-Optic Force Sensor Utilizing Fabry-Perot Interferometer. In *Mems and Nanotechnology*; Springer: New York, NY, USA, 2011; pp. 131–136.
54. Su, H.; Zervas, M.; Cole, G.A.; Furlong, C.; Fischer, G.S. Real-Time Mri-Guided Needle Placement Robot with Integrated Fiber Optic Force Sensing. In Proceedings of 2011 IEEE International Conference on Robotics and Automation (ICRA 2011), Shanghai, China, 9–13 May 2011; pp. 1583–1588.
55. Liu, X.; Iordachita, I.I.; He, X.; Taylor, R.H.; Kang, J.U. Miniature fiber-optic force sensor based on low-coherence Fabry-Pérot interferometry for vitreoretinal microsurgery. *Biomed. Opt. Express* **2012**, *3*, 1062–1076.
56. *Magnetic Resonance Imaging Units, Total*; OECD iLibrary: Paris, France; No. 36, doi:10.1787/magesimaging-table-2013-1-en.
57. Al-Fakih, E.; Osman, N.A.A.; Adikan, F.R.M. The use of fiber Bragg grating sensors in biomechanics and rehabilitation applications: The state-of-the-art and ongoing research topics. *Sensors* **2007**, *12*, 12890–12926.
58. Ho, S.C.M.; Razavi, M.; Nazeri, A.; Song, G. FBG sensor for contact level monitoring and prediction of perforation in cardiac ablation. *Sensors* **2012**, *12*, 1002–1013.

Fetal Electrocardiogram (fECG) Gated MRI

Martyn N.J. Paley, Janet E. Morris, Debbie Jarvis and Paul D. Griffiths

Abstract: We have developed a Magnetic Resonance Imaging (MRI)-compatible system to enable gating of a scanner to the heartbeat of a foetus for cardiac, umbilical cord flow and other possible imaging applications. We performed radiofrequency safety testing prior to a fetal electrocardiogram (fECG) gated imaging study in pregnant volunteers ($n = 3$). A compact monitoring device with advanced software capable of reliably detecting both the maternal electrocardiogram (mECG) and fECG simultaneously was modified by the manufacturer (Monica Healthcare, Nottingham, UK) to provide an external TTL trigger signal from the detected fECG which could be used to trigger a standard 1.5 T MR (GE Healthcare, Milwaukee, WI, USA) gating system with suitable attenuation. The MR scanner was tested by triggering rapidly during image acquisition at a typical fetal heart rate (123 beats per minute) using a simulated fECG waveform fed into the gating system. Gated MR images were also acquired from volunteers who were attending for a repeat fetal Central Nervous System (CNS) examination using an additional rapid cardiac imaging sequence triggered from the measured fECG. No adverse safety effects were encountered. This is the first time fECG gating has been used with MRI and opens up a range of new possibilities to study a developing foetus.

Reprinted from *Sensors*. Cite as: Paley, M.N.J.; Morris, J.E.; Jarvis, D.; Griffiths, P.D. Fetal Electrocardiogram (fECG) Gated MRI. *Sensors* **2013**, *13*, 11271–11279.

1. Introduction

Triggering of *in utero* Magnetic Resonance Imaging (iuMRI) by the fetal ECG (fECG) would be useful for fetal cardiac studies or flow measurements in the umbilical cord. Currently no manufacturers provide the facility to gate to the fECG. The aim of this study was to perform MRI safety tests of a fECG sensor modified for MRI triggering capability together with a preliminary *in vivo* imaging feasibility study using the device on pregnant volunteers.

Real time imaging such as echo planar or single shot fast spin echo imaging can be used to effectively freeze fetal motion, but scans are not synchronized to the fetal cardiac cycle and generally have worse spatial resolution than can be achieved with gated acquisitions [1–3]. Self-gating, navigator-based methods avoid having to detect the fECG by acquiring a signal from the center of k-space with each k-space line acquisition, but have varying degrees of success dependent on patient motion and other factors [4–8]. Retrospective gating uses continuous acquisition of data together with labeling of each acquisition of the cardiac phase at the time of acquisition, but this is only possible with an fECG signal. The data is then retrospectively binned and reconstructed resulting in a more efficient acquisition strategy and ensuring the data is in steady state at all times throughout the acquisition. Metric-optimized gated imaging is a variant on retrospective gating where the ECG signal cannot be measured directly. The data are acquired continually over periods longer than the anticipated heart beat interval and then assigned to various bins according to a model of the fetal heart rate. The ghosting errors which arise in the reconstructed data are then minimized using a

measure such as time-entropy through an iterative procedure by moving acquired k-space lines between the different cardiac cycle intervals [9,10].

Ultrasound is an established method for looking at flow in the foetus, placenta and umbilical cord providing non-invasive high resolution images with the possible of Doppler velocity imaging and the potential to gate an MRI scanner. However, ultrasound can have problems due to acoustic shadowing from, for example, bone, which can be a problem in cases with low amniotic fluid levels, maternal obesity or with difficult fetal positioning within the uterus. In addition quantitative ultrasound flow measurements rely on the shape of the vessels, the insonation angle and the velocity profile which are difficult to quantify in a single study [11].

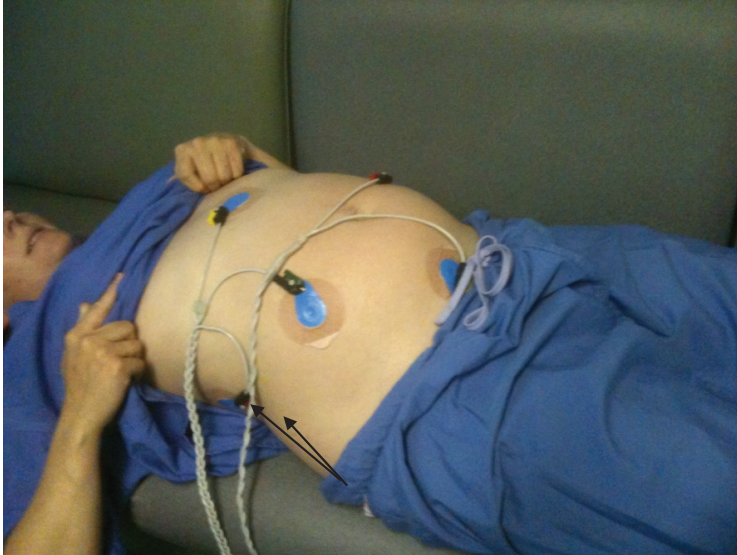
A modified cardiac triggering device has previously been used to examine the fetal sheep heart [12] but in this paper we attempt to use the directly detected human fetal ECG to obviate many of the difficulties discussed above and gain access to a full range of gated imaging sequences in terms of image contrast and acquisition speed. Combined with maternal breath hold, fECG gating should allow cardiac imaging and phase contrast velocity mapping to be acquired from the foetus and umbilical cord in future.

2. Experimental Section

A compact monitoring device (Figure 1) with advanced software capable of reliably detecting both the maternal ECG (mECG) and fECG traces simultaneously was modified by the manufacturer (Model AN24, Monica Healthcare, Nottingham, UK) to provide an external TTL trigger signal from the detected fECG signal. Six meter long high resistance carbon ECG leads were fed through waveguides into the MR scan room from the device (Figure 2a). The leads were attached to MR compatible electrodes and placed on a large torso shaped imaging test object in locations similar to those which would be used for fetal gating. The surface of the test object was covered with conducting gel as used for the electrodes to provide a circuit for any possible RF pickup (Figure 2b). A single shot fast spin echo (SSFSE) sequence was run with the same imaging parameters as used for clinical in-utero scanning using the body transmit coil. The radiofrequency voltage generated at 64 MHz was measured across the leads using a 100 MHz input bandwidth digital oscilloscope (Tektronix, Beaverton, OR, USA).

A waveform file provided by the device manufacturer produced a voltage using the sound card of a laptop computer to simulate the mECG and fECG signals. To test gating performance, the fECG signal measured through the MR compatible leads was converted into a digital gating pulse which was attenuated by 30 db and fed back into the standard MR ECG system. A balanced steady state gradient echo FIESTA sequence with SLT = 5 mm, in-plane resolution = 2 mm, NEX = 1, TR/TE = 3.3/1.4 ms was acquired with fECG gating at 123 bpm.

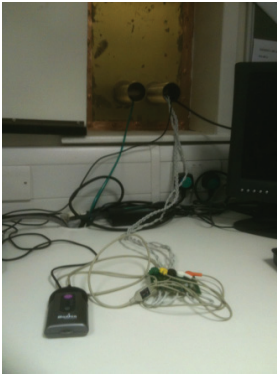
Figure 1. Placement of the ECG electrodes on a pregnant volunteer. The electrodes used were Ambu Blue Sensor VLC single patient use ECG electrodes (Ambu A/S, Ballerup, Denmark) with a skin contact diameter of 68 mm. The skin was gently abraded using a dermal abrasive tape (3 M, Bracknell, UK) prior to locating the electrodes.



fECG Monitor Twisted Pair Leads and ECG electrodes positioned on a volunteer.

This work was performed with the approval of and under the guidance of the NHS Research Ethics Service (reference 10/H1308). All women provided written informed consent prior to their studies. Pregnant women ($n = 3$) with known Central Nervous System (CNS) pathology of their foetus coming for a follow up examination (so they already had experience of an MRI examination) were assessed using the fetal ECG system. The leads were attached to five MR compatible electrodes and placed on the lower abdomen close to the anticipated location of the fetal heart prior to all scanning and presence of the fetal trigger pulse checked after patient positioning in the magnet. Images were acquired using a 1.5 T HDx MR System (GE Healthcare, Milwaukee, WI, USA) using all the sequences included in our standard in-utero CNS imaging protocol plus an additional fECG gated cardiac cine sequence at the end of the examination using the same geometry as planned for the CNS examination to comply with granted ethical permission. Typical overall in magnet time was 30 min.

Figure 2. (a) The portable fetal and maternal ECG used for the study (AN24, Monica Healthcare, Nottingham, UK). The device records the data into internal memory over long periods but also transmits the maternal and fetal ECG data (four channels) in real time over a Bluetooth interface. The fECG monitor was connected to the six metre MR compatible high resistance leads which go through a waveguide into the scan room. The five leads were twisted as a pair and as a triplet. The trigger signal from the device was attenuated by 30 db and fed back into the scan room using a BNC cable (unfiltered in this case, although filtering could be used in future); (b) The leads attached to the MR compatible electrodes positioned on a torso phantom on a bed of conducting gel prior to location within the magnet for confirmatory safety tests.



(a)



(b)

3. Results and Discussion

Radiofrequency voltages at 63.9 MHz measured across the leads were always significantly less than ± 1 V peak to peak using the single shot fast spin echo sequence set up for a 70 kg load which is much lower than would produce a radiofrequency burn. The electrodes and test object were relocated within the RF body coil four times to assess reproducibility and the same result was observed each time. Images were acquired with the electrodes in place using a gradient echo sequence and there was no evidence of RF or B_0 interference.

The fECG and mECG signals could be measured in real time using the Bluetooth interface (Figure 3). Occasionally, when the fetal and maternal ECG signals coincided, the fetal gating signal was lost due to software checks within the device which excluded it during this time. Test object images were acquired at the fetal heart rate (123 bpm) to demonstrate the rapid gating capability of the MR system (Figure 4).

Figure 3. (a) Five maternal cycles of the simulated maternal and fetal ecg waveform used for the gating tests. This waveform was played from a PC soundcard and attenuated to the peak level expected for maternal *in vivo* signals (100 μ V); (b) Two cycles of the signal received over the Bluetooth interface using the six metre, high resistance MR compatible leads showing the additional noise introduced. The measured ‘fetal’ signal from the simulator measured about 10 μ V.

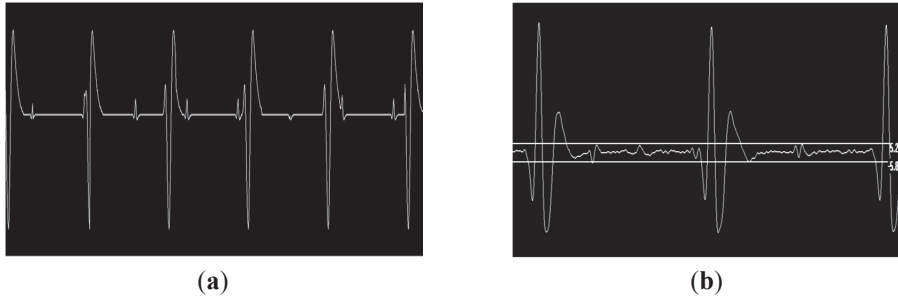
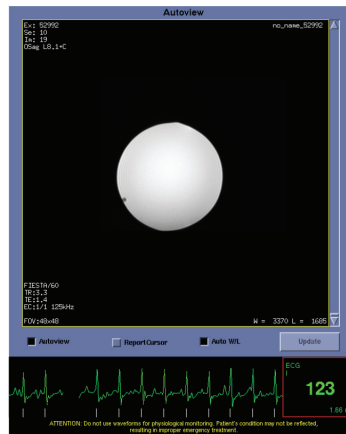


Figure 4. A FIESTA sequence with TR = 3.3 ms, TR = 1.4 ms, NEX = 1, in-plane spatial resolution = 1 \times 1 mm, SLT = 5 mm acquired with the cardiac gating signal from the simulated fetal ECG at 123 beats per minute acquired over the 6 m MR compatible leads. The images show no artifacts from the leads or electrodes.



Following satisfactory safety testing on test objects, the volunteer study was initiated. No safety issues were encountered using the device to record the fECG during fetal imaging on the pregnant volunteers. The gating system was present for all imaging sequences. Figure 5 shows raw and Finite Impulse Response (FIR)-filtered (4 Hz–45 Hz bandpass provided with the Monica Healthcare software) ECG data acquired in the magnet without imaging gradients present clearly showing mECG and fECG components at different rates. The mECG was approximately 80 bpm and the fECG was approximately 140 bpm for all three volunteers and fetuses.

Figure 6 illustrates the effects of burst of gradient waveforms from a single shot spin echo sequence on the fECG trace. Filtering, as contained in the fECG hardware largely removes the effects of this rapid train of pulses.

Figure 5. The effects of Finite Impulse Response (FIR) filtering with a standard bandpass filter (4–45 Hz) on the combined mECG and fECG signals which were acquired from a volunteer within the magnet (without imaging applied). ECG data was recorded during the entire imaging session and subsequently downloaded from the device and analysed using a developmental software tool from the monitor manufacturer DK V1.5 (Monica Healthcare, Nottingham, UK).

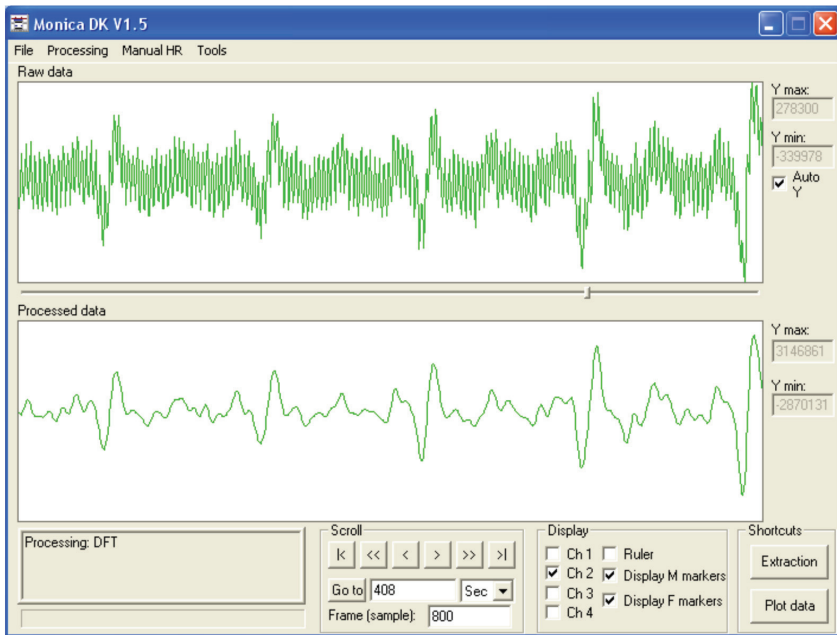


Figure 6. The effects of a single shot fast spin echo sequence gradient burst on the fECG trace (upper plot). The effects of a bandpass FIR filter are shown in the lower trace. The effects of the gradient pulses are largely removed from the trace but the phase of the ECG signal is temporarily altered.

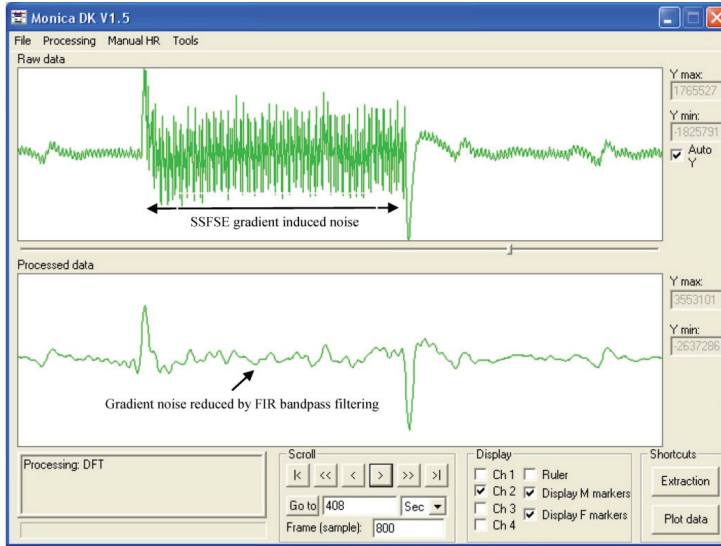


Figure 7 show a fECG gated fetal image from one of the volunteers at the end of the normal CNS exam using a gradient echo cardiac gated imaging sequence (Right Ventricle Long Axis (RVLA) sequence) but using the geometry as planned for the CNS examination.

Figure 7. A fECG gated rapid image acquired from a foetus in an oblique plane from one of the pregnant volunteers. As this feasibility study was performed at the end of a fetal CNS pathology examination, it was not possible to specifically plan and visualise the heart under ethical guidance. None of the volunteers reported any adverse effects during imaging.



4. Conclusions/Outlook

Availability of a reliable fetal ECG gating signal should open up a wealth of new opportunities for non-invasively measuring the fetal cardio-vascular system. Although self-gating techniques are reasonably successful in detecting the cardiac cycle, other MR related issues can modify the detected self-gating signal such as approach to steady state, contrast preparation as well as maternal and/or fetal bulk motion which can limit the applicability and accuracy.

In this study it has been demonstrated for the first time that it is possible to safely gate an MR scanner to the fECG using a modified fECG monitor and carbon fibre lead system. It was also possible to observe the mECG and fECG signals in real-time on a linked computer display using a Bluetooth interface available on the fECG device. The fECG signals reliably triggered a fast MR image acquisition sequence at the fetal heart rate from the simulated signal at 123 bpm. No interference between the gating system and the MR system was observed in terms of generated noise lines on the images in these preliminary studies.

Some gradient interference on the gating signal was observed which occasionally resulted in mis-triggering if the fetal gating signal occurred during gradient activity. This was minimized by using a short duration data acquisition relative to the fetal ECG period. To improve reliability of fetal triggering for longer duration data acquisitions such as used for single shot fast spin echo, improved real-time filtering of the ECG signal as demonstrated in Figure 6 could be included in the device firmware. In addition, locating the device in the scan room and shortening the twisted pair leads would also improve sensitivity and reliability. The device was kept out of the magnet room and long leads were used in this study as the device contained magnetic components which could have lead to a projectile hazard and also contained components sensitive to the effects of the RF pulses generated by the MR scanner.

Fetal cardiac gated images were acquired from three pregnant volunteers showing the capability of the fetal monitor to operate successfully within the MR environment using extended leads. This should provide new opportunities for examining the developing cardiovascular system and umbilical blood supply gated to the fetal rather than maternal circulation. This should also allow development of quantitative flow protocols through gated velocity phase mapping sequences.

Acknowledgments

We acknowledge the support of Barrie Hayes-Gill, Jean-Francois Pieri and James Bushby of Monica Healthcare for modifying the AN24 device to support MRI triggering. We also acknowledge the support of Westfield Healthcare and GE Healthcare.

Conflicts of Interest

The authors declare no conflict of interest.

References

1. Hinks, R.S. Monitored Echo Gating for the Reduction of Motion Artifacts. U.S. Patent 4,761,613, Picker International Inc.: Cleveland, OH, USA, August 1988.
2. Spraggins, T.A. Wireless retrospective gating: Application to cine cardiac imaging. *Magn. Reson. Imaging* **1990**, *8*, 675–681.
3. Crowe, M.; Larson, A.; Zhang, Q.; Carr, J.; White, R.; Li, D.; Simonetti, O. Automated rectilinear self-gated cardiac cine imaging. *Magn. Reson. Med.* **2004**, *52*, 782–788.
4. Larson, A.; White, R.; Laub, G.; McVeigh, E.; Li, D.; Simonetti, O. Self-gated cardiac cine MRI. *Magn. Reson. Med.* **2004**, *51*, 93–102.
5. Thompson, R.B.; Mcveigh, E.R. Flow-gated phase-contrast MRI using radial acquisitions. *Magn. Reson. Med.* **2004**, *52*, 598–604.
6. Holmes, W.; McCabe, C.; Mullin, J.; Condon, B.; Bain, M. Noninvasive selfgated magnetic resonance cardiac imaging of developing chick embryos in ovo. *Circulation* **2008**, *117*, e346–e347.
7. Nieman, B.J.; Szulc, K.U.; Turnbull, D.H. Three-dimensional, *in vivo* MRI with self-gating and image coregistration in the mouse. *Magn. Reson. Med.* **2009**, *61*, 1148–1157.
8. Xiang, Q.S.; Henkelman, R.M. K-space description for MR imaging of dynamic objects. *Magn. Reson. Med.* **1993**, *29*, 422–428.
9. Atkinson, D.; Hill, D.; Stoyale, P.; Summers, P.; Keevil, S. Automatic correction of motion artifacts in magnetic resonance images using an entropy focus criterion. *IEEE Trans. Med. Imaging* **1997**, *16*, 903–910.
10. Jansz, M.S.; Seed, M.; van Amerom, J.F.P.; Wong, D.; Grosse-Wortmann, L.; Yoo, S.J.; Macgowan, C.K. Metric optimized gating for fetal cardiac MRI. *Magn. Reson. Med.* **2010**, *64*, 1304–1314.
11. Eik-Nes, S.; Marsal, K.; Brubakk, A.; Kristofferson, K.; Ulstein, M. Ultrasonic measurement of human fetal blood flow. *J. Biomed. Eng.* **1982**, *4*, 28–36.
12. Yamamura, J.; Kopp, I.; Frisch, M.; Fischer, R.; Valett, K.; Hecher, K.; Adam, G.; Wedegärtner, U. Cardiac MRI of the fetal heart using a novel triggering method: Initial results in an animal model. *J. Magn. Reson. Imaging* **2012**, *5*, 1071–1076.

Simultaneous Magnetic Resonance Imaging and Consolidation Measurement of Articular Cartilage

Robert Mark Wellard, Jean-Philippe Ravasio, Samuel Guesne, Christopher Bell, Adekunle Oloyede, Greg Tevelen, James M. Pope and Konstantin I. Momot

Abstract: Magnetic resonance imaging (MRI) offers the opportunity to study biological tissues and processes in a non-disruptive manner. The technique shows promise for the study of the load-bearing performance (consolidation) of articular cartilage and changes in articular cartilage accompanying osteoarthritis. Consolidation of articular cartilage involves the recording of two transient characteristics: the change over time of strain and the hydrostatic excess pore pressure (HEPP). MRI study of cartilage consolidation under mechanical load is limited by difficulties in measuring the HEPP in the presence of the strong magnetic fields associated with the MRI technique. Here we describe the use of MRI to image and characterize bovine articular cartilage deforming under load in an MRI compatible consolidometer while monitoring pressure with a Fabry-Perot interferometer-based fiber-optic pressure transducer.

Reprinted from *Sensors*. Cite as: Wellard, R.M.; Ravasio, J.; Guesne, S.; Bell, C.; Oloyede, A.; Tevelen, G.; Pope, J.M.; Momot, K.I. Simultaneous Magnetic Resonance Imaging and Consolidation Measurement of Articular Cartilage. *Sensors* **2014**, *14*, 7940–7958.

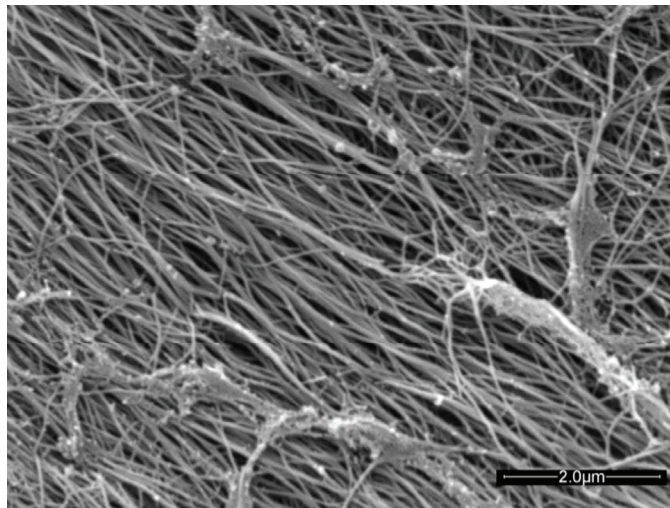
1. Introduction

Articular cartilage (AC) is an avascular connective tissue lining the articulating surfaces of long bones in mammals. Healthy adult human cartilage is 2–4 mm thick and comprises extracellular biopolymers (collagen, 15%–20%; proteoglycans, 3%–10%; and lipids, 1%–5%) with the primary function of enabling load bearing in a mobile joint. The structural collagen component of cartilage is highly aligned, being normal to the supporting bone surface and arching to a parallel alignment at the synovial surface [1] (see Figure 3 in [1]). The highly aligned nature of the collagen fibers can be seen in the scanning electron micrograph of trypsin treated cartilage in Figure 1.

AC is both structurally heterogenous and mechanically anisotropic [3]. The anisotropy is associated with collagen fiber alignment, which varies throughout the thickness of the cartilage [1,4] and the distribution of hydrated proteoglycans [5], which together generate the osmotic pressure-based load bearing stiffness of the tissue. Under static compression, AC exhibits a complex behavior referred to as consolidation [6], with an initial rapid increase in strain to a plateau, which is maintained. At the same time a proportion of the load is transferred to the tissue fluid, resulting in a rise in hydrostatic excess pore pressure (HEPP) to a maximum, after which the fluid pressure decays as the solid component of the AC bears more of the applied load. The equilibrium between compressive tissue deformation and out-flow of extracellular water is maintained by an increase in osmotic pressure that resists the outflow of tissue water [6,7]. In functionally compromised states such as osteoarthritis, the degradation and loss of proteoglycans in AC results in a loss of mechanical function and eventual degradation of the tissue as a whole. This, in turn, leads to reduced patient

mobility and is responsible for increased health-care costs to the individual and the community. With a prevalence of 13.9% in adults aged 25 years and older [8], costs of osteoarthritis were estimated to be \$185.5 billion using 1996–2005 data from the USA [9] and account for 1%–2.5% of gross national product in the USA, Canada, UK, France, and Australia [10]. Understanding of the characteristics responsible for the load bearing efficiency of AC and the factors leading to its degradation is incomplete. The importance of water and its local environment in load bearing by cartilage makes it an ideal candidate for study by magnetic resonance imaging (MRI), a technique that is sensitive to the mobility of water molecules in biological tissue. MRI is a technique that is ideally suited to the study of structural changes in soft tissues such as AC [11–13], with a range of characterization techniques available [3,4,11,12,14].

Figure 1. Scanning electron micrograph showing the high degree of collagen fiber alignment in articular cartilage, 30,000× magnification (reprinted with permission from [2]).



MRI utilizes the magnetic moments of certain nuclei, such as ^1H , which partially align with a strong magnetic field, resulting in a net nuclear magnetization of the sample. Brief irradiation with an appropriate radiofrequency pulse tips the magnetization vector out of its equilibrium direction; this is known as RF excitation. Excited magnetization undergoes two dynamic processes: (1) its transverse component precesses, inducing a current in a tuned radiofrequency coil; and (2) the magnetization vector gradually returns to equilibrium. The decay of the MRI signal as the sample returns to equilibrium is associated with characteristic time constants, T_1 and T_2 , representing the relaxation time constant of the longitudinal and transverse components of the magnetization, respectively. Relaxation time constants vary with the tissue environment, with shorter relaxation times observed in more restricted environments. For an anisotropic tissue such as cartilage, T_2 also varies with the angle of collagen alignment, relative to the static magnetic field [15] due to the intramolecular dipolar interactions of water and cartilage [3]. The inverse of T_2 represents a measure

of relaxation rate (R_2) of the nucleus and is used as the measure of relaxation in this study. The R_2 of each voxel is plotted as a parametric map of tissue relaxation rate, showing highest intensity for the regions with greatest relaxation rates. This information can be used to investigate the molecular environment of cartilage tissue in various states of compression and disease.

Attempts to assess load-dependent changes in cartilage water T_2 *in vivo* have demonstrated a potential role for MRI [16], however the variability and resolution of *in vivo* measurements indicate a need for more precise *in vitro* measurements to enable modeling of cartilage behavior and to identify factors associated with early loss of cartilage viability.

Highly aligned and structured, cartilage is an example of a poroelastic material having a supporting collagen matrix associated with a viscous liquid component [17] that osmotically interacts with proteoglycans. As such it can be investigated and modeled using traditional poroelastic models, as used in engineering [18].

One mechanical testing technique commonly used to assess cartilage function is consolidometry. This involves application of a constant load and measuring the time dependent change in thickness or stress creep, together with the change in pressure as the sample responds. This response is determined by the osmotically active components of the cartilage as they oppose the pressure-induced egress of water from the matrix over time and is defined as the hydrostatic excess pore pressure (HEPP).

While methods are available to assess late stages of cartilage damage *in vivo* [19–22], *in vitro* mechanical testing is the only non-destructive experimental method able to assess the load bearing function in healthy and diseased cartilage. To gain maximum information about cartilage response to load and the influences of disease and stress on structural change, it is desirable to combine mechanical and image-based measurements. Before simultaneously performing MR imaging in conjunction with mechanical testing, as a means to study the complex behavior of cartilage, there is a requirement to incorporate physical measurements to enable quantification of performance under controlled mechanical load in real time. This is difficult due to the confined space of the MRI magnet and the impact on transducers of the strong magnetic field-strengths associated with the MRI technique. A number of groups have used different characteristics of the magnetic resonance signal to examine cartilage behaviour (reviewed in [23,24]). The stress in joints has been estimated using MRI imaging by others, who have reported creep-type strain and stress in cartilage [25] and joints [26,27], however neither the influence of hydrostatic excess pore pressure as a measure of the osmotic contribution to the load bearing behavior, nor the long-time dynamics of cartilage consolidation, have been well studied by MRI.

Here we describe a method that allows the MR imaging of cartilage before and after loading without the inaccuracies associated with repositioning the sample, while at the same time allowing the recording of changes in hydrostatic excess pore pressure associated with constant load. We have used a fiber-optic transducer to avoid the influence of the strong magnetic field on transducer performance within the magnetic field of the MRI. Here we describe an MRI-compatible cartilage consolidometer capable of recording time-resolved hydrostatic pore pressure and strain curves inside the confined space of an MRI magnet for the study of cartilage function.

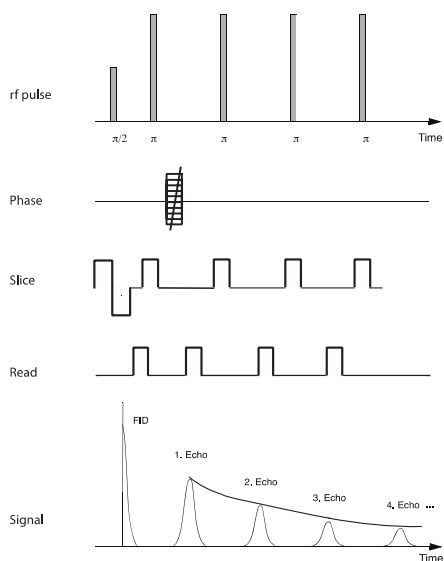
2. Experimental Section

2.1. NMR Measurements

Measurement of cartilage consolidation in an MRI spectrometer places limitations on the construction materials, dimensions of the equipment and access to the tissue being measured. The instrument used for this work utilizes a 7 tesla (T) super-conducting vertical-bore magnet (Bruker WB300, Rheinstetten, Germany) coupled with a DRX NMR spectrometer (Bruker) and triple-axis imaging gradients (Bruker). The working region of the MRI magnet comprises a transmit/receiver coil of 20 mm diameter, which is centered within the imaging gradients (1.5 T/m) of the 1.5 m long and 50 mm working-diameter superconducting magnet bore. The sample is lowered into the MRI coil from above.

Relaxation measurements utilized a standard multi-spin-multi-echo (MSME) pulse sequence [28] in which a 90° excitation radiofrequency pulse is followed by a train of 180° refocusing pulses, separated by a constant interval or echo-time. Recording the refocused signal intensity after each echo time enables determination of the decay in signal intensity over time (Figure 2). A repetition time of 2 s was used with an echo time of 7.375 ms, which enabled acquisition of 50 equidistantly spaced echo times for each relaxation curve before the signal had decayed to the noise level of the instrument. Other acquisition parameters included 10 averages, with a repetition time of 2 s, an effective spectral bandwidth of 90 kHz, field of view $22.1 \text{ mm} \times 22.1 \text{ mm}$, a slice thickness of 1 mm and an in-plane matrix size of 192 (phase) \times 256 (read), zero-filled to 256×256 yielding an in-plane resolution of $86.3 \times 86.3 \text{ }\mu\text{m}$ and a total acquisition time of 64 min.

Figure 2. An MSME imaging sequence (simplified; for further detail see [28]). Read, phase and slice refer to the transient gradients that are superimposed on the main magnetic field to achieve spatial resolution. The relaxation time T_2 is determined from the signal intensity at the echo-times following each refocusing pulse (π).



Each voxel in an image was fitted to a single exponential using Matlab (Mathworks) to provide a map of the relaxation time throughout the sample. The inverse of the T_2 relaxation time, R_2 , provides a relaxation map in which the faster relaxing components have higher intensity.

Each R_2 map was obtained from the series of 50 T_2 -weighted images sampling the T_2 decay curve. The TE dependence of the measured intensities of every individual voxel was fitted with a three-parameter exponential fit:

$$S(TE) = A \cdot e^{-TE \cdot R_2} + B \quad (1)$$

where S is the intensity at echo time TE ; A is the intensity at $TE = 0$ and B is a measure of average noise in the magnitude image. The three adjustable parameters of the fit are A , B and R_2 .

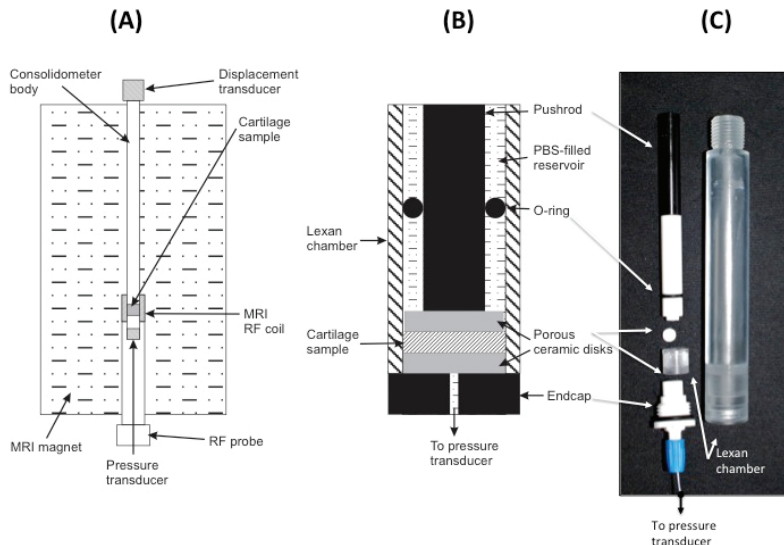
2.2. R_2 Depth Profiles

In order to construct the depth profile of the R_2 values within a given sample, the following procedure was used. The articular surface and the bone-cartilage interface in the sample were approximated by a polynomial fit of the order of between 1 and 3, depending on the amount of curvature in the respective interface. For each voxel, the shortest distance from the voxel centre to the polynomial curve approximating the articular surface was determined [29]. The thickness of the cartilage at the respective location was determined as the distance from the articular surface to the bone-cartilage interface. The relative depth (x) was then calculated for each voxel as the ratio of the distance to the AS to the cartilage thickness. The voxels were then grouped in histogram bins according to their x values. For each histogram bin, the average R_2 value and the standard deviation of the R_2 were calculated. This procedure was repeated for each R_2 map obtained (each sample, each compression state). The resulting data were used to construct the R_2 profiles.

2.3. Consolidometer Construction

To avoid MRI imaging artifacts, all material used in the construction of the consolidometer must be non-magnetic and transparent to radiofrequencies in the region of the transmit/receive coil of the instrument. The equipment constructed for this work was based around an 80 cm \times 2 cm tubular aluminium housing to support all other components (Figure 3A). Attached to the top of this tube is a low voltage displacement transducer (DT; Solartron Metrology DG 2.5; RS Components, Sydney, Australia) to record the position of a regulated pneumatic 5 mm plunger for applying a known load to cartilage samples. An in-line pressure transducer (1000 kPa, 0–100 mV; RS Components) the applied pneumatic pressure. A Lexan[®] extension is screwed to the base of the aluminium housing (Figure 3B,C).

Figure 3. The schematic (A) shows the orientation of the consolidometer with respect to the superconducting MR magnet; The centre schematic (B) shows the arrangement of the sample chamber components; The image on the right (C) shows the Lexan[®] extension and its components (from the top): the plunger; ceramic spacer; sample chamber and fiber-optic cable in the base of the sample holder. When assembled, these are screwed to the base of the aluminium consolidometer body.



A small ceramic sample support (Macor[®]; Corning Inc., Corning, NY, USA) is screwed to the base of the Lexan[®] extension. Figure 3C shows this sample support and the Lexan[®] extension, which form a chamber to locate the cartilage sample and provide access from below via a small hole for a fibre-optic pressure transducer (SAMBA-201 Preclin 360 MR Special; Biopac Systems Inc., Goleta, CA, USA), incorporating a Fabry-Perot interferometer sensor [30]. Pressure calibration relied on the built-in self-calibration protocol based on atmospheric pressure. The fiber-optic cable from the sensor is held in place with an O-ring compression fitting. All components of the sample chamber are sealed by O-rings to prevent leakage of solution into the MRI magnet. Data recorded by the two transducers are transmitted via USB connection to a Windows XP personal computer and processed using Labview software (Version 7.1; National Instruments, Austin, TX, USA).

2.4. Tissue Preparation

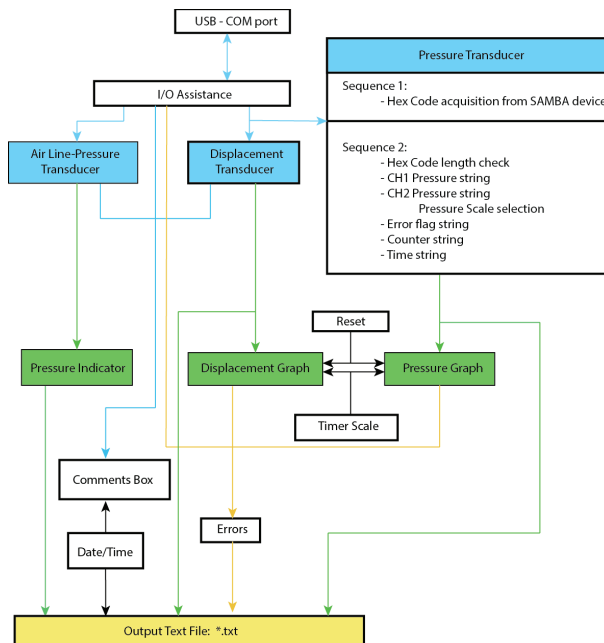
Bovine patellar cartilage from 4 animals, 2–3 years old, was collected from a local abattoir and stored on ice. A battery operated drill with 10 mm diamond-tipped hole saw (DTA, Victoria, Australia), designed for ceramics and glass, was used to remove a plug of cartilage attached to underlying bone. Five samples were drilled, two from the same animal. Measurements are presented for four samples. The results from one of the duplicate samples were not of sufficiently high quality and are not presented here. To prevent air-bubble induced image artifacts, all components are immersed in a bath of physiological saline solution prior to assembly into the consolidometer.

Figure 3 shows the components of the sample holder and the position of the fiber-optic transducer. Because the samples were obtained as discarded material from a commercial abattoir, the institutional ethics committee deemed that formal approval was not required for this study.

2.5. Software for Control of Consolidometer and Recording Results

A Labview software routine was written to coordinate the recording of the consolidometer transducer output as shown in Figure 4. The outputs from the air line-pressure, and displacement transducers are transferred via a “personal measurement device” (PMD1208LS, RS Electronics), to the LabView program by means of a high-speed USB connection. The Labview program provides the following outputs in a graphical interface: (a) real-time graph of the transducer displacement as a function of time, showing the distance that the cartilage is compressed (in millimetres) in the time since monitoring was started (in seconds), updated every 1 s; (b) a real-time graph of the pressure as a function of time provides the hydrostatic pore pressure of the cartilage, as measured by the SAMBA transducer during the time since monitoring was started (in seconds), also updated every 1 s; (c) the real-time distance as recorded by the distance (compression) transducer in the top end of the consolidometer body; (d) a view of the pressure being applied to the system as measured by the air line-pressure transducer at the air supply point; (e) a HEX key that is transmitted from the SAMBA unit before it has been decoded, available for diagnostic work; and (f) an error display panel to warn of incorrect performance.

Figure 4. A block diagram of the components utilized in the module developed for the Labview program to interface with the signal transducers and screen output (blue and green boxes, respectively).



The following operator input options are also available for the Labview module: a comments field; an option to filter (not used in this work) the signal before graphical display, while the unfiltered signal is still recorded in the log file; a pull-down menu for selection of units used in the pressure graph display and data in the log file; a reset option that allows the clearing of data from the graphs while the system is running.

3. Results

3.1. Consolidation Curves

The dynamics of unconstrained mechanical consolidation of articular cartilage samples were characterised by measuring the time dependence of two quantities: hydrostatic excess pore pressure (HEPP) and compressive displacement. These consolidation curves (hereafter referred to as the HEPP and the DT curve, respectively) were recorded for the four samples studied. Figure 5 shows the HEPP and the DT for the four articular cartilage samples. A representative example of the time dependence of the applied pressure is also shown in Figure 6; the small periodic oscillations of the applied pressure correspond to the oscillations of the efficiency of the pneumatic compressor related to pressure regulation. The compression ratio of the samples was defined as:

$$C = \frac{h_0 - \Delta h}{h_0} \cdot 100\% \quad (2)$$

where h_0 and Δh are the thickness of the uncompressed cartilage and the compressive displacement, respectively, measured from MRI images. Consolidometry data were not used for its calculation because the displacement-vs.-time curve provides information about the dynamics of Δh but not about h_0 ; therefore, it is not possible to calculate C on the basis of consolidometry measurements alone. The value of C ranged from ~80% at the applied pressure of 50 kPa to ~25% at the applied pressure of 500 kPa. The ratio C was calculated on the basis of the *average* change of cartilage thickness between uncompressed and compressed MR images. In cartilage samples with a curved articular surface or bone-cartilage interface the local compression ratio may vary across the sample due to lateral variation of the stress. In such samples the definition of C may be somewhat ambiguous. For this reason, C was used here only as an overall guide of the degree of sample compression; it was not used in data processing or interpretation. The typical excursion of HEPP over the course of consolidation typically ranged between 100 and 300 kPa, depending on the applied pressure. The approach of both the HEPP and the compressive displacement to their respective asymptotic values could be characterized as multiexponential. The HEPP curves in Figure 5 also show the line obtained using a double exponential fit. The initial buildup and subsequent decay of HEPP to 50% of the maximum value typically took several minutes, but it usually took ~120 min for the consolidation process to be considered near complete.

Figure 5. Unconstrained consolidation curves of the four articular cartilage samples showing HEPP curves (black) and the corresponding compressive displacement vs. time. The fluctuations of the applied pressure are an artifact of the compressed air supply shown in Figure 6. The samples were bone-cartilage plugs similar to that seen in Figure 7.

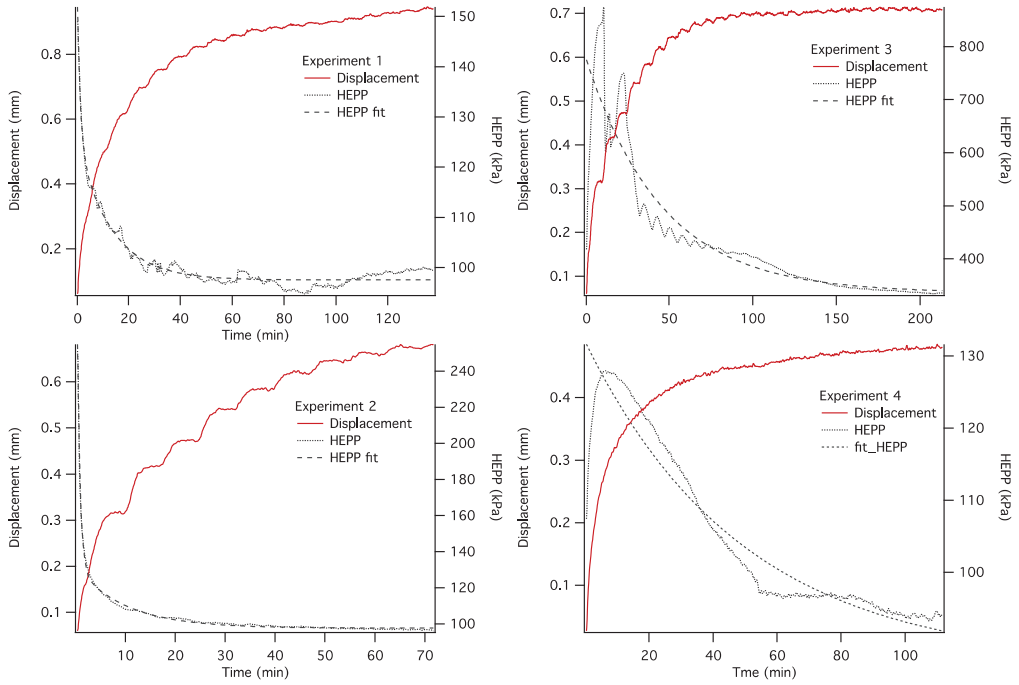
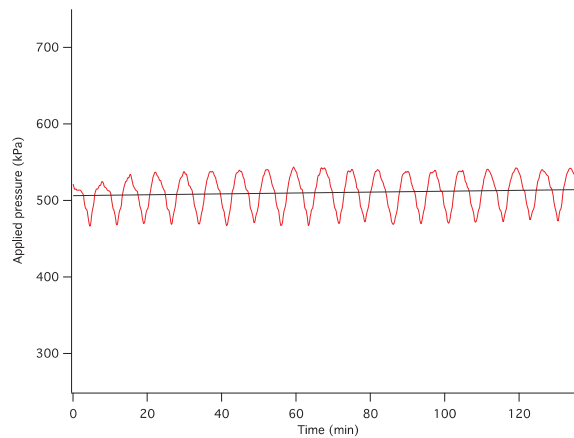


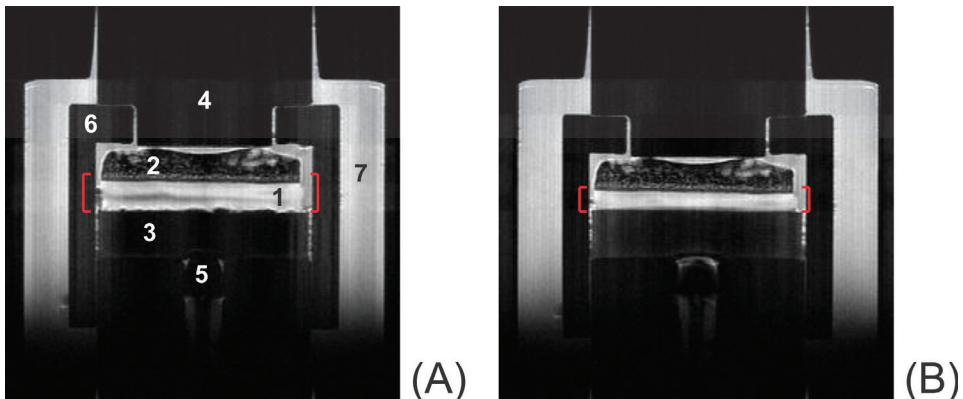
Figure 6. A representative plot showing the fluctuations in the supplied air pressure vs. time consistent with the fluctuations of the applied pressure shown in Figure 5 being an artifact of the compressed air supply.



3.2. T_2 -Weighted Images

Figure 7 shows typical T_2 -weighted images of uncompressed (Figure 7A) and compressed (Figure 7B) articular cartilage Sample 2. The images shown in this figure were acquired near the full image intensity (short echo time, $TE = 7.375$ ms). In all, 50 T_2 -weighted images were acquired in the same data set in order to sample the T_2 decay curve: the TE values were sampled equidistantly in the range from 7.375 to 368.75 ms. The components of the consolidometer and the elements of the sample visible in the images are labeled in the figure and identified in the figure caption.

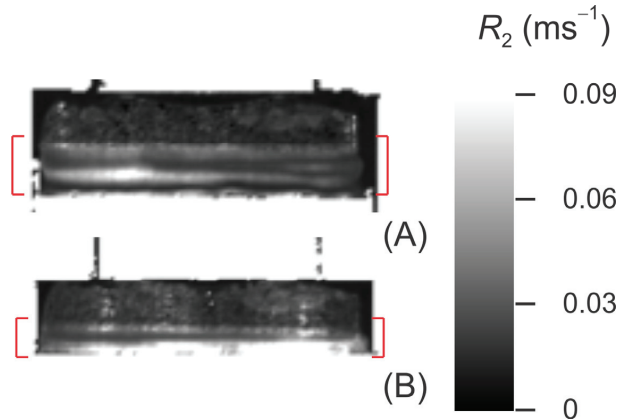
Figure 7. Representative T_2 -weighted images of bone-cartilage plugs: (A) uncompressed Sample 4 and (B) Sample 4 compressed under the applied pressure of 110 kPa. Both images were taken at the echo time of 7.375 ms. Labeled with the numerals are: (1) articular cartilage; (2) subchondral bone; (3) compression disc made of permeable ceramic; (4) compression rod; (5) Fabry-Perot pressure sensor; (6) sample housing; and (7) phosphate-buffered saline filling the compression chamber. The compressed image (B) was obtained in the quasistatic limit of the consolidation curve (~ 2 h after the start of consolidation). The compressive displacement, C , was 64%.



3.3. R_2 Map

Figure 8 shows the R_2 maps for Sample 2, the fitted value of R_2 (as defined in Equation (1)) taken as the transverse spin relaxation rate for the given voxel. For the sake of clarity, the regions that produce no MRI signal (*i.e.*, the metal and plastic components of the consolidometer) have been masked out, and only bone-cartilage plugs and PBS are shown in this figure.

Figure 8. R_2 maps of Sample 4. Metal and plastic components of the consolidometer, which produce no MRI signal, have been masked out. The red brackets show the cartilage before (A) and after (B) compression, with the remaining signal arising from the supporting bone. A linear greylevel scale is used, with white corresponding to $R_2 = 0.09 \text{ ms}^{-1}$ and black, to $R_2 = 0$.



3.4. Effect of Compression on T_2 Depth Profiles

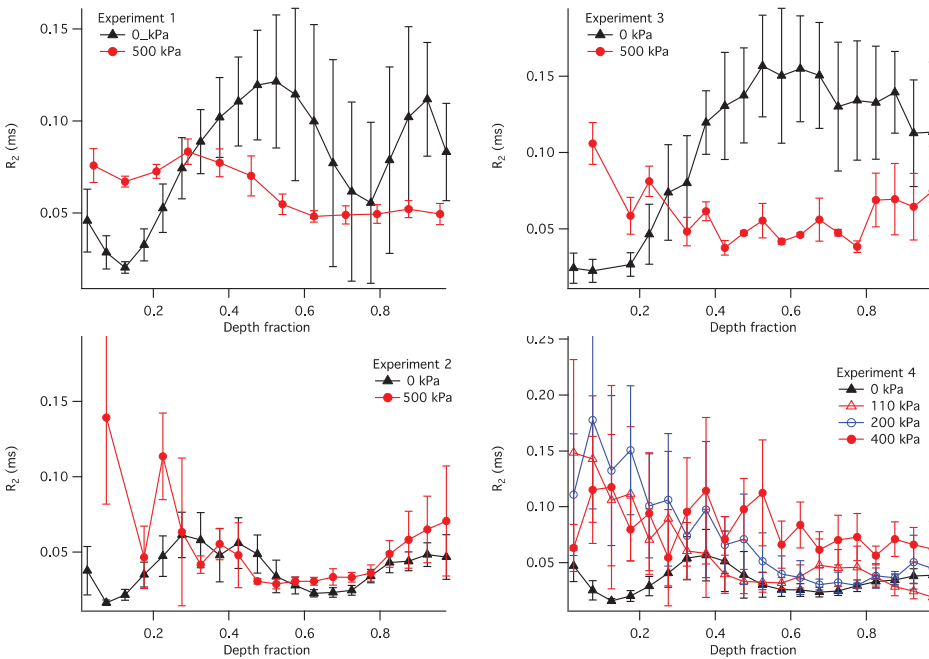
The observed R_2 within the articular cartilage exhibited a non-uniform and compression-dependent depth profile. The uncompressed and compressed R_2 depth profiles for the four samples are presented in Figure 9. In order to adequately compare the profiles in uncompressed and compressed samples, the R_2 in this figure is plotted vs. the normalised depth (x): a unit-less quantity equal to the depth divided by the thickness of the articular cartilage where the cartilage surface is zero. It is used here instead of the actual depth in order to enable a comparison between compressed and uncompressed samples. Each point in the plots illustrates a distribution of the R_2 values at a given normalized depth: the solid lines show the means, with error bars showing the standard deviations.

4. Discussion

4.1. Consolidation Curves

Construction of an MRI compatible consolidometer, utilising a Fabry-Perot pressure transducer that is unaffected by strong magnetic fields, enabled the recording of consolidation curves comparable to those previously reported [6,31]. While MRI micro-imaging of static cartilage has been reported previously [15], the ability to undertake biophysical measurements of cartilage under compressive load has extended the potential of the cartilage consolidation technique to contribute to our understanding of the functional behaviour of cartilage. The irregular consolidation curve observed for Sample 3 in Figure 5 can be explained by a combination of o-ring stiction and the presence of bubbles in the system.

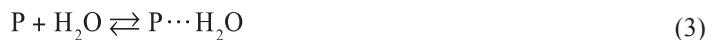
Figure 9. Depth profiles of the transverse spin relaxation rate (R_2) in uncompressed (black plot) and compressed (red plot) articular cartilage in each of the four samples (panels correspond to the panels in Figure 5). Depth fraction is the normalised depth (relative to the cartilage surface) The “compressed” data were obtained at the load of 500 kPa for all except sample four in which a series of pressures (110, 200 and 400 kPa) were applied sequentially. In each plot, the solid line shows the average value of R_2 , and the error bars show the standard deviations. The plot demonstrates that static load carriage in articular cartilage involves primarily regions consistent with the superficial and transitional zones, where the greatest compression-induced change in the R_2 is observed.



4.2. Transverse Spin Relaxation Rates (R_2) in Articular Cartilage

Transverse relaxation rate (R_2) of water protons in articular cartilage is determined by two principal factors: the volume fraction of the ECM biopolymers (collagen and proteoglycans) and the degree of collagen fibre alignment. The nature of this relationship can be understood in terms of the following model.

Water in articular cartilage undergoes chemical exchange between “free” water and “bound” water (water associated with the ECM macromolecules) [3,32]:



where P is a biopolymer and \cdots denotes hydrogen bonding. This exchange process is rapid on the NMR time scale; as a result, the observed spin relaxation rate of water protons is the weighted average of the contributions from the different water populations [33]:

$$R_2 = p_F R_{2F} + p_C R_{2C} + p_{PG} R_{2PG} \quad (4)$$

Here, p_F , p_C and p_{PG} are the molar fractions of free water, water associated with collagen fibres and water associated with proteoglycans, respectively; $p_F + p_C + p_{PG} = 1$; and R_{2F} , R_{2C} and R_{2PG} are the intrinsic spin relaxation rates associated with these populations of water.

The other important factor affecting R_2 is the alignment of the collagen fibres within the ECM. The intrinsic relaxation rate of water associated with collagen, R_{2C} , follows the so-called magic-angle orientational dependence, whereby the efficiency of spin relaxation is minimised when the collagen fibre is aligned at the “magic angle” $\theta_{MA} = \arccos(1/\sqrt{3}) \approx 54.7^\circ$ [3,34,35]. As a result, the weighted-average relaxation rate also follows the magic-angle dependence:

$$R_2 = R_2^I + R_2^A(\theta) = R_2^I + R_2^{A0} \left(\frac{3 \cos^2 \theta - 1}{2} \right)^2 \quad (5)$$

where θ is the angle between the collagen fibres and the applied static magnetic field \mathbf{B}_0 [36]. R_2 on the left-hand side of Equation (5) is identical to the R_2 on the left-hand side of Equation (4); both represent the experimentally measured R_2 at a given physical location within a cartilage sample at a given orientation with respect to \mathbf{B}_0 . R_2^I is the isotropic component of the relaxation rate, which is independent of the orientation of the sample relative to \mathbf{B}_0 and can be attributed to free, PG-bound and, to some extent, collagen-bound water. R_2^A is the anisotropic component of the relaxation rate; this component can be attributed exclusively to collagen-bound water. In other words, the R_2 contributions R_{2F} and R_{2PG} in Equation (4) are entirely isotropic, while the contribution R_{2C} contains an isotropic and an anisotropic term. The anisotropic component R_2^A is non-zero only in the case of partially aligned collagen scaffold, and its amplitude is dependent both on the degree of the alignment and on the angle between the predominant direction of the alignment and the static magnetic field (R_2^{A0} is the anisotropic component or relaxation rate when the cartilage is predominantly aligned with the static magnetic field).

The “free” water is the dominant water population in articular cartilage: both p_C and p_{PG} can be estimated to be ~ 0.1 or less, based on studies of similar hydrated macromolecular systems [37]. However, the intrinsic spin relaxation rates of the two “bound” populations, R_{2C} and R_{2PG} , significantly exceed that of the free water, R_{2F} , due to the lower molecular hydrodynamic mobility of the former. As a result, despite its relatively small molar fraction, the R_2 contribution from bound water can significantly exceed that from free water. This can be seen, e.g., in references [34,35], where the amplitude of the anisotropic component of R_2 within the radial zone of AC exceeds the isotropic component by a factor of 3–4. It also means that, when the cartilage sample is perpendicular to \mathbf{B}_0 , the R_2 value tends to vary with the depth and exhibits a zonal behaviour corresponding to the histological zones of collagen fibre alignment.

4.3. Interpretation of Compression-Induced R_2 Changes

Compression of articular cartilage effects two principal changes at the microstructural level, both of which bring about a change in the R_2 value. First, due to the incompressible nature of interstitial water, compression can only be achieved via the outflow of water from the sample. Therefore,

compression increases the volume fraction of the biopolymers within the sample and thus serves to increase the R_2 . Second, sample compression can result in reorientation of collagen fibres within the ECM scaffold [12,38], which can result in changes in the anisotropic component of the spin relaxation rate. This change can be either positive or negative, depending on whether the angle between the fibres and \mathbf{B}_0 moves further away from or closer to θ_{MA} .

In general, these two contributions to compression-induced R_2 changes are superimposed and it is not possible to separate them based on the mathematical considerations alone. However, it is often possible to attribute the observed change primarily to one of these two factors, based on the knowledge of the macromolecular factors underpinning cartilage biomechanics.

As a case study, it is instructive to interpret the depth profiles of R_2 shown in Figure 9. In the uncompressed samples (the black profiles), the lowest values of R_2 (and therefore the lowest R_2^A) is consistently exhibited at the normalised depth $x \sim 0.1$. This region of cartilage is consistent with the centre of the transitional zone of AC, where collagen is completely disordered and therefore possesses $R_2^A = 0$. With compression the R_2 in these regions increased in all four samples, consistent with compression-induced loss of water in the superficial and transitional zones of the cartilage, compression-induced partial alignment of collagen fibres, or a combination of these two factors. It should be noted that some of the compression-induced evolution of the R_2 profile observed in Sample 4 could be attributed to the use of the relative depth, as seen, e.g., in [39]; however, this does not appear to be a factor for the other three samples.

With the increasing depth ($x = 0.3-0.4$), the R_2 in uncompressed samples increases to $\sim 0.05 \text{ ms}^{-1}$; this is consistent with an increased degree of collagen alignment and the consequent non-zero R_2 contribution from its anisotropic component. The R_2 continues to increase in Sample 3 and to some extent in Sample 1, suggesting the maximum collagen alignment near the bone. These two samples are therefore consistent with the classic three-zone collagen alignment pattern (superficial, transitional and radial zones). On the other hand, in Samples 2 and 4 the R_2 significantly decreases after $x = 0.4$ and reaches a secondary minimum at $x \sim 0.6$. This suggests the presence of a secondary transitional zone near the bone.

Below the region of cartilage consistent with the primary transitional zone ($x > 0.3$), the response of the R_2 profiles to compression varied markedly. Samples 1 and 3 demonstrate a decrease in R_2 throughout the depth range between 0.3 and 1. This can be explained as follows. Assuming that cartilage compression results in a decrease in the water content throughout the tissue, the isotropic contribution to R_2 (R_2^I) can only be expected to rise at a given depth. However, the anisotropic contribution (R_2^A) is capable of decreasing if the compression results in a realignment of collagen fibres closer to the Magic Angle relative to \mathbf{B}_0 . If Samples 1 and 3 possess the classical alignment pattern, then the collagen fibres in their radial zones are likely near-perpendicular to the bone in the uncompressed state. Therefore, any compression-induced realignment of the collagen fibres would increase the angle between the fibres and \mathbf{B}_0 and, according to Equation (5), would reduce the magnitude of the anisotropic R_2 contribution. Such fibre realignment has also been observed experimentally from diffusion-tensor images of articular cartilage under intermediate load [14]. Therefore, fibre realignment appears to be a plausible explanation of the compression-induced decrease in R_2 in these two samples.

Sample 2 exhibits no significant compressive changes in the R_2 profile at $x > 0.3$. A likely explanation of this observation is that the load bearing in this sample was borne exclusively by its transitional zone. An alternative explanation may be that the increase in R_2^1 due to water loss is exactly compensated by the fibre realignment-induced reduction in R_2^A ; however, the scenario appears improbable.

Sample 4 shows a R_2 profile in the uncompressed state that is somewhat similar to that of Sample 2. This sample was measured at three different pressures, 120, 200 and 400 kPa. All three pressures produced an increase in R_2 at $x < 0.35$, but no significant change in the R_2 profiles was seen at greater depth fractions for pressures of 120 and 200 kPa. This suggests that at the lower pressures the regions corresponding to the superficial and transitional zones carried the majority of the load. At a pressure of 400 kPa, a near-uniform and significant increase in R_2 is seen at $x > 0.35$. This suggests that the deeper cartilage regions in this sample contributed to the load processing at the greater loading pressures.

4.4. Load Processing in Articular Cartilage

As discussed above, Figure 9 reveals that the degree of compression within mechanically loaded AC is not uniform but varies between structural regions of the cartilage with different degrees of collagen alignment. The compression-induced change in the depth profile of R_2 in Sample 4 suggests that, at the applied load of 100–200 kPa, the greatest compression is observed in the superficial and transitional zones of AC, while the radial zone exhibits no significant compression. This is consistent with previously published studies, where at a low compression ratio significant changes in the collagen fibre alignment were limited to the superficial and transitional zones, and significant compressive response in the radial zone was observed only at a higher compression [40,41].

The other feature evident from Figure 4 is the significant differences in the compressive response at high pressure exhibited by the deep zones ($x > 0.35$) of the four samples studied. This is consistent with the variability of collagen fibre alignment patterns observed in previous studies [12]. While the deep zone of Sample 4 exhibited a modest but significant compressive response at 400 kPa, the corresponding zone of Sample 2 exhibited no apparent response at a comparable pressure (500 kPa). This difference is interesting, especially in light of the similarity of uncompressed R_2 profiles of Samples 2 and 4. Furthermore, the radial zones of Samples 1 and 3 exhibited a compressive response that was significant but different to that of Sample 4. This suggests that the macromolecular scenarios involved in load processing may vary significantly between cartilage samples, even in animals of the same species and comparable age. Further investigation of these differences may be significant to the understanding of the biophysical mechanisms involved in the development of the early stages of osteoarthritis and calls for a further, in-depth study of the spatial distribution of load processing in articular cartilage.

4.5. MRI Consolidometry as a Tool for the Study of Cartilage Biomechanics

The limitations of this study relate to the relatively long acquisition times required for MRI measurements on a biological time-scale, the time during which an organism might experience load

and for equilibration of changes to the cartilage to occur. Time resolution could be improved, at the expense of spatial resolution, using larger voxels to improve signal-to-noise ratios (SNR). Greater SNR could also be achieved with higher magnetic fields to gain better time-resolution. In this study, the maximum pressure achieved was similar to normal physiological pressures achieved *in vivo* although the results are not relevant to peak transient working loads experienced *in vivo*. The application of higher pressures would reduce the thickness of tissue available for imaging, making it difficult to reliably differentiate regions within the cartilage.

Imaging measurements could be made during the consolidation process, however, because the consolidation process is dynamic, compression of the cartilage is likely to reduce the image quality, particularly in the early stages when fluid extrusion is greatest. For our purposes, the initial and final states of the cartilage after compression were of most interest to demonstrate the ability to make measurements before and after consolidation without moving the sample within the MRI magnet.

Because the cartilage is compressed after the second measurement, it is not possible to differentiate between changes in thickness due to collagen compression from changes due to egress of water. T_1 mapping in future studies may assist with this differentiation.

The successful measurement of cartilage consolidation within an MRI magnet will enable the application of other MRI techniques to further examine the dynamic structural changes accompanying load-bearing articular cartilage and disease-related changes. Examples include assessing changes in the alignment of collagen using diffusion tensor methods, imaging of bulk water flow in response to compression and the role of proteoglycan distribution, potentially measured by ^{23}Na distribution. The method is also applicable to assessing treatment effects and compression cycling.

5. Conclusions

The construction of a MRI compatible cartilage consolidometer, for sensitive pressure measurements in the confined space and high magnetic field strength of the MRI magnet was made possible by the use of a fiber-optic pressure transducer and non-magnetic construction materials. The consolidometer enables the concurrent *in vitro* study of cartilage structure and performance while under mechanical load. The results of this study indicate that the static load is predominantly borne by the superficial and transitional zones of articular cartilage. This technique will enable characterization of cartilage tissue load-bearing performance in different states of health, as well as differences in load processing in individual animals.

Acknowledgments

The authors would like to thank Tim Markwell for discussions relating to the implementation of the fiber-optic transducer. This work was supported by ARC discovery project DP0880346. (KIM, JMP and RMW). We thank Sean Powell for permission to use the SEM image shown in Figure 1.

Author Contributions

The consolidometer was designed by James M. Pope and Adekunle Oloyede, and constructed by Greg Tevelen. Jean-Philippe Ravasio developed the software to regulate the consolidometer and data

recording. Konstantin I. Momot developed the imaging and sample compression protocol. Christopher Bell compiled the documentation for the consolidometer. Robert Mark Wellard, Konstantin I. Momot, Jean-Philippe Ravasio and Samuel Guesne were responsible for data acquisition. Konstantin I. Momot performed the processing and analysis of the data. R Mark Wellard and Konstantin I. Momot wrote the manuscript with additional input from James M. Pope and Adekunle Oloyede.

Conflicts of Interest

The authors declare no conflict of interest.

References

21. Jeffery, A.K.; Blunn, G.W.; Archer, C.W.; Bentley, G. Three-dimensional collagen architecture in bovine articular cartilage. *J. Bone Joint Surg. Br.* **1991**, *73*, 795–801.
22. Powell, S. Langevin Dynamics Study of Water Diffusion in Model Articular Cartilage. Master's Thesis, Queensland University of Technology Brisbane, Brisbane, Australia, 2010.
23. Momot, K.I.; Pope, J.M.; Wellard, R.M. Anisotropy of spin relaxation of water protons in cartilage and tendon. *NMR Biomed.* **2010**, *23*, 313–324.
24. Xia, Y. Heterogeneity of cartilage laminae in MR imaging. *J. Magn. Reson. Imaging* **2000**, *11*, 686–693.
25. Oswald, E.S.; Chao, P.H.; Bulinski, J.C.; Ateshian, G.A.; Hung, C.T. Dependence of zonal chondrocyte water transport properties on osmotic environment. *Cell. Mol. Bioeng.* **2008**, *1*, 339–348.
26. Oloyede, A.; Broom, N.D. Complex nature of stress inside loaded articular cartilage. *Clin. Biomech. (Bristol, Avon)* **1994**, *9*, 149–156.
27. Ateshian, G.A.; Rajan, V.; Chahine, N.O.; Canal, C.E.; Hung, C.T. Modeling the matrix of articular cartilage using a continuous fiber angular distribution predicts many observed phenomena. *J. Biomech. Eng.* **2009**, *131*, 061003.
28. Lawrence, R.C.; Felson, D.T.; Helmick, C.G.; Arnold, L.M.; Choi, H.; Deyo, R.A.; Gabriel, S.; Hirsch, R.; Hochberg, M.C.; Hunder, G.G.; *et al.* Estimates of the prevalence of arthritis and other rheumatic conditions in the United States. Part II. *Arthritis Rheum.* **2008**, *58*, 26–35.
29. Kotlarz, H.; Gunnarsson, C.L.; Fang, H.; Rizzo, J.A. Insurer and out-of-pocket costs of osteoarthritis in the US: Evidence from national survey data. *Arthritis Rheum.* **2009**, *60*, 3546–3553.
30. March, L.M.; Bachmeier, C.J. Economics of osteoarthritis: A global perspective. *Bailliere Clin. Rheumatol.* **1997**, *11*, 817–834.
31. Meder, R.; de Visser, S.K.; Bowden, J.C.; Bostrom, T.; Pope, J.M. Diffusion tensor imaging of articular cartilage as a measure of tissue microstructure. *Osteoarthr. Cartil.* **2006**, *14*, 875–881.
32. De Visser, S.K.; Bowden, J.C.; Wentrup-Byrne, E.; Rintoul, L.; Bostrom, T.; Pope, J.M.; Momot, K.I. Anisotropy of collagen fibre alignment in bovine cartilage: Comparison of polarised light microscopy and spatially resolved diffusion-tensor measurements. *Osteoarthr. Cartil.* **2008**, *16*, 689–697.

33. Pierce, D.M.; Trobin, W.; Raya, J.G.; Trattng, S.; Bischof, H.; Glaser, C.; Holzapfel, G.A. DT-MRI Based Computation of Collagen Fiber Deformation in Human Articular Cartilage: A Feasibility Study. *Ann. Biomed. Eng.* **2010**, *38*, 2447–2463.
34. De Visser, S.K.; Crawford, R.W.; Pope, J.M. Structural adaptations in compressed articular cartilage measured by diffusion tensor imaging. *Osteoarthr. Cartil.* **2008**, *16*, 83–89.
35. Xia, Y. Averaged and depth-dependent anisotropy of articular cartilage by microscopic imaging. *Semin. Arthritis Rheum.* **2008**, *37*, 317–327.
36. Nishii, T.; Kuroda, K.; Matsuoka, Y.; Sahara, T.; Yoshikawa, H. Change in knee cartilage T₂ in response to mechanical loading. *J. Magn. Reson. Imaging* **2008**, *28*, 175–180.
37. McCutchen, C.W. Cartilage is Poroelastic, Not Viscoelastic (Including an Exact Theorem about Strain-Energy and Viscous Loss, and an Order of Magnitude Relation for Equilibration Time). *J. Biomech.* **1982**, *15*, 325–327.
38. Soulhat, J.; Buschmann, M.D.; Shirazi-Adl, A. A fibril-network-reinforced biphasic model of cartilage in unconfined compression. *J. Biomech. Eng.* **1999**, *121*, 340–347.
39. Larsen, A.; Dale, K.; Eek, M. Radiographic evaluation of rheumatoid arthritis and related conditions by standard reference films. *Acta Radiol. Diagn.* **1977**, *18*, 481–491.
40. Borthakur, A.; Mellon, E.; Niyogi, S.; Witschey, W.; Kneeland, J.B.; Reddy, R. Sodium and T1rho MRI for molecular and diagnostic imaging of articular cartilage. *NMR Biomed.* **2006**, *19*, 781–821.
41. Reddy, R.; Li, S.; Noyszewski, E.A.; Kneeland, J.B.; Leigh, J.S. *In vivo* sodium multiple quantum spectroscopy of human articular cartilage. *Magn. Reson. Med.* **1997**, *38*, 207–214.
42. Wang, L.; Chen, S.; An, K.N.; Yang, H.L.; Luo, Z.P. Theoretical prediction of ultrasound elastography for detection of early osteoarthritis. *Sci. World J.* **2013**, *2013*, 565717.
43. Potter, H.G.; Black, B.R.; Chong, L.R. New techniques in articular cartilage imaging. *Clin. Sports Med.* **2009**, *28*, 77–94.
44. Chan, D.D.; Neu, C.P. Probing articular cartilage damage and disease by quantitative magnetic resonance imaging. *J. Royal Soc. Interface* **2013**, *10*, 20120608.
45. Neu, C.P.; Walton, J.H. Displacement encoding for the measurement of cartilage deformation. *Magn. Reson. Med.* **2008**, *59*, 149–155.
46. Chan, D.D.; Neu, C.P.; Hull, M.L. *In situ* deformation of cartilage in cyclically loaded tibiofemoral joints by displacement-encoded MRI. *Osteoarthr. Cartil.* **2009**, *17*, 1461–1468.
47. Butz, K.D.; Chan, D.D.; Nauman, E.A.; Neu, C.P. Stress distributions and material properties determined in articular cartilage from MRI-based finite strains. *J. Biomech.* **2011**, *44*, 2667–2672.
48. Meiboom, S.; Gill, D. Modified Spin-Echo Method for Measuring Nuclear-Relaxation Times. *Rev. Sci. Instrum.* **1958**, *29*, 688–691.
49. Korn, G.A.; Korn, T.M. *Mathematical Handbook for Scientists and Engineers: Definitions, Theorems, and Formulas for Reference and Review*, 2nd ed.; McGraw-Hill: New York, NY, USA, 1968.
50. Siegmann, A.E. *Lasers*; University Sciences Books: Mills Valley, CA, USA, 1986.

51. Oloyede, A.; Gudimetla, P.; Crawford, R.; Hills, B.A. Biomechanical responses of normal and delipidized articular cartilage subjected to varying rates of loading. *Connect Tissue Res.* **2004**, *45*, 86–93.
52. Cavanagh, J.; Fairbrother, W.J.; Palmer, A.G.; Rance, M.; Skelton, N.J. *Protein NMR Spectroscopy: Principles and Practice*, 2nd ed.; Academic Press: Boston, MA, USA, 2007.
53. Xia, Y. Magic-angle effect in magnetic resonance imaging of articular cartilage—A review. *Invest. Radiol.* **2000**, *35*, 602–621.
54. Navon, G.; Eliav, U.; Demco, D.E.; Blumich, B. Study of order and dynamic processes in tendon by NMR and MRI. *J. Magn. Reson. Imaging* **2007**, *25*, 362–380.
55. Xia, Y. Relaxation anisotropy in cartilage by NMR microscopy (muMRI) at 14-microm resolution. *Magn. Reson. Med.* **1998**, *39*, 941–949.
56. Henkelman, R.M.; Huang, X.M.; Xiang, Q.S.; Stanisz, G.J.; Swanson, S.D.; Bronskill, M.J. Quantitative Interpretation of Magnetization-Transfer. *Magn. Reson. Med.* **1993**, *29*, 759–766.
57. Momot, K.I. Microstructural magnetic resonance imaging of articular cartilage. *Biomed. Spectrosc. Imaging* **2012**, *1*, 27–37.
58. Filidoro, L.; Dietrich, O.; Weber, J.; Rauch, E.; Oerther, T.; Wick, M.; Reiser, M.F.; Glaser, C. High-resolution diffusion tensor imaging of human patellar cartilage: Feasibility and preliminary findings. *Magn. Reson. Med.* **2005**, *53*, 993–998.
59. Alhadlaq, H.A.; Xia, Y. The structural adaptations in compressed articular cartilage by microscopic MRI (microMRI) T(2) anisotropy. *Osteoarthr. Cartil.* **2004**, *12*, 887–894.
60. Gannon, A.R.; Nagel, T.; Kelly, D.J. The role of the superficial region in determining the dynamic properties of articular cartilage. *Osteoarthr. Cartil.* **2012**, *20*, 1417–1425.
61. Maroudas, A. Physico-Chemical Properties of Articular Cartilage. In *Adult Articular Cartilage*; Freeman, M.A.R., Ed.; Pitman Medical: Tunbridge Wells, UK, 1979; pp. 215–290.

Extrinsic Contrast

Sensing Lanthanide Metal Content in Biological Tissues with Magnetic Resonance Spectroscopy

Dina V. Hingorani, Sandra I. Gonzalez, Jessica F. Li, and Mark D. Pagel

Abstract: The development and validation of MRI contrast agents consisting of a lanthanide chelate often requires a determination of the concentration of the agent in *ex vivo* tissue. We have developed a protocol that uses 70% nitric acid to completely digest tissue samples that contain Gd(III), Dy(III), Tm(III), Eu(III), or Yb(III) ions, or the MRI contrast agent gadodiamide. NMR spectroscopy of coaxial tubes containing a digested sample and a separate control solution of nitric acid was used to rapidly and easily measure the bulk magnetic susceptibility (BMS) shift caused by each lanthanide ion and gadodiamide. Each BMS shift was shown to be linearly correlated with the concentration of each lanthanide ion and gadodiamide in the 70% nitric acid solution and in digested rat kidney and liver tissues. These concentration measurements had outstanding precision, and also had good accuracy for concentrations ≥ 10 mM for Tm(III) Eu(III), and Yb(III), and ≥ 3 mM for Gd(III), gadodiamide, and Dy(III). Improved sample handling methods are needed to improve measurement accuracy for samples with lower concentrations.

Reprinted from *Sensors*. Cite as: Hingorani, D.V.; Gonzalez, S.I.; Li, J.F.; Pagel, M.D. Sensing Lanthanide Metal Content in Biological Tissues with Magnetic Resonance Spectroscopy. *Sensors* **2013**, *13*, 13732–13743.

1. Introduction

MRI contrast agents that consist of Gd(III) chelates are often used to enhance the image contrast of anatomical features during clinical diagnoses. Examples include the identification cerebral lesions during neuroimaging [1], the localization of ischemia and acutely infarcted myocardium during cardiac imaging [2], and the diagnoses of solid tumor morphology during oncological imaging [3]. These MRI contrast agents are also used to assess tissue function, including the tracking of vascular flow for large arteries and veins using MRI angiography [4], and the evaluation of vascular perfusion and permeability in capillary networks using Dynamic Contrast Enhancement MRI [5]. Gd(III) and Dy(III) chelates have been used for similar diagnoses of animal models [6–8].

Lanthanide chelates have also been used for molecular imaging. Gd(III) chelates have been used to detect enzyme activities, metabolites, ions, pH, and temperature by monitoring changes in T1- or T2-relaxation [9]. Dy(III), Tm(III), Eu(III) and Yb(III) chelates have also been developed for molecular imaging, primarily through the mechanism of Chemical Exchange Saturation Transfer (CEST) [10]. These lanthanide chelates contain a labile proton that can be selectively saturated, which reduces the coherent MR signal of the proton. The labile proton of the agent can exchange with water, which transfers the saturation to water and effectively reduces the MR signal of water. The magnitude of this change in MR water signal is sensitive to the chemical exchange rate of the CEST agent, which can be modulated

by enzymatic catalysis of the agent's chemical structure, a change in temperature or pH that directly affect the kinetic rates of chemical exchange processes, or binding interactions with metabolites and ions [9].

Clinical translation of MRI contrast agents that consist of lanthanide chelates requires evaluations of biodistributions to assess potential toxicities. In particular, slow clearance from the body can lead to extended retention and subsequent dissociation of a lanthanide ion from the organic chelator, which can cause Nephrogenic Systemic Fibrosis [11]. *Ex vivo* measurements of lanthanide chelate concentrations in various tissues of animal models are often one of the first steps of toxicological assessments. In addition, molecular imaging studies of animal models require the accurate measurement of tissue concentrations of MRI contrast agents to validate imaging results. However, T1 relaxation caused by a Gd(III) chelate, and CEST generated from other lanthanide chelates, are dependent on multiple physico-chemical characteristics, so that converting T1-weighted MR images or CEST MRI results to a measurement of contrast agent concentration is not necessarily accurate [12,13]. Therefore, *ex vivo* validation of contrast agent concentrations can improve *in vivo* studies with MRI contrast agents.

Two methods are currently used to measure concentration of lanthanide chelates in *ex vivo* tissues. Inductively coupled plasma mass spectrometry (ICP-MS) provides outstanding measurement accuracy of concentrations of lanthanide ions as low as 1 ng/mL [14]. However, ICP-MS is relatively expensive, has limited availability at many research institutions, requires frequent calibration with known samples, and requires careful sample preparation and handling. A colorimetric test with xylenol orange, methyl thymol blue, or arsenazo dye can also be used to measure concentration of lanthanide ions as low as 8–50 μM depending on the pH and temperature of the sample [15–17]. These spectrophotometric methods are popular because spectrophotometers are relatively inexpensive and available at most research institutions. Yet colorimetric analyses require samples that are optically transparent except for the dye, which severely limits the ability to assess tissue samples for lanthanide chelate concentration.

The concentrations of lanthanide chelates have also been measured by employing the Evans method with a NMR spectrometer [18]. Paramagnetic lanthanide ions have an effective magnetic moment, μ_{eff} , that can cause a bulk magnetic susceptibility (BMS) shift of the solvent [19]. This shift in MR frequency can be compared to the shift of a solvent without the lanthanide ion, which is directly related to the concentration of the ion, $[\text{Ln}]$ (Equation (1)) [20]. In this relationship, T represents temperature and s is set to 1/3, $-1/6$, or 0 for a sample geometry that consists of a cylinder parallel to the main magnetic field, a cylinder perpendicular to the main field, or a sphere, respectively [21,22]. This relationship assumes that the measurement temperature is above the Curie-Weiss temperature and that the diamagnetic and the hyperfine shifts are negligible relative to the BMS shift, which is a good assumption for all paramagnetic lanthanide ions. Equation (1) also assumes that direct interactions between paramagnetic lanthanide chelates have negligible influence on the BMS shift, which has been shown to be a good assumption at practical concentrations [23]:

$$\Delta_{\chi} = \frac{1558s[\text{Ln}]\mu_{\text{eff}}^2}{T} \quad (1)$$

We investigated whether a protocol could be developed that can measure the BMS shift with NMR spectroscopy to accurately measure lanthanide ion concentrations in *ex vivo* tissues of animal models.

We evaluated the accuracies and precisions of measuring the concentrations of Gd(III), Dy(III), Tm(III), Eu(III), and Yb(III) ions and a Gd(III) chelate in solutions of 70% nitric acid. We tested conditions of the NMR spectrometer and sample that may affect the concentration measurement. After establishing correlations for these ions, we then performed similar evaluations with *ex vivo* rat liver and kidney tissues that were completely digested in 70% nitric acid. Our results establish a protocol and analytical criteria for measuring *ex vivo* concentrations of lanthanide-based MRI concentrations using the BMS shift.

2. Experimental Section

TmCl₃ hydrate was acquired from Strem Chemicals Inc. (Newburyport, MA, USA). EuCl₃, YbCl₃, DyCl₃, GdCl₃ were obtained from Acros Organics (Fair Lawn, NJ, USA). Bovine serum albumin and NaCl were purchased from Thermo Fisher Scientific Inc. (Waltham, MA, USA). ACS-grade, 68%–70% nitric acid was purchased from Mallinckrodt Chemical Inc. (St. Louis, MO, USA). Gadodiamide (Omniscan™, GE Healthcare Inc., Waukesha, WI, USA) was obtained from the Department of Radiology at Case Western Reserve University (Cleveland, OH, USA). Rat liver and kidney tissues were provided by the Small Animal Medical Imaging Services of the University of Arizona (Tucson, AZ, USA).

Stock solutions were prepared at 5 mM for GdCl₃, 10 mM for DyCl₃, and 50 mM for TmCl₃, EuCl₃, and YbCl₃ using distilled water. The concentration of each stock solution was verified with ICP-MS (Department of Geosciences, University of Arizona). A stock solution of gadodiamide was prepared at 5 mM concentration based on the concentration of the clinical product. A series of concentrations ranging between 0.1–5.0 mM for GdCl₃ and gadodiamide, 0.5–10 mM for DyCl₃, and 1.0–50.0 mM for TmCl₃, EuCl₃, and YbCl₃ were then created by serially diluting each stock with distilled water. To maintain accuracy, solutions with concentrations less than 5 mM were created with a final volume of 5 mL. Solutions with higher concentrations were created with a final volume of 1 mL. These samples were then frozen in liquid nitrogen and lyophilized for 24–48 h depending on the sample volume. Concentrated nitric acid was then added to the dried sample, using a volume of 5 mL for dilute samples and 1 mL for concentrated samples.

To test the effect of salt, samples at 15 mM TmCl₃ or 5 mM GdCl₃ were prepared with NaCl concentrations ranging from 40 mOsm/L to 300 mOsm/L, using a 1 Osm/L stock solution of NaCl and the TmCl₃ and GdCl₃ stock solutions listed above. In addition, samples ranging between 0.1–5.0 mM for GdCl₃ and 1.0–50.0 mM for TmCl₃ were prepared with NaCl at 300 mOsm/L. To test the effect of protein content, the same series of samples of TmCl₃ and GdCl₃ were prepared with 90 μM of albumin, using a 300 μM stock solution of albumin and the TmCl₃ and GdCl₃ stock solutions listed above.

Rat liver and kidney tissues were excised and placed into 10% neutral buffered formalin and stored at 4 °C before they were used for each tissue sample preparation. Rat kidney and liver tissue samples weighing 100 mg were tested, and the density of each tissue was assumed to be 1 g/mL to determine the volume of the tissue. Tissue samples that weighed 50, 100, 150, 200 and 250 gm were also tested. A stock solution of each lanthanide ion or gadodiamide was then added to a tissue sample, and diluted with distilled water, to create a range of tissue samples that ranged between 0.1–5.0 mM for GdCl₃ and gadodiamide, 0.5–10 mM for DyCl₃, and 1.0–50.0 mM for TmCl₃, EuCl₃, and YbCl₃. A final

volume of 5 mL was used for tissue samples with a concentration less than 5 mM, and tissue samples with a greater concentration were prepared with a final volume of 1 mL. The tissue samples were allowed to stand at room temperature for 30 min before lyophilization. Upon complete removal of water, the samples were suspended in 1 mL or 5 mL of conc. nitric acid for 3–5 h to allow for complete decomposition of the biological material.

A volume of 200 μ L of each sample was added to a clean 3 mm NMR tube, and this narrow NMR tube was then placed in a 5 mm NMR tube that contained 300 μ L of concentrated nitric acid as a reference solution. The heights of the sample volumes in the co-axial tubes exceeded the height of the NMR transceiver coil. Thus the sample approximated an infinite cylinder parallel to the static magnetic field of the NMR spectrometer, which provided the greatest BMS shift (*i.e.*, $s = 1/3$ in Equation (1)). Samples were equilibrated at each temperature before acquiring spectra. A one-dimensional NMR spectrum was acquired for each sample, with a 2.19 s repetition time; 7 μ sec excitation pulse; 12.5 ppm spectral width; 16,384 acquired data points; 0.114 Hz/point spectra resolution after zero-filling; and four repetitions with phase cycling. A deuterium lock was not used, because adding deuterium to the sample may have changed the BMS effect. Sample spinning was not used and shimming was not required, because the resulting lineshapes were sufficiently narrow and symmetric for accurately measuring the BMS shifts in each spectrum. The separation between the two spectral peaks was recorded in Hz to ensure measurement precision, and the Larmor frequency was used to convert this measurement to units of ppm. NMR spectra were recorded using a 300 MHz (7 T) Varian Unity+ spectrometer with an inverse transceiver probe, and a 600 MHz (14 T) Varian Inova spectrometer with an inverse transceiver cryoprobe. Measurements were acquired at 22.0 $^{\circ}$ C, except for some measurements performed at temperatures as high as 67.0 $^{\circ}$ C, using the calibrated temperature unit of the spectrometer.

For each tissue study, three samples at each concentration of lanthanide ion and gadodiamide were prepared and measured with BMS NMR spectroscopy to ensure reproducibility. The other studies were performed with only one sample per concentration of lanthanide ion and gadodiamide. The BMS shift measured for each tissue sample was converted to a concentration of lanthanide ion and gadodiamide using each calibration determined with lanthanide ion and gadodiamide solutions. The calculated concentrations were compared with the concentrations used during preparation of the sample for BMS NMR spectroscopic analyses.

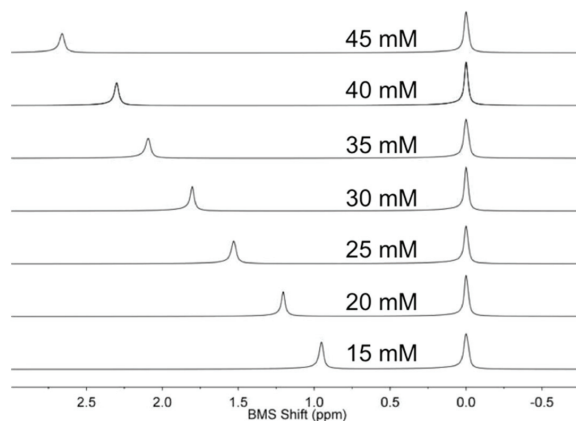
3. Results and Discussion

A variety of methods for preparing samples were initially tested, including combinations of burning tissue samples to ash in a 600 $^{\circ}$ C furnace, homogenizing tissue samples to a paste, and high-speed centrifugation that have been previously used to extract metals from tissues [24–26]. These methods provided disappointing 8%–10% yields of recovered lanthanide ion in tissues. Therefore, these other methods were abandoned when a simplistic treatment with nitric acid was found to provide excellent yields [27]. The nitric acid completely digested tissues within 20 min, resulting in clear solution with a yellow color.

NMR spectroscopy of the sample and control solution in co-axial tubes generated outstanding spectral results (Figure 1). An initial study demonstrated that the BMS shift was invariant within one

minute of inserting the sample in the magnet at 22.0 °C, indicating that the sample equilibrated from room temperature to 22.0 °C within one minute. The acquisition of the NMR spectrum required 8.76 s. Data processing and analysis required less than one minute. Therefore, the total time to analyze one sample was approximately two minutes. Thirty samples were routinely analyzed within one hour.

Figure 1. NMR spectra of coaxial samples of Tm(III) ion in nitric acid (left peak) and nitric acid without Tm(III) (right peak) were rapidly acquired and easily analyzed to measure the BMS shift of each sample.



The concentrations of each lanthanide ion and gadodiamide in nitric acid were linearly correlated with BMS shifts acquired at 7T magnetic field strength. (Figure 2a,b). The calibrations with Gd(III) and gadodiamide were identical, indicating that the nitric acid digested the chelator, or the chelator had negligible effect on the BMS shift. Gd(III), gadodiamide, and Dy(III) were analyzed using concentration ranges that were lower than the ranges used for the other lanthanide ions, because very high concentrations for Gd(III) and Dy(III) caused rapid T2 relaxation that led to substantial line broadening in the NMR spectrum. These correlations showed outstanding linearity with R² correlation coefficients greater than 0.98. The slope of each calibration was used to determine μ_{eff} for each lanthanide ion, which agreed with previously published results (Table 1; Equation (2)). This agreement validated that the concentration dependence of the measured chemical shifts arose from a BMS shift:

$$\mu_{eff}^2 = \frac{T}{519.3} \frac{\Delta\chi}{[Ln]} = \frac{T}{519.3} (slope) \quad (2)$$

Figure 2. Correlation of BMS shift and lanthanide ion concentration. **(a,b)** The correlation of BMS shift and concentration for each lanthanide ion or gadodiamide at 7 T magnetic field strength showed outstanding linearity with $R^2 > 0.98$. **(c,d)** The concentration dependence of BMS shift at 7 T (filled symbols) and 14 T (open symbols) for Tm(III) and Gd(III) showed that the calibration was independent of magnetic field strength.

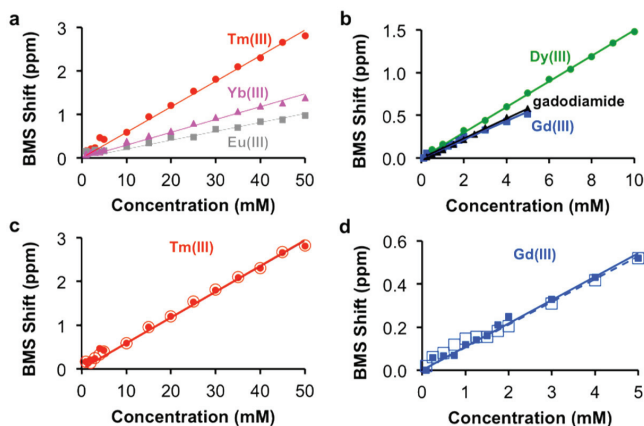
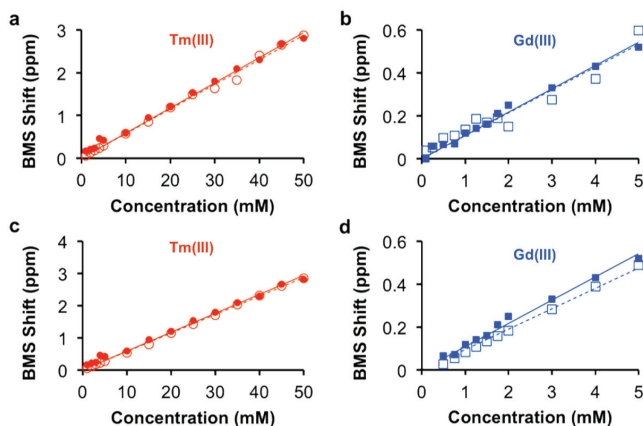


Table 1. Estimates of μ_{eff} from BMS shifts.

Lanthanide Ion	μ_{eff} (Figure 2a,b)	μ_{eff} (Figure 4a)	μ_{eff} ([22])
Dy(III)	10.38	---	10.6
Gd(III)	7.86	8.10	7.94
Tm(III)	6.56	7.54	7.6
Yb(III)	3.81	---	4.5
Eu(III)	3.18	---	3.40–3.51

This study with Tm(III) and Gd(III) samples at different concentrations was repeated at 14 T magnetic field strength, which generated the same calibration (Figure 2c,d). This result indicated that NMR spectrometers at any field strength may be used to measure lanthanide ion concentration via BMS shift measurements. The calibration of BMS shift with the concentration of Tm(III) or Gd(III) was not affected by the addition of 300 mOsm/L salt or 90 μ M protein (Figure 3). In addition, samples of 15 mM Tm(III) and 5 mM Gd(III) that had varying concentrations of salt generated identical BMS shifts (data not shown), which further verified that salt had no effect on the BMS measurement. These results indicated that estimates of lanthanide ion concentrations via BMS shift measurements with sample preparation using nitric acid could be translated to tissue samples that have high salt and protein contents.

Figure 3. Effect of sample conditions on the concentration-BMS shift calibration. The calibrations of (a) Tm(III) and (b) Gd(III) without (filled symbols) and with 300 mOsm/L NaCl (open symbols) showed that salt had a negligible effect on the concentration-dependent BMS shift. The calibrations of (c) Tm(III) and (d) Gd(III) without (filled symbols) and with 90 μ M albumin (open symbols) showed that proteins had a negligible effect on the concentration-dependent BMS shift.



The BMS shifts of Tm(III) and Gd(III) decreased with increasing temperature, as predicted by Equation (1) (Figure 4a). This result indicated that analyses of lanthanide ion concentrations should be conducted at lower temperatures to improve measurement precision. We elected to perform measurements at 22 °C, the lowest temperature tested in our studies, to avoid delays required to equilibrate the sample at lower temperatures. The values of μ_{eff} for Tm(III) and Gd(III) were estimated based on the dependence of the BMS shift on concentration and temperature (Table 1; Equation (3); Figure 4b). Once again, these estimates of μ_{eff} agreed with published results, which further validated that the BMS shift was the primary mechanism responsible for the differences in chemical shifts observed using NMR spectroscopy:

$$\mu_{eff}^2 = \frac{1}{519.3} \frac{T\Delta\chi}{[Ln]} = \frac{1}{519.3} (slope) \quad (3)$$

The concentrations of each lanthanide ion and gadodiamide in kidney and liver tissues treated with nitric acid were linearly correlated with BMS shifts acquired at 7T magnetic field strength. (Figure 5). These relationships had R^2 correlation coefficients greater than 0.96. These outstanding linear correlations with a 0 y-intercept indicated that endogenous metals such as iron had negligible effects on the BMS measurements. Furthermore, the average standard deviations from triplicate evaluations of each sample were less than 10%, and the great majority of standard deviations were much smaller than 10%, as evidenced by many error bars that are smaller than the size of the data symbol in Figure 5. These results demonstrated that the concentration of lanthanide ion or gadodiamide in tissues was measured with outstanding precision. In addition, the correlations for Gd(III) and gadodiamide were the same, which once again indicated that nitric acid digested the chelator

during tissue digestion, or the chelator had negligible effect on the BMS shift. Identical results were obtained using samples that ranged from 50 to 250 mg of tissue, indicating that the tissue volume did not influence the measurement precision (data not shown), which further verified that protein content within the processed solution did not influence the measurement of lanthanide ion concentration with BMS NMR spectroscopy.

Figure 4. Effect of temperature on the concentration-BMS shift calibration. (a) The greatest BMS shifts were observed at lowest temperatures. (b) The BMS shift, $\Delta\chi$, had a linear dependence on lanthanide ion concentration and inverse temperature, as predicted by theory (Equation (3)). Each line is labeled with its concentration in mM, with labels for data with solid symbols on the left and labels for data with open symbols on the right.

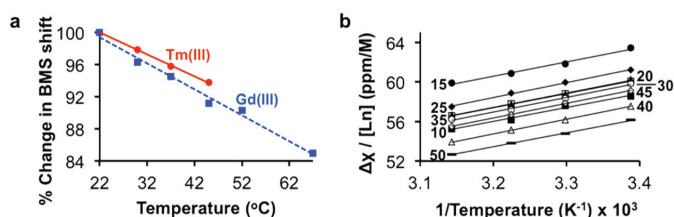
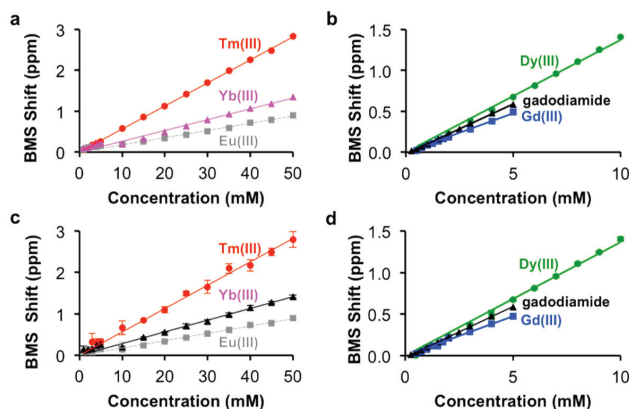


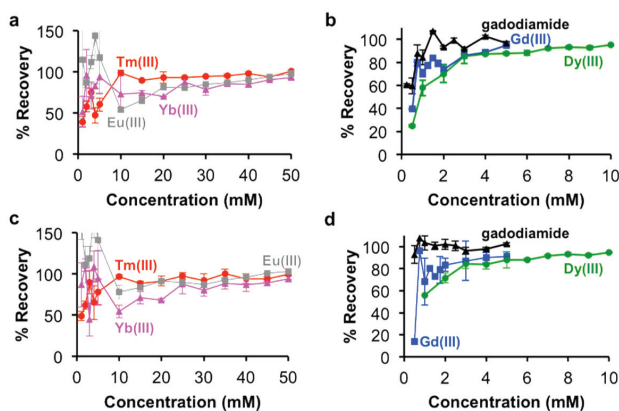
Figure 5. Correlation of BMS shift and concentration of lanthanide ion or gadodiamide in (a,b) rat kidney tissues and (c,d) rat liver tissues showed outstanding linearity with $R^2 > 0.97$.



The percent recovery of lanthanide ions from the tissue samples was determined by using the calibrations in Figure 2 to estimate the ion concentrations from the BMS shifts of the tissue samples (Figure 6). These results showed greater than 85% recovery with samples containing at least 3 mM with Gd(III), gadodiamide, or Dy(III), and greater than 80% recovery with samples containing at least 25 mM of Tm(III), Yb(III), and Eu(III). However, the recovery was less accurate for more dilute samples. This result reflects the difficulty in sample handling, which affects dilute samples to a greater extent than concentrated samples. In particular, the development of our methodology showed

that care needs to be taken to handle nitric acid without loss due to evaporation, which can be substantial over time and especially during outdoor transport in a southwest desert environment.

Figure 6. The recovery of lanthanide ions from (a,b) rat kidney tissues and (c,d) rat liver tissues. (a,c) At least 80% recovery was obtained for samples with ≥ 25 mM Tm(III), Yb(III), and Eu(III). (b,d) At in 85% recovery was obtained for samples with ≥ 3 mM Gd(III), gadodiamide, and Dy(III).



These results established a protocol for measuring the lanthanide ion concentration in *ex vivo* tissues. Nitric acid can be used to digest any tissue or lanthanide chelate, which allows this method to be applied to many biomedical studies. NMR spectrometers at any magnetic field strength are commonly available at many research institutions for a nominal usage fee. Many samples can be quickly analyzed with this method. As an additional benefit, the completely digested tissues are not biohazardous, which facilitates waste handling (however, care should be taken to properly dispose of samples with lanthanide ions).

Our results show that lanthanide ion content can be measured in *ex vivo* tissues with outstanding precision. In addition, accurate measurements can be made with concentrations ≥ 25 mM for Tm(III), Eu(III) or Yb(III), and ≥ 3 mM for Gd(III), gadodiamide, or Dy(III). Unfortunately, T1 and T2 MRI contrast agents typically accumulate in tissues at 10 μ M to 1 mM concentrations, and paramagnetic CEST agents likely accumulate in tissues at concentrations less than 10 mM. Therefore, the current concentration thresholds for accurate measurements are too high to apply this method for most biodistribution studies of MRI contrast agents. The lower yields at low concentrations are attributed to the loss of lanthanide ions or chelates during tissue processing. Therefore, improved tissue handling methods are warranted to facilitate this methodology. For example, extreme care is needed for handling and processing lanthanide chelates for optical imaging studies, and these careful handling methods may be adopted for measuring BMS shifts with NMR spectroscopy [28]. As an alternative, lyophilization of a large volume of tissue may be digested with a small volume of nitric acid, which would effectively concentrate the lanthanide ion in the acidic solution used for BMS NMR measurements. The volume of tissue that can be digested by 1 or 5 mL of nitric oxide (the volumes of acid used in this study) would need to be tested for each tissue type to assess the

improvement in detection sensitivity by using this approach. Also, the influence of concentrating endogenous metals such as iron would also need to be assessed.

Other biological and non-biological samples besides *ex vivo* tissues also require testing for lanthanide concentrations. For example, biosorption of lanthanide metals has been monitored in microbial species [29], plants [30], and biomass [31] to assess environmental quality and bioremediation. The concentrations of lanthanide metals are also assessed in soils [32,33] and stream waters [34,35], especially near mining sites and industrial complexes. These environmental assessments are likely to continue, considering the ~10%/year increase in lanthanide ore production to meet rising demands for glass polishing, catalysts, phosphors, magnets and electronic products [36]. As with the analyses of tissues in this report, the application of acid treatment and BMS shifts for measuring lanthanide concentrations in other samples will require consideration for the minimum detection level and/or consideration for concentrating the sample to meet the minimum detection level for accurate and precise measurements of lanthanide metal concentrations.

4. Conclusions/Outlook

The BMS shift was successfully used to measure the concentration of lanthanide ions and a MRI contrast agent, gadodiamide, in solution and within *ex vivo* tissue samples. Key steps in this process included the use of nitric acid to completely digest tissues, and the use of coaxial tubes for simultaneous NMR spectroscopy of experimental and control samples. The concentration dependence of the measured chemical shifts was shown to be due to the BMS shift. Although the methodology had outstanding precision, concentration measurements were accurate only for samples with higher concentrations. Improvements to sample handling during tissue processing are warranted to improve the accuracy of measuring lanthanide ion concentrations of more dilute samples.

Acknowledgments

This work was supported by the Phoenix Friends of the Arizona Cancer Center, and NIH grants R01 CA169774-01 and P50 CA95060. DVH was sponsored by the TRIF Fellowship Program of the University of Arizona. SIG was sponsored by the MARC Program of the University of Arizona through NIH grant T34 GM008718.

Conflicts of Interest

The authors declare no conflict of interest.

References

1. Runge V.M.; Muroff, L.R.; Wells, J.W. Principles of contrast enhancement in the evaluation of brain diseases: An overview. *J. Mag. Reson. Imag.* **2005**, *7*, 5–13.
2. Moriarty, J.M.; Finn, J.P.; Fonesca, C.G. Contrast agents used in cardiovascular magnetic resonance imaging: Current issues and future directions. *Am. J. Cardiovasc. Drugs* **2010**, *10*, 227–237.

3. Zhou, Z.; Lu, Z.R. Gadolinium-based contrast agents for magnetic resonance cancer imaging. *Nanomed. Nanobiotechnol.* **2013**, *5*, 1–18.
4. Stafford Johnson, D.B.; Prince, M.R.; Chenevert, T.L. Magnetic resonance angiography: A review. *Acad. Radiol.* **1998**, *5*, 289–305.
5. O'Connor, J.P.B.; Jackson, A.; Parker, G.J.M.; Jayson, G.C. DCE-MRI biomarkers in the clinical evaluation of antiangiogenic and vascular disrupting agents. *Brit. J. Cancer* **2007**, *96*, 189–195.
6. Dijkhuizen, R.M. Advances in MRI-Based detection of cerebrovascular changes after experimental traumatic brain injury. *Translat. Stroke Res.* **2011**, *2*, 524–532.
7. Geelen, T.; Paulis, L.E.M.; Coolen, B.F.; Nicolay, K.; Strijkers, G.J. Contrast-enhanced MRI of murine myocardial infarction—part I. *NMR Biomed.* **2012**, *25*, 953–968.
8. Gore, J.C.; Manning, H.C.; Quarles, C.C.; Waddell, K.W.; Yankeelov, T.E. Magnetic resonance in the era of molecular imaging of cancer. *Mag. Reson. Imag.* **2011**, *29*, 587–600.
9. Yoo, B.; Pagel, M.D. An overview of responsive MRI contrast agents for molecular imaging. *Front. Biosci.* **2008**, *13*, 1733–1752.
10. Sheth, V.R.; Pagel, M.D. CEST & PARACEST MRI Contrast Agents for Imaging Cancer Biomarkers. In *Molecular Imaging Probes for Cancer Research*; Chen, X., Ed.; World Scientific Publishing: Hackensack, NJ, USA, 2012, pp. 689–713.
11. Kuo, P.H.; Kanal, E.; Abu-Alfa, A.K.; Cowper, S.E. Gadolinium-based MR contrast agents and nephrogenic systemic fibrosis. *Radiology* **2007**, *242*, 847–849.
12. Buckley, D.L.; Parker, G.J.M. Measuring Contrast Agent Concentration in T1-Weighted Dynamic Contrast-Enhanced MRI. In *Medical Radiology—Diagnostic Imaging and Radiation Oncology*. Jackson, A., Buckley, D., Parker, G.J.M., Eds.; Springer: New York, NY, USA, 2005, pp. 69–79.
13. Ali, M.M.; Liu, G.; Shah, T.; Flask, C.A.; Pagel, M.D. Using two chemical exchange saturation transfer magnetic resonance imaging contrast agents for molecular imaging studies. *Acc. Chem. Res.* **2009**, *42*, 915–924.
14. Crayton, S.H.; Elias, D.R.; Al Zaki, A.; Cheng, Z.; Tsourkas, A. ICP-MS analysis of lanthanide-doped nanoparticles as a non-radiative, multiplex approach to quantify biodistribution and blood clearance. *Biomater* **2012**, *33*, 1509–1519.
15. Barge, A.; Cravotto, G.; Gianolio, E.; Fedeli, F. How to determine free Gd and free ligand in solution of Gd chelates. A technical note. *Contrast Media Mol. Imag.* **2006**, *1*, 184–188.
16. Brown, R.; Clarke, D.W.; Daffner, R.H. Is a mixture of gadolinium and iodinated contrast material safe during MR arthrography? *Am. J. Roentgenol.* **2000**, *175*, 1087–1090.
17. Rohwer, H.; Collier, N.; Hosten, E. Spectrophotometric study of arsenazo III and its interactions with lanthanides. *Anal. Chim. Acta.* **1995**, *314*, 219–223.
18. Evans, D.F. The determination of the paramagnetic susceptibility of substances in solution by nuclear magnetic resonance. *J. Chem. Soc.* **1959**, doi:10.1039/JR9590002003.
19. Peters, J.A.; Huskens, J.; Raber, D.J. Lanthanide induced shifts and relaxation rate enhancements. *Prog. Nucl. Mag. Reson. Spect.* **1996**, *28*, 283–350.

20. Corsi, D.M.; Platas-Iglesias, C.; von Békum, H.; Peters, J.A. Determination of paramagnetic lanthanide(III) concentrations from bulk magnetic susceptibility shifts in NMR spectra. *Mag. Reson. Chem.* **2001**, *39*, 723–726.
21. Gysling, H.; Tsutsui, M. Organolanthanides and Organoactinides. *Adv. Organomet. Chem.* **1971**, *9*, 361–395.
22. Gerothanassis, I.P.; Lauterwein, J. Oxygen-17 NMR spectroscopy: Referencing in diamagnetic and paramagnetic solutions. *Mag. Reson. Chem.* **1986**, *24*, 1034–1038.
23. Fossheim, S.; Johansson, C.; Fahlvik, A.K.; Grace, D.; Klaveness, J. Lanthanide-based susceptibility contrast agents: Assessment of the magnetic properties. *Mag. Reson. Med.* **1996**, *35*, 201–206.
24. Parker, M.M.; Humoller, F.L.; Mahler, D.J. Determination of copper and zinc in biological material. *Clin. Chem.* **1967**, *13*, 40–48.
25. Schulten, H.R.; Ziskoven, R. Determination of thallium in brain tissue of the mouse by stable isotope dilution and field desorption mass spectrometry. *J. Physiol.* **1978**, *284*, 170P–171P.
26. Dos Santos, W.P.C.; Hatje, V.; da Santil, D.; Fernandes, A.P.; Korn, M.G.A.; de Souza, M.M. Optimization of a centrifugation and ultrasound-assisted procedure for the determination of trace and major elements in marine invertebrates by ICP OES. *Microchemical. J.* **2010**, *95*, 169–173.
27. O'Brien, R.D. Nitric acid digestion of tissues for liquid scintillation counting. *Anal. Biochem.* **1964**, *7*, 251–254.
28. Josan, J.S.; de Silva, C.R.; Yoo, B.; Lynch, R.M.; Pagel, M.D.; Vagner, J.; Hruby, V.J. Fluorescent and lanthanide labeling for ligand screens, assays, and imaging. *Meth. Mol. Biol.* **2011**, *716*, 89–126.
29. Andres, Y.; Thouand, G.; Boulalam, M.; Mergeay, M. Factors influencing the biosorption of gadolinium by microorganisms and its mobilisation from sand. *Appl. Microbiol. Biotech.* **2000**, *54*, 262–267.
30. Anan, Y.; Awaya, Y.; Ogihara Y.; Yosida, M.; Yawata, A.; Ogra, Y. Comparison in accumulation of lanthanide elements among three brassicaceae plant sprouts. *Bull. Environ. Contam. Toxicol.* **2012**, *89*, 133–137.
31. Parsons, J.G.; Peralta-Videa, J.R.; Tiemann, K.J.; Saupe, G.B.; Gardea-Torresdey, J.L. Use of chemical modification and spectroscopic techniques to determine the binding and coordination of gadolinium(III) and neodymium(III) ions by alfalfa biomass. *Talanta* **2005**, *67*, 34–45.
32. Vodyanitskii, Y.N.; Savichev, A.T. Lanthanides in Soils: X-ray Determination, Spread in Background and Contaminated Soils in Russia. In *Geochemistry: Earth's System Processes*; InTech: New York, NY, USA, 2012; pp. 389–412.
33. Shumilin, E.; Rodriguez-Figueroa, G.; Sapozhnikov, D. Lanthanide contamination and lanthanide concentration and strong positive Europium Anomalies in the Surface Sediments of the Santa Rosalia Copper Mining Region, Baja California Peninsula, Mexico. *Bull. Environ. Contamin. Toxicol.* **2005**, *75*, 308–315.
34. Neal, C. Rare earth element concentrations in dissolved and acid available particulate forms for eastern UK rivers. *Hydrol. Earth Syst. Sci.* **2007**, *11*, 313–327.

35. Protano, G.; Riccobono, F. High contents of rare earth elements (REEs) in stream waters of a Cu-Pb-Zn mining area. *Environ. Pollut.* **2002**, *117*, 499–514.
36. Naumov, A.V. Review of the world market of rare-earth metals. *Russ. J. Non-Ferrous Metals* **2008**, *49*, 14–22.

Magnetic Resonance Imaging of Ischemia Viability Thresholds and the Neurovascular Unit

Philip A. Barber

Abstract: Neuroimaging has improved our understanding of the evolution of stroke at discrete time points helping to identify irreversibly damaged and potentially reversible ischemic brain. Neuroimaging has also contributed considerably to the basic premise of acute stroke therapy which is to salvage some portion of the ischemic region from evolving into infarction, and by doing so, maintaining brain function and improving outcome. The term neurovascular unit (NVU) broadens the concept of the ischemic penumbra by linking the microcirculation with neuronal-glia interactions during ischemia reperfusion. Strategies that attempt to preserve the individual components (endothelium, glia and neurons) of the NVU are unlikely to be helpful if blood flow is not fully restored to the microcirculation. Magnetic resonance imaging (MRI) is the foremost imaging technology able to bridge both basic science and the clinic via non-invasive real time high-resolution anatomical delineation of disease manifestations at the molecular and ionic level. Current MRI based technologies have focused on the mismatch between perfusion-weighted imaging (PWI) and diffusion weighted imaging (DWI) signals to estimate the tissue that could be saved if reperfusion was achieved. Future directions of MRI may focus on the discordance of recanalization and reperfusion, providing complimentary pathophysiological information to current compartmental paradigms of infarct core (DWI) and penumbra (PWI) with imaging information related to cerebral blood flow, BBB permeability, inflammation, and oedema formation in the early acute phase. In this review we outline advances in our understanding of stroke pathophysiology with imaging, transcending animal stroke models to human stroke, and describing the potential translation of MRI to image important interactions relevant to acute stroke at the interface of the neurovascular unit.

Reprinted from *Sensors*. Cite as: Barber, P.A. Magnetic Resonance Imaging of Ischemia Viability Thresholds and the Neurovascular Unit. *Sensors* **2013**, *13*, 6981–7003.

1. Introduction

Evolution of brain damage due to stroke is a highly complex process, involving cerebrovascular and parenchymal tissues through the interaction of multiple mechanisms. Neuroimaging has contributed considerably to the understanding the pathophysiology of stroke in living animals and humans, and has been the keystone to therapeutic advancement for stroke care [1]. The concept of the *ischemic penumbra* and *infarct core* in the early 1970s has transcended from a basic understanding of ischemic core and salvageable ischemic brain based on the observation of anoxic depolarization and energy metabolism [2]. Recently, this compartmentalized concept has incorporated important processes at the level of the microvasculature following cerebral ischemia. The ischemic penumbra implies the basic premise that acute stroke therapy can salvage some portion of the ischemic region from evolving into infarction and by doing so maintaining brain function and improving outcome [1].

The concept of the Neurovascular Unit (NVU) incorporates critical and metabolic tissue viability thresholds with cellular interactions involving endothelium, with astrocytes, and neurons with the blood brain barrier (BBB) and extracellular matrix. Under physiological conditions the BBB provides the critical, physical, metabolic, and neurological barrier that separates the CNS from the peripheral circulation [3]. Focal cerebral ischaemia, as is observed in acute stroke, is responsible for the loss of endothelial cell integrity resulting in an increase of vascular permeability [4]. The disruption of the BBB results in the formation of a vasogenic oedema, which causes further damage in the surrounding tissue, especially when associated with hemorrhagic transformation [5]. Several mediators may contribute to the stroke-induced alterations of the BBB: reactive oxygen species (ROS) [6,7], platelet activating factor, tumour necrosis factor- α [8], vascular endothelial growth factor [9], and matrix metalloproteinases [10].

Positron emission tomography (PET) translated the early concept of the penumbra by visualizing the relationship of cerebral blood flow changes to the metabolic demands of ischemic tissue. This initial step of translating electrophysiological observations to human imaging was followed by further iterations in the evolution of clinical imaging paradigms that has transformed the concept of the penumbra to one of “mismatch” between ischemic core and potentially salvageable tissue by clinically available technologies-MRI and computed tomography [11,12]. With the help of this imaging technology came refinements in selecting, for clinical trials, patients for therapeutic intervention for acute stroke with thrombolysis and endovascular therapy. Such advanced neuroimaging techniques have been studied in clinical trials [12–15].

Despite inclusion of increasingly sophisticated neuroimaging there has been a failure of numerous neuroprotective clinical trials. This has led to the realization that refinements to the imaging of ischemic injury is needed to visualize additional aspects of the complex process of stroke, that includes imaging assessment of cerebrovascular and parenchymal tissue. The introduction of the NVU offers a conceptual and practical approach, which fundamentally links the integrity of the microvessel with neuronal and glial interactions [16,17]. From a therapeutic perspective this unitary conceptual framework implies that there will be limited recovery of function unless blood flow is re-established and all parts of the unit recover because of the ischemic vulnerability of individual sensitive components of the unit [17,18]. Biological understanding of the processes of ischemia and the NVU has now developed through technological advancements in molecular biology and *in vivo* imaging including non-invasive imaging techniques. Recent work with MRI has evolved from imaging ischemic viability to include imaging of the microvasculature, specifically pathological processes resulting in BBB dysfunction, and concurrent molecular and cellular inflammatory events [19,20]. This review focuses on stroke related pathophysiological processes that can be currently imaged, describing the shortcomings of each. The unmet needs of currently available imaging modalities are identified that may be achieved in the future with more sophisticated molecular imaging.

2. Basic Mechanisms of Stroke

Acute cerebral ischemia occurs following mechanical occlusion of cerebral blood vessels, usually by embolus [21]. When blood flow to the brain is reduced survival of brain tissue depends on the

intensity and duration of the ischemia and the availability of collateral blood flow. During moderate to severe cerebral ischemia, autoregulation is impaired. This has allowed investigators to reduce cerebral blood flow (CBF) and assess the critical flow thresholds for certain functions. At blood-flow levels around 20 mL/100 g/min, the oxygen extraction fraction (OEF) becomes maximal, the cerebral metabolic rate for oxygen (CMRO₂) begins to fall [22]. Normal neuronal function of the cerebral cortex is affected, and cortical electroencephalographic activity ceases [23]. This degree of ischemia represents a viability threshold defined as the *loss of neuronal electrical function*. At levels below 10 mL/100 g/min, cell membranes and function are severely affected [24]. At this threshold, lack of oxygen inhibits the mitochondrial metabolism and activates the inefficient anaerobic metabolism of glucose causing a local rise in lactate production and so a fall in pH, leading to intra- and extracellular acidosis. The energy dependent function of the cell membrane to maintain ion homeostasis becomes progressively impaired. Potassium ions leak out of cells into the extracellular space, Na⁺ and water enter cells (cytotoxic oedema), and Ca²⁺ enters the cell, where it impairs mitochondrial function and compromises intracellular membranes to control subsequent ion fluxes, leading to further cytotoxicity. This degree of ischemia represents a *threshold of loss of cellular ion homeostasis*.

These two concepts of critical thresholds of electrical and membrane failure define upper and lower flow limits of the ischemic penumbra, a fundamental component of the concept being that penumbra tissue is reversibly injured [2,24] but this is dependent on both the severity and the duration of ischemia; with increasing time the infarct core grows into the penumbra (Figure 1) [25,26]. From a pragmatic perspective the penumbra is also characterized by a response to pharmacological agents [14]. However, recent studies of functional and metabolic disturbances suggest a more complex pattern of thresholds. During the initial few hours of vascular occlusion, different metabolic functions breakdown at varying CBF levels. At declining flow rates in both global and focal models of ischemia, protein synthesis is first inhibited in neurons, followed by anaerobic glycolysis, the release of neurotransmitters, impaired energy metabolism, and finally membrane depolarization [27]. Mechanisms that give rise to ischemic cell death occur via three major mediators: unregulated increases of Ca²⁺ concentration intracellularly, tissue acidosis, nitric oxide and free radical production. In the early phases of ischemia, the injury is compromised by waves of spreading depression that further compromise regional CBF. In the minutes, hours, days after this initial ischemic insult, brain injury is modulated by: inflammatory processes, the induction of immediate early genes, free radicals, and later by apoptotic mechanisms [28].

Figure 1. (A) Cerebral Blood Flow and Metabolic Thresholds. With falling Cerebral Perfusion Pressure (CPP) as occurs distal to a cerebral artery occlusion, intracranial arteries dilate to maintain CBF- a process termed autoregulation. This results in an increase in Cerebral Blood Volume. When vasodilation is maximal, further falls in CPP result in a fall in CBF and results in increase in Oxygen Extraction Fraction (OEF) to maintain tissue oxygenation. When OEF is maximal further falls in CPP lead to reduction in Cerebral Metabolic Rate for Oxygen utilization (CMRO₂). **(B)** The combined effects of residual CBF and duration of ischemia on reversibility of neuronal dysfunction during focal ischemia. The gray shaded region outlines the limits of severity and duration of ischemia, distinguishing tissue “not at risk” from functionally impaired tissue. Schematics are drawn from concepts attributed to Baron and Heiss *et al* [25,26].

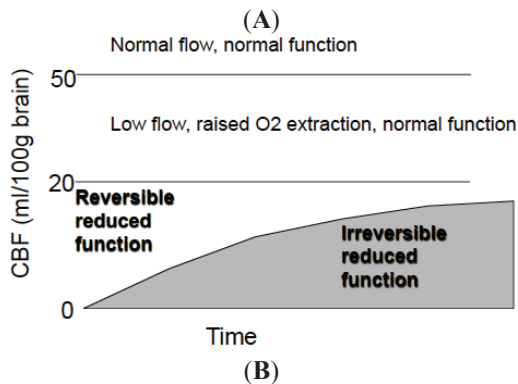
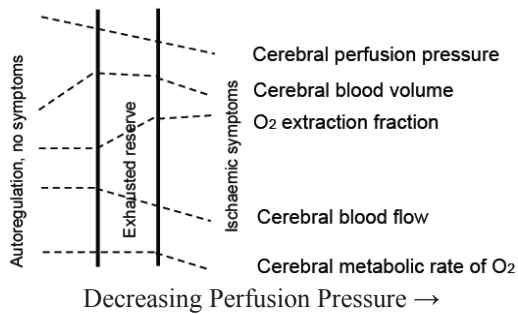
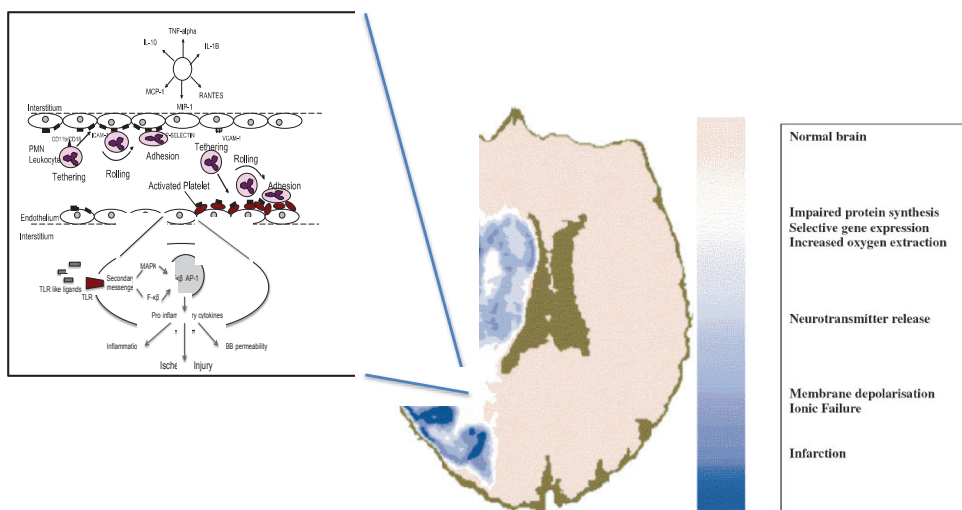


Figure 2. Two conceptual frameworks of Ischemic Stroke: the Penumbra and the Neurovascular Unit. The heterogeneity of the ischemic penumbra is illustrated. From the onset of focal ischemia the core and the penumbra are dynamic in space and time. A region of low perfusion in which cells have lost their membrane potential (core) is surrounded by an area in which intermediate perfusion prevails (penumbra) and cells depolarize intermittently. The CBF and metabolic viability thresholds (scale on right of figure) identify reversible and irreversibly injured tissue. The potentially reversible injury is modified by microvascular cellular and molecular responses at the level of the neurovascular unit (NVU, inset figure on left), mechanisms that include vasogenic oedema, BBB dysfunction and hemorrhagic transformation. During ischemia endothelial cells express PAR1, tissue factor (TF) and matrix metalloproteinases (MMPs). Together these facilitate the endothelial inflammatory response causing aggregation of platelets, fibrin degradation and leukocyte recruitment. These phenomenon potentially contribute to microvascular “no reflow”. Also leukocytes adherent to endothelium can cause endothelial dysfunction, transvascular protein leakage and oedema, leading to brain injury. MMPs contribute to the degradation of extracellular matrix causing an increase in BBB permeability. Endogenous ligands from damaged cells cause the expression of Toll Like Receptors (TLRs). Through complex signaling pathways pro-inflammatory cytokines are produced via transcription factors such as NF κ B and AP-1.



The microvasculature responds very quickly to the changes in CBF, and when critical thresholds are reached, endothelial cells rapidly convert into a pro-inflammatory and pro-thrombotic state by the up regulation of various humoral intermediaries, such as proteinase activated receptor 1 (PAR 1), endothelial tissue factor and matrix metalloproteinases (MMPs) [29,30] in the ischemic core and penumbra which facilitate inflammation and BBB dysfunction [31–33]. This process facilitates the accumulation of fibrin, platelets and neutrophils, which results in micro vascular obstruction. Matrix metalloproteinases degrade the neurovascular matrix on the abluminal side causing acute BBB

disruption. The release of endogenous ligands from damaged cells leads to the activation of Toll Like Receptors (TLRs). Their signaling causes several mediators to promote the production of pro-inflammatory cytokines via the activation of transcription factors such as NF- κ B and AP1, perpetuating a cycle of neurovascular damage (Figure 2) [34–36]. Endothelial cells facilitate selective leukocyte recruitment by a sequence of interactions with brain endothelial cell adhesion molecules [37,38], controlling leukocyte rolling, tethering, and adhesion along endothelial cells. Ultimately, leukocytes transmigrate from the luminal to the abluminal side of the endothelial layer. One consequence of these events is that microvessels become obstructed within the territory-at-risk, with focal loss of permeability barriers and changes in endothelium-astrocyte-neuron relationships. The obstruction is most prominent in end arteries, for instance, the microvasculature of the striatum [39,40]. Activated platelets and fibrin, caused by the generation of thrombin, are also inherently involved in the microvessel obstruction. The microvessel wall undergoes rapid and dynamic change affecting matrix integrity of the basal lamina and matrix receptors. The change is concomitant with neuronal injury. Also, at this time the expression of the matrix constituents (basal lamina, laminin, collagen IV, cellular fibronectin, and perlecan) decrease substantially [41,42]. It has also been established that endothelial and astrocyte cytoskeletal structures are compromised by a decrease in endothelial cell β_1 -integrin receptor and integrin $\alpha_6\beta_4$ on astrocyte end-feet in the first hour following middle cerebral artery (MCA) occlusion [40–43].

3. Imaging Tissue Viability during Ischemia

The imaging surrogates of infarct core should reflect histological markers of irreversible cellular injury, unresponsive to increases of blood flow during reperfusion or dynamic changes of flow in and around the injury. They should also reflect what we understand from the pathophysiology that with time the core enlarges and the severity increases [43,44]. Markers to assess morphological integrity achieved in experimental studies are predicated on invasive procedures, and therefore such markers cannot be determined in humans [44]. There are several challenges for imaging penumbra in human beings: (1) most techniques used clinically do not provide information about tissue viability; and, (2) ischemia is a highly dynamic process and physiological variables can only be measured at a few discrete time points and repeated measures are extremely challenging in contrast with animal experiments.

The identification of penumbra necessitates measuring reduced CBF less than the functional threshold and biochemically differentiating morphologically viable from dead brain tissue. An early demonstration of the functional threshold was demonstrated in monkeys exposed to focal cerebral ischemia [45]. A reduction in blood flow following middle cerebral artery occlusion led to the developmental of a neurological deficit at flow rates of 23 mL/100 g of brain per minute, and if lowered further caused irreversible paralysis at blood flow rates of 8 mL/100 g per minute [45]. This observation confirmed the concept of CBF viability thresholds but considerable variability exists determined by complex interactions dependent on the functional threshold of individual neurons, age of subject, and brain location (grey vs. white matter) [46,47]. Biochemical substrate biomarkers show similar thresholds but the pattern is more complex and the CBF values fall within a wider range; with declining flow rates in the range of 15–35 mL/100 g of brain per minute, protein synthesis is inhibited followed by

the preference for an aerobic glycolysis at 35 mL/100 g of brain per minute, followed by the release of neurotransmitters and the impairment of energy metabolism at around 20 mL/100 g of brain per minute. Finally, terminal depolarization and concomitant potassium influx is observed at 6–15 mL/100 g of brain per minute [27].

The use of positron emission tomography (PET) in human subjects has been aimed at identifying irreversibly damaged and ischemically compromised brain. PET utilizing 15-oxygen tracers are considered to provide the reference standard for the CBF measurements [9,48–50]. The imaging paradigm clinically has been a CBF measure combined with metabolic surrogates of tissue viability signaling permanent tissue destruction. PET using 15 oxygen tracers allows quantitative assessment of CBF, cerebral metabolic rate of oxygen (CMRO₂), oxygen extraction (OEF) and cerebral blood volume (CBV), independently measuring perfusion and energy metabolism and demonstrating the uncoupling of each at discrete time intervals following ischemia (Figure 1). The core is defined by reduced CBF and CMRO₂, and the penumbra as a region beyond this where CBF is reduced, but OEF is increased and CMRO₂ is normal.

Understanding the limitations of a single cerebral blood flow threshold has evolved from PET imaging in focal ischemia and this knowledge base could be applied to more conventional clinical imaging paradigms like CT and MRI. Five main factors account individually to the variance of the PET acquired data: blood flow discrepancies between grey and white matter, age determinants, methodological variability related to blood flow between regions of interest (ROI), voxel-based analysis (VBA), and duration of ischemia as an independent predictor of tissue viability. Blood flow measurements are dynamic represented visually in the clinical scenario at variable time points without knowledge of CBF before or after. This contrasts dramatically with the relatively controlled environment of animal experiments; in humans the duration of ischemia cannot be controlled, nor the site of occlusion, nor the location of ischemia.

During ischemia OEF compensates for the ischemic challenge by increases of up to 80% compared to approximately 30% in the resting state [50]. This elevation of OEF along with reduction of CBF can discriminate the ischemic compartments of non-viable tissue *vs.* penumbra. The combination of OEF and CBF x arterial oxygen content is CMRO₂. Data supports that CMRO₂ is the preferred marker to delineate infarcted from viable tissue [50]. However, there are logistical challenges with obtaining OEF measurements, as the technique requires a steady-state inhalation approach, which makes it impractical for imaging stroke patients. However, alternative techniques have been successfully developed; these include ¹¹C-flumazenil (FMZ) and ¹⁸F-fluoromidoanzol (F MISO). ¹¹C-FMZ is a marker of cortical neuronal integrity and may be a reliable surrogate of ischemic core capable of delineating penumbra in combination of ¹⁵O-water PET [18,46,51,52]. F MISO is a marker of hypoxic tissue that may allow direct visualization of hypoxia impairment [53].

There are other limitations with PET imaging. Many clinical studies recruited small numbers of subjects, providing data on blood flow, metabolic values, and final infarction [46,54–56]. These studies have shown that two variables are consistently correlated with respect to viability, namely contemporaneously measured CBF and CMRO₂ utilization. However, the identification of CBF values corresponding to metabolic determinants of tissue viability values of infarcted *vs.* non-infarcted penumbra tissue is a matter of controversy; CBF values are dependent on the separation

of cortex and white matter, measurement error at low trace levels and methodological differences between applied region of interest techniques vs. voxel-based analysis [50]. Given the PET limitations, preliminary MR methods have been developed to image OEF and CMRO₂ in animals and humans [57–59].

Figure 3. CT and MR imaging for an acute stroke patient (76-year-old female). **(A)** The CT image shows slight hypointensity in the left anterior insular ribbon, as indicated by the yellow arrow. The apparent loss of structural definition suggests ischemia in the middle cerebral artery (MCA) territory; **(B)** DWI image shows very hyperintense areas interpreted as a region of infarction; **(C)** ADC map shows decreased diffusion of water in absolute units within the markedly hyperintense DW region; **(D)** Time-to-peak (TTP) map calculated from a DSC perfusion sequence showing delayed flow to ischemic region; **(E)** Cerebral blood flow (CBF) map computed using deconvolution with an arterial input function as a reference, and then calibrated to white matter in the contralateral side to provide a semi-quantitative depiction of blood flow; **(F)** FLAIR image from day 30 follow-up MR exam shows final infarct to match closely with acute infarct. There was a delay time of 1.2 h from stroke onset to CT imaging, and an additional delay of 2.6 h to MR imaging. The patient was treated with intravenous tPA 1.5 h after onset—before the MR exam. DWI typically depicts infarction with greater lesion contrast as is the case here. The lack of a distinct perfusion-diffusion mismatch and no evident growth on follow-up may be at least partly attributable to recanalization occurring as a result of tPA administration (courtesy of Robert K Kosior, University of Calgary).

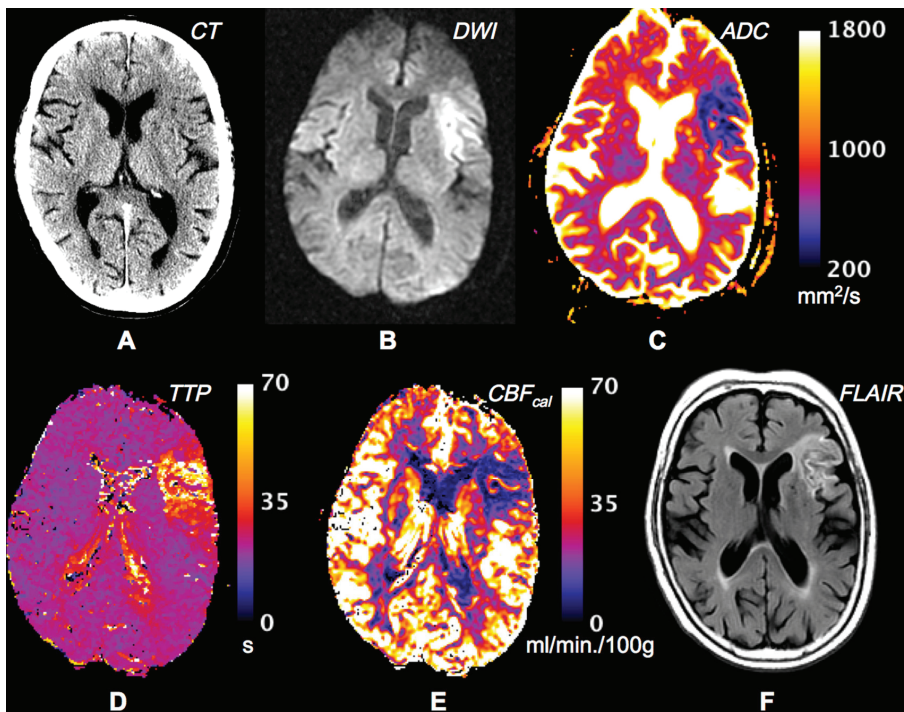


Figure 4. Co-registered PET and DW Images from an ischemic stroke patient. Figure 4A illustrates the main finding that the DWI lesion contains both core and penumbral tissue. Row 5 illustrates the core (CMRO2, CBF) and penumbra (OEF) voxels (*red* and *green* contours, respectively) with the DWI ROI superimposed (*black* contours). As expected, the relative proportion of penumbra was highest at the dorsal- and ventral-most regions of the middle cerebral artery territory, and lowest in its centre. In Figure 4B Co-registered day 30 high-resolution spoiled gradient echo sequence scan show final infarct (equivalent slices to Figure 4A). Superimposed are the PET core defined by CMRO2 and CBF (*red*) and penumbra defined by OEF (*green*). The PET-derived ROIs were interpolated to the higher-resolution magnetic resonance image. Visual assessment confirms that, bearing in mind a 95% probabilistic threshold, the core ROI translates into infarcted tissue, whereas the penumbra ROIs (as expected) have a mixed outcome, which would fit with the documented associated clinical improvement of the patient from an NIHSS of 16 to 9. Comparing the DWI lesion ROI from Figure 4A, it can be seen that most of it progresses to infarction, but note the variable DWI lesion intensity. In these images, the right hemisphere is on the right. Modified and reproduced with permission [60].

(A)

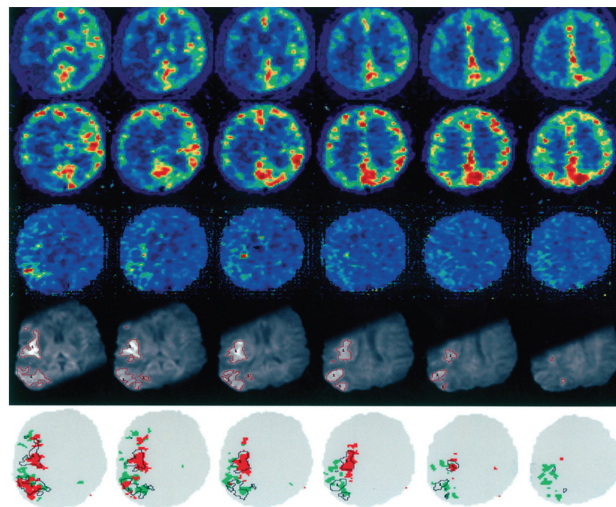
Cerebral Blood Flow (CBF)

Cerebral Metabolic Rate of
Oxygen (CMRO2)

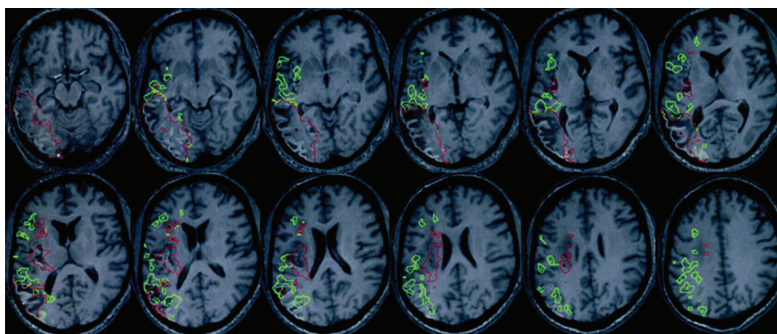
Oxygen Extraction Fraction
(OEF)

Diffusion Weighted Imaging

Core (red voxels) and penumbra
(green voxels)



(B)



4. MRI Perfusion/Diffusion “Mismatch”

The introduction of MR diffusion-weighted imaging (DWI) and perfusion-weighted imaging opened a new era of stroke imaging and a second evolution of imaging technology was conceived from the PET based concept of penumbra to the MR based concept of mismatch. The term mismatch applies a two-compartment approach: the infarct core is delineated on maps of DWI intensity or the apparent diffusion coefficient (ADC), and the area of low perfusion is delineated on maps of perfusion-weighted imaging (Figure 3) [61–63]. The volumetric difference of normal appearing tissue on DWI and hypoperfusion on perfusion-weighted imaging is termed “mismatch” between these two maps. The mismatch is considered at risk of infarct growth without reperfusion and shows characteristics of the penumbra. To support the concept it has been shown that the core volume correlates with stroke severity and predicts large parts of the final infarcted tissue and the rescue of so-called penumbral tissue correlates with clinical improvement [64–67]. Two types of study methodology have been used to validate the mismatch hypothesis: the first method has reviewed DWI/PWI magnetic resonance imaging to define imaging patterns that show irreversibly infarcted tissue vs. salvageable tissue in the presence or absence of reperfusion. This approach utilizes large patient numbers but the longitudinal design of these studies is limited by the absence of CBF data between imaging time points [50]. The second and alternative approach that has been undertaken has compared MR findings with a “gold standard” reference method typically PET (Figure 4). Recent clinical trials using the mismatch paradigm to select patients treated with thrombolysis did not show superior outcome, further questioning the validity and utility of the paradigm for making clinical stroke management decisions [1,12,14,68]. The mismatch concept can be scrutinized by asking two broad questions: (1) Does diffusion-weighted imaging identify ischemic core; (2) Can MR mismatch reliably identify the ischemic penumbra?

(1) Does diffusion-weighted imaging identify ischemic core?

The Apparent Diffusion Coefficient (ADC) quantifies the diffusibility of water and absolute thresholds of ADC reduction have been quoted as an absolute viability threshold in the controlled environment of animal stroke models but not humans. Clinically the timing of the ADC measurement is critical to its interpretation as it normalizes and then increases over time. It is also recognized that there is regional tissue susceptibility reflected by a variance of vulnerabilities; reduction of ADC in the striatum correlated with reduced ATP and tissue necrosis. The response of ADC upon reperfusion is an observed return of the ADC toward normal values [69,70]. There are numerous examples in the clinical literature that support that that ADC is reversible under the circumstances of prompt reperfusion, but as yet there is no agreed upon standard ADC value that predicts final infarct size. Despite potential ambiguity in interpreting DWI changes, [71,72] regions of DWI hyperintensity currently provide the best estimate of infarct core and often correspond well to regions of permanent damage.

T2-weighted imaging is sensitive to inter-parenchymal water accumulation, and increased T2 becomes apparent within several hours. T2 has become generally accepted as a reliable technique to predict an ischemic lesion beyond the acute stages. It correlates with histological measures of hemispheric swelling and the area of infarction by TTC and H&E histological sections [73]. The detection of increased intensities in T2 weighted images within first 10 hours of stroke onset

represents tissue destined for final infarction and is a robust marker of final infarction demonstrated histopathologically [74]. However, again the infarct size defined by T2 is dependent on time because the maximum T2 response occurs within 48 hours, and beyond this time point dramatic changes in both size and the heterogeneity of the hyperintense T2 region occurs reflecting heterogeneous pathology in the regenerative phase of the stroke injury [74]. By acquiring different combinations of MRI signal (ADC, T2) complementary information can be gathered about the histopathological injury correlate. Reduced ADC in the presence of normal T2 may imply a less severe injury (sub lethal) consisting of compromised tissue without significant increased blood brain barrier permeability. On the contrary, the presence of an elevated T2 value may reflect more severely damaged tissue (lethal) [74–76].

(2) Can MR mismatch reliably identify the ischemic penumbra?

Dynamic contrast perfusion-weighted imaging uses bolus tracking techniques and intravenous administration of paramagnetic contrast agents. Different curve patterns can be derived with or without deconvolution using an arterial input function obtained from large intracranial vessels such as the middle cerebral artery [77]. There are fundamental limitations with this approach. Time-to-peak (TTP), a single measure of arrival of contrast agent, does not represent the hemodynamic principle of CBF. There are other limitations. Hitherto, there is no consensus which perfusion map (TTP, relative Mean Transit Time (MTT), CBF, T_{MAX}) most accurately identifies hypoperfusion and infarct growth or response to thrombolysis [78]. Also, superiority of deconvolved maps compared to non-deconvolved maps has not shown to be superior in clinical studies [79,80].

To differentiate penumbra from benign hypoperfusion (oligemia) a visual analysis is inadequate. Numerous MRI thresholds have been used, including relative TTP, relative MTT, CBF and T_{MAX} [69,79–81]. Studies that have compared PET and MR thresholds have shown large variability of a calculated mismatch according to TTP and CBF which consistently over-estimates penumbra [80,82]. A recent study shows greater concordance of MR perfusion thresholds with PET thresholds. Increase in the TTP threshold has partially improved results [82]. One of the major problems encountered is the large inter-individual variability. For the mismatch concept to be generalizable there has to be conformity on the definition applied. Up to 49 different definitions for MR mismatch and CT penumbra have been applied in the literature to date [83]. Comparative PET and MRI studies attempted to validate the mismatch hypothesis, finding that mismatch overestimated the penumbra [60,82]. There was also no agreement on the percentage of mismatch required for therapeutic decisions. The way forward for the mismatch concept has been compromised by small, unblinded studies and the absence of data from large randomized controlled trials. An arbitrary use of a volumetric difference between diffusion lesion and perfusion lesion of 20% has been used in many studies without scientific basis [50]. This is a concern because in the clinical setting patients could be inappropriately stratified by a surrogate measure of penumbra that has not been validated. Furthermore, the mismatch phenomenon may simply be difficult to identify because the penumbra determined using a single flow threshold is not capable of representing the complexity of the physiological condition. Despite these issues, proponents note that most of these studies were

performed with early non-quantitative methods. More recent trials suggest there may be utility for penumbral selection when using automated, standardized, and quantitative techniques [12,84].

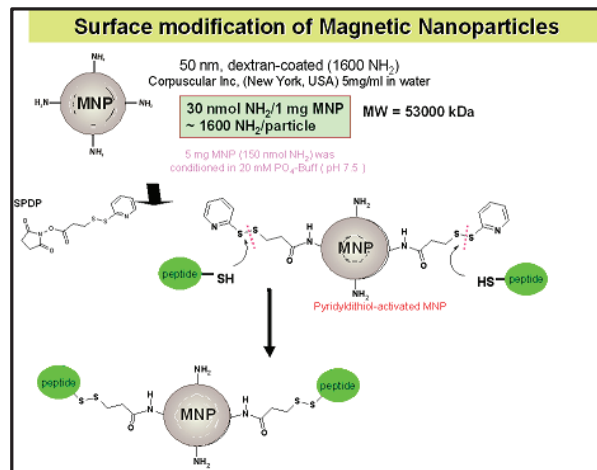
5. Imaging of the Neurovascular Unit Dysfunction (NVU)

It has been acknowledged that understanding injury at the NVU following ischemia reperfusion is fundamental to therapeutic advancement for stroke. To date, tissue plasminogen activator (tPA) is an effective yet vastly underused treatment for acute ischemic stroke associated with several limitations to its use. First, the six-fold increase in morbidity and four-fold increase in fatality related to tPA-induced hemorrhagic transformation have deterred physician use of the therapy [85]. Second, current guidelines on thrombolysis post-stroke with tissue plasminogen activator exclude its use when time of onset is unknown [13]. Most patients do not respond to thrombolysis and mechanisms for such blunted response are not well characterized. Current MRI criteria using diffusion and perfusion imaging have concentrated attempts to define salvageable brain tissue. The relationship between stroke severity, the early inflammatory responses, BBB permeability, risk of hemorrhagic transformation, and incomplete microvascular reperfusion has largely been underdeveloped.

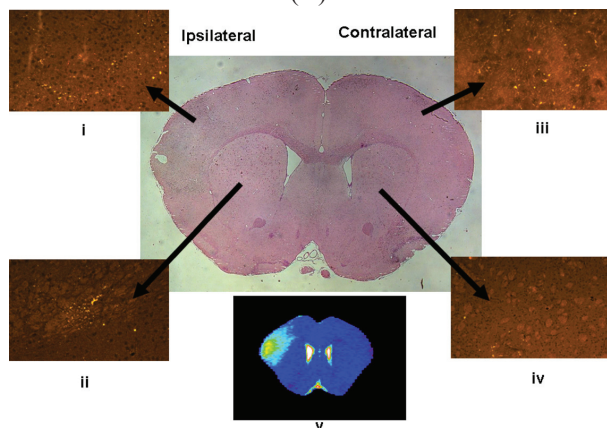
While our understanding of molecular and biochemical responses that ensue following cerebral ischaemia in individual cell types (neurons, glia, endothelium) has grown appreciably there is a demand to understand these processes together at the microvascular level. MRI has allowed us to study animals over time, increasing our understanding of the temporal and spatial evolution of ischemic brain injury, while also reducing the large number of animals that are required for traditional histological experiments. In addition to making assessments of what injury might be reversible vs. irreversible during ischemia, the use of MR paramagnetic contrast agents allows complimentary assessments of vascular flow, tissue perfusion and BBB integrity. Relevant mechanisms of injury to tissue viability and the ischemic penumbra that can be imaged are the early inflammatory responses to ischemia in the microvasculature, BBB dysfunction and CBF/neuronal changes (already discussed above).

The potential of imaging molecular and cellular events that are critically involved in stroke pathophysiology and infarct evolution at the neurovascular level has capitalized on advancements in contrast agent design and synthesis. Cellular labeling and molecular targeting with contrast agents may enable both detection and quantification of neuroinflammatory processes such as infiltration of leukocytes and upregulation of markers of endothelial activation [86,87]. These developments have promoted MRI based detection of inflammatory cells and molecular markers in pre-clinical studies, which has recently led to the parallel studies in human subjects [88,89]. MR imaging has several advantages over other commonly used molecular imaging techniques such as nuclear [90], optical [91,92], and positron emission tomography (PET), including a lack of radioactivity, high spatial anatomical resolution [93] and clinical accessibility. The intrinsic contrast can be augmented by the use of targeted contrast agents in both the experimental and clinical setting [90].

Figure 5. Iron-Based Magnetic Nanoparticles (MNP). **(A)** The paramagnetic core of the modified MNP consists of an iron oxide particle 10 nm in diameter and possessing a $\text{Fe}_2\text{O}_3:\text{FeO}$ ratio of 2:1. This iron oxide core is enclosed within a dextran coat, thus providing numerous sites for surface modification. This allows conjugation of the MNP to an appropriate ligand of a specific biomolecular target. In this specific case, the MNP is conjugated to a unique dual peptide construct consisting of a 15-residue domain with high affinity for P-selectin linked to a second 24-residue thrombin-binding domain. The P-selectin binding domain consists of the primary amino acid sequence LVSVDLEPLDAAWL and was discovered through the use of phage display technology. **(B)** Hematoxylin and eosin coronal section (7 micron slice thickness, bregma +1.00 mm) 26 hours after ischemia/reperfusion and two hours after MNP-PBPI injection. (i) Ipsilateral cortex, Cy5.5-anti-P-selectin-IgG, (ii) Ipsilateral striatum, (iii) Contralateral cortex, (iv) Contralateral striatum, (v) T2 map coronal slice (bregma +1.18 mm) showing the infarct as a light blue area with yellow-green center [87].



(A)



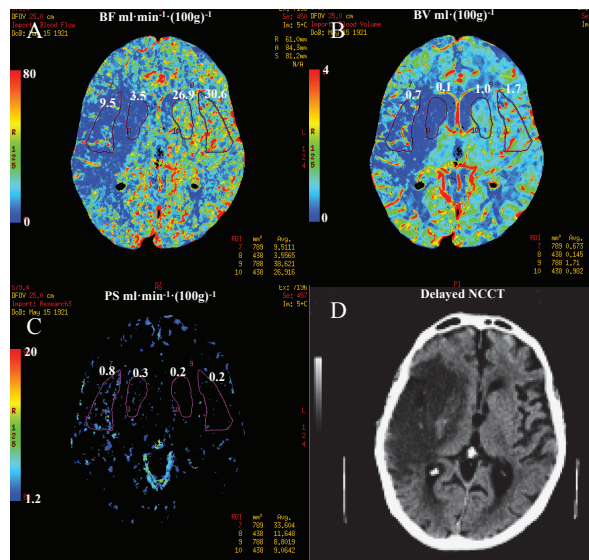
(B)

In the pursuit of determining specific disease process, the evolving field of molecular imaging requires the development of novel classes of MR detectable agents with improved image contrast. The aim of Magnetic Resonance Molecular Imaging is to provide an anatomical visualization of specific molecular processes ideally with high temporal and spatial resolution. There are some basic imaging requirements of Magnetic Resonance Molecular Imaging that should be considered: (1) the imaging target should be well-characterized with respect to its anatomical localization, the time course and the extent of expression; (2) the targeting ligand should be able to access the target, have high binding affinity and a pharmacokinetic profile suited for the needs of the imaging; (3) the signal should unambiguously be a consequence of ligand-target binding, representing specific binding.

Currently two major classes of contrast agents exist: paramagnetic (gadolinium based); and super-paramagnetic agents [94]. The paramagnetic contrast agents shorten both T1 and T2 relaxation, but preferentially T1. They create a hyperintense contrast on conventional T1 weighted spin echo sequences. The second class of agent is based on superparamagnetic iron oxide (SPIO) particles. In a magnetic field the net magnetic moment is several orders of magnitude greater than the paramagnetic agents (Figure 5). This creates extremely large microscopic field gradients for dephasing nearby protons [95,96], and that is accompanied by a substantial decrease in T2. Beyond conventional MRI sequences, T2 imaging causes further shortening of the relaxation properties of the tissue.

Techniques capable of characterizing BBB integrity may prove particularly valuable because there is a credible association between BBB disruption and risk of hemorrhagic transformation with thrombolytic therapy. For the assessments of BBB permeability paramagnetic contrast agent is administered intravenously using a bolus injection. With an intact blood brain barrier the contrast agent passes through the microvasculature of the brain, being contained to the intravascular space. During stroke there are areas of the brain that are associated with BBB breakdown and it is in these areas that the contrast agent can extravasate into the interstitium. There are two methods of detecting BBB breakdown: (1) static T1-weighted MR imaging; and, (2) dynamic contrast enhanced MRI (DCE MRI) [97]. Post contrast T1-weighted MRI is specific for BBB breakdown implying that it is not visualized when the BBB is not dysfunctional but its limitations relate to the infrequency of its detection during the early period after symptom onset and it is relatively insensitive to predicting hemorrhagic transformation (sensitivity 39%) [98,99]. Therefore, post contrast T1-weighted MRI does not have sufficient diagnostic accuracy for routine clinical decision-making. The low sensitivity of post contrast T1 MRI may be partially explained by the failure of contrast arriving to the ischemic during either microvascular or large artery occlusion. The addition of continuous low dose infusion of contrast to the initial bolus dose could improve the sensitivity of post contrast T1-weighted MRI [100]. The downside of this technique is that it requires a long image acquisition, which may be impractical in the context of acute ischemic stroke. The availability, speed and accessibility of CT are the main reasons that CT remains the diagnostic procedure of choice for the treatment of stroke with thrombolysis. CT is capable of generating physiological information about the penumbra. This can be achieved by a 40–50 s DCE or CT perfusion examination. By extending the acquisition time information about BBB integrity or permeability can be obtained (Figure 6) [101].

Figure 6. Permeability surface (PS) area product map from a patient with a large area of contrast leakage into the ischemic region: (A) CBF map of a 5 mm thick brain slice from the admission CTP study displayed with a color scale from 0 (dark blue) to 150 (red) $\text{mL}\cdot\text{min}^{-1}\cdot(100\text{ g})^{-1}$ (B) of pixels with CBF less than $25\text{ mL}\cdot\text{min}^{-1}\cdot(100\text{ g})^{-1}$; (C) corresponding PS map to CBF map in (a) showing the superimposed ischemic ROI and the mirrored ROI in the contralateral hemisphere. PS values in the ischemic and mirrored ROI were 0.40 and $0.122\text{ mL}\cdot\text{min}^{-1}\cdot(100\text{ g})^{-1}$ respectively; (D) corresponding delayed non-contrast CT scan of the same slice showing infarct and hemorrhagic transformation (red arrow). Courtesy of Chris d’Esterre, Richard Aviv and Ting-Yim Lee (University of Western Ontario).



More research is required in this area but it is hypothesized that dynamic contrast MRI or CT may be useful in the prediction of hemorrhagic transformation in acute ischemic stroke. It has been proposed that measurements of BBB permeability in acute stroke may aid in selecting acute ischemic stroke patients for treatment based on imaging criteria of BBB integrity, avoiding the restrictive eligibility criteria mandated by the time window paradigm. Knight *et al.* showed that DCE MRI in a rat model of progressive parenchymal enhancement was highly correlated with the presence of hemorrhagic transformation [102,103]. The main potential drawback is that BBB permeability following ischemic stroke is physiologically a highly dynamic process, and therefore, the imaging at one time point may only provide “snapshot” may not be represent the disease process at a later time point [97]. Such techniques have been performed in human subjects, but it is as yet too early to formalize a permeability threshold facilitating treatment allocation.

6. Conclusions/Outlook

Neuroimaging has been fundamental to translating pathophysiological concepts to clinical trials. The target for stroke therapy remains the ischemic penumbra, *i.e.*, brain with reduced blood flow at risk of infarction. PET is considered to be the gold standard for CBF quantification with the additional parameter of tissue viability in terms of maintained rates of cerebral oxygen metabolism. MR diffusion and perfusion-weighted imaging have been used to translate the imaging concept of penumbra to one of diffusion-perfusion mismatch. This conceptual framework of penumbra is not absolute and controversies remain regarding whether diffusion can correctly identify infarct core and perfusion-weighted imaging can identify tissue at risk outside the DWI lesion. Other problems exist regarding consensus over definitions of penumbra, the consistency of post-processing software used between research groups, and, mismatch has not been shown to be a reliable surrogate to target patient populations in prospective studies. There remain several voids clinically of what we understand of reversible and irreversible injury from the imaging technology and what we understand of the disease at the microscopic level, specifically our concept of the neurovascular unit, its cellular inter-relationships and clinical importance in terms of its dependence of tissue viability on blood flow return. The combination of neuroimaging modalities that include biomarkers of both blood flow, metabolism and blood brain barrier breakdown along with molecular imaging markers of cell injury may clearly delineate reversible *vs.* irreversible and potentially salvageable tissue in the penumbra. This will also expand our perspective that the identification of tissue at risk is only one of many predictors of therapeutic success. The treatment related risks have to be considered and limit therapeutic options for instance related to intracerebral hemorrhage with thrombolysis. Therefore the mismatch concept has to be extended to the assessment of the regional integrity of the neurovascular unit to estimate the response and risk associated with treatment. Under certain therapeutic situations the response of ischemic tissue to reperfusion is likely to exacerbate injury and therefore BBB integrity may provide a useful surrogate to assess ability to rescue tissue. A more physiological based approach complementary to our current understanding of the biological mechanisms, should allow decision processes that alleviate our dependence on the current time based treatment window to an imaging based treatment window [104,105]. Future directions of MRI will refine the mismatch concept by providing complimentary pathophysiological information to current compartmental paradigms of ischemic viability (DWI) and perfusion (PWI) with imaging information related to CBF, BBB permeability, early inflammation, oedema formation in the early acute phase, and further refinements developed (e.g., with microglial or cell death molecular imaging markers) and enhanced BBB permeability markers).

Conflict of Interest

The authors declare no conflict of interest.

References

1. Albers, G.W.; Thijs, V.N.; Wechsler, L.; Kemp, S.; Schlaug, G.; Skalabrin, E.; Bammer, R.; Kakuda, W.; Lansberg, M.G.; Shuaib, A.; *et al.* Magnetic resonance imaging profiles predict clinical response to early reperfusion: The diffusion and perfusion imaging evaluation for understanding stroke evolution (DEFUSE) study. *Ann. Neurol.* **2006**, *60*, 508–517.
2. Astrup, J.; Siesjo, B.K.; Symon, L. Thresholds in cerebral ischemia—the ischemic penumbra. *Stroke* **1981**, *12*, 723–725.
3. Reese, T.; Bochen, D.; Sauter, A.; Beckmann, N.; Rudin, M. Magnetic resonance angiography of the rat cerebrovascular system without the use of contrast agents. *NMR Biomed.* **1999**, *12*, 189–196.
4. Haorah, J.; Heilman, D.; Knipe, B.; Chrastil, J.; Leibhart, J.; Ghorpade, A.; Miller, D.W.; Persidsky, Y. Ethanol-induced activation of myosin light chain kinase leads to dysfunction of tight junctions and blood-brain barrier compromise. *Alcohol. Clin. Exp. Res.* **2005**, *29*, 999–1009.
5. Simard, J.M.; Kent, T.A.; Chen, M.; Tarasov, K.V.; Gerzanich, V. Brain oedema in focal ischaemia: molecular pathophysiology and theoretical implications. *Lancet Neurol.* **2007**, *6*, 258–268.
6. Haorah, J.; Ramirez, S.H.; Schall, K.; Smith, D.; Pandya, R.; Persidsky, Y. Oxidative stress activates protein tyrosine kinase and matrix metalloproteinases leading to blood-brain barrier dysfunction. *J. Neurochem.* **2007**, *101*, 566–576.
7. Han, F.; Shirasaki, Y.; Fukunaga, K. Microsphere embolism-induced endothelial nitric oxide synthase expression mediates disruption of the blood-brain barrier in rat brain. *J. Neurochem.* **2006**, *99*, 97–106.
8. Marchal, G.; Serrati, C.; Rioux, P.; Petit-Taboue, M.C.; Viader, F.; de, I. S.V.; Le, D.F.; Lochon, P.; Derlon, J.M.; Orgogozo, J.M. PET imaging of cerebral perfusion and oxygen consumption in acute ischaemic stroke: relation to outcome. *Lancet* **1993**, *341*, 925–927.
9. Marchal, G.; Rioux, P.; Serrati, C.; Furlan, M.; Derlon, J.M.; Viader, F.; Baron, J.C., Value of acute-stage positron emission tomography in predicting neurological outcome after ischemic stroke: further assessment. *Stroke* **1995**, *26*, 524–525.
10. Ding, G.; Jiang, Q.; Zhang, L.; Zhang, Z.; Knight, R.A.; Soltanian-Zadeh, H.; Lu, M.; Ewing, J.R.; Li, Q.; Whitton, P.A.; *sss* Multiparametric ISODATA analysis of embolic stroke and rt-PA intervention in rat. *J. Neurol. Sci.* **2004**, *223*, 135–143.
11. Lansberg, M.G.; Thijs, V.N.; Bammer, R.; Olivot, J.M.; Marks, M.P.; Wechsler, L.R.; Kemp, S.; Albers, G.W. The MRA-DWI mismatch identifies patients with stroke who are likely to benefit from reperfusion. *Stroke* **2008**, *39*, 2491–2496.
12. Lansberg, M.G.; Straka, M.; Kemp, S.; Mlynash, M.; Wechsler, L.R.; Jovin, T.G.; Wilder, M.J.; Lutsep, H.L.; Czartoski, T.J.; Bernstein, R.A.; *et al.* MRI profile and response to endovascular reperfusion after stroke (DEFUSE 2): A prospective cohort study. *Lancet Neurol.* **2012**, *11*, 860–867.

13. Lees, K.R.; Bluhmki, E.; von Kummer, R.; Brott, T.G.; Toni, D.; Grotta, J.C.; Albers, G.W.; Kaste, M.; Marler, J.R.; Hamilton, S.A.; *et al.* Time to treatment with intravenous alteplase and outcome in stroke: an updated pooled analysis of ECASS, ATLANTIS, NINDS, and EPITHET trials. *Lancet* **2010**, *375*, 1695–1703.
14. Davis, S.M.; Donnan, G.A.; Parsons, M.W.; Levi, C.; Butcher, K.S.; Peeters, A.; Barber, P.A.; Bladin, C.; De Silva, D.A.; Byrnes, G.; *et al.* Effects of alteplase beyond 3 h after stroke in the Echoplanar Imaging Thrombolytic Evaluation Trial (EPITHET): A placebo-controlled randomised trial. *Lancet Neurol.* **2008**, *7*, 299–309.
15. De Silva, D.A.; Fink, J.N.; Christensen, S.; Ebinger, M.; Bladin, C.; Levi, C.R.; Parsons, M.; Butcher, K.; Barber, P.A.; Donnan, G.A.; *et al.* Assessing reperfusion and recanalization as markers of clinical outcomes after intravenous thrombolysis in the echoplanar imaging thrombolytic evaluation trial (EPITHET). *Stroke* **2009**, *40*, 2872–2874.
16. Del Zoppo, G.J. The neurovascular unit, matrix proteases, and innate inflammation. *Ann. N. Y. Acad. Sci.* **2010**, *1207*, 46–49.
17. Lo, E.H. A new penumbra: Transitioning from injury into repair after stroke. *Nat. Med.* **2008**, *14*, 497–500.
18. Lees, K.R.; Zivin, J.A.; Ashwood, T.; Davalos, A.; Davis, S.M.; Diener, H.C.; Grotta, J.; Lyden, P.; Shuaib, A.; Hardemark, H.G.; *et al.* NXY-059 for acute ischemic stroke. *N Engl. J. Med.* **2006**, *354*, 588–600.
19. Knight, R.A.; Ordidge, R.J.; Helpers, J.A.; Chopp, M.; Rodolosi, L.C.; Peck, D. Temporal evolution of ischemic damage in rat brain measured by proton nuclear magnetic resonance imaging. *Stroke* **1991**, *22*, 802–808.
20. Nagaraja, T.N.; Karki, K.; Ewing, J.R.; Croxen, R.L.; Knight, R.A. Identification of variations in blood-brain barrier opening after cerebral ischemia by dual contrast-enhanced magnetic resonance imaging and T1sat measurements. *Stroke* **2008**, *39*, 427–432.
21. Raichle, M. E., The pathophysiology of brain ischemia. *Ann. Neurol.* **1983**, *13*, 2–10.
22. Wise, R.J.; Rhodes, C.G.; Gibbs, J.M.; Hatazawa, J.; Palmer, T.; Frackowiak, R.S.; Jones, T. Disturbance of oxidative metabolism of glucose in recent human cerebral infarcts. *Ann. Neurol* **1983**, *14*, 627–637.
23. Heiss, W.D.; Hayakawa, T.; Waltz, A.G. Cortical neuronal function during ischemia. Effects of occlusion of one middle cerebral artery on single-unit activity in cats. *Arch. Neurol* **1976**, *33*, 813–820.
24. Hakim, A.M. The cerebral ischemic penumbra. *Can. J. Neurol Sci.* **1987**, *14*, 557–559.
25. Baron, J.C.; Bousser, M.G.; Rey, A.; Guillard, A.; Comar, D.; Castaigne, P. Reversal of focal “misery-perfusion syndrome” by extra-intracranial arterial bypass in hemodynamic cerebral ischemia. A case study with 15O positron emission tomography. *Stroke* **1981**, *12*, 454–459.
26. Heiss, W.D.; Rosner, G. Functional recovery of cortical neurons as related to degree and duration of ischemia. *Ann. Neurol* **1983**, *14*, 294–301.
27. Hossmann, K.A. Viability thresholds and the penumbra of focal ischemia. *Ann. Neurol.* **1994**, *36*, 557–565.

28. Dirnagl, U.; Iadecola, C.; Moskowitz, M.A. Pathobiology of ischaemic stroke: An integrated view. *Trends Neurosci.* **1999**, *22*, 391–397.
29. Tagaya, M.; Haring, H.P.; Stuiver, I.; Wagner, S.; Abumiya, T.; Lucero, J.; Lee, P.; Copeland, B.R.; Seiffert, D.; del Zoppo, G.J. Rapid loss of microvascular integrin expression during focal brain ischemia reflects neuron injury. *J. Cereb. Blood Flow Metab* **2001**, *21*, 835–846.
30. Rosenberg, G.A. Matrix metalloproteinases in neuroinflammation. *Glia* **2002**, *39*, 279–291.
31. Rosell, A.; Foerch, C.; Murata, Y.; Lo, E.H. Mechanisms and markers for hemorrhagic transformation after stroke. *Acta Neurochir. Suppl.* **2008**, *105*, 173–178.
32. Rosell, A.; Lo, E.H. Multiphasic roles for matrix metalloproteinases after stroke. *Curr. Opin. Pharmacol.* **2008**, *8*, 82–89.
33. del Zoppo, G.J.; Milner, R. Integrin-matrix interactions in the cerebral microvasculature. *Arterioscler. Thromb. Vascul. Biol.* **2006**, *26*, 1966–1975.
34. Chakravarty, S.; Herkenham, M. Toll-like receptor 4 on nonhematopoietic cells sustains CNS inflammation during endotoxemia, independent of systemic cytokines. *J. Neurosci.* **2005**, *25*, 1788–1796.
35. Marsh, B.J.; Stevens, S.L.; Hunter, B.; Stenzel-Poore, M.P. Inflammation and the emerging role of the toll-like receptor system in acute brain ischemia. *Stroke* **2009**, *40*, S34–S37.
36. Abe, T.; Shimamura, M.; Jackman, K.; Kurinami, H.; Anrather, J.; Zhou, P.; Iadecola, C. Key role of CD36 in Toll-like receptor 2 signaling in cerebral ischemia. *Stroke* **2010**, *41*, 898–904.
37. Greenwood, J.; Heasman, S.J.; Alvarez, J.I.; Prat, A.; Lyck, R.; Engelhardt, B. Review: Leucocyte-endothelial cell crosstalk at the blood-brain barrier: A prerequisite for successful immune cell entry to the brain. *Neuropathol. Appl. Neurobiol.* **2011**, *37*, 24–39.
38. Huang, J.; Upadhyay, U.M.; Tamargo, R.J. Inflammation in stroke and focal cerebral ischemia. *Surg. Neurol.* **2006**, *66*, 232–245.
39. del Zoppo, G.J.; Schmid-Schonbein, G.W.; Mori, E.; Copeland, B.R.; Chang, C.M. Polymorphonuclear leukocytes occlude capillaries following middle cerebral artery occlusion and reperfusion in baboons. *Stroke* **1991**, *22*, 1276–1283.
40. Mori, E.; Del Zoppo, G.J.; Chambers, J.D.; Copeland, B.R.; Arfors, K.E. Inhibition of polymorphonuclear leukocyte adherence suppresses no-reflow after focal cerebral ischemia in baboons. *Stroke* **1992**, *23*, 712–718.
41. Okada, Y.; Copeland, B.R.; Fitridge, R.; Koziol, J.A.; Del Zoppo, G.J. Fibrin contributes to microvascular obstructions and parenchymal changes during early focal cerebral ischemia and reperfusion. *Stroke* **1994**, *25*, 1847–1853.
42. Wagner, S.; Tagaya, M.; Koziol, J.A.; Quaranta, V.; del Zoppo, G.J. Rapid disruption of an astrocyte interaction with the extracellular matrix mediated by integrin alpha 6 beta 4 during focal cerebral ischemia/reperfusion. *Stroke* **1997**, *28*, 858–865.
43. Hossmann, K.A. The two pathophysiologicals of focal brain ischemia: implications for translational stroke research. *J. Cereb. Blood Flow Metab* **2012**, *32*, 1310–1316.
44. Hossmann, K.A. Pathophysiological basis of translational stroke research. *Folia Neuropathol.* **2009**, *47*, 213–227.

45. Jones, T.H.; Morawetz, R.B.; Crowell, R.M.; Marcoux, F.W.; FitzGibbon, S.J.; DeGirolami, U.; Ojemann, R.G. Thresholds of focal cerebral ischemia in awake monkeys. *J. Neurosurg.* **1981**, *54*, 773–782.
46. Heiss, W.D.; Sobesky, J.; Smekal, U.; Kracht, L.W.; Lehnhardt, F.G.; Thiel, A.; Jacobs, A.H.; Lackner, K. Probability of cortical infarction predicted by flumazenil binding and diffusion-weighted imaging signal intensity: A comparative positron emission tomography/magnetic resonance imaging study in early ischemic stroke. *Stroke* **2004**, *35*, 1892–1898.
47. Heiss, W.D.; Fink, G.R.; Huber, M.; Herholz, K. Positron emission tomography imaging and the therapeutic window. *Stroke* **1993**, *24*, I50–I56.
48. Baron, J.C.; Rougemont, D.; Soussaline, F.; Bustany, P.; Crouzel, C.; Bousser, M.G.; Comar, D. Local interrelationships of cerebral oxygen consumption and glucose utilization in normal subjects and in ischemic stroke patients: a positron tomography study. *J. Cereb. Blood Flow Metab* **1984**, *4*, 140–149.
49. Marchal, G.; Rioux, P.; Petit-Tabouç, M.C.; Sette, G.; Traväre, J.M.; Le Poec, C.; Courtheoux, P.; Derlon, J.M.; Baron, J.C. Regional cerebral oxygen consumption, blood flow, and blood volume in healthy human aging. *Arch. Neurol.* **1992**, *49*, 1013–1020.
50. Sobesky, J. Refining the mismatch concept in acute stroke: Lessons learned from PET and MRI. *J. Cereb. Blood Flow Metab* **2012**, *32*, 1416–1425.
51. Baron, J.C.; Cohen, L.G.; Cramer, S.C.; Dobkin, B.H.; Johansen-Berg, H.; Loubinoux, I.; Marshall, R.S.; Ward, N.S. Neuroimaging in stroke recovery: A position paper from the First International Workshop on Neuroimaging and Stroke Recovery. *Cerebrovasc. Dis.* **2004**, *18*, 260–267.
52. Heiss, W.D. The ischemic penumbra: Correlates in imaging and implications for treatment of ischemic stroke. The Johann Jacob Wepfer award 2011. *Cerebrovasc. Dis.* **2011**, *32*, 307–320.
53. Takasawa, M.; Beech, J.S.; Fryer, T.D.; Jones, P.S.; Ahmed, T.; Smith, R.; Aigbirhio, F.I.; Baron, J.C. Single-subject statistical mapping of acute brain hypoxia in the rat following middle cerebral artery occlusion: a microPET study. *Exp. Neurol.* **2011**, *229*, 251–258.
54. Baron, J.C.; Marchal, G. Cerebral and cardiovascular ageing and brain energy metabolism. Studies with positron emission tomography. *Presse. Med.* **1992**, *21*, 1231–1237.
55. Baron, J.C.; Petit-Tabouç, M.C.; Le Doze, F.; Desgranges, B.; Ravenel, N.; Marchal, G. Right frontal cortex hypometabolism in transient global amnesia. A PET study. *Brain* **1994**, *117*, 545–552.
56. Heiss, W.D.; Graf, R.; Wienhard, K.; Lüttgen, J.; Saito, R.; Fujita, T.; Rosner, G.; Wagner, R. Dynamic penumbra demonstrated by sequential multitracer PET after middle cerebral artery occlusion in cats. *J. Cereb. Blood Flow Metab.* **1994**, *14*, 892–902.
57. Griffeth, V.E.; Buxton, R.B. A theoretical framework for estimating cerebral oxygen metabolism changes using the calibrated-BOLD method: Modeling the effects of blood volume distribution, hematocrit, oxygen extraction fraction, and tissue signal properties on the BOLD signal. *Neuroimage* **2011**, *58*, 198–212.

58. Mark, C.I.; Pike, G.B. Indication of BOLD-specific venous flow-volume changes from precisely controlled hyperoxic vs. hypercapnic calibration. *J. Cereb. Blood Flow Metab* **2012**, *32*, 709–719.
59. Zhu, X.H.; Chen, J.M.; Tu, T.W.; Chen, W.; Song, S.K. Simultaneous and noninvasive imaging of cerebral oxygen metabolic rate, blood flow and oxygen extraction fraction in stroke mice. *Neuroimage* **2013**, *64*, 437–447.
60. Guadagno, J.V.; Warburton, E.A.; Aigbirhio, F.I.; Smielewski, P.; Fryer, T.D.; Harding, S.; Price, C.J.; Gillard, J.H.; Carpenter, T.A.; Baron, J.C. Does the acute diffusion-weighted imaging lesion represent penumbra as well as core? A combined quantitative PET/MRI voxel-based study. *J. Cereb. Blood Flow Metab* **2004**, *24*, 1249–1254.
61. Baird, A.E.; Warach, S. Magnetic resonance imaging of acute stroke. *J. Cereb. Blood Flow Metab.* **1998**, *18*, 583–609.
62. Parsons, M.W.; Barber, P.A.; Davis, S.M. Relationship between severity of MR perfusion deficit and DWI lesion evolution. *Neurology* **2002**, *58*, 1707.
63. Schellinger, P.D.; Kohrmann, M. MRA/DWI mismatch: A novel concept or something one could get easier and cheaper? *Stroke* **2008**, *39*, 2423–2424.
64. Furlan, A.J.; Eydling, D.; Albers, G.W.; Al-Rawi, Y.; Lees, K.R.; Rowley, H.A.; Sachara, C.; Soehngen, M.; Warach, S.; Hacke, W. Dose Escalation of Desmoteplase for Acute Ischemic Stroke (DEDAS): Evidence of safety and efficacy 3 to 9 hours after stroke onset. *Stroke* **2006**, *37*, 1227–1231.
65. Marshall, R.S.; Rundek, T.; Sproule, D.M.; Fitzsimmons, B.F.; Schwartz, S.; Lazar, R.M. Monitoring of cerebral vasodilatory capacity with transcranial Doppler carbon dioxide inhalation in patients with severe carotid artery disease. *Stroke* **2003**, *34*, 945–949.
66. Heiss, W.D.; Huber, M.; Fink, G.R.; Herholz, K.; Pietrzyk, U.; Wagner, R.; Wienhard, K. Progressive derangement of periinfarct viable tissue in ischemic stroke. *J. Cereb. Blood Flow Metab.* **1992**, *12*, 193–203.
67. Muir, K.W.; Buchan, A.; von Kummer, R.; Rother, J.; Baron, J.C. Imaging of acute stroke. *Lancet Neurol.* **2006**, *5*, 755–768.
68. Kidwell, C.S.; Jahan, R.; Gornbein, J.; Alger, J.R.; Nenov, V.; Ajani, Z.; Feng, L.; Meyer, B.C.; Olson, S.; Schwamm, L.H.; *et al.* A trial of imaging selection and endovascular treatment for ischemic stroke. *N. Engl. J. Med.* **2013**, *368*, 914–923.
69. Neumann-Haefelin, T.; Kastrup, A.; de Crespigny, A.; Yenari, M.A.; Ringer, T.; Sun, G.H.; Moseley, M.E. Serial MRI after transient focal cerebral ischemia in rats: Dynamics of tissue injury, blood-brain barrier damage, and edema formation. *Stroke* **2000**, *31*, 1965–1972.
70. van Lookeren Campagne, M.; Thomas, G.R.; Thibodeaux, H.; Palmer, J.T.; Williams, S.P.; Lowe, D.G.; van Bruggen, N. Secondary reduction in the apparent diffusion coefficient of water, increase in cerebral blood volume, and delayed neuronal death after middle cerebral artery occlusion and early reperfusion in the rat. *J. Cereb. Blood Flow Metab.* **1999**, *19*, 1354–1364.
71. Kranz, P.G.; Eastwood, J.D. Does diffusion-weighted imaging represent the ischemic core? An evidence-based systematic review. *AJNR. Amer. J. Neuroradiol.* **2009**, *30*, 1206–1212.

72. Rivers, C.S.; Wardlaw, J.M. What has diffusion imaging in animals told us about diffusion imaging in patients with ischaemic stroke? *Cerebrovasc. Dis.* **2005**, *19*, 328–336.
73. Barone, F.C.; Clark, R.K.; Feuerstein, G.; Lenkinski, R.E.; Sarkar, S.K. Quantitative comparison of magnetic resonance imaging (MRI) and histologic analyses of focal ischemic damage in the rat. *Brain Res. Bull.* **1991**, *26*, 285–291.
74. Jiang, Q.; Chopp, M.; Zhang, Z.G.; Knight, R.A.; Jacobs, M.; Windham, J.P.; Peck, D.; Ewing, J.R.; Welch, K.M. The temporal evolution of MRI tissue signatures after transient middle cerebral artery occlusion in rat. *J. Neurol. Sci.* **1997**, *145*, 15–23.
75. Kaur, J.; Tuor, U.I.; Zhao, Z.; Barber, P.A. Quantitative MRI reveals the elderly ischemic brain is susceptible to increased early blood-brain barrier permeability following tissue plasminogen activator related to claudin 5 and occludin disassembly. *J. Cereb. Blood Flow Metab* **2011**, *31*, 1874–1885.
76. Kaur, J.; Tuor, U.I.; Zhao, Z.; Petersen, J.; Jin, A.Y.; Barber, P.A. Quantified T1 as an adjunct to apparent diffusion coefficient for early infarct detection: A high-field magnetic resonance study in a rat stroke model. *Offi. J. Int. Stroke Soc.* **2009**, *4*, 159–168.
77. Ostergaard, L.; Weisskoff, R.M.; Chesler, D.A.; Gyldensted, C.; Rosen, B.R. High resolution measurement of cerebral blood flow using intravascular tracer bolus passages. Part I: Mathematical approach and statistical analysis. *Magn. Reson. Med.* **1996**, *36*, 715–725.
78. Kane, I.; Sandercock, P.; Wardlaw, J. Magnetic resonance perfusion diffusion mismatch and thrombolysis in acute ischaemic stroke: A systematic review of the evidence to date. *J. Neurol Neurosurg. Psych.* **2007**, *78*, 485–491.
79. Grandin, C.B.; Duprez, T.P.; Smith, A.M.; Oppenheim, C.; Peeters, A.; Robert, A.R.; Cosnard, G., Which MR-derived perfusion parameters are the best predictors of infarct growth in hyperacute stroke? Comparative study between relative and quantitative measurements. *Radiology* **2002**, *223*, 361–370.
80. Zaro-Weber, O.; Moeller-Hartmann, W.; Heiss, W.D.; Sobesky, J. The performance of MRI-based cerebral blood flow measurements in acute and subacute stroke compared with 15O-water positron emission tomography: Identification of penumbral flow. *Stroke* **2009**, *40*, 2413–2421.
81. Rivers, C.S.; Wardlaw, J.M.; Armitage, P.A.; Bastin, M.E.; Carpenter, T.K.; Cvorovic, V.; Hand, P.J.; Dennis, M.S. Do acute diffusion- and perfusion-weighted MRI lesions identify final infarct volume in ischemic stroke? *Stroke* **2006**, *37*, 98–104.
82. Sobesky, J.; Zaro, W.O.; Lehnhardt, F.G.; Hesselmann, V.; Neveling, M.; Jacobs, A.; Heiss, W.D. Does the mismatch match the penumbra? Magnetic resonance imaging and positron emission tomography in early ischemic stroke. *Stroke* **2005**, *36*, 980–985.
83. Dani, K.A.; Thomas, R.G.; Chappell, F.M.; Shuler, K.; MacLeod, M.J.; Muir, K.W.; Wardlaw, J.M. Computed tomography and magnetic resonance perfusion imaging in ischemic stroke: Definitions and thresholds. *Ann. Neurol* **2011**, *70*, 384–401.
84. Parsons, M.; Spratt, N.; Bivard, A.; Campbell, B.; Chung, K.; Miteff, F.; O'Brien, B.; Bladin, C.; McElduff, P.; Allen, C.; *et al.* A randomized trial of tenecteplase versus alteplase for acute ischemic stroke. *N. Engl. J. Med.* **2012**, *366*, 1099–1107.

85. Wardlaw, J.M.; Murray, V.; Berge, E.; Del Zoppo, G.J. Thrombolysis for acute ischaemic stroke. *Cochrane. Database. Syst. Rev.* **2009**, *4*, CD000213.
86. Barber, P.A.; Foniok, T.; Kirk, D.; Buchan, A.M.; Laurent, S.; Boutry, S.; Muller, R.N.; Hoyte, L.; Tomanek, B.; Tuor, U.I. MR molecular imaging of early endothelial activation in focal ischemia. *Ann. Neurol.* **2004**, *56*, 116–120.
87. Jin, A.Y.; Tuor, U.I.; Rushforth, D.; Filfil, R.; Kaur, J.; Ni, F.; Tomanek, B.; Barber, P.A. Magnetic resonance molecular imaging of post-stroke neuroinflammation with a P-selectin targeted iron oxide nanoparticle. *Contrast. Med. Mol. Imag.* **2009**, *4*, 305–311.
88. Weissleder, R.; Ntziachristos, V. Shedding light onto live molecular targets. *Nat. Med.* **2003**, *9*, 123–128.
89. Chauveau, F.; Cho, T.H.; Berthezene, Y.; Nighoghossian, N.; Wiart, M. Imaging inflammation in stroke using magnetic resonance imaging. *Int. J. Clin. Pharmacol. Therap.* **2010**, *48*, 718–728.
90. Jin, A.Y.; Tuor, U.I.; Rushforth, D.; Kaur, J.; Muller, R.N.; Petterson, J.L.; Boutry, S.; Barber, P.A. Reduced blood brain barrier breakdown in P-selectin deficient mice following transient ischemic stroke: A future therapeutic target for treatment of stroke. *BMC. Neurosci.* **2010**, *11*, 12.
91. Benaron, D.A.; Stevenson, D.K. Optical time-of-flight and absorbance imaging of biologic media. *Science* **1993**, *259*, 1463–1466.
92. Barber, P.A.; Rushforth, D.; Agrawal, S.; Tuor, U.I. Infrared optical imaging of matrix metalloproteinases (MMPs) up regulation following ischemia reperfusion is ameliorated by hypothermia. *BMC Neurosci.* **2012**, *13*, 76.
93. Johnson, G.A.; Benveniste, H.; Black, R.D.; Hedlund, L.W.; Maronpot, R.R.; Smith, B.R. Histology by magnetic resonance microscopy. *Magn. Reson. Quart.* **1993**, *9*, 1–30.
94. Weinmann, H.J.; Ebert, W.; Misselwitz, B.; Schmitt-Willich, H. Tissue-specific MR contrast agents. *Eur. J. Radiol.* **2003**, *46*, 33–44.
95. Bulte, J.W.; Brooks, R.A.; Moskowitz, B.M.; Bryant, L.H., Jr.; Frank, J.A. T1 and T2 relaxometry of monocrySTALLINE iron oxide nanoparticles (MION-46L): Theory and experiment. *Acad. Radiol.* **1998**, S137–S140.
96. Bulte, J.W.; Frank, J.A. Imaging macrophage activity in the brain by using ultrasmall particles of iron oxide. *AJNR Amer. J. Neuroradiol.* **2000**, *21*, 1767–1768.
97. Kassner, A.; Mandell, D.M.; Mikulis, D.J. Measuring permeability in acute ischemic stroke. *Neuroimag. Clin. North Amer.* **2011**, *21*, 315–325.
98. Jacobs, M.A.; Knight, R.A.; Windham, J.P.; Zhang, Z.G.; Soltanian-Zadeh, H.; Goussev, A.V.; Peck, D.J.; Chopp, M. Identification of cerebral ischemic lesions in rat using Eigenimage filtered magnetic resonance imaging. *Brain Res* **1999**, *837*, 83–94.
99. Merten, C.L.; Knetelius, H.O.; Assheuer, J.; Bergmann-Kurz, B.; Hedde, J.P.; Bewermeyer, H. MRI of acute cerebral infarcts, increased contrast enhancement with continuous infusion of gadolinium. *Neuroradiology* **1999**, *41*, 242–248.
100. Patlak, C.S.; Blasberg, R.G.; Fenstermacher, J.D. Graphical evaluation of blood-to-brain transfer constants from multiple-time uptake data. *J. Cereb. Blood Flow Metab* **1983**, *3*, 1–7.

101. Aviv, R.I.; d'Este, C.D.; Murphy, B.D.; Hopyan, J.J.; Buck, B.; Mallia, G.; Li, V.; Zhang, L.; Symons, S.P.; Lee, T.Y. Hemorrhagic transformation of ischemic stroke: prediction with CT perfusion. *Radiology* **2009**, *250*, 867–877.
102. Knight, R.A.; Barker, P.B.; Fagan, S.C.; Li, Y.; Jacobs, M.A.; Welch, K.M. Prediction of impending hemorrhagic transformation in ischemic stroke using magnetic resonance imaging in rats. *Stroke* **1998**, *29*, 144–151.
103. Knight, R.A.; Nagesh, V.; Nagaraja, T.N.; Ewing, J.R.; Whitton, P.A.; Bershad, E.; Fagan, S.C.; Fenstermacher, J.D. Acute blood-brain barrier opening in experimentally induced focal cerebral ischemia is preferentially identified by quantitative magnetization transfer imaging. *Magn. Reson. Med.* **2005**, *54*, 822–832.
104. Baron, J.C.; Vonkummer, R.; Delzoppo, G.J. Treatment of acute ischemic stroke: Challenging the concept of a rigid and universal time window. *Stroke* **1995**, *26*, 2219–2221.
105. Barber, P.A.; Wechsler, L.R. The ischemic penumbra: From celestial body to imaging technology. *Neurology* **2010**, *75*, 844–845.

Hyperpolarized NMR Probes for Biological Assays

Sebastian Meier, Pernille R. Jensen, Magnus Karlsson and Mathilde H. Lerche

Abstract: During the last decade, the development of nuclear spin polarization enhanced (hyperpolarized) molecular probes has opened up new opportunities for studying the inner workings of living cells in real time. The hyperpolarized probes are produced *ex situ*, introduced into biological systems and detected with high sensitivity and contrast against background signals using high resolution NMR spectroscopy. A variety of natural, derivatized and designed hyperpolarized probes has emerged for diverse biological studies including assays of intracellular reaction progression, pathway kinetics, probe uptake and export, pH, redox state, reactive oxygen species, ion concentrations, drug efficacy or oncogenic signaling. These probes are readily used directly under natural conditions in biofluids and are often directly developed and optimized for cellular assays, thus leaving little doubt about their specificity and utility under biologically relevant conditions. Hyperpolarized molecular probes for biological NMR spectroscopy enable the unbiased detection of complex processes by virtue of the high spectral resolution, structural specificity and quantifiability of NMR signals. Here, we provide a survey of strategies used for the selection, design and use of hyperpolarized NMR probes in biological assays, and describe current limitations and developments.

Reprinted from *Sensors*. Cite as: Meier, S.; Jensen, P.R.; Karlsson, M.; Lerche, M.H. Hyperpolarized NMR Probes for Biological Assays. *Sensors* **2014**, *14*, 1576–1597.

1. Introduction

Technological and methodological improvements allow for the study of increasingly complex processes and systems, not least for studying the inner workings of living cells [1,2]. Various detection modalities are used to this end, providing complementary advantages and information for probing and labeling cellular metabolites. For example, several small-molecule and genetically encoded fluorescent probes are under examination for their potential to measure steady-state concentrations, enzyme activities and resulting intracellular reaction kinetics [1,3]. Other methods include IR [4], UV-Vis, luminescence, Raman [5] and NMR spectroscopy as well as destructive detection by mass spectrometry [2]. The choice of appropriate methods requires consideration of the ease of use, commercial availability, sensitivity, biocompatibility, selectivity, spatiotemporal resolution, general applicability, non-invasiveness and quantifiability [1].

NMR spectroscopy is a robust, generally applicable and noninvasive method yielding quantifiable and high-resolution spectroscopic data that can distinguish analytes by resolving individual atomic sites. On the other hand, NMR spectroscopy has shortcomings in terms of sensitivity. In addition, the detection of individual atomic sites usually also leads to complex spectra, as a consequence of the overlap of signals of interest with non-informative cosolute and solvent signals. Isotope enrichment of NMR active atoms with low natural abundance, in particular ^{13}C and ^{15}N , has been a means to use NMR active probes that are selectively enhanced over background signals by a factor given by their isotope enrichment. NMR spectroscopy is understood from first principles and the interaction

between magnetic moments can be used to enhance otherwise weak signals in a controlled manner by transfer of polarization from spins with high magnetic moments (usually protons and electrons) to nuclear spins with lower magnetic moments (e.g., ^{13}C and ^{15}N). During the last decade, a new generation of nuclear magnetic resonance probes has become popular that affords signal improvements relative to spectral noise and biological backgrounds of at least 3–4 orders of magnitude. This review consecutively covers nuclear spin hyperpolarization, assay designs for hyperpolarized NMR probing, emerging strategies and applications using designed and natural probes, current technological developments and future hopes for NMR assays based on hyperpolarized probes and labels. Several excellent reviews have recently described the development of hyperpolarized contrast agents for functional magnetic resonance imaging [6–9], an application area that is therefore not discussed herein.

2. Hyperpolarization of Molecular Probes

High-resolution nuclear magnetic resonance (NMR) spectroscopy has established itself as a principal detection modality in a remarkable variety of disciplines [10–12]. In the life sciences, many of these applications rely on the use of NMR for retrieving molecular information in close to natural environments and intact biofluids, often in order to probe molecular recognition events and biocatalysis. A principal shortcoming of NMR spectroscopy has remained its moderate sensitivity owing to the low equilibrium polarization of nuclear spins as defined for spin-1/2 nuclei by:

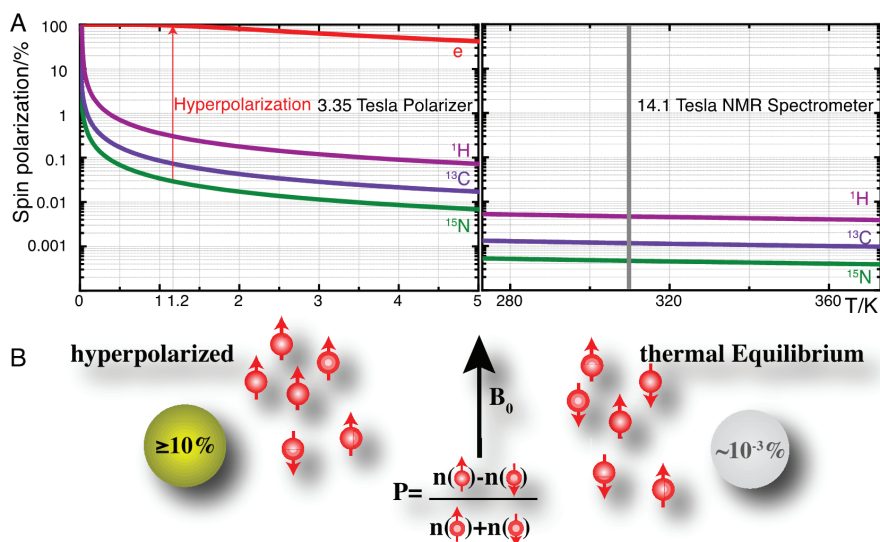
$$P_{\text{eq}} = \frac{n^- - n^+}{n^- + n^+} \cong \tanh \frac{\gamma \hbar B_0}{2k_b T} \quad (1)$$

where n^- and n^+ are the numbers of nuclear spins in the lower and higher energy Zeeman eigenstates, $\gamma \hbar B_0$ is the energy gap between the Zeeman eigenstates and $k_b T$ is the thermal energy [13]. The equilibrium nuclear spin determines the fraction of nuclear spins contributing to the detected signal. This fraction remains well below 0.1% for all nuclear spins at currently available NMR spectrometer fields (Figure 1).

Hyperpolarization strategies, such as parahydrogen induced polarization [14], transfer of photon angular momentum to noble gases by optical pumping [15,16], conversion of rotational energy into nuclear polarization upon cooling (Haupt effect) [17,18] and dynamic nuclear polarization (DNP) [19–21] can redistribute the populations of nuclear spin eigenstates far away from equilibrium. DNP is the technique that is most generally applicable in the production of hyperpolarized molecular probes and the principle of these methods is briefly detailed as follows. DNP hinges on the transfer of electron spin polarization from a free radical to nuclear spins by microwave irradiation [19,22,23]. This transfer is best conducted in amorphous samples that assure the homogenous distribution of electron and nuclear spins. DNP is typically performed at low temperatures (<1.5 K) and at high magnetic fields (>3 T) where the electron spin polarization approaches 100% (Figure 1A). Dedicated instruments for DNP under these conditions achieve solid-state polarizations of NMR active nuclei above 10% and are commercially available as so-called “polarizers” (<http://www.oxford-instruments.com> [24]). The DNP approach to hyperpolarization has gained broad chemical and biological relevance due to a dissolution setup that harvests a hyperpolarized molecular probe by washing the frozen glass of ~1 K temperature rapidly out of a polarizer with heated buffer [25].

Hyperpolarization losses during this dissolution step can be kept to a minimum and molecular probes with polarizations enhanced by several orders of magnitude can be produced for use in biological assays at ambient temperature and for detection with high-resolution liquid state NMR spectroscopy. A principal limitation of using hyperpolarized molecular probes is the short hyperpolarization lifetime of seconds to a few minutes for non-protonated sites in small molecules.

Figure 1. (A) Spin polarizations of electrons (“e”), ^1H , ^{13}C and ^{15}N nuclei in a 3.35 Tesla DNP polarizer near liquid helium temperature, compared to spin polarizations of ^1H , ^{13}C and ^{15}N in a 14.1 Tesla (600 MHz) spectrometer at 273–373 K. An approach to hyperpolarization is the transfer of electron spin polarization to nuclei near 1.2 K prior to dissolution of the hyperpolarized sample in hot aqueous buffer; (B) resultant hyperpolarized samples in aqueous solutions achieve spin polarizations P that are $\sim 3\text{--}4$ orders of magnitude enhanced relative to the thermal equilibrium polarization in an NMR spectrometer.



Hyperpolarized tracers employ a variety of NMR active nuclei with sufficiently slow hyperpolarization loss (determined by the longitudinal T_1 relaxation time of the nucleus) to perform assays on the minute time scale (Table 1). In practice, these probes combine isotope enrichment with hyperpolarization in order to achieve up to $>10^6$ fold signal enhancement over non-informative cellular background signals due to the combined (multiplicative) effect of isotope enrichment and hyperpolarization. The generation and detection of hyperpolarized NMR signal is particularly useful for the nuclei in Table 1 [15,16,25–28], as the low magnetogyric ratios relative to ^1H leads to small equilibrium polarizations (Figure 1A) and the generation of smaller recorded signal by Faraday induction in the NMR coil (see molar receptivity in Table 1) [29]. At the same time, long relaxation times necessitate long inter-scan recycle delays for some of these nuclei in conventional NMR, thus aggravating their poor utility in conventional NMR detecting nuclear magnetism under conditions of equilibrium spin polarization.

Table 1. Nuclei used in hyperpolarized NMR probes.

Nucleus	Spin I	Natural Abundance	Molar Receptivity ^a rel. to ¹ H
³ He	1	<<0.1%	44.2%
⁶ Li	1	7.6%	0.85%
¹³ C	1/2	1.1%	1.59%
¹⁵ N	1/2	0.4%	0.10%
¹⁹ F	1/2	100%	83.3%
²⁹ Si	1/2	4.7%	0.08%
⁸⁹ Y	1/2	100%	0.01%
¹⁰⁷ Ag	1/2	51.8%	<0.01%
¹⁰⁹ Ag	1/2	48.2%	0.01%
¹²⁹ Xe	1/2	26.4%	2.16%

^a NMR signal detection in a coil by Faraday induction is proportional to a factor $|\gamma^3| I(I+1)$ where γ is the magnetogyric ratio; the molar receptivity thus describes the NMR signal generated by identical amounts of nuclear isotopes (*i.e.*, enriched to 100%) relative to ¹H [30].

Considering the sensitivity limitation of conventional NMR spectroscopy, it is little surprise that technological and methodological advances resulting in increased sensitivity directly increase the scope of NMR spectroscopy in the study of complex systems. As an example, the ~4-fold sensitivity gain resulting from cryogenically cooled detection systems has greatly facilitated the in-cell study of recombinant or microinjected isotope-enriched proteins [31,32]. Hyperpolarization approaches yielding 10³–10⁴-fold sensitivity gains for molecular probes clearly have significant potential for investigating complex molecular systems such as the inner workings of living cells in a time-resolved and non-invasive manner. The information content of NMR spectroscopic detection is diverse and includes rapid high-resolution spectroscopic readouts of various NMR parameters such as signal frequency, structural motifs and bound nuclei, rotational correlation time and translational diffusion. Spectral information in conventional and hyperpolarized NMR is adaptable by modulating the timing, frequency, power, duration and phase of electromagnetic excitation pulses.

In the current methodological implementations as described above, hyperpolarized probes are produced *ex situ* in a first step, which is specifically designed to optimize signal that is detectable in NMR spectroscopic assays (Figure 2). These assays have been used in diverse experiments for the rapid measurement of steady state concentrations, transporter and enzyme activities and kinetic profiles of cellular reactions. An overview of the hitherto employed probes and assays is provided in Table 2. Predictably, this list may change rapidly as a consequence of the generality of DNP approaches for producing a growing suite of small molecular probes [33], the increasing commercial availability (and popularity) of the technology, improved protocols for probe formulations [33–35] and the recent development of increasingly adaptable platforms for the versatile development of novel probes [36–38].

Figure 2. Principle of biological assays using hyperpolarized NMR probes. Hyperpolarization is optimized *ex situ* and the hyperpolarized probe or label is added to a biomolecule, cell extracts or living cells to conduct biological assays for detection inside an NMR spectrometer.



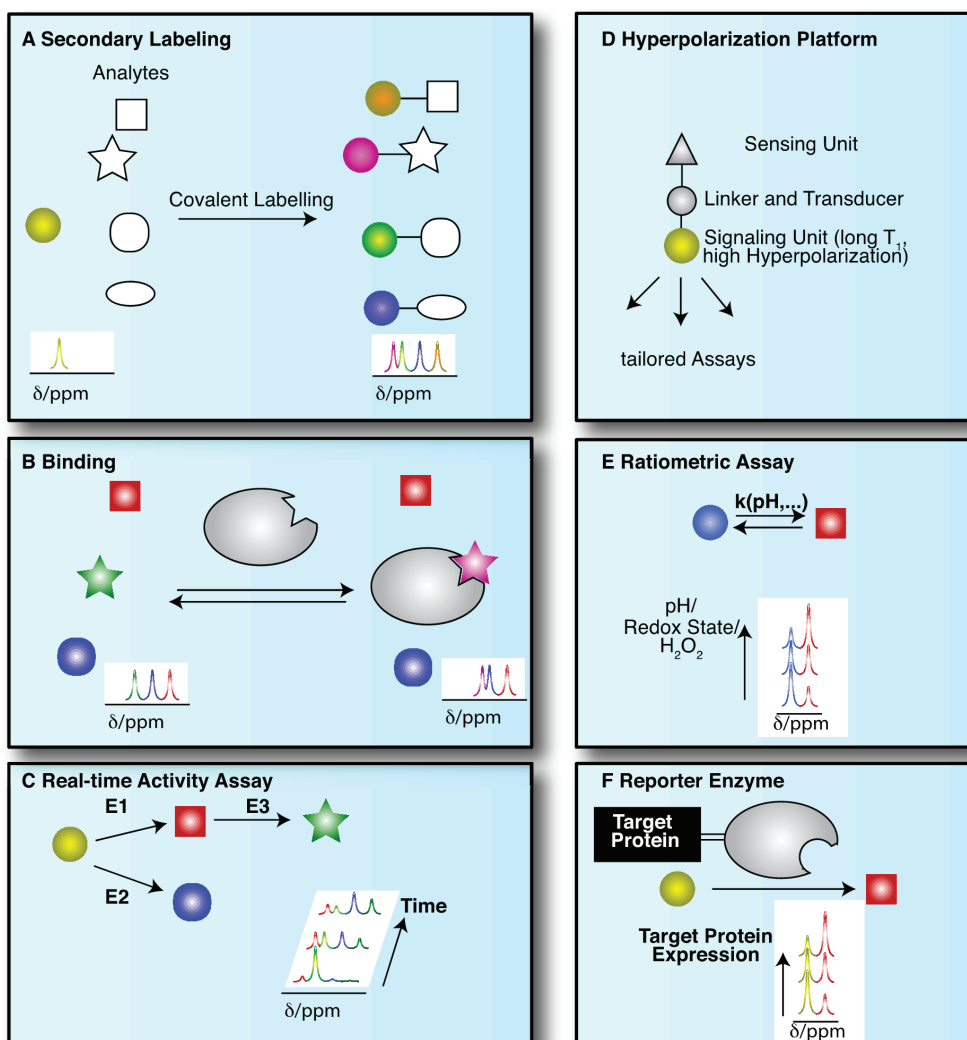
3. Assay Types

NMR spectroscopic detection of hyperpolarized molecular probes provides rich and adaptable information from versatile assay platforms. Some viable assay types are sketched in Figure 3 with hyperpolarized probes depicted as small colored shapes. Figure 3A indicates an approach taken in the determination of amino acids by “secondary labelling” of amino acids with hyperpolarized $[1,1'\text{-}^{13}\text{C}_2]$ acetic anhydride [39]. The approach is an adaptation of a chemical derivatization method in conventional NMR at thermal equilibrium. A class of analytes (here amines) is selected from a complex mixture with minimal sample pretreatment by the acetylation with $[1,1'\text{-}^{13}\text{C}_2]$ acetic anhydride [40]. Upon reaction with different amines, the acetyl label yields resolvable and quantifiable signals for the covalent adducts in thermal and—with improved sensitivity—in hyperpolarized NMR.

NMR spectroscopy has major applications in drug discovery and in particular in hit and lead generation due to the detection of weak binders and the knowledge-based improvement of initial hits [41]. Hyperpolarization of potential binders or mixtures thereof improves assay sensitivity and reduces material demand. As a consequence, the ^{13}C -NMR spectroscopic detection of small molecules becomes feasible with good signal-to-noise ratios, thus allowing the observation of binding reactions even at natural isotope abundance of ^{13}C , in the absence of solvent (water) signal and with a ~ 20 fold larger signal dispersion than ^1H -NMR [42–44]. Figure 3B sketches the use of hyperpolarized probes for the detection of molecular interactions. Binding reactions are also instructive examples for the versatile readout of processes involving hyperpolarized molecular probes beyond chemical shift changes (Figure 3B). Binding to a macromolecular target changes the molecular environment and thus chemical shift of the hyperpolarized probe. In addition, binding to a macromolecular target affects the rotational tumbling of the tracer and leads to a significant shortening of relaxation times, provoking a shortening of the hyperpolarization lifetime by more than an order of magnitude. In consequence, binders can be identified as signals that exhibit changed chemical shift, line widths or strongly accelerated fading of hyperpolarization. This approach likewise has been used to probe hyperpolarized fluorine in drug molecules at several thousand fold improved sensitivity, reducing the material needed to detect and quantify ligand binding in the strong-, intermediate-, and weak-binding regimes [44]. Yet another readout of probe binding is the

transfer of hyperpolarization between competitive binders mediated by the binding pocket of the target [42]. The rapid decay of hyperpolarized binders does not require binding partners that are macromolecular, as demonstrated in the magnetic resonance imaging of benzoic acid binding to cyclodextrins by employing the decreased hyperpolarization lifetime upon binding for contrast generation [45].

Figure 3. Schematics of different strategies for the use of hyperpolarized labels and probes for NMR spectroscopic biological assays: Hyperpolarized molecules have been used for (A) readout by covalent chemical labeling of analytes; (B) probing of non-covalent binding; (C) the tracking of enzymatic transformations; (D) the design of versatile probe platforms; (E) ratiometric measurements of physicochemical states and (F) interrogating protein expression by probing attached reporter enzymes.



In addition to probing drug binding, hyperpolarization was also used in monitoring drug metabolism by discontinuous assays. Here, medication levels in blood plasma were monitored for an anticonvulsant (carbamazepine) that was specifically ^{13}C enriched in a position with long hyperpolarization lifetime. Monitoring ^{13}C signals rather than ^1H signals of carbamazepine permitted the resolution and identification of the drug in deproteinized blood plasma with accurate and robust quantifications [46]. Additional contrast relative to background signals can be envisioned by monitoring signals with long hyperpolarization lifetime in backgrounds of faster relaxing signals, for instance by following deuterated ^{13}C groups in non-deuterated, rapidly relaxing natural backgrounds.

The most common use of hyperpolarized molecules has been their application in the real-time probing of enzymatic reaction kinetics. In such applications, the chemical conversion of a hyperpolarized organic substrate or metabolite molecule is followed over time, yielding real-time reaction progress curves, also for sequential or parallel reactions (Figure 3C). Once excited to detectable transverse magnetization for detection, hyperpolarization is not recovered. Rather, the transverse component fades with a characteristic transverse relaxation time T_2 that is shorter than the longitudinal T_1 time. Hence, progression in binding, transport or chemical reactions is monitored with weak excitation pulses to divide the available hyperpolarized signal for serial, time-resolved readouts [47].

Increased versatility of hyperpolarized probes is recently sought by means of optimized probe design (Figure 3D). Analogous to small fluorescence probe design, hyperpolarized probes have been devised that contain a sensing moiety that is separate from the moiety providing the hyperpolarized NMR signal. Sensing and signaling moieties are then coupled by a transmitter that ensures significant chemical shift changes in the hyperpolarized reporter unit upon events probed by the sensing unit. As the hyperpolarization lifetime is a principal restriction of hyperpolarized NMR probes, the reporter moiety will be selected to provide an atomic site with a hyperpolarization lifetime that is as long as possible. The sensing part of the probe on the other hand is variable and is modified by the analyte of interest.

Hyperpolarized probes have been used to measure concentrations and conditions such as pH, H_2O_2 and redox state with ratiometric assays, where these conditions affect reaction rates and equilibrium constants of detectable reactions. Hence, the ratio of signals from two reactants has been used both for rapidly established equilibria and in kinetic experiments (of irreversible reactions, at a defined time point) (Figure 3E).

As a final example, enzymatic conversion of hyperpolarized NMR probes has been suggested for a use analogous to the application of optical reporter enzyme/substrate pairs (e.g., luciferase and luciferin) for monitoring the expression of a target gene in cell biology [37,48,49]. *In vivo* applications of luciferase are limited to observations near the body surface because biological tissues strongly scatter light [37]. Hence, the development of magnetic resonance based reporter protein assays could be advantageous to deep imaging *in vivo*. In one version employing hyperpolarized probes, the gene of a reporter enzyme is fused to the target gene by genetic engineering (Figure 3F). A hyperpolarized substrate of the reporter enzyme then is used to probe the expression of the chimeric target and reporter gene. The hyperpolarized substrate should be a specific substrate of the reporter enzyme and not be converted by endogenous enzymes [37] (Figure 3F). Readout of exogenous

enzymatic activities by hyperpolarized NMR has also been suggested for enzymes that are not intracellularly expressed. Such enzymes were for instance targeted to tissues of interest for the activation of prodrugs to cytotoxic drugs in tumors [48].

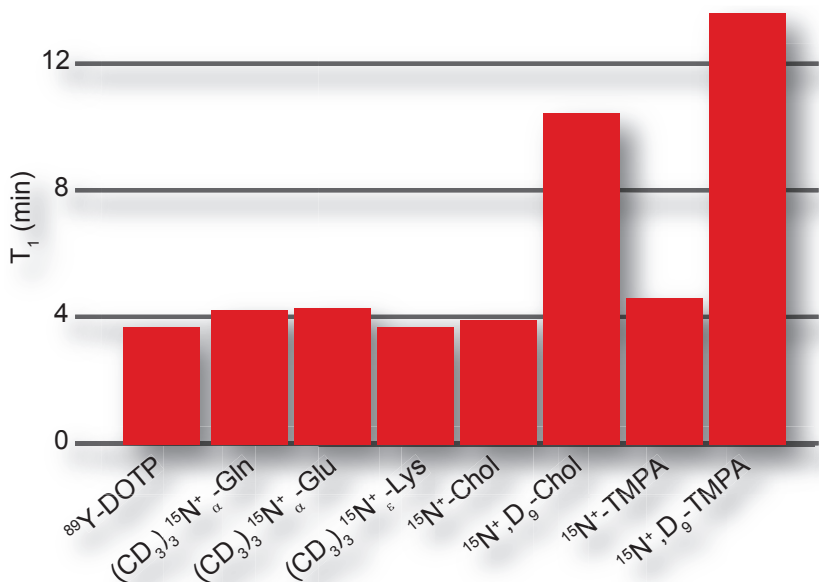
4. Lifetime of Hyperpolarized NMR Probes

Due to the limited hyperpolarization lifetime even for small molecules, general considerations in the development of hyperpolarized NMR probes primarily concern the optimization of hyperpolarization levels and lifetimes and the choice of probe and assay conditions favoring a rapid readout. The polarization decays with a longitudinal relaxation rate constant $R_1 = 1/T_1$ that is characteristic for the atomic site at a given temperature, magnetic field and molecular tumbling rate. For spin-1/2 nuclei, relaxation is caused by fluctuating magnetic fields at the sites of the nuclear spins. In the absence of paramagnetic relaxation mechanisms [50], relaxation is usually dominated by a dipolar contribution and a chemical shift anisotropy (CSA) contribution [13].

The dipolar contribution to longitudinal relaxation of a nucleus X in a molecular probe depends on the nature and distance of nuclear spins as described by the proportionality $R_d \sim \frac{\gamma_X^2 \gamma_{1H}^2}{r^6}$, where γ is the magnetogyric ratio and r the distance from the probe nucleus X to the dipolar coupled ^1H (or other nuclei with large magnetic moment). Hence, hyperpolarized probes will be designed to observe hyperpolarization at a molecular site that is distant from protons, such as quaternary ^{13}C and ^{15}N atoms [51]. The CSA contribution to longitudinal relaxation is $R_{\text{CSA}} \sim \gamma_X^2 \Delta\sigma^2 B_0^2$, where B_0 is the magnetic field and $\Delta\sigma$ is the CSA, which is smaller for symmetrical environments. Hence, hyperpolarized probes preferably contain symmetrical environments around the molecular site serving as the reporter or signaling unit. Bearing these considerations in mind, hyperpolarization moieties have been devised that have exponential decay time constants of up to ~15 minutes (Figure 4), where hyperpolarized probing is usually considered feasible on a time scale that is 3-5-fold longer than the exponential decay time.

In addition to the direct readout of hyperpolarized signal, magnetization transfer from long T_1 nuclei storing hyperpolarized magnetization to other, possibly more informative, molecular sites has been reported in various applications [52–54]. As the hyperpolarization lifetime is the Achilles heel of the method in most applications, approaches to manipulate hyperpolarized nuclear spins with pulse sequences to store hyperpolarization in long lived states are currently under vigorous development [55,56].

Figure 4. Exponential decay time constants for hyperpolarized reporter groups in various designed probes, reaching up to several minutes in symmetrically substituted, non-protonated sites. The reported time constants were derived at 9.4 T and 25 °C for ^{89}Y -DOTP [28], at 14.1 T and 37 °C for permethylated amino acids [51] and at 14.1 T and 30 °C for choline- and TMPA-based probes [38].



5. Hyperpolarized NMR Probes

Hyperpolarized NMR probes are advantageously categorized into three classes: (i) Non-endogenous probes that are designed for faster delivery or to contain long lived hyperpolarization units for readout of NMR chemical shift changes upon response of an indicator unit to concentrations or conditions in the analyzed system [28,34,36–38]; (ii) Derivatized endogenous molecules, in particular esters [37,57,58], anhydrides [59] and permethylated amino acids [51], that are modified to improve assay properties such as cellular uptake and hyperpolarization lifetimes; and (iii) Endogenous molecules (bicarbonate, vitamin C, metabolites, nutrients) that are used for minimally invasive assays.

Hyperpolarized probes have been designed to obtain beneficial properties relative to natural substrates. In order to enhance probe response during the hyperpolarization timescale, designed hyperpolarized probes have been devised to provide either longer hyperpolarization lifetimes or faster delivery to the site of action, for instance to the intracellular milieu. Permethylation of amino acids, especially with deuterated methyl groups, reduces the proton spin density in the vicinity of amino acid nitrogens and thus decreases relaxation rates of hyperpolarized nitrogen nuclei (Figure 4). When used for perfusion studies, these methylated amino acids do not rapidly enter any metabolic networks [51]. In addition to improving hyperpolarization lifetimes, probes can be derivatized to optimize sample delivery into metabolic networks, for example by esterification of

organic acids in order to achieve improved cellular uptake [57,58]. Appropriate balances between hydrophobicity and hydrophilicity should be increasingly considered in optimized probe design particularly for living cell studies, achieving the desired water solubility, membrane permeability and cellular retention of hyperpolarized probes. At the same time, non-natural probes should be biocompatible and bioorthogonal, with the probes exerting no toxic effect in living cells both in their initial or modified forms.

Small natural molecules lend themselves to the direct use as molecular probes if they have non-protonated ^{13}C or ^{15}N sites. Such sites occur in many metabolites (for instance organic ketones, acids) or can be generated by replacing protons with deuterons, which have much smaller magnetic moments [60,61]. Beyond these considerations, optimization of this class of probes is largely limited to the optimization of hyperpolarization recipes and protocols. As a main benefit, such probes inherently provide biocompatibility if used at near-physiological concentrations. In addition, natural substrates ensure little doubt about the relevance of observed enzyme and pathway activities. The chemical design of small molecule probes, on the other hand, modulates their function relative to the natural substrates [62].

Table 2. Examples of hyperpolarized NMR probing.

Observable	Probe	References
(i) Designed probes		
Amino acid concentrations	acetic anhydride	[39]
Binding	^1H , ^{13}C and ^{19}F in binders	[42–44]
Drug metabolism	Carbamazepine	[46]
Ca^{2+} concentration	trimethylphenylammonium substituted with triacetic acid	[38]
Contrast agent	$^6\text{LiCl}$	[63]
Enzyme activity	trimethylphenylammonium substituted with methyl ester	[38]
HOCl	<i>p</i> -Anisidine	[36]
Hydrogen peroxide	benzoylformic acid trimethylphenylammonium substituted with boronic acid ester	[38,64]
pH	^{89}Y -complexes	[28,34]
Protein expression	N-acetyl-L-methionine	[49]
(ii) Derivatized endogenous probes		
Enzyme activity	3,5-Difluorobenzoyl-L-glutamic acid (carboxypeptidase prodrug)	[48]
Enzyme activity	ethyl pyruvate	[57]
Perfusion	permethylated amino acids (betains)	[51]
Protein expression	pyruvate derivatives as reporter groups	[37]

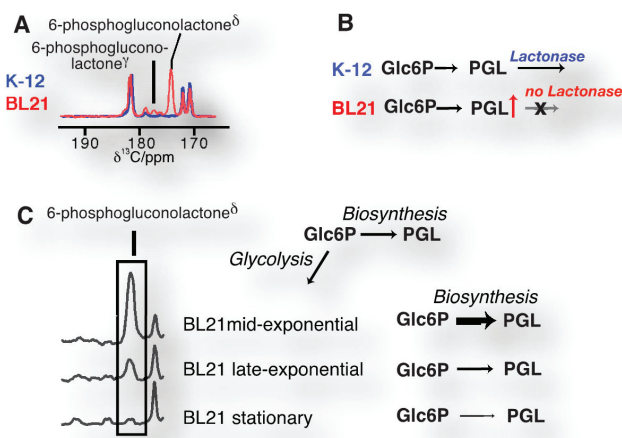
Table 2. Cont.

Observable	Probe	References
(iii) Endogenous probes		
Cell permeability, lysis	fumarate metabolism	[65]
	pyruvate diffusion	[66]
Drug efficacy	pyruvate	[67–69]
	fumarate	[65]
Enzyme activities and reaction fluxes		
• Ldh	pyruvate, lactate	[70,71]
• Alt	alanine, pyruvate	[50]
• Bcat	ketoisocaproic acid	[72]
• Glutaminase	glutamine	[73,74]
• Carnitine acetyltransferase, AcetylCoA synthetase	acetate	[75]
• Betaine aldehyde metabolism	choline analog	[76]
• Pyruvate decarboxylase	pyruvate	[77]
• Pyruvate dehydrogenase	pyruvate	[78,79]
Enzyme mechanistic studies	fructose	[61]
	alanine	[80]
Gene expression, gene loss	glucose	[61,81]
Intracellular pH	acetate	[82]
	pyruvate	[83]
Metabolic strategies in different genomes	glucose	[61]
Oncogene signalling	pyruvate	[84]
	ketoisocaproic acid	[72]
Pathway activity, bottlenecks		
• Glycolysis	glucose	[61,85–87]
• Indicator of aerobic glycolysis	[1- ¹³ C]pyruvate	[71,88,89]
• TCA cycle	[2- ¹³ C]pyruvate	[90]
• Fatty acid and ketone body metabolism	butyrate	[91]
Redox status	dehydroascorbic acid	[92,93]
Sulfite cytotoxicity	glucose	[94]
Tissue pH	bicarbonate	[95]
Transporter level and activity		
• Glucose transporter	glucose	[86]
• Monocarboxylate transporter	pyruvate	[88,96]
• Urea carrier	urea	[97]
Tumor grading	alanine, pyruvate, lactate	[98]

Accordingly, enzyme substrates predominate in this class of molecular probes, even if cellular states and concentrations (pH, redox state) are measured. Enzymatic substrates provide the advantage of fairly rapid turnover on the time scale of the hyperpolarization lifetime and of amplified signal through catalytic turnover as compared to binding probes [29]. Observed enzymatic and pathway

activities report—amongst others—on qualitative and quantitative changes to reaction usage in disease biology, altered signaling pathways and cellular modifications in treatment, genetic and genomic changes in cells (including transgenic cells) as well as regulation of reaction usage by nutritional states (Figure 5). Besides chemical turnover in enzyme catalyzed reactions, transport processes have been probed by real-time observation with endogenous substrates to determine estimates of the Michaelis-Menten steady-state kinetic constants of the transporters, specifically the maximal velocities and Michaelis constants of glucose, monocarboxylate or urea transporters [86,88,96,99].

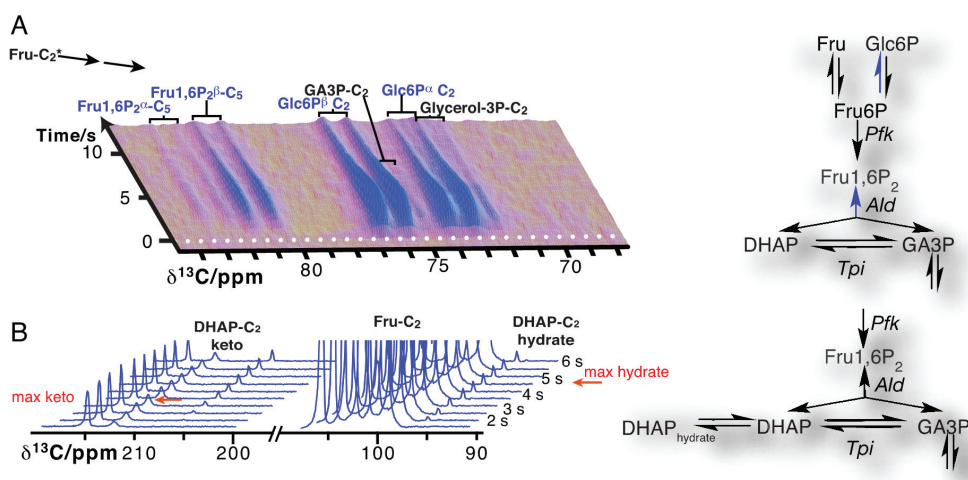
Figure 5. The direct detection of glucose metabolism in *Escherichia coli* strains shows the accumulation of a lactone intermediate of the pentose phosphate pathway in strain BL21 (A,B) due to the absence of the lactonase in the BL21 genome, thus affording genomic probing by direct observation of intracellular reaction kinetics; Glc6P = glucose 6-phosphate; PGL = 6-phosphogluconolactone; (C) Accumulation of the lactone occurs in a growth phase dependent manner due to reduced usage of a hyperpolarized glucose probe in biosynthetic pathways as cells approach the stationary phase.



Due to the resolution of individual atomic sites by high-resolution NMR spectroscopic readout, hyperpolarized NMR probes enable the detection of multiple sequential and parallel reactions. Full kinetic reaction profiles of more than ten metabolites, for instance in microbial glycolysis and fermentation reactions, signify the advantage of using high-resolution readouts to the probing of cellular chemistry [61,85]. In doing so, NMR spectroscopic readouts not only identify a plethora of metabolites, but distinguish their precise molecular forms and the reactivity of these forms. Figure 6A displays the kinetic profiles of sugar phosphate isomer formation by gluconeogenic reactions using a hyperpolarized [2- ^{13}C]fructose probe as the glycolytic substrate. Isomer ratios underline the gluconeogenic formation of glucose 6-phosphate and fructose 1,6-bisphosphate from acyclic reaction intermediates under thermodynamic reaction control. Using data from the same *in vivo* experiment, Figure 6B indicates the slow formation and decay of hydrated dihydroxyacetonephosphate relative to the on-pathway ketone signal upon using hyperpolarized [2- ^{13}C]fructose as the probe. Both

examples in Figure 6 thus probe the *in vivo* flux of the hyperpolarized signal into off-pathway reactions. On a related note, high spectral resolution also provides the possibility of using several hyperpolarized probes at the same time [100].

Figure 6. Time-resolved observation of metabolite isomers upon feeding a hyperpolarized [2- ^{13}C]fructose probe to a *Saccharomyces cerevisiae* cell cultures at time 0: **(A)** Glucose 6-phosphate (Glc6P) and fructose 1,6-bisphosphate (Fru1,6P₂) C₅ signals arise from gluconeogenic reactions of the glycolytic substrate. Isomer ratios are consistent with the formation of the isomers from acyclic intermediates; **(B)** real-time observation of dihydroxyacycylone phosphate (DHAP) hydrate formation as an off-pathway glycolytic intermediate (other abbreviations are: GA3P = glyceraldehyde 3-phosphate, *Ald* = aldolase; *Pfk* = phosphofructokinase; *Tpi* = triose phosphate isomerase).



6. Current Developments and Outlook

Hyperpolarized NMR probes have rapidly shown their biological, biotechnological and recently also clinical [101] potential. The synergistic co-evolution of probe design and probe formulation as well-glassing preparations [33], in conjunction with technical and methodological developments within hyperpolarization and NMR experimentation leave little doubt of an ongoing improvement of hyperpolarized NMR probe technology and applications within the foreseeable future. An increasing selection of metabolite isotopomers—especially ^{13}C and ^2H labeled compounds—will enable more diversified uses of natural (endogenous) hyperpolarized probe molecules for examining biological processes. Diligent choices of probe platforms and the optimization of hyperpolarization conditions will serve to improve probe sensitivity and biocompatibility [102]. Combined optimizations of hyperpolarization lifetime, polarization levels, cellular uptake and retention as well as biocompatibility are yet to be performed for biological assays using hyperpolarized NMR with non-natural probes.

In order to improve assay throughput, approaches employing multiple hyperpolarization chambers [103–105] have been used for multiplexed probe generation. In addition, polarization of ^1H and subsequent transfer to nuclei with low magnetogyric ratio [106] is a means towards faster hyperpolarization with the DNP method. In addition to using several chambers for probe generation, the use of several chambers for parallel detection in assays, e.g., in multi-chamber bioreactors, will improve assay throughput [107]. The development and use of bioreactors for sustained cell cultures will support assay reproducibility in this context [88,89].

Various NMR methods have been described that provide increased temporal and spatial resolution as well as information content in hyperpolarized probe detection [108–114]. The approaches include modified detection schemes to generate multidimensional spectra from rapid single-scan NMR experiments [54,115–117] or the indirect, amplified detection of signals by saturation transfer methods [86,118]. As mentioned above, a major undertaking is to store hyperpolarization in slowly fading nuclear spin states in order to enhance the utility of hyperpolarized NMR probes in the detection of slower reactions or more pathway steps. Additionally, the assay time window has been extended towards the short end of the time scale by establishing rapid delivery of hyperpolarized substrates into the NMR detection system [119,120]. Resultant time-resolved reaction progression curves over an expanding time scale predictably will increasingly need to be analysed with realistic mathematical models in order to extract quantitative kinetic data [70,71,99,121]. Besides such methodological and technological improvements, ease of use and affordability clearly constitute a major point of concern, especially if hyperpolarized NMR probes are meant to experience routine use in cell biological and clinical assays. While there is room for improvement, hyperpolarized NMR probes already offer a plethora of unique benefits, such as: molecular information and spectral resolution; low background polarization and interference; simultaneous analyte detection; minimal invasiveness especially when using endogenous molecules as probes; the use of non-ionizing electromagnetic radiation with virtually unlimited permeation into tissues and other samples.

Overall, NMR spectroscopy allows minimally invasive observation of complex processes and systems. The development of hyperpolarized probes enables the direct quantitative understanding of such processes and systems in selective assay developed directly for biofluid and cellular settings. In consequence, analytical methods using hyperpolarized NMR help avoid overly optimistic conclusions regarding biological utility and specificity, which can occur with less direct methods that use few selected targets under test tube conditions. Therefore, the use of hyperpolarized probes on complex systems, in conjunction with atomic-resolution NMR detection of probe transport and conversion, has great potential in enhancing our understanding of biological systems.

Acknowledgments

We gratefully acknowledge Ole Hindsgaul for continued support of DNP NMR projects and Sophie Beeren for critically reading the manuscript and for helpful discussions.

Conflicts of Interest

The authors declare no conflict of interest.

References

1. Palmer, A.E.; Qin, Y.; Park, J.G.; McCombs, J.E. Design and application of genetically encoded biosensors. *Trends Biotechnol.* **2011**, *29*, 144–152.
2. Svatos, A. Single-cell metabolomics comes of age: New developments in mass spectrometry profiling and imaging. *Anal. Chem.* **2011**, *83*, 5037–5044.
3. Chan, J.; Dodani, S.C.; Chang, C.J. Reaction-based small-molecule fluorescent probes for chemoselective bioimaging. *Nat. Chem.* **2012**, *4*, 973–984.
4. Holman, H.Y.; Bechtel, H.A.; Hao, Z.; Martin, M.C. Synchrotron IR spectromicroscopy: Chemistry of living cells. *Anal. Chem.* **2010**, *82*, 8757–8765.
5. Evans, C.L.; Xie, X.S. Coherent anti-stokes raman scattering microscopy: Chemical imaging for biology and medicine. *Annu. Rev. Anal. Chem.* **2008**, *1*, 883–909.
6. Schroeder, M.A.; Clarke, K.; Neubauer, S.; Tyler, D.J. Hyperpolarized magnetic resonance: A novel technique for the in vivo assessment of cardiovascular disease. *Circulation* **2011**, *124*, 1580–1594.
7. Gallagher, F.A.; Kettunen, M.I.; Day, S.E.; Hu, D.-E.; Karlsson, M.; Gisselsson, A.; Lerche, M.H.; Brindle, K.M. Detection of tumor glutamate metabolism *in vivo* using ^{13}C magnetic resonance spectroscopy and hyperpolarized $[1-^{13}\text{C}]\text{glutamate}$. *Magn. Reson. Med.* **2011**, *66*, 18–23.
8. Kurhanewicz, J.; Vigneron, D.B.; Brindle, K.; Chekmenev, E.Y.; Comment, A.; Cunningham, C.H.; Deberardinis, R.J.; Green, G.G.; Leach, M.O.; Rajan, S.S.; *et al.* Analysis of cancer metabolism by imaging hyperpolarized nuclei: Prospects for translation to clinical research. *Neoplasia* **2011**, *13*, 81–97.
9. Terreno, E.; Castelli, D.D.; Viale, A.; Aime, S. Challenges for molecular magnetic resonance imaging. *Chem. Rev.* **2010**, *110*, 3019–3042.
10. Derome, A.E. *Modern NMR Techniques for Chemistry Research*, 1st ed.; Pergamon Press: Oxford, UK, 1987.
11. De Graaf, R.A. *In vivo NMR Spectroscopy : Principles and Techniques*, 2nd ed.; Wiley: Chichester, UK; Hoboken, NJ, USA, 2007.
12. Cavanagh, J. *Protein NMR Spectroscopy : Principles and Practice*, 2nd ed.; Academic Press: Amsterdam, The Netherland; Boston, MA, USA, 2007.
13. Levitt, M.H. *Spin Dynamics: Basics of Nuclear Magnetic Resonance*, 2nd ed.; Wiley: Chichester, England, UK; Hoboken, NJ, USA, 2008.
14. Bowers, C.R.; Weitekamp, D.P. Transformation of symmetrization order to nuclear-spin magnetization by chemical reaction and nuclear magnetic resonance. *Phys. Rev. Lett.* **1986**, *57*, 2645–2648.
15. Middleton, H.; Black, R.D.; Saam, B.; Cates, G.D.; Cofer, G.P.; Guenther, R.; Happer, W.; Hedlund, L.W.; Johnson, G.A.; Juvan, K.; *et al.* MR imaging with hyperpolarized ^3He gas. *Magn. Reson. Med.* **1995**, *33*, 271–275.

16. Spence, M.M.; Rubin, S.M.; Dimitrov, I.E.; Ruiz, E.J.; Wemmer, D.E.; Pines, A.; Yao, S.Q.; Tian, F.; Schultz, P.G. Functionalized xenon as a biosensor. *Proc. Natl. Acad. Sci. USA* **2001**, *98*, 10654–10657.
17. Haupt, J. A new effect of dynamic polarization in a solid obtained by rapid change of temperature. *Phys. Lett. A* **1972**, *38*, 389–390.
18. Günther, U.L. Dynamic nuclear hyperpolarization in liquids. *Top. Curr. Chem.* **2013**, *335*, 23–69.
19. Carver, T.R.; Slichter, C.P. Polarization of nuclear spins in metals. *Phys. Rev.* **1953**, *92*, 212–213.
20. Abragam, A.; Goldman, M. Principles of dynamic nuclear polarisation. *Rep. Prog. Phys.* **1978**, *41*, 395.
21. Abraham, M.; McCausland, M.A.H.; Robinson, F.N.H. Dynamic nuclear polarization. *Phys. Rev. Lett.* **1959**, *2*, 449–451.
22. Carver, T.R.; Slichter, C.P. Experimental verification of the overhauser nuclear polarization effect. *Phys. Rev.* **1956**, *102*, 975–980.
23. Abragam, A.; Goldman, M. *Nuclear Magnetism: Order and Disorder*; Oxford University Press: New York, NY, USA, 1982.
24. Comment, A.; van den Brandt, B.; Uffmann, K.; Kurdzesau, F.; Jannin, S.; Konter, J.A.; Hautle, P.; Wenckebach, W.T.; Grütter, R.; van der Klink, J.J. Design and performance of a DNP prepolarizer coupled to a rodent MRI scanner. *Concepts Magn. Reson. B* **2007**, *31B*, 255–269.
25. Ardenkjær-Larsen, J.H.; Fridlund, B.; Gram, A.; Hansson, G.; Hansson, L.; Lerche, M.H.; Servin, R.; Thaning, M.; Golman, K. Increase in signal-to-noise ratio of >10,000 times in liquid-state NMR. *Proc. Natl. Acad. Sci. USA* **2003**, *100*, 10158–10163.
26. Lumata, L.; Merritt, M.E.; Hashami, Z.; Ratnakar, S.J.; Kovacs, Z. Production and NMR characterization of hyperpolarized ^{107,109}Ag complexes. *Angew. Chem. Int. Ed. Engl.* **2012**, *51*, 525–527.
27. Dementyev, A.E.; Cory, D.G.; Ramanathan, C. Dynamic nuclear polarization in silicon microparticles. *Phys. Rev. Lett.* **2008**, *100*, 127601.
28. Jindal, A.K.; Merritt, M.E.; Suh, E.H.; Malloy, C.R.; Sherry, A.D.; Kovacs, Z. Hyperpolarized ⁸⁹Y complexes as pH sensitive NMR probes. *J. Am. Chem. Soc.* **2010**, *132*, 1784–1785.
29. Schröder, L. Xenon for NMR biosensing—Inert but alert. *Phys. Med.* **2013**, *29*, 3–16.
30. Harris, R.K.; Becker, E.D.; Cabral de Menezes, S.M.; Goodfellow, R.; Granger, P. NMR nomenclature: Nuclear spin properties and conventions for chemical shifts. Iupac recommendations 2001. *Solid State Nucl. Magn. Reson.* **2002**, *22*, 458–483.
31. Sakakibara, D.; Sasaki, A.; Ikeya, T.; Hamatsu, J.; Hanashima, T.; Mishima, M.; Yoshimasu, M.; Hayashi, N.; Mikawa, T.; Wälchli, M.; *et al.* Protein structure determination in living cells by in-cell NMR spectroscopy. *Nature* **2009**, *458*, 102–105.
32. Serber, Z.; Dotsch, V. In-cell NMR spectroscopy. *Biochemistry* **2001**, *40*, 14317–14323.

33. Karlsson, M.; Jensen, P.; Duus, J.Ø.; Meier, S.; Lerche, M. Development of dissolution DNP-MR substrates for metabolic research. *Appl. Magn. Reson.* **2012**, *43*, 223–236.
34. Lumata, L.; Jindal, A.K.; Merritt, M.E.; Malloy, C.R.; Sherry, A.D.; Kovacs, Z. DNP by thermal mixing under optimized conditions yields >60,000-fold enhancement of ⁸⁹Y NMR signal. *J. Am. Chem. Soc.* **2011**, *133*, 8673–8680.
35. Bowen, S.; Ardenkjær-Larsen, J.H. Formulation and utilization of choline based samples for dissolution dynamic nuclear polarization. *J. Magn. Reson.* **2013**, *236*, 26–30.
36. Doura, T.; Hata, R.; Nonaka, H.; Ichikawa, K.; Sando, S. Design of a ¹³C magnetic resonance probe using a deuterated methoxy group as a long-lived hyperpolarization unit. *Angew. Chem. Int. Ed. Engl.* **2012**, *51*, 10114–10117.
37. Nishihara, T.; Nonaka, H.; Naganuma, T.; Ichikawa, K.; Sando, S. Mouse lactate dehydrogenase X: A promising magnetic resonance reporter protein using hyperpolarized pyruvic acid derivative Y. *Chem. Sci.* **2012**, *3*, 800–806.
38. Nonaka, H.; Hata, R.; Doura, T.; Nishihara, T.; Kumagai, K.; Akakabe, M.; Tsuda, M.; Ichikawa, K.; Sando, S. A platform for designing hyperpolarized magnetic resonance chemical probes. *Nat. Commun.* **2013**, *4*, doi:10.1038/ncomms3411.
39. Wilson, D.M.; Hurd, R.E.; Keshari, K.; Van Criekinge, M.; Chen, A.P.; Nelson, S.J.; Vigneron, D.B.; Kurhanewicz, J. Generation of hyperpolarized substrates by secondary labeling with [1,1-¹³C] acetic anhydride. *Proc. Natl. Acad. Sci. USA* **2009**, *106*, 5503–5507.
40. Shanaiah, N.; Desilva, M.A.; Nagana Gowda, G.A.; Raftery, M.A.; Hainline, B.E.; Raftery, D. Class selection of amino acid metabolites in body fluids using chemical derivatization and their enhanced ¹³C NMR. *Proc. Natl. Acad. Sci. USA* **2007**, *104*, 11540–11544.
41. Pellecchia, M.; Bertini, I.; Cowburn, D.; Dalvit, C.; Giralt, E.; Jahnke, W.; James, T.L.; Homans, S.W.; Kessler, H.; Luchinat, C.; *et al.* Perspectives on NMR in drug discovery: A technique comes of age. *Nat. Rev. Drug Discov.* **2008**, *7*, 738–745.
42. Lee, Y.; Zeng, H.; Mazur, A.; Wegstroth, M.; Carlomagno, T.; Reese, M.; Lee, D.; Becker, S.; Griesinger, C.; Hilty, C. Hyperpolarized binding pocket nuclear overhauser effect for determination of competitive ligand binding. *Angew. Chem. Int. Ed. Engl.* **2012**, *51*, 5179–5182.
43. Lerche, M.H.; Meier, S.; Jensen, P.R.; Baumann, H.; Petersen, B.O.; Karlsson, M.; Duus, J.Ø.; Ardenkjær-Larsen, J.H. Study of molecular interactions with ¹³C DNP-NMR. *J. Magn. Reson.* **2010**, *203*, 52–56.
44. Lee, Y.; Zeng, H.; Rüdissler, S.; Gossert, A.D.; Hilty, C. Nuclear magnetic resonance of hyperpolarized fluorine for characterization of protein-ligand interactions. *J. Am. Chem. Soc.* **2012**, *134*, 17448–17451.
45. Keshari, K.R.; Kurhanewicz, J.; Macdonald, J.M.; Wilson, D.M. Generating contrast in hyperpolarized ¹³C MRI using ligand-receptor interactions. *Analyst* **2012**, *137*, 3427–3429.
46. Lerche, M.H.; Meier, S.; Jensen, P.R.; Hustvedt, S.O.; Karlsson, M.; Duus, J.Ø.; Ardenkjær-Larsen, J.H. Quantitative dynamic nuclear polarization-NMR on blood plasma for assays of drug metabolism. *NMR Biomed.* **2011**, *24*, 96–103.

47. Golman, K.; Zandt, R.I.; Lerche, M.; Pehrson, R.; Ardenkjær-Larsen, J.H. Metabolic imaging by hyperpolarized ^{13}C magnetic resonance imaging for *in vivo* tumor diagnosis. *Cancer Res.* **2006**, *66*, 10855–10860.
48. Jamin, Y.; Gabellieri, C.; Smyth, L.; Reynolds, S.; Robinson, S.P.; Springer, C.J.; Leach, M.O.; Payne, G.S.; Eykyn, T.R. Hyperpolarized ^{13}C magnetic resonance detection of carboxypeptidase G2 activity. *Magn. Reson. Med.* **2009**, *62*, 1300–1304.
49. Chen, A.P.; Hurd, R.E.; Gu, Y.P.; Wilson, D.M.; Cunningham, C.H. ^{13}C MR reporter probe system using dynamic nuclear polarization. *NMR Biomed.* **2011**, *24*, 514–520.
50. Jensen, P.R.; Karlsson, M.; Meier, S.; Duus, J.Ø.; Lerche, M.H. Hyperpolarized amino acids for *in vivo* assays of transaminase activity. *Chemistry* **2009**, *15*, 10010–10012.
51. Chiavazza, E.; Viale, A.; Karlsson, M.; Aime, S. ^{15}N -permethylated amino acids as efficient probes for MRI-DNP applications. *Contrast Media Mol. Imaging* **2013**, *8*, 417–421.
52. Barb, A.W.; Hekmatyar, S.K.; Glushka, J.N.; Prestegard, J.H. Exchange facilitated indirect detection of hyperpolarized $^{15}\text{ND}_2$ -amido-glutamine. *J. Magn. Reson.* **2011**, *212*, 304–310.
53. Sarkar, R.; Comment, A.; Vasos, P.R.; Jannin, S.; Grütter, R.; Bodenhausen, G.; Hall, H.; Kirik, D.; Denisov, V.P. Proton NMR of ^{15}N -choline metabolites enhanced by dynamic nuclear polarization. *J. Am. Chem. Soc.* **2009**, *131*, 16014–16015.
54. Ludwig, C.; Marin-Montesinos, I.; Saunders, M.G.; Emwas, A.H.; Pikramenou, Z.; Hammond, S.P.; Günther, U.L. Application of *ex situ* dynamic nuclear polarization in studying small molecules. *Phys. Chem. Chem. Phys.* **2010**, *12*, 5868–5871.
55. Theis, T.; Feng, Y.; Wu, T.-L.; Warren, W.S. Spin lock composite and shaped pulses for efficient and robust pumping of dark states in magnetic resonance. 2013, arXiv:1308.5666. arXiv.org e-Print archive. Available online: <http://arxiv.org/ftp/arxiv/papers/1308/1308.5666.pdf> (accessed on 16 January 2014).
56. Levitt, M.H. Singlet nuclear magnetic resonance. *Annu. Rev. Phys. Chem.* **2012**, *63*, 89–105.
57. Hurd, R.E.; Yen, Y.F.; Mayer, D.; Chen, A.; Wilson, D.; Kohler, S.; Bok, R.; Vigneron, D.; Kurhanewicz, J.; Tropp, J.; *et al.* Metabolic imaging in the anesthetized rat brain using hyperpolarized $[1-^{13}\text{C}]$ pyruvate and $[1-^{13}\text{C}]$ ethyl pyruvate. *Magn. Reson. Med.* **2010**, *63*, 1137–1143.
58. Zacharias, N.M.; Chan, H.R.; Sailasuta, N.; Ross, B.D.; Bhattacharya, P. Real-time molecular imaging of tricarboxylic acid cycle metabolism *in vivo* by hyperpolarized $1-^{13}\text{C}$ diethyl succinate. *J. Am. Chem. Soc.* **2012**, *134*, 934–943.
59. Colombo Serra, S.; Karlsson, M.; Giovenzana, G.B.; Cavallotti, C.; Tedoldi, F.; Aime, S. Hyperpolarized ^{13}C -labelled anhydrides as DNP precursors of metabolic MRI agents. *Contrast Media Mol. Imaging* **2012**, *7*, 469–477.
60. Allouche-Arnon, H.; Lerche, M.H.; Karlsson, M.; Lenkinski, R.E.; Katz-Brull, R. Deuteration of a molecular probe for DNP hyperpolarization—A new approach and validation for choline chloride. *Contrast Media Mol. Imaging* **2011**, *6*, 499–506.
61. Meier, S.; Jensen, P.R.; Duus, J.Ø. Real-time detection of central carbon metabolism in living *escherichia coli* and its response to perturbations. *FEBS Lett.* **2011**, *585*, 3133–3138.
62. Xie, X.S.; Yu, J.; Yang, W.Y. Living cells as test tubes. *Science* **2006**, *312*, 228–230.

63. Van Heeswijk, R.B.; Uffmann, K.; Comment, A.; Kurdzesau, F.; Perazzolo, C.; Cudalbu, C.; Jannin, S.; Konter, J.A.; Hautle, P.; van den Brandt, B.; *et al.* Hyperpolarized lithium-6 as a sensor of nanomolar contrast agents. *Magn. Reson. Med.* **2009**, *61*, 1489–1493.
64. Lippert, A.R.; Keshari, K.R.; Kurhanewicz, J.; Chang, C.J. A hydrogen peroxide-responsive hyperpolarized ^{13}C MRI contrast agent. *J. Am. Chem. Soc.* **2011**, *133*, 3776–3779.
65. Gallagher, F.A.; Kettunen, M.I.; Hu, D.E.; Jensen, P.R.; Zandt, R.I.; Karlsson, M.; Gisselsson, A.; Nelson, S.K.; Witney, T.H.; Bohndiek, S.E.; *et al.* Production of hyperpolarized $[1,4-^{13}\text{C}_2]$ malate from $[1,4-^{13}\text{C}_2]$ fumarate is a marker of cell necrosis and treatment response in tumors. *Proc. Natl. Acad. Sci. USA* **2009**, *106*, 19801–19806.
66. Schilling, F.; Duwel, S.; Kollisch, U.; Durst, M.; Schulte, R.F.; Glaser, S.J.; Haase, A.; Otto, A.M.; Menzel, M.I. Diffusion of hyperpolarized ^{13}C -metabolites in tumor cell spheroids using real-time NMR spectroscopy. *NMR Biomed.* **2013**, *26*, 557–568.
67. Day, S.E.; Kettunen, M.I.; Gallagher, F.A.; Hu, D.E.; Lerche, M.; Wolber, J.; Golman, K.; Ardenkjær-Larsen, J.H.; Brindle, K.M. Detecting tumor response to treatment using hyperpolarized ^{13}C magnetic resonance imaging and spectroscopy. *Nat. Med.* **2007**, *13*, 1382–1387.
68. Lodi, A.; Woods, S.M.; Ronen, S.M. Treatment with the MEK inhibitor U0126 induces decreased hyperpolarized pyruvate to lactate conversion in breast, but not prostate, cancer cells. *NMR Biomed.* **2013**, *26*, 299–306.
69. Venkatesh, H.S.; Chaumeil, M.M.; Ward, C.S.; Haas-Kogan, D.A.; James, C.D.; Ronen, S.M. Reduced phosphocholine and hyperpolarized lactate provide magnetic resonance biomarkers of PI3K/Akt/mTOR inhibition in glioblastoma. *Neuro Oncol.* **2012**, *14*, 315–325.
70. Harrison, C.; Yang, C.; Jindal, A.; DeBerardinis, R.J.; Hooshyar, M.A.; Merritt, M.; Sherry, A.D.; Malloy, C.R. Comparison of kinetic models for analysis of pyruvate-to-lactate exchange by hyperpolarized ^{13}C NMR. *NMR Biomed.* **2012**, *25*, 1286–1294.
71. Witney, T.H.; Kettunen, M.I.; Brindle, K.M. Kinetic modeling of hyperpolarized ^{13}C label exchange between pyruvate and lactate in tumor cells. *J. Biol. Chem.* **2011**, *286*, 24572–24580.
72. Karlsson, M.; Jensen, P.R.; in't Zandt, R.; Gisselsson, A.; Hansson, G.; Duus, J.Ø.; Meier, S.; Lerche, M.H. Imaging of branched chain amino acid metabolism in tumors with hyperpolarized ^{13}C ketoisocaproate. *Int. J. Cancer* **2010**, *127*, 729–736.
73. Gallagher, F.A.; Kettunen, M.I.; Day, S.E.; Lerche, M.; Brindle, K.M. ^{13}C MR spectroscopy measurements of glutaminase activity in human hepatocellular carcinoma cells using hyperpolarized ^{13}C -labeled glutamine. *Magn. Reson. Med.* **2008**, *60*, 253–257.
74. Cabella, C.; Karlsson, M.; Canape, C.; Catanzaro, G.; Colombo Serra, S.; Miragoli, L.; Poggi, L.; Uggeri, F.; Venturi, L.; Jensen, P.R.; *et al.* *In vivo* and *in vitro* liver cancer metabolism observed with hyperpolarized $[5-^{13}\text{C}]$ glutamine. *J. Magn. Reson.* **2013**, *232*, 45–52.
75. Jensen, P.R.; Peitersen, T.; Karlsson, M.; in't Zandt, R.; Gisselsson, A.; Hansson, G.; Meier, S.; Lerche, M.H. Tissue-specific short chain fatty acid metabolism and slow metabolic recovery after ischemia from hyperpolarized NMR *in vivo*. *J. Biol. Chem.* **2009**, *284*, 36077–36082.

76. Allouche-Arnon, H.; Gamliel, A.; Sosna, J.; Gomori, J.M.; Katz-Brull, R. *In vitro* visualization of betaine aldehyde synthesis and oxidation using hyperpolarized magnetic resonance spectroscopy. *Chem. Commun.* **2013**, *49*, 7076–7078.
77. Merritt, M.E.; Harrison, C.; Sherry, A.D.; Malloy, C.R.; Burgess, S.C. Flux through hepatic pyruvate carboxylase and phosphoenolpyruvate carboxykinase detected by hyperpolarized ^{13}C magnetic resonance. *Proc. Natl. Acad. Sci. USA* **2011**, *108*, 19084–19089.
78. Merritt, M.E.; Harrison, C.; Storey, C.; Jeffrey, F.M.; Sherry, A.D.; Malloy, C.R. Hyperpolarized ^{13}C allows a direct measure of flux through a single enzyme-catalyzed step by NMR. *Proc. Natl. Acad. Sci. USA* **2007**, *104*, 19773–19777.
79. Schroeder, M.A.; Cochlin, L.E.; Heather, L.C.; Clarke, K.; Radda, G.K.; Tyler, D.J. *In vivo* assessment of pyruvate dehydrogenase flux in the heart using hyperpolarized carbon-13 magnetic resonance. *Proc. Natl. Acad. Sci. USA* **2008**, *105*, 12051–12056.
80. Barb, A.W.; Hekmatyar, S.K.; Glushka, J.N.; Prestegard, J.H. Probing alanine transaminase catalysis with hyperpolarized $^{13}\text{CD}_3$ -pyruvate. *J. Magn. Reson.* **2013**, *228*, 59–65.
81. Meier, S.; Jensen, P.R.; Duus, J.Ø. Direct observation of metabolic differences in living escherichia coli strains K-12 and BL21. *ChemBioChem* **2012**, *13*, 308–310.
82. Jensen, P.R.; Karlsson, M.; Lerche, M.H.; Meier, S. Real-time DNP NMR observations of acetic acid uptake, intracellular acidification, and of consequences for glycolysis and alcoholic fermentation in yeast. *Chemistry* **2013**, *19*, 13288–13293.
83. Schroeder, M.A.; Swietach, P.; Atherton, H.J.; Gallagher, F.A.; Lee, P.; Radda, G.K.; Clarke, K.; Tyler, D.J. Measuring intracellular pH in the heart using hyperpolarized carbon dioxide and bicarbonate: A ^{13}C and ^{31}P magnetic resonance spectroscopy study. *Cardiovasc. Res.* **2010**, *86*, 82–91.
84. Hu, S.; Balakrishnan, A.; Bok, R.A.; Anderton, B.; Larson, P.E.; Nelson, S.J.; Kurhanewicz, J.; Vigneron, D.B.; Goga, A. ^{13}C -pyruvate imaging reveals alterations in glycolysis that precede c-myc-induced tumor formation and regression. *Cell. Metab.* **2011**, *14*, 131–142.
85. Meier, S.; Karlsson, M.; Jensen, P.R.; Lerche, M.H.; Duus, J.Ø. Metabolic pathway visualization in living yeast by DNP-NMR. *Mol. Biosyst.* **2011**, *7*, 2834–2836.
86. Harris, T.; Degani, H.; Frydman, L. Hyperpolarized ^{13}C NMR studies of glucose metabolism in living breast cancer cell cultures. *NMR Biomed.* **2013**, *26*, 1831–1843.
87. Rodrigues, T.B.; Serrao, E.M.; Kennedy, B.W.; Hu, D.E.; Kettunen, M.I.; Brindle, K.M. Magnetic resonance imaging of tumor glycolysis using hyperpolarized ^{13}C labeled glucose. *Nat. Med.* **2013**, doi:10.1038/nm.3416.
88. Harris, T.; Eliyahu, G.; Frydman, L.; Degani, H. Kinetics of hyperpolarized $^{13}\text{C}_1$ -pyruvate transport and metabolism in living human breast cancer cells. *Proc. Natl. Acad. Sci. USA* **2009**, *106*, 18131–18136.
89. Keshari, K.R.; Kurhanewicz, J.; Jeffries, R.E.; Wilson, D.M.; Dewar, B.J.; Van Criekinge, M.; Zierhut, M.; Vigneron, D.B.; Macdonald, J.M. Hyperpolarized ^{13}C spectroscopy and an NMR-compatible bioreactor system for the investigation of real-time cellular metabolism. *Magn. Reson. Med.* **2010**, *63*, 322–329.

90. Schroeder, M.A.; Atherton, H.J.; Ball, D.R.; Cole, M.A.; Heather, L.C.; Griffin, J.L.; Clarke, K.; Radda, G.K.; Tyler, D.J. Real-time assessment of krebs cycle metabolism using hyperpolarized ^{13}C magnetic resonance spectroscopy. *FASEB J.* **2009**, *23*, 2529–2538.
91. Ball, D.R.; Rowlands, B.; Dodd, M.S.; Le Page, L.; Ball, V.; Carr, C.A.; Clarke, K.; Tyler, D.J. Hyperpolarized butyrate: A metabolic probe of short chain fatty acid metabolism in the heart. *Magn. Reson. Med.* **2013**, doi:10.1002/mrm.24849.
92. Bohndiek, S.E.; Kettunen, M.I.; Hu, D.E.; Kennedy, B.W.; Boren, J.; Gallagher, F.A.; Brindle, K.M. Hyperpolarized [$1\text{-}^{13}\text{C}$]-ascorbic and dehydroascorbic acid: Vitamin C as a probe for imaging redox status in vivo. *J. Am. Chem. Soc.* **2011**, *133*, 11795–11801.
93. Keshari, K.R.; Kurhanewicz, J.; Bok, R.; Larson, P.E.; Vigneron, D.B.; Wilson, D.M. Hyperpolarized ^{13}C dehydroascorbate as an endogenous redox sensor for in vivo metabolic imaging. *Proc. Natl. Acad. Sci. USA* **2011**, *108*, 18606–18611.
94. Meier, S.; Solodovnikova, N.; Jensen, P.R.; Wendland, J. Sulfite action in glycolytic inhibition: *In vivo* real-time observation by hyperpolarized ^{13}C NMR spectroscopy. *ChemBioChem* **2012**, *13*, 2265–2269.
95. Gallagher, F.A.; Kettunen, M.I.; Day, S.E.; Hu, D.E.; Ardenkjær-Larsen, J.H.; in't Zandt, R.; Jensen, P.R.; Karlsson, M.; Golman, K.; Lerche, M.H.; *et al.* Magnetic resonance imaging of pH *in vivo* using hyperpolarized ^{13}C -labelled bicarbonate. *Nature* **2008**, *453*, 940–943.
96. Keshari, K.R.; Sriram, R.; Koelsch, B.L.; Van Criekinge, M.; Wilson, D.M.; Kurhanewicz, J.; Wang, Z.J. Hyperpolarized ^{13}C -pyruvate magnetic resonance reveals rapid lactate export in metastatic renal cell carcinomas. *Cancer Res.* **2013**, *73*, 529–538.
97. Pages, G.; Puckeridge, M.; Liangfeng, G.; Tan, Y.L.; Jacob, C.; Garland, M.; Kuchel, P.W. Transmembrane exchange of hyperpolarized ^{13}C -urea in human erythrocytes: Subminute timescale kinetic analysis. *Biophys. J.* **2013**, *105*, 1956–1966.
98. Albers, M.J.; Bok, R.; Chen, A.P.; Cunningham, C.H.; Zierhut, M.L.; Zhang, V.Y.; Kohler, S.J.; Tropp, J.; Hurd, R.E.; Yen, Y.F.; *et al.* Hyperpolarized ^{13}C lactate, pyruvate, and alanine: Noninvasive biomarkers for prostate cancer detection and grading. *Cancer Res.* **2008**, *68*, 8607–8615.
99. Pagès, G.; Kuchel, P.W. Mathematical modeling and data analysis of NMR experiments using hyperpolarized ^{13}C metabolites. *Magn. Reson. Insights* **2013**, *6*, 13–21.
100. Wilson, D.M.; Keshari, K.R.; Larson, P.E.; Chen, A.P.; Hu, S.; Van Criekinge, M.; Bok, R.; Nelson, S.J.; Macdonald, J.M.; Vigneron, D.B.; *et al.* Multi-compound polarization by DNP allows simultaneous assessment of multiple enzymatic activities *in vivo*. *J. Magn. Reson.* **2010**, *205*, 141–147.
101. Nelson, S.J.; Kurhanewicz, J.; Vigneron, D.B.; Larson, P.E.; Harzstark, A.L.; Ferrone, M.; van Criekinge, M.; Chang, J.W.; Bok, R.; Park, I.; *et al.* Metabolic imaging of patients with prostate cancer using hyperpolarized [$1\text{-}^{13}\text{C}$]pyruvate. *Sci. Transl. Med.* **2013**, *5*, 198ra108.
102. Ludwig, C.; Marin-Montesinos, I.; Saunders, M.G.; Günther, U.L. Optimizing the polarization matrix for *ex situ* dynamic nuclear polarization. *J. Am. Chem. Soc.* **2010**, *132*, 2508–2509.

103. Hu, S.; Larson, P.E.; Vancrackinge, M.; Leach, A.M.; Park, I.; Leon, C.; Zhou, J.; Shin, P.J.; Reed, G.; Keselman, P.; *et al.* Rapid sequential injections of hyperpolarized [1-¹³C]pyruvate *in vivo* using a sub-kelvin, multi-sample DNP polarizer. *Magn. Reson. Imaging* **2013**, *31*, 490–496.
104. Ardenkjær-Larsen, J.H.; Leach, A.M.; Clarke, N.; Urbahn, J.; Anderson, D.; Skloss, T.W. Dynamic nuclear polarization polarizer for sterile use intent. *NMR Biomed.* **2011**, *24*, 927–932.
105. Batel, M.; Krajewski, M.; Weiss, K.; With, O.; Däpp, A.; Hunkeler, A.; Gimersky, M.; Pruessmann, K.P.; Boesiger, P.; Meier, B.H.; *et al.* A multi-sample 94 GHz dissolution dynamic-nuclear-polarization system. *J. Magn. Reson.* **2012**, *214*, 166–174.
106. Bornet, A.; Melzi, R.; Perez Linde, A.J.; Hautle, P.; van den Brandt, B.; Jannin, S.; Bodenhausen, G. Boosting dissolution dynamic nuclear polarization by cross polarization. *J. Phys. Chem. Lett.* **2012**, *4*, 111–114.
107. Bucur, A.; Reynolds, S.; Kazan, S.; Alizadeh, T.; Port, M.; Tozer, G.M.; Paley, M. Parallel acquisition of hyperpolarized ¹³C₁ pyruvate metabolism: Multi-chamber MR compatible bioreactor. *Proc. Intl. Soc. Mag. Reson. Med. Salt Lake City* **2013**, 3951.
108. Cunningham, C.H.; Chen, A.P.; Albers, M.J.; Kurhanewicz, J.; Hurd, R.E.; Yen, Y.F.; Pauly, J.M.; Nelson, S.J.; Vigneron, D.B. Double spin-echo sequence for rapid spectroscopic imaging of hyperpolarized ¹³C. *J. Magn. Reson.* **2007**, *187*, 357–362.
109. Cunningham, C.H.; Chen, A.P.; Lustig, M.; Hargreaves, B.A.; Lupo, J.; Xu, D.; Kurhanewicz, J.; Hurd, R.E.; Pauly, J.M.; Nelson, S.J.; *et al.* Pulse sequence for dynamic volumetric imaging of hyperpolarized metabolic products. *J. Magn. Reson.* **2008**, *193*, 139–146.
110. Larson, P.E.; Kerr, A.B.; Chen, A.P.; Lustig, M.S.; Zierhut, M.L.; Hu, S.; Cunningham, C.H.; Pauly, J.M.; Kurhanewicz, J.; Vigneron, D.B. Multiband excitation pulses for hyperpolarized ¹³C dynamic chemical-shift imaging. *J. Magn. Reson.* **2008**, *194*, 121–127.
111. Larson, P.E.; Bok, R.; Kerr, A.B.; Lustig, M.; Hu, S.; Chen, A.P.; Nelson, S.J.; Pauly, J.M.; Kurhanewicz, J.; Vigneron, D.B. Investigation of tumor hyperpolarized [1-¹³C]-pyruvate dynamics using time-resolved multiband RF excitation echo-planar MRSI. *Magn. Reson. Med.* **2010**, *63*, 582–591.
112. Larson, P.E.; Hu, S.; Lustig, M.; Kerr, A.B.; Nelson, S.J.; Kurhanewicz, J.; Pauly, J.M.; Vigneron, D.B. Fast dynamic 3D MR spectroscopic imaging with compressed sensing and multiband excitation pulses for hyperpolarized ¹³C studies. *Magn. Reson. Med.* **2011**, *65*, 610–619.
113. Lau, A.Z.; Chen, A.P.; Hurd, R.E.; Cunningham, C.H. Spectral-spatial excitation for rapid imaging of DNP compounds. *NMR Biomed.* **2011**, *24*, 988–996.
114. Puckeridge, M.; Pages, G.; Kuchel, P.W. Simultaneous estimation of T₁ and the flip angle in hyperpolarized NMR experiments using acquisition at non-regular time intervals. *J. Magn. Reson.* **2012**, *222*, 68–73.
115. Frydman, L.; Blazina, D. Ultrafast two-dimensional nuclear magnetic resonance spectroscopy of hyperpolarized solutions. *Nat. Phys.* **2007**, *3*, 415–419.

116. Zeng, H.; Lee, Y.; Hilty, C. Quantitative rate determination by dynamic nuclear polarization enhanced NMR of a diels-alder reaction. *Anal. Chem.* **2010**, *82*, 8897–8902.
117. Chen, H.Y.; Hilty, C. Hyperpolarized hadamard spectroscopy using flow NMR. *Anal. Chem.* **2013**, *85*, 7385–7390.
118. Schröder, L.; Lowery, T.J.; Hilty, C.; Wemmer, D.E.; Pines, A. Molecular imaging using a targeted magnetic resonance hyperpolarized biosensor. *Science* **2006**, *314*, 446–449.
119. Bowen, S.; Hilty, C., Time-resolved dynamic nuclear polarization enhanced NMR spectroscopy. *Angew. Chem. Int. Ed. Engl.* **2008**, *47*, 5235–5237.
120. Leggett, J.; Hunter, R.; Granwehr, J.; Panek, R.; Perez-Linde, A.J.; Horsewill, A.J.; McMaster, J.; Smith, G.; Köckenberger, W. A dedicated spectrometer for dissolution DNP NMR spectroscopy. *Phys. Chem. Chem. Phys.* **2010**, *12*, 5883–5892.
121. Hill, D.K.; Orton, M.R.; Mariotti, E.; Boulton, J.K.; Panek, R.; Jafar, M.; Parkes, H.G.; Jamin, Y.; Miniotti, M.F.; Al-Saffar, N.M.; *et al.* Model free approach to kinetic analysis of real-time hyperpolarized ^{13}C magnetic resonance spectroscopy data. *PLoS One* **2013**, *8*, e71996, doi:10.1371/journal.pone.0071996.

MRI Optimisation

Optimal Configuration for Relaxation Times Estimation in Complex Spin Echo Imaging

Fabio Baselice, Giampaolo Ferraioli, Alessandro Grassia and Vito Pascazio

Abstract: Many pathologies can be identified by evaluating differences raised in the physical parameters of involved tissues. In a Magnetic Resonance Imaging (MRI) framework, spin-lattice T_1 and spin-spin T_2 relaxation time parameters play a major role in such an identification. In this manuscript, a theoretical study related to the evaluation of the achievable performances in the estimation of relaxation times in MRI is proposed. After a discussion about the considered acquisition model, an analysis on the ideal imaging acquisition parameters in the case of spin echo sequences, *i.e.*, echo and repetition times, is conducted. In particular, the aim of the manuscript consists in providing an empirical rule for optimal imaging parameter identification with respect to the tissues under investigation. Theoretical results are validated on different datasets in order to show the effectiveness of the presented study and of the proposed methodology.

Reprinted from *Sensors*. Cite as: Fabio Baselice , Giampaolo Ferraioli , Alessandro Grassia and Vito Pascazio Optimal Configuration for Relaxation Times Estimation in Complex Spin Echo Imaging. *Sensors* **2014**, *14*, 168–185.

1. Introduction

Relaxation times define the rate of spin magnetic equilibrium recovery in nuclear magnetic resonance (NMR) [1,2]. For each tissue, several relaxation times can be defined. Besides, the main interest is in the evaluation of two of them: the spin-lattice and the spin-spin relaxation times, commonly referred to as T_1 and T_2 , respectively. Such time constants, together with the hydrogen nuclei abundance, ρ , define the behavior of the signal generated by each resolution element.

It is largely known that the knowledge of relaxation times can provide interesting information about imaged tissues. Concerning the medical diagnostic field, many pathologies have been found to involve a significant variation of the relaxation time constants more than a variation of ρ , such as Alzheimer's disease [3], Parkinson's disease [4] and cancer [5,6]. The evaluation of the tissue relaxation times can be considered an excellent tool for improving clinical diagnosis.

Classic approaches for retrieving relaxation parameter maps of imaged tissue slices propose the estimation of T_1 and T_2 separately. In particular, the “gold standard” for spin-lattice relaxation time T_1 estimation exploits inversion recovery (IR) sequences [7,8]. However, this approach is too slow for *in vivo* clinical applications. Different evolutions have been proposed in the literature. In particular, the exploitation of spoiled gradient-recalled echo (SPGR) sequences has shown interesting results [9,10]. With respect to spin-spin relaxation time T_2 estimation, a widely used imaging sequence is the spin echo (SE) [11,12].

The magnitude of the acquired signal is typically used for relaxation parameter estimation [12–15]. Within this framework, the exponential curve fitting via the least squares (LS) algorithm is the commonly adopted estimator [11,13]. Although being very easy to be implemented and not computationally heavy, it has the disadvantage of producing biased estimations [11,16]. The alternative consists in using a maximum likelihood estimator (MLE) [12]. The MLE is asymptotically unbiased and optimal, but the function to be maximized, which is related to the statistical distribution of the MRI amplitude data, is computationally heavy, as it contains the Bessel function [17].

Recently, new approaches based on the complex decomposition of acquired data have been proposed [10,18]. The exploitation of the complex model leads to a main advantage concerning the estimation: due to the circular Gaussian distribution of the complex noise, the LS-based estimator coincides with the MLE and is asymptotically unbiased and optimal.

While much effort has been directed to improving the estimation procedures, only a little effort has been directed to the choice of the optimal imaging parameter selection (*i.e.*, the optimal choice of the MRI scanner imaging parameters). In particular, in [19], the ideal repetition times have been investigated in the case of saturation recovery spin-lattice measurements at 4.7 T, while in [20], the optimization of T_2 measurements in the case of bi-exponential systems is considered. Following the approach proposed by [15], within this paper we investigate the possibility of finding the optimal imaging parameter configuration for relaxation time estimation. As an alternative to [15], we investigate the optimal configuration not only for the T_2 time estimation, but for the joint T_2 and T_1 estimation.

Since the SE sequence-based model allows the simultaneous estimation of both spin-spin and spin-lattice relaxation times, we focus our attention on this imaging sequence. In any case, the theoretical study reported in the following could be easily adapted to different imaging sequences. Considering an SE sequence [2], the two imaging parameters involved in the acquisition procedure are the repetition time, T_R , and the echo time, T_E . We briefly recall that these two parameters allow the scanner to differently interact with tissues characterized by different T_1 and T_2 values. By exploiting different T_R and T_E combinations, it is possible to emphasize the effect of one tissue intrinsic parameter with respect to others, obtaining the well-known ρ -weighted, T_1 -weighted or T_2 -weighted images.

Given the previously mentioned motivations, we present a deeper analysis of the complex SE model considered in [18] extended to three parameters (*i.e.*, ρ , T_1 and T_2). The analysis is conducted exploiting the Cramer–Rao lower bounds (CRLBs) [16]. Since CRLBs provide the best achievable performances in the unbiased estimation of one or more parameters, by minimizing them with respect to the MR scanner imaging parameters, it is possible to find the optimal acquisition configuration for the relaxation time estimation. Practically speaking, we look for the acquisition parameters that allow achieving lower relaxation time estimation errors. The result of the study is the introduction of a general empirical rule for determining the optimal (with respect to CRLBs) MRI scanner parameter configuration. In particular, the identification of these parameters in the case of several tissues has been conducted. The effectiveness of the theoretical results and of the empirical rule is validated and verified on different datasets.

The manuscript is organized as follows: in Section 2, the acquisition model for an MRI spin echo sequence is presented, and in Section 3, the achievable performances of the estimation are analyzed via the CRLBs. In Section 4, the CRLB-based empirical rule for the optimal acquisition parameter configuration is presented. Finally, validation on different datasets is presented in Section 5, and conclusions are drawn.

2. The Model

Let us consider an MRI acquisition system using a spin echo imaging sequence. The amplitude of the recorded complex signal after the image formation process, *i.e.*, after the computation of the 2D Fourier transform, is related to the tissue parameters, ρ , T_1 and T_2 , via [2,21]:

$$f(\boldsymbol{\theta}) = \rho \exp\left(-\frac{T_E}{T_2}\right) \left(1 - \exp\left(-\frac{T_R}{T_1}\right)\right) \quad (1)$$

where T_E and T_R are the echo and repetition time, respectively, which are two imaging parameters that can be set in the MRI scanner, and $\boldsymbol{\theta} = [\rho \ T_1 \ T_2]^T$ is the vector containing the tissue parameters in which we are interested. Note that Equation (1) is valid in the case of a homogeneous imaged object. In the case of clinical data, the presence of different hydrogen environments within each voxel has to be taken into account. The acquisition model reported in Equation (1), which is a solution to Bloch equations, assuming that T_E is short with respect to T_R , is related to the noise-free case and does not take into account the dependency on the static magnetic field, B . Considering noise, in the complex domain, the model becomes:

$$y = y_R + iy_I = f(\boldsymbol{\theta}) \exp(i\phi) + (n_R + in_I) \quad (2)$$

where n_R and n_I are the real and imaginary parts of the noise samples, which are distributed as independent circularly Gaussian variables [22], and ϕ represents the angle of the complex data [23, 24]. Thus, the statistical distributions of the real and imaginary parts of the acquired signal are:

$$\begin{aligned} f_{Y_R}(y_R) &= \frac{1}{\sqrt{2\pi\sigma^2}} \exp\left(-\frac{(y_R - f(\boldsymbol{\theta}) \cos(\phi))^2}{2\sigma^2}\right) \\ f_{Y_I}(y_I) &= \frac{1}{\sqrt{2\pi\sigma^2}} \exp\left(-\frac{(y_I - f(\boldsymbol{\theta}) \sin(\phi))^2}{2\sigma^2}\right) \end{aligned} \quad (3)$$

where σ^2 is the variance of real and imaginary noise components. Due to the independence of the real and imaginary parts of noise, the joint statistical distribution of y_R and y_I is the product of the two probability density functions of Equation (3).

Once N acquisitions with different T_R and T_E combinations have been recorded and collected in the data vector $\mathbf{y} = [\mathbf{y}_R, \mathbf{y}_I]$, with $\mathbf{y}_R = [y_R(1), \dots, y_R(N)]$ and $\mathbf{y}_I = [y_I(1), \dots, y_I(N)]$, we can derive the likelihood function from the factorization of the Probability Density Functions (PDFs):

$$p(\mathbf{y}; \boldsymbol{\theta}) = \prod_{k=1}^N \left(\frac{1}{\sqrt{2\pi\sigma^2}}\right)^2 \exp\left\{-\frac{[y_R(k) - f(\boldsymbol{\theta}) \cos(\phi)]^2}{2\sigma^2} - \frac{[y_I(k) - f(\boldsymbol{\theta}) \sin(\phi)]^2}{2\sigma^2}\right\} \quad (4)$$

Starting from the likelihood function of Equation (4), the CRLBs for θ are derived and analyzed in the following sections.

3. Cramer–Rao Lower Bounds Evaluations

In order to evaluate the performances of the optimal estimator for the model presented in Section 2, the Cramer–Rao lower bounds have to be computed. According to Statistical Estimation Theory [16], given an observation model, the accuracy of any estimator can be evaluated according to its mean and its variance. In particular, in order to be optimal, an estimator needs to have its mean equal to the value to be estimated (*i.e.*, unbiased estimator) and to have the smallest possible variance. CRLBs represent the lower bound of the variance of any unbiased estimator, resulting an interesting and powerful tool for evaluating the achievable performances of a considered model. By computing the CRLBs for different configuration of the parameters involved in the acquisition model, it is possible to find the best parameter configuration, the one that provides the minimum values of CRLBs (*i.e.*, the minimum achievable variances). Considering the vector parameter θ , the minimum variance that any unbiased estimator of parameter θ_i can reach is provided by the i -th diagonal element of the inverse of matrix \mathbf{I} [16]:

$$\text{var}(\hat{\theta}_i) \geq [\mathbf{I}^{-1}(\theta)]_{ii} \quad (5)$$

with \mathbf{I} being the Fisher matrix, which is equal to:

$$\mathbf{I}(\theta) = \begin{bmatrix} -E \left[\frac{\partial^2 \ln p(y;\theta)}{\partial \rho^2} \right] & -E \left[\frac{\partial^2 \ln p(y;\theta)}{\partial \rho \partial T_1} \right] & -E \left[\frac{\partial^2 \ln p(y;\theta)}{\partial \rho \partial T_2} \right] \\ -E \left[\frac{\partial^2 \ln p(y;\theta)}{\partial \rho \partial T_1} \right] & -E \left[\frac{\partial^2 \ln p(y;\theta)}{\partial T_1^2} \right] & -E \left[\frac{\partial^2 \ln p(y;\theta)}{\partial T_1 \partial T_2} \right] \\ -E \left[\frac{\partial^2 \ln p(y;\theta)}{\partial \rho \partial T_2} \right] & -E \left[\frac{\partial^2 \ln p(y;\theta)}{\partial T_1 \partial T_2} \right] & -E \left[\frac{\partial^2 \ln p(y;\theta)}{\partial T_2^2} \right] \end{bmatrix} \quad (6)$$

where $E[\cdot]$ is the expected value operator.

A closed form for the second order derivatives of Equation (6) has been derived and reported in the Appendix. The closed form greatly improves the computational accuracy of the CRLB evaluation and decreases the computational burden of the simulations reported in the following.

In order to experimentally compute the matrix of Equation (6), Monte Carlo simulations with 10^5 iterations have been considered for statistical average computation.

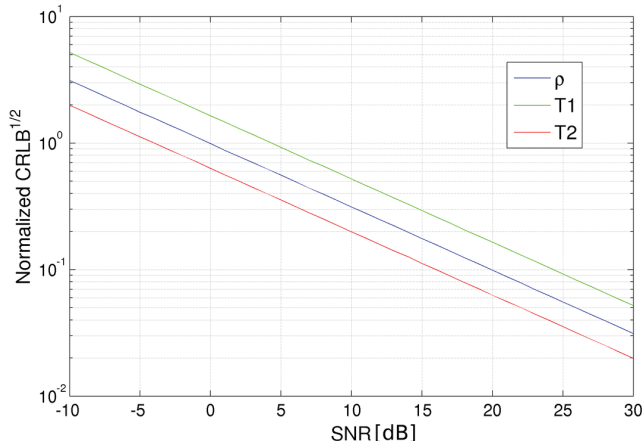
For the following evaluations, we considered a tissue, named A , with parameters $\theta = [\rho \ T_1 \ T_2]^T = [2.5 \ 1600 \ 90]^T$. Note that within the paper, all relaxation times are expressed in milliseconds, while the proton density is in percentage. The following simulations are reported and analyzed in order to investigate CRLB dependency and behavior with respect to the signal-to-noise ratio (SNR), the number of acquisitions and the scanner acquisition parameters.

3.1. CRLB vs. SNR

Let us start by computing CRLBs varying the noise standard deviation (*i.e.*, the SNR). Sixteen images have been considered, which refer to the all combinations of four T_R and four T_E values

equally spaced in the intervals [500, 3500] ms and [80, 350] ms, respectively. Note that the lower T_E value has been set according to the minimum echo time for the SE sequence accepted by the Philips Achieva 3.0 T, the MR scanner we worked on, while the maximum value of T_R has been set in order to limit the global acquisition time. The CRLBs in the case of different SNRs are shown in Figure 1. As expected, the square root of the CRLBs related to all considered parameters decreases with respect to SNR growth, *i.e.*, high SNRs positively affect the estimator performances. In the considered range of SNRs, no saturation appears. Very similar behaviors are obtained varying T_R and T_E combinations. Globally, it can be stated that SNR linearly affects CRLBs, so in the following the results of each simulation can be easily extended to any SNR configuration.

Figure 1. Square root of the Cramer–Rao lower bound (CRLB) for proton density (blue), spin-lattice (T_1) relaxation time (green) and spin-spin (T_2) relaxation time (red) for different signal-to-noise ratio values expressed in decibels (logarithmic scale). CRLB values have been normalized for the parameter values in order to be plotted in the same graph.

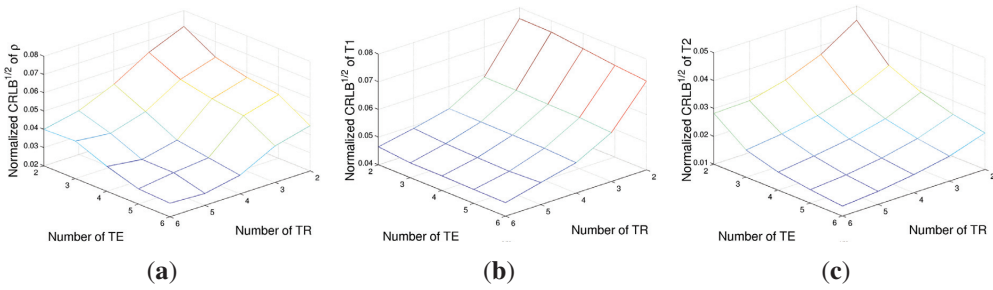


3.2. CRLB vs. the Number of Acquisitions

A second case study has been conducted in order to evaluate the advantage of increasing the number of acquisitions. Two vectors of T_R and T_E , of a length of N_R and N_E , respectively, have been generated in the [500, 3500] ms (for T_R) and [80, 350] ms (for T_E) intervals. The square root of CRLBs, *i.e.*, the minimum achievable standard deviations, are reported in Figure 2 for ρ , T_1 and T_2 , respectively, for different N_R and N_E combinations. The noise variance has been fixed in order to obtain an SNR of 16 dB for the image with the lowest signal intensity (*i.e.*, $T_R = 500$ ms and $T_E = 80$ ms). It can be noted that the number of T_R values mainly affects the achievable performances with respect to T_1 estimation, while CRLBs of ρ and T_2 are dependent on the number of both T_E and T_R values, with a higher dependency on echo times. The results confirm the strict connections between T_R and T_1 and also between T_E and T_2 , as expected from the exponential terms of the SE signal

model (Equation (1)). However, it is interesting to stress how the CRLB of ρ is very tightly related to T_E values rather than to T_R ones.

Figure 2. The square root of the CRLB of proton density ρ (a), T_1 relaxation time (b) and T_2 relaxation time (c) for different numbers of acquisitions.



3.3. CRLB vs. T_R and T_E Values

As a further case study, an evaluation of CRLBs with respect to T_R and T_E values with a fixed number of acquisition has been performed. Four acquisitions have been considered, corresponding to all the combinations of $\mathbf{T}_R = [T_R(1), T_R(2)]$ and $\mathbf{T}_E = [T_E(1), T_E(2)]$. CRLBs have been computed while varying $T_R(1)$ and $T_E(2)$ and considering $T_R(2) = 3,500$ ms and $T_E(1) = 80$ ms, again in the case of tissue *A* parameters. Results are reported in Figures 3. Figure 4a shows that the ρ estimation would prefer low $T_R(1)$ and high $T_E(2)$ values. The behaviors of CRLBs for T_1 and T_2 differ remarkably from Figure 4a, as it can be noticed that the estimation of T_1 is almost unresponsive with respect to $T_E(2)$ values, as far as T_2 estimation with respect to $T_R(1)$. In particular, for the estimation of T_1 , the ideal $T_R(1)$ is as low as possible, while the ideal $T_E(2)$ for the estimation of T_2 is between 150 and 250 ms. For this experiment, a second dataset has also been considered: the same simulation has been conducted in the case of a second tissue, named *B*, with parameters $\boldsymbol{\theta} = [\rho \ T_1 \ T_2]^T = [2.8 \ 1800 \ 60]^T$, in order to know if the results of Figure 3 are always valid or if they are highly dependent on the considered tissue. The results are reported in Figure 4. It can be noticed that the lower regions remain in the same position, although being increased in value, but for CRLBs of ρ and T_2 , the ideal $T_E(2)$ range reduces to [130, 180] ms. This is mainly due to the lower T_2 value of tissue *B* with respect to tissue *A*. Thus, it can be concluded that the general trend is confirmed, although the position of the global minimum is strictly related to the considered tissue. These two simulations show that the choice of optimal parameters is strictly dependent on the relaxation times of the imaged tissues. In the next section, we investigate the possibility of finding a rule for ideal imaging parameter identification.

Figure 3. The square root of the CRLB of proton density ρ (a), T_1 relaxation time (b) and T_2 relaxation time (c) for different combinations of T_R and T_E values in the case of $\rho = 2.5$, $T_1 = 1,600$ ms and $T_2 = 90$ ms.

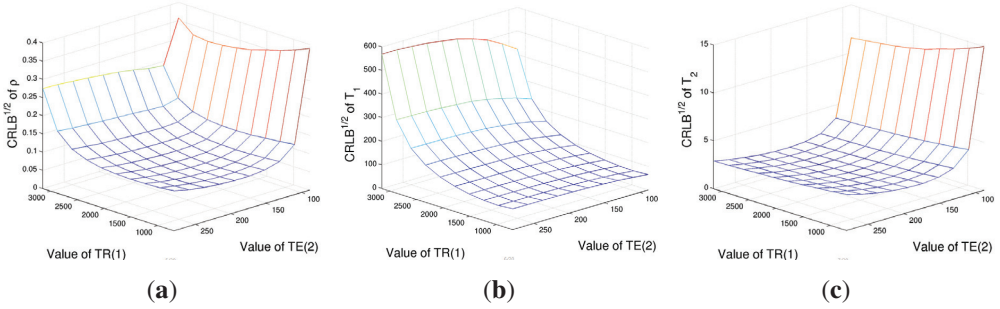
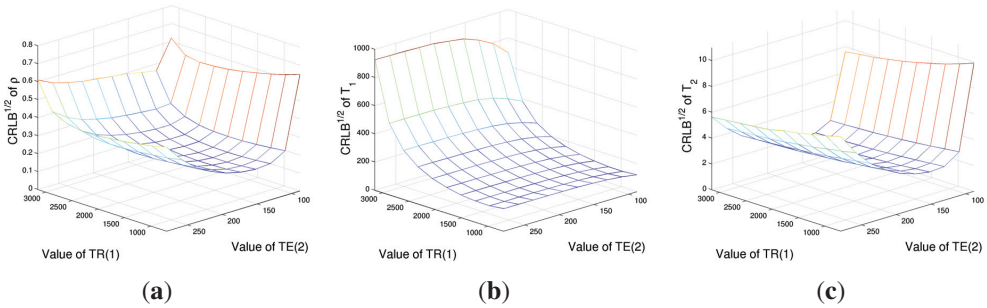


Figure 4. The square root of the CRLB of proton density ρ (a), T_1 relaxation time (b) and T_2 relaxation time (c) for different combinations of T_R and T_E values in the case of $\rho = 2.8$, $T_1 = 1,800$ ms and $T_2 = 60$ ms.



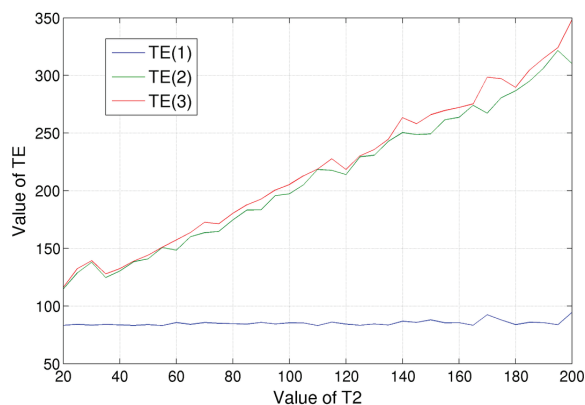
4. Optimal Parameter Configuration

After the evaluation of ρ , T_1 and T_2 CRLB behaviors, an analysis dedicated to the computation of optimal T_R and T_E combinations is presented. In the following, it will be shown that a proper imaging configuration can greatly improve the performances with respect to such a choice. In particular, the aim of this section is to identify the ideal imaging parameters with respect to imaged tissues.

Let us show how the optimal imaging parameters can be determined. Initially, we have focused on the minimization of T_2 CRLB, which consist in finding T_E values that minimize the element (3, 3) of the inverse of the Fisher matrix, $\mathbf{I}(\theta)$, of Equation (6) for different spin-spin relaxation times T_2 . The optimization has been performed by searching the three optimal T_E values in the [82, 350] ms range for a fixed value of T_R . The evaluation has been done varying the tissue T_2 relaxation times in the [20, 200] ms range, obtaining the results shown in Figure 5. Some considerations can be drawn:

- there is no T_E value combination that is simultaneously ideal for tissues with different spin-spin relaxation times. As a consequence, we can only find the T_E combination that is ideal for a specific tissue;
- by analyzing Figure 5, it can be noticed that the lowest T_E value of the ideal configuration is always equal to the lower bound of the considered variability range, which, in our case, was fixed to 82 ms. As stated before, this value is the minimum echo time for the SE sequence accepted by the Philips Achieva 3.0 T, the MR scanner we worked on;
- the two higher T_E values, which are the red and the green lines of Figure 5, practically coincide. This can be explained considering that we are interested in the estimation of relaxation times, *i.e.*, of decay rates. In order to achieve such a goal, it is crucial that the measurement of the signal decrease, *i.e.*, the ratio of the signal acquired in two different echo times. Therefore, instead of values T_E , it is only important the difference between them. A third echo time, $T_E(3)$, equal to $T_E(2)$, allows us to compute twice the signal decay, which is the quantity in which we are interested;
- the red and the green lines of Figure 5 show a clear trend: their values grow linearly when increasing T_2 . In particular, we found that the distance with the blue line (*i.e.*, lowest T_E , 82 ms) is a little bit bigger than the value of the considered spin-spin relaxation time, T_2 . For example, in the case of $T_2 = 100$ ms, the ideal echo times were $T_E = [83, 197, 205]$ ms; the last two values are approximately 110% of $(T_E(1) + T_2)$. By considering the other simulated T_2 values, we found that this coefficient is $110\% \pm 10\%$. Within this range, the CRLB of T_2 can be considered constant.

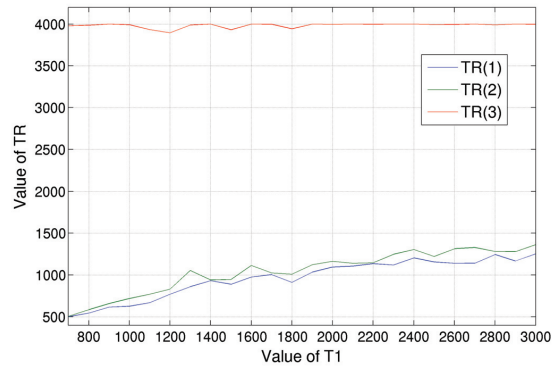
Figure 5. T_E values that minimize the CRLB of T_2 for tissues with different spin-spin relaxation times, T_2 . Three values have been considered: the blue line is for the lowest T_E value, the red line for the highest one and green for the intermediate one.



From these simulations, we can derive an empirical rule for the optimal T_E selection: the lower one should be fixed to the minimum value accepted by the MR scanner, while the other values should be set in the range of 100%–120% of the value of $(T_E(1) + T_2)$, considering the T_2 of the tissue in which we are interested.

A similar evaluation has been conducted for the minimization of T_1 CRLB varying MRI scanner repetition times T_R , with a fixed value of T_E ; the results are shown in Figure 6. The higher T_R value is fixed to the right edge of the considered variability range, which we set equal to 4,000 ms. The intermediate and low T_R s have similar values, which, starting from 500 ms in the case of tissue with $T_1 = 700$ ms, grow almost linearly up to 1,400 ms for tissues with higher T_1 (about 3,000 ms). It is hard to determine an empirical rule in this case; anyway, we can say that a choice of around 1,000 ms for $T_R(1)$ and $T_R(2)$ will fit a wide class of tissues, *i.e.*, those with $1,200 < T_1 < 2,000$ ms.

Figure 6. T_R values that minimize the CRLB of T_1 for tissues with different spin-lattice relaxation times, T_1 . Three values have been considered: the red line is for the highest T_R value, the blue line for the lowest one and green for the intermediate one.



Concluding this section, one more evaluation has been conducted. Instead of optimizing T_R and T_E values separately, a joint minimization has been done. Nine acquisitions have been considered, related to three repetition and three echo times. Among the three values, the lower and the higher have been fixed to the search range bounds, so only the intermediate T_E and T_R values were variable. Results are shown in Figure 7, respectively. It is evident from the figure that T_E values can be considered independent from T_1 , as far as T_R from T_2 , proving the correctness of the separate optimization of the echo and repetition times. In particular, from Figure 7a, we can state that tissues with equal T_2 , but very different T_1 values share the same three optimal echo times for T_2 estimation, and *vice versa*. That said, the behaviors of Figures 5 and 6, *i.e.*, the minimization, one parameter at a time, are confirmed.

In order to easily apply the obtained results, the ideal acquisition parameters for different tissues have been computed exploiting CRLB minimization in the case of a 1.5 T and a 3 T MRI scanner. The results are shown in Tables 1 and 2 for T_1 and T_2 , respectively. According to the results reported in Figure 7, the minimizations have been computed independently for spin-lattice and spin-spin relaxation time estimation. Tissue relaxation times have been simulated according to reference values present in the literature [25], which are reported in Table 3.

In Table 4, optimal echo times in the case of gray matter T_2 estimation for different minimum T_E are reported. It can be noticed that the lower optimal echo time is always the minimum and that the empirical rule is confirmed.

Figure 7. Optimal $T_E(2)$ (a) and $T_R(2)$ (b) values considering nine acquisitions in the case of tissues with different T_1 and T_2 relaxation times. It can be noticed that the $T_E(2)$ value is substantially independent from tissue spin-lattice relaxation time T_1 , as far as $T_R(2)$ from spin-spin relaxation time T_2 .

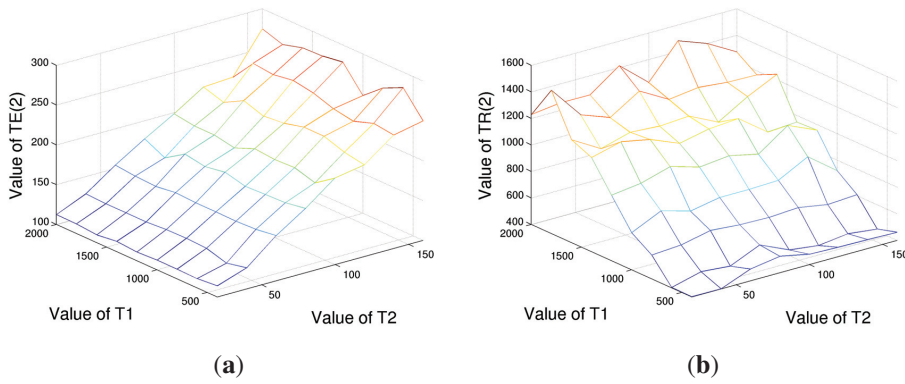


Table 1. Optimal repetition times, T_R , for T_1 estimation in case of different tissues and numbers of acquisitions at 1.5 T and 3 T.

Tissue	1.5T			3T		
	2 images	3 images	4 images	2 images	3 images	4 images
liver	490; 4000	490; 510; 4,000	380; 490; 510; 4,000	650; 4,000	570; 650; 4,000	570; 570; 650; 4,000
skeletal muscle	720; 4,000	720; 720; 4,000	680; 720; 720; 4,000	1,090; 4,000	990; 1,090; 4,000	870; 990; 1,090; 4,000
heart	840; 4,000	770; 840; 4,000	770; 790; 840; 4,000	1,060; 4,000	910; 1,060; 4,000	770; 910; 1,060; 4,000
kidney	570; 4,000	430; 570; 4,000	430; 460; 570; 4,000	910; 4,000	790; 910; 4,000	750; 790; 910; 4,000
cartilage	760; 4,000	690; 760; 4,000	630; 690; 760; 4,000	880; 4,000	770; 880; 4,000	770; 780; 880; 4,000
white matter	690; 4,000	690; 710; 4,000	640; 690; 710; 4,000	850; 4,000	780; 850; 4,000	730; 780; 850; 4,000
gray matter	920; 4,000	840; 920; 4,000	800; 840; 920; 4,000	1,150; 4,000	980; 1,150; 4,000	910; 980; 1,150; 4,000
optic nerve	960; 4,000	960; 1,060; 4,000	960; 1,060; 1,100; 4,000	970; 4,000	910; 970; 4,000	910; 970; 1,030; 4,000
spinal cord	600; 4,000	550; 600; 4,000	450; 550; 600; 4,000	760; 4,000	660; 760; 4,000	660; 700; 760; 4,000
blood	1,120; 4,000	840; 1,120; 4,000	830; 840; 1,120; 4,000	1,120; 4,000	1,040; 1,120; 4,000	1,030; 1,040; 1,120; 4,000

Note that the usefulness of a proper T_R and T_E selection, besides the lower estimation variance, consists also in reducing the acquisition time. In order to make such an advantage evident, Table 5 reports the achievable performance in the case of 16 images ($4 T_R$ and $4 T_E$ values) when moving from equally spaced to optimized acquisition parameters. In particular, the last column of Table 5 shows that 12 acquisitions, with properly chosen parameters, can lead to better results with respect to 16 equally spaced images, while definitely reducing the global acquisition time.

Table 2. Optimal echo times T_E for T_2 estimation in case of different tissues and numbers of acquisitions at 1.5 T and 3 T.

Tissue	1.5T			3T		
	2 images	3 images	4 images	2 images	3 images	4 images
liver	82; 134	82; 134; 138	82; 134; 138; 146	82; 134	82; 134; 134	82; 134; 134; 142
skeletal muscle	82; 130	82; 130; 138	82; 130; 138; 1;400	82; 132	82; 132; 144	82; 132; 144; 146
heart	82; 124	82; 124; 134	82; 124; 134; 136	82; 132	82; 132; 140	82; 132; 140; 148
kidney	82; 158	82; 158; 168	82; 158; 168; 188	82; 144	82; 144; 154	82; 144; 154; 164
cartilage	82; 116	82; 116; 116	82; 116; 116; 122	82; 114	82; 112; 114	82; 112; 114; 120
white matter	82; 162	82; 162; 188	82; 162; 188; 208	82; 162	82; 162; 178	82; 162; 178; 214
gray matter	82; 210	82; 210; 244	82; 210; 244; 280	82; 192	82; 192; 218	82; 192; 218; 240
optic nerve	82; 192	82; 192; 222	82; 192; 222; 250	82; 168	82; 168; 196	82; 168; 196; 240
spinal cord	82; 160	82; 160; 192	82; 160; 192; 208	82; 174	82; 174; 190	82; 174; 190; 212
blood	82; 516	82; 516; 558	82; 516; 558; 620	82; 436	82; 436; 562	82; 436; 562; 588

Table 3. Mean spin-lattice and spin-spin relaxation times for the considered tissues at 1.5 T and 3 T.

Tissue	1.5T		3T	
	T_1	T_2	T_1	T_2
liver	576	46	818	42
skeletal muscle	1,008	44	1,412	50
heart	1,030	40	1,471	47
kidney	690	55	1,194	56
cartilage	1,038	44	1,156	43
white matter	884	72	1,084	69
gray matter	1,124	95	1,820	99
optic nerve	815	77	1,083	78
spinal cord	745	74	993	78
blood	1,441	290	1,932	275

Table 4. Optimal echo times for T_2 estimation of gray matter for acquisitions at 1.5 T in the case of different minimum T_E values.

	2 images	3 images	4 images
minimum $T_E = 82$ ms	82, 210	82, 210, 244	82, 210, 244, 280
minimum $T_E = 50$ ms	50, 182	50, 182, 212	50, 182, 212, 234
minimum $T_E = 20$ ms	20, 158	20, 158, 180	20, 158, 180, 210

Table 5. CRLBs for equally and optimally spaced T_R and T_E values.

Tissue parameter	CRLB: 16 images Equispaced	CRLB: 16 images Optimized	Improvement (%)	CRLB: 12 images Optimized	Improvement (%)
ρ	0.1562	0.1291	17.34%	0.1506	3.58%
T_1	3144	1483	52.83%	1.960	37.66%
T_2	2.708	1.808	33.23%	2.144	20.83%

5. Numerical Experiments

Within this section, some numerical results are shown in order to validate the advantage of the optimal selection of the imaging parameters according to the previously reported theoretical studies. A tissue with parameters $[\rho \ T_1 \ T_2] = [5.5 \ 775 \ 44.5]$ has been considered. Three noisy datasets (SNR = 30 dB) have been simulated, each one composed of four acquisitions. The parameters of Dataset 1 have been chosen according to the results of Figures 5 and 6 in order to optimize the estimation for the considered tissue. Datasets 2 and 3 have been generated with non-ideal parameters. The dataset characteristics are summarized in Table 6.

Table 6. Acquisition parameters: three datasets composed of four images.

	Repetition Times (s)	Echo Times (ms)	SNR (dB)
Dataset 1	0.55, 4.0	80, 140	30
Dataset 2	0.75, 4.0	80, 170	30
Dataset 3	0.90, 4.0	80, 200	30

To asses and validate the CRLB studies, the estimation of the relaxation times has been implemented via Monte Carlo simulation. In particular, a maximum likelihood estimator (MLE) has been set up in the complex domain. Considering that the noise is circularly Gaussian distributed, MLE corresponds to a non-linear least squares (NLLS) estimator [18]. It is important to note that the previously reported theoretical studies about the optimal selection of the imaging parameters are valid for any unbiased estimator, since CRLBs are related only to the acquisition model. Among different estimators, NLLS has been chosen thanks to its low computational times and complexity. We recall that the choice of the optimal estimator is not the aim of this paper.

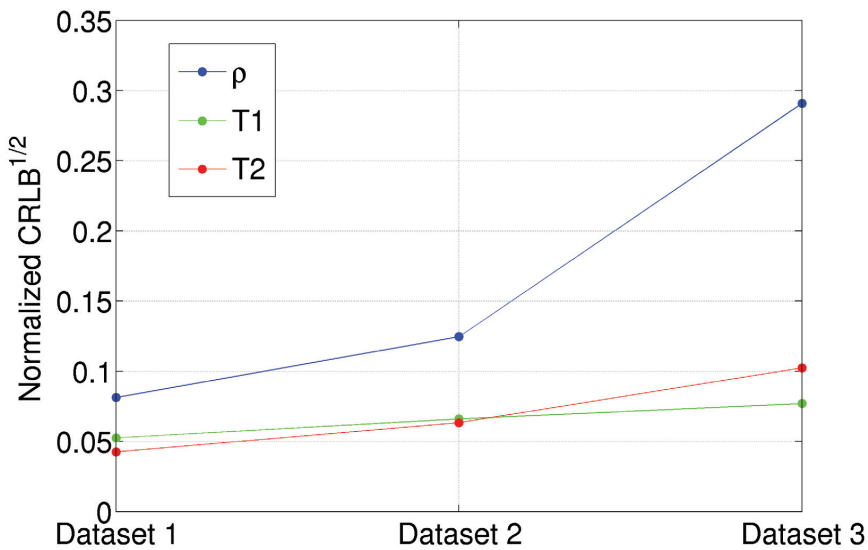
Table 7. Estimator performances: three datasets composed of four images.

Parameter	True Value	Dataset 1		Dataset 2		Dataset 3	
		Mean	Variance	Mean	Variance	Mean	Variance
$\hat{\rho}$	5.5	5.52	0.20	5.58	0.47	5.79	2.56
\hat{T}_1	775	776.1	1662	776.5	2615	776.5	3,566
\hat{T}_2	44.5	44.54	3.58	44.49	7.95	44.32	20.82

The NLLS estimator for the ρ , T_1 and T_2 parameters has been implemented on the three datasets of Table 6. A quantitative analysis of the results, in terms of estimation means and variances, has been reported in Table 7. By analyzing it, it is possible to infer that the estimator means are very close, while variances significantly vary from one dataset to the other. In particular, the smallest variances are obtained in the case of Dataset 1. This fully agrees with the theoretical studies reported in Section 4; as a matter of fact, Dataset 1 has been generated by using the previously developed optimal

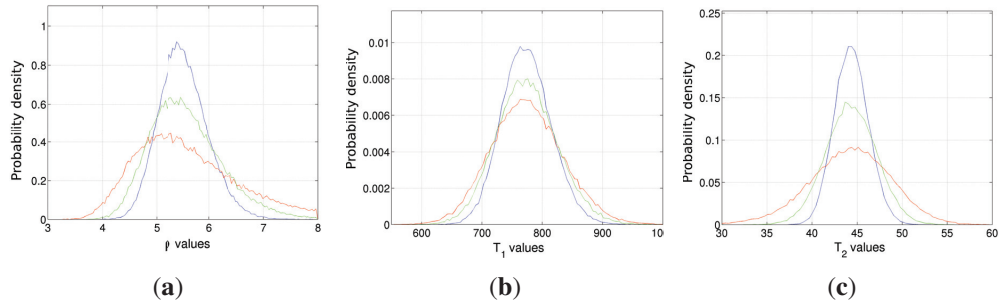
T_E and T_R parameter selection for the considered relaxation times. It is evident that choosing a non-ideal imaging parameters configuration can lead to very inaccurate results. For example, the T_2 estimator variance of Dataset 3 is approximately six times larger than the one of Dataset 1. In order to visualize such results, the normalized standard deviations of ρ , T_1 and T_2 in the case of Datasets 1, 2 and 3 are reported in Figure 8.

Figure 8. Square root of the CRLB for proton density (blue), spin-lattice (T_1) relaxation time (green) and spin-spin (T_2) relaxation time (red) for the dataset with different acquisition parameters. CRLBs values have been normalized for the parameter values in order to be plotted in the same graph.



The higher achievable accuracy in the case of optimal imaging parameters selection can also be inferred from the empirical probability density functions of the estimators, reported in Figure 9. In each image, the blue, the green and the red curves refer to Datasets 1, 2 and 3 of Table 6. As expected, most of the presented estimators follow a Gaussian distribution, with a different width. Blue curves obtained using Dataset 1, characterized by the optimal T_R/T_E values for the simulated tissue, are always the narrowest (smallest variances). Moving to curves obtained from Datasets 2 and 3, the estimation error becomes larger. Moreover, in the case of the ρ estimator, the results start showing a bias in the case of Dataset 3, *i.e.*, the one with the *worst* acquisition parameters, and the empirical PDF does not look like a Gaussian function any more.

Figure 9. The empirical probability density function of the ρ (a), T_1 (b) and T_2 (c) estimators in the case of Dataset 1 (blue line), Dataset 2 (green line) and Dataset 3 (red line). The true values are $\rho = 5.5$, $T_1 = 775$ and $T_2 = 44.5$, respectively.



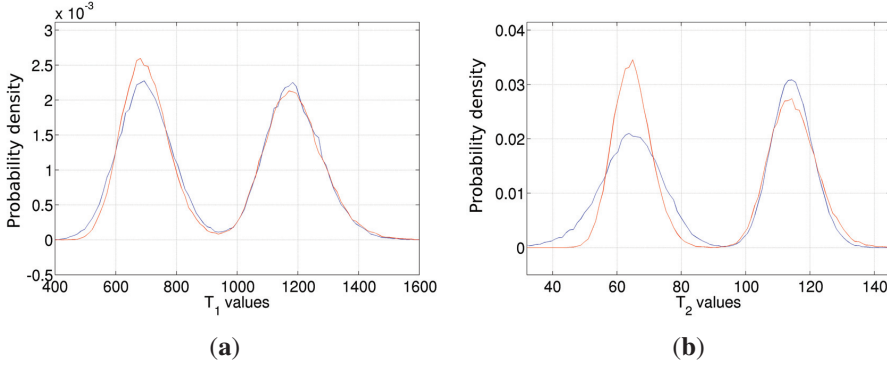
Finally, one further simulation is presented. Signals from two different tissues have been simulated, with parameters $[\rho \ T_1 \ T_2] = [5 \ 700 \ 68]$ (spinal cord) and $[\rho \ T_1 \ T_2] = [5 \ 1190 \ 115]$ (gray matter). Two datasets composed of four acquisitions have been generated, with parameters reported in Table 8. Taking into account the developed procedure, Dataset 1 parameters represent the ideal configuration for the first tissue, while Dataset 2 is the ideal for the second one.

The empirical probability density functions for T_1 and T_2 estimators have been computed for both datasets and are shown in Figures 10, respectively. Once again, The results validate the theoretical study of Section 4. Estimation based on Dataset 1 (red line) shows lower variance in the case of spinal cord, *i.e.*, the tissue with the lowest relaxation times (the left peaks of Figures 10). Considering gray matter, Dataset 2 (blue line) -based estimation gives better results, although the improvement of the T_1 estimator is not pronounced. Once again, the result highlights the need of properly tuning the acquisition parameters.

Table 8. Acquisition parameters in the case of two tissues; the datasets are composed of four images.

	Repetition Times (s)	Echo Times (ms)	SNR (dB)
Dataset 1	0.55 4.0	82, 160	26
Dataset 2	0.80, 4.0	82, 250	26

Figure 10. The empirical probability density function of the T_1 (a) and T_2 (b) estimators in the case of Dataset 1 (blue line) and Dataset 2 (red line). Dataset 1 (blue line) imaging parameters are ideal for tissues with lower T_1 and T_2 . On the contrary, Dataset 2 (red line) is ideal for the tissue with higher relaxation times.



6. Conclusions

Within this paper, an analysis on the spin echo signal model in MR imaging has been addressed. In particular, Cramer–Rao lower bounds for relaxation time estimation in the case of a complex Gaussian acquisition model have been evaluated. Several CRLB-based evaluations have been presented in order to investigate the possibility of finding the optimal, in terms of reconstruction accuracy, imaging parameter configuration for the estimation of T_1 and T_2 maps. According to these theoretical studies, an empirical rule together with the identification of the optimal imaging parameter combination (echo and repetition times) in case of different tissues (different T_1 and T_2) has been proposed. Moreover, the optimal acquisition parameters for several tissues have been computed for both 1.5 T and 3 T acquisitions. The theoretical results have been numerically validated on different datasets. It should be underlined that such optimal parameters are independent from the implemented estimators, as CRLBs only depend on the signal model. Once the data have been acquired, different estimators proposed in the literature can be applied. It is important to underline that the theoretical studies reported within the paper can be easily adapted to different imaging sequences.

Appendix

From [16], CRLBs may also be expressed in a slightly different form with respect to Equation (6). In particular, it yields:

$$- E \left[\frac{\partial^2 \ln p(y; \boldsymbol{\theta})}{\partial \boldsymbol{\theta}^2} \right] = E \left[\left(\frac{\partial \ln p(y; \boldsymbol{\theta})}{\partial \boldsymbol{\theta}} \right)^2 \right] \quad (7)$$

From Equation (4), the log-likelihood function related to N complex acquisitions is:

$$\log[p(\mathbf{y}; \boldsymbol{\theta})] = -N \log(2\pi\sigma^2) - \frac{1}{2\sigma^2} \sum_{k=1}^N [f^2(\boldsymbol{\theta}) + y_R^2(k) + y_I^2(k) - 2f(\boldsymbol{\theta})y_R(k) \cos(\phi) - 2f(\boldsymbol{\theta})y_I(k) \sin(\phi)]$$

where subscript k refers to k -th acquisition, *i.e.*, the MRI scan with parameters $T_R(k)$, $T_E(k)$.

The partial derivatives can be computed as:

$$\begin{aligned} \frac{\partial \ln p(\mathbf{y}; \boldsymbol{\theta})}{\partial \rho} &= -\frac{1}{2\sigma^2} \sum_{k=1}^N \left[\frac{\partial f^2(\boldsymbol{\theta})}{\partial \rho} - 2 \frac{\partial f(\boldsymbol{\theta})}{\partial \rho} (y_R(k) \cos(\phi) + y_I(k) \sin(\phi)) \right] \\ \frac{\partial \ln p(\mathbf{y}; \boldsymbol{\theta})}{\partial T_1} &= -\frac{1}{2\sigma^2} \sum_{k=1}^N \left[\frac{\partial f^2(\boldsymbol{\theta})}{\partial T_1} - 2 \frac{\partial f(\boldsymbol{\theta})}{\partial T_1} (y_R(k) \cos(\phi) + y_I(k) \sin(\phi)) \right] \\ \frac{\partial \ln p(\mathbf{y}; \boldsymbol{\theta})}{\partial T_2} &= -\frac{1}{2\sigma^2} \sum_{k=1}^N \left[\frac{\partial f^2(\boldsymbol{\theta})}{\partial T_2} - 2 \frac{\partial f(\boldsymbol{\theta})}{\partial T_2} (y_R(k) \cos(\phi) + y_I(k) \sin(\phi)) \right] \end{aligned}$$

where the first order derivatives are:

$$\begin{aligned} \frac{\partial f(\boldsymbol{\theta})}{\partial \rho} &= \exp\left(-\frac{T_E}{T_2}\right) \left[1 - \exp\left(\frac{T_R}{T_1}\right)\right] \\ \frac{\partial f^2(\boldsymbol{\theta})}{\partial \rho} &= 2\rho \exp\left(-\frac{2T_E}{T_2}\right) \left[1 - \exp\left(\frac{T_R}{T_1}\right)\right]^2 \\ \frac{\partial f(\boldsymbol{\theta})}{\partial T_1} &= -\rho \frac{T_R}{T_1^2} \exp\left(-\frac{T_E}{T_2}\right) \exp\left(-\frac{T_R}{T_1}\right) \\ \frac{\partial f^2(\boldsymbol{\theta})}{\partial T_1} &= -2\rho^2 \frac{T_R}{T_1^2} \exp\left(-\frac{2T_E}{T_2}\right) \exp\left(-\frac{T_R}{T_1}\right) \left[1 - \exp\left(-\frac{T_R}{T_1}\right)\right] \\ \frac{\partial f(\boldsymbol{\theta})}{\partial T_2} &= \rho \frac{T_E}{T_2^2} \exp\left(-\frac{T_E}{T_2}\right) \left[1 - \exp\left(\frac{T_R}{T_1}\right)\right] \\ \frac{\partial f^2(\boldsymbol{\theta})}{\partial T_2} &= 2\rho^2 \frac{T_E}{T_2^2} \exp\left(-\frac{2T_E}{T_2}\right) \left[1 - \exp\left(\frac{T_R}{T_1}\right)\right]^2 \end{aligned}$$

In order to compute the expected value of Equation (7), Monte Carlo simulations have to be implemented.

Author Contributions

The author contributions are substantially equal. In particular, the main contribution of Vito Pascazio, Giampaolo Ferraioli and Fabio Basalice was the methodology development. Moreover, Giampaolo Ferraioli and Fabio Basalice were specifically focused on the numerical implementation. Alessandro Grassia worked both on code implementation and on software simulation tasks.

Conflict of Interest

The authors declare no conflict of interest.

References

1. Slichter, P. *Principles of Magnetic Resonance*, 3rd ed.; Springer: New York, NY, USA, 1996.
2. Cho, Z.H.; Jones, J.; Singh, M. *Foundations of Medical Imaging*; Wiley Interscience: New York, NY, USA, 1993.
3. Haley, A.P.; Knight-Scott, J.; Fuchs, K.L.; Simnad, V.I.; Manning, C. Shortening of hippocampal spin-spin relaxation time in probable Alzheimer's disease: A 1H magnetic resonance spectroscopy study. *Neurosci. Lett.* **2004**, *362*, 167–170.
4. Antonini, A.; Leenders, K.L.; Meier, D.; Oertel, W.H.; Boesiger, P.; Anliker, M. T2 relaxation time in patients with Parkinson's disease. *Neurologyn* **1993**, *43*, 697–700.
5. Mariappan, S.V.S.; Subramanian, S.; Chandrakumar, N.; Rajalakshmi, K.R.; Sukumaran, S.S. Proton relaxation times in cancer diagnosis. *Magn. Reson. Med.* **1988**, *8*, 119–128
6. Roebuck, J.R.; Haker, S.J.; Mitsouras, D.; Rybicki, F.J.; Tempany, C.M.; Mulkern, R.V. Carr-Purcell-Meiboom-Gill imaging of prostate cancer: Quantitative T2 values for cancer discrimination. *Magn. Reson. Imaging* **2009**, *27*, 497–502.
7. Drain, L.E. A direct method of measuring nuclear spin-lattice relaxation times. *Proc. Phys. Soc.* **1949**, *62*, 301.
8. Barral, J.K.; Gudmundson, E.; Stikov, N.; Etezadi-Amoli, M.; Stoica, P.; Nishimura, D.G. A robust methodology for in vivo T1 mapping. *Magn. Reson. Med.* **2010**, *64*, 1057–1067.
9. Chang, L.C.; Koay, C.G.; Basser, P.J.; Pierpaoli, C. Linear least-squares method for unbiased estimation of T1 from SPGR signals. *Magn. Reson. Med.* **2013**, *60*, 496–501.
10. Trzasko, J.D.; Mostardi, P.M.; Riederer, S.J.; Manduca, A. Estimating T1 from multichannel variable flip angle SPGR Sequences. *Magn. Reson. Med.* **2013**, *69*, 1787–1794.
11. Bonny, J.M.; Zanca, M.; Boire, J.Y.; Veyre, A. T2 maximum likelihood estimation from multiple spin-echo amplitude images. *Magn. Reson. Med.* **1996**, *36*, 287–293.
12. Sijbers, J.; den Dekker, A.J.; Raman, E.; van Dyck, D. Parameter estimation from Magnitude MR images. *Int. J. Imaging Syst. Technol.* **1999**, *10*, 109–114.
13. Liu, J.; Nieminen, A.O.; Koenig, J.L. Calculation of T1 T2 and proton spin density in nuclear magnetic resonance imaging. *J. Magn. Reson.* **1989**, *85*, 95–110.
14. Fennessy, F.M.; Fedorov, A.; Gupta, S.N.; Schmidt, E.J.; Tempany, C.M.; Mulkern, R.V. Practical considerations in T1 mapping of prostate for dynamic contrast enhancement pharmacokinetic analyses. *Magn. Reson. Imaging* **2012**, *30*, 1224–1233.
15. Jones, A.J.; Hodgkinson, P.; Barker, A.L.; Hore, P.J. Optimal Sampling Strategies for the Measurement of Spin-Spin Relaxation Times. *J. Magn. Reson.* **1996**, *113*, 25–34.
16. Kay, S.M. *Fundamentals of Statistical Signal Processing*; Prentice Hall: Upper Saddle River, NJ, USA, 1993.
17. Gudbjartsson, H.; Patz, S. The Rician distribution of noisy MRI data. *Magn. Reson. Med.* **1995**, *34*, 910–914.
18. Baselice, F.; Ferraioli, G.; Pascazio, V. Relaxation time estimation from complex magnetic resonance images. *Sensors* **2010**, *10*, 3611–3625.

19. Spandonis, Y.; Heese, F.P.; Hall, D.H. High resolution MRI relaxation measurements of water in the articular cartilage of the meniscectomized rat knee at 4.7T. *Magn. Reson. Imaging* **2004**, *22*, 943–951.
20. Anastasiou, A.; Hall, L.D. Optimisation of T_2 and M_0 measurements of bi-exponential systems. *Magn. Reson. Imaging* **2004**, *22*, 67–80.
21. Wright, G.A. Magnetic resonance imaging. *IEEE Signal Process. Mag.* **1997**, *14*, 56–66.
22. Wang, Y.; Lei, T. Statistical Analysis of MR Imaging and Its Applications in Image Modeling. In Proceedings of IEEE International Conference Image Processing, Austin, TX, USA, 13–16 November 1994; pp. 866–870.
23. Baselice, F.; Ferraioli, G.; Shabou, A. Field map reconstruction in magnetic resonance imaging using Bayesian estimation. *Sensors* **2010**, *10*, 266–279.
24. Eggers, H.; Knopp, T.; Potts, D. Field inhomogeneity correction based on gridding reconstruction for magnetic resonance imaging. *IEEE Trans. Med. Imaging* **2007**, *26*, 374–384.
25. Stanis, G.J.; Odrobina, E.E.; Pun, J.; Escaravage, M.; Graham, S.J.; Bronskill, M.J.; Henkelman, R.M. T1, T2 relaxation and magnetization transfer in tissue at 3T. *Magn. Reson. Med.* **2005**, *54*, 507–512.

Calibrationless Parallel Magnetic Resonance Imaging: A Joint Sparsity Model

Angshul Majumdar, Kunal Narayan Chaudhury and Rabab Ward

Abstract: State-of-the-art parallel MRI techniques either explicitly or implicitly require certain parameters to be estimated, e.g., the sensitivity map for SENSE, SMASH and interpolation weights for GRAPPA, SPIRiT. Thus all these techniques are sensitive to the calibration (parameter estimation) stage. In this work, we have proposed a parallel MRI technique that does not require any calibration but yields reconstruction results that are at par with (or even better than) state-of-the-art methods in parallel MRI. Our proposed method required solving non-convex analysis and synthesis prior joint-sparsity problems. This work also derives the algorithms for solving them. Experimental validation was carried out on two datasets—eight channel brain and eight channel Shepp-Logan phantom. Two sampling methods were used—Variable Density Random sampling and non-Cartesian Radial sampling. For the brain data, acceleration factor of 4 was used and for the other an acceleration factor of 6 was used. The reconstruction results were quantitatively evaluated based on the Normalised Mean Squared Error between the reconstructed image and the originals. The qualitative evaluation was based on the actual reconstructed images. We compared our work with four state-of-the-art parallel imaging techniques; two calibrated methods—CS SENSE and 11SPIRiT and two calibration free techniques—Distributed CS and SAKE. Our method yields better reconstruction results than all of them.

Reprinted from *Sensors*. Cite as: Majumdar, A.; Chaudhury, K.N.; Ward, R. Calibrationless Parallel Magnetic Resonance Imaging: A Joint Sparsity Model. *Sensors* **2013**, *13*, 16714–16735.

1. Introduction

In parallel MRI (pMRI), the object under study is scanned by multiple receiver coils. In order to expedite scanning, the K-space is partially sampled at each of the channels. The problem is to reconstruct the image given the partial K-space samples. The problem is rendered even more challenging by the fact that, each of the receiver coils has their own sensitivity profiles depending on their field of view; these sensitivity profiles are not accurately known beforehand.

In the past, all pMRI techniques required the sensitivity profile to be estimated either explicitly (SENSE [1], SMASH [2]) or implicitly (GRAPPA [3,4], SPIRiT [5]). All the aforementioned methods assume that the sensitivity maps are smooth and hence have a compact support in the Fourier domain. Thus, while acquiring the MRI scan, the centre of the K-space is densely sampled from which the sensitivity map is either explicitly estimated (SENSE or SMASH) or the interpolation weights (dependent on the sensitivity maps) are estimated (GRAPPA, SPIRiT). Unfortunately joint estimation of sensitivity maps (or related interpolation weights) is an ill-posed problem.

All the aforementioned pMRI reconstruction methods proceed in two stages—(i) In the calibration stage, the sensitivity maps or the interpolation weights are estimated; (ii) Based on these estimates, the image is reconstructed in the reconstruction stage. The reconstruction accuracy of the

images is sensitive to the accuracy of the calibration stage. The calibration in turn depends on the choice of certain parameters, e.g., the window size—size of the central K-space region that has been fully sampled (for all the aforementioned methods) and the kernel size for estimating the interpolation weights (for GRAPPA and SPIRiT). These parameters are manually tuned and the best results are reported. The GRAPPA formulation has been studied in detail, and there is a study which claims to offer insights regarding the choice of GRAPPA reconstruction parameters [6]; however for other techniques such as SPIRiT and CS SENSE, there are no detailed studies on parameter tuning.

In this work, we improve upon our previous work on calibration free reconstruction (see Section 2.2). Our method reconstructs each of the different multi-coil images, which are then combined by the sum-of-squares approach (used in GRAPPA and SPIRiT). We compare our method with state-of-the-art parallel MRI reconstruction methods; two of these are calibrated techniques—CS SENSE [7] and SPIRiT and the other two are calibration free methods—DCS and SAKE. Our proposed method outperforms all of them.

Mathematically the sensitivity encoding of MR images is a modulation operation where the signal (image) is modulated by the sensitivity function (map) of the coils. All the aforesaid studies are based on the assumption the sensitivity map is smooth. Moreover the design on the receiver coils ensure that there sensitivity does not vanish anywhere, *i.e.*, there is no portion of the sensitivity map that has zeroes. This is to ensure that each of the coils collects information about the entire object under scan and no portion of the object is “invisible” to any of the coils. The sensitivity maps can thus be represented as smooth functions without any singularities. When this assumption holds, the sensitivity maps will not affect the location of the singularities/discontinuities/edges in the image. Sparsifying transforms like wavelet and finite difference, capture the discontinuities in the images, *i.e.*, the transform coefficients have high values at positions corresponding to the edges and zeros elsewhere. Since sensitivity encoding (modulation), do not affect the position of the discontinuities in the sensitivity encoded coil images, the positions of the high valued transform coefficients of the coil images will be the same for all.

Our reconstruction method is based on the fact that the position of the high valued transform coefficients in the different sensitivity encoded coil images remain the same. Based on the precepts of Compressed Sensing (CS) we formulated the reconstruction as a row-sparse Multiple Measurement Vector (MMV) recovery problem. Our method produces one sensitivity encoded image corresponding to each receiver coil in a fashion similar to GRAPPA and SPIRiT. Both of these methods reconstruct the final image as a sum-of-squares of the sensitivity encoded images. In this paper, we will follow the same combination technique.

Row-sparse MMV optimization can be either formulated as a synthesis prior or an analysis prior problem. However it is not known apriori which of these formulations will yield a better result. Even though the synthesis prior is more popular, it has been found that the analysis prior yields better results than the synthesis prior. Both of the analysis and the synthesis prior formulations can either be convex or non-convex. The Spectral Projected Gradient algorithm [8] can solve the convex synthesis prior problem efficiently. There is no efficient algorithm to solve the analysis prior problem. In the past, it has been found that for both synthesis and analysis prior, better

reconstruction results can be obtained with non-convex optimization [9–11]. Following previous studies, we intend to employ non-convex optimization for solving the reconstruction problem. Since algorithms for solving such optimization problems do not exist, in this work, we derive fast but simple algorithms to solve the non-convex synthesis and analysis prior problems.

2. Proposed Reconstruction Technique

The K-space data acquisition model for multi-coil parallel MRI scanner is given by:

$$y_i = F_{\Omega}x_i + \eta_i, i = 1 \dots C \quad (1)$$

where y_i is the K-space data for the i^{th} coil, F_{Ω} is the Fourier mapping from the image space to the K-space (Ω is the set of sample points, for Cartesian sampling, F_{Ω} can be expressed as RF , where R is a mask and F is the Fast Fourier Transform, but for non-Cartesian sampling, viz. Spiral, rosetta and radial, F_{Ω} is a non-uniform Fourier transform), x_i is the vectorized sensitivity encoded image (formed by row concatenation) corresponding to the i^{th} coil, η_i is the noise and C is the total number of receiver coils.

Since the receiver coils only partially sample the K-space, the number of K-space samples for each coil is less than the size of the image to be reconstructed. Thus, the reconstruction problem is under-determined. Following the works in CS based MR image reconstruction [12], one can reconstruct the individual coil images separately by exploiting their sparsity in some transform domain, *i.e.*, each of the images can be reconstructed by solving,

$$\min_{x_i} \|\Psi x_i\|_1 \quad \text{subject to} \quad \|y_i - F_{\Omega}x_i\|_2^2 \leq \varepsilon_i \quad (2)$$

where Ψ is the wavelet transform ε_i is the variance of noise times the number of pixels in the image.

The analysis prior optimization directly solves for the images. The synthesis prior formulation solves for the transform coefficients. In situations where the sparsifying transform is orthogonal (Orthogonal: $\Psi^T\Psi = I = \Psi\Psi^T$) or a tight-frame (Tight-frame: $\Psi^T\Psi = I \neq \Psi\Psi^T$), the inverse problem Equation (2) can be solved via the following synthesis prior optimization:

$$\min_{z_i} \|z_i\|_1 \quad \text{subject to} \quad \|y_i - F_{\Omega}\Psi^T z_i\|_2^2 \leq \varepsilon_i \quad (3)$$

where $z_i = \Psi x_i$ are the sparse transform coefficients.

However, such piecemeal reconstruction of coil images does not yield optimal results. In this paper, we will reconstruct all the coil images simultaneously by solving a MMV recovery problem. Equation (1) can be compactly represented in the MMV forms as follows:

$$Y = F_{\Omega}X + N \quad (4)$$

where $Y = [y_1 | \dots | y_C]$, $X = [x_1 | \dots | x_C]$ and $N = [\eta_1 | \dots | \eta_C]$. Here “|” denotes that the vectors are stacked as columns. In this work, we recover all the coil images X by solving the inverse problem Equation (4).

2.1. Joint Sparsity Formulation

The multi-coil images (x_i 's) are formed by sensitivity encoding of the original image (to be reconstructed). All previous studies in parallel MRI assume that the sensitivity maps are smooth and have a compact support in the Fourier domain. Since the sensitivity maps are smooth, they do not alter the positions of the edges of the images although they might change the absolute values.

This can be clarified with a toy example. Figure 1a shows a prominent edge (say after sensitivity encoding by first coil) and Figure 1b shows a less prominent edge (say after sensitivity encoding by second coil).

Figure 1. (a) Sharp edge and (b) Less prominent edge.

$$\begin{array}{cccccccc}
 1 & 1 & 0 & 0 & 0.5 & 0.5 & 0 & 0 \\
 1 & 1 & 0 & 0 & 0.5 & 0.5 & 0 & 0 \\
 1 & 1 & 0 & 0 & 0.5 & 0.5 & 0 & 0 \\
 \text{(a)} & & & & \text{(b)} & & &
 \end{array}$$

If finite difference is used as the sparsifying transform, the discontinuities along the edges are captured, *i.e.*, there are high values along the edges but zeroes elsewhere. The positions of the discontinuities are maintained, although the absolute values change as can be seen from Figure 2.

Figure 2. (a) Finite differencing of sharp edge and (b) Finite differencing of less prominent edge.

$$\begin{array}{cccccccc}
 0 & 1 & 0 & 0 & 0 & 0.5 & 0 & 0 \\
 0 & 1 & 0 & 0 & 0 & 0.5 & 0 & 0 \\
 0 & 1 & 0 & 0 & 0 & 0.5 & 0 & 0 \\
 \text{(a)} & & & & \text{(b)} & & &
 \end{array}$$

Based on this toy example, we consider the MMV formulation Equation (4). All the columns of X are images corresponding to different coils. Since the sensitivity maps of all the coils are smooth, the positions of the edges remain intact. For better clarity, we look at the images in a transform domain:

$$\Psi X = Z = \begin{bmatrix} z_{1,1} & \dots & z_{1,C} \\ \dots & \dots & \dots \\ z_{r,1} & \dots & z_{r,C} \\ \dots & \dots & \dots \\ z_{n,1} & \dots & z_{n,C} \end{bmatrix} \quad (5)$$

where Ψ is the sparsifying transform that encodes the edges of the images, Z is the matrix formed by stacking the transform coefficients as columns.

In Equation (5), each row corresponds to one position. Based on the discussion so far, since the positions of the edges in the different images do not change, the positions of the high valued

coefficients in the transform domain do not change either. Therefore for all the coil images the high valued transform coefficients appear at the same position. Thus the matrix Z is row-sparse, *i.e.*, there are a few rows with high valued coefficients while most of the rows are zeros.

We propose to solve Equation (4) by incorporating this row-sparsity information into the optimization problem. The analysis prior formulation for solving Equation (4) is as follows:

$$\min_X \|\Psi X\|_{2,p}^p \quad \text{subject to} \quad \|Y - F_\Omega X\|_F^2 \leq \varepsilon, \quad 0 < p \leq 1 \quad (6)$$

where $\|Z\|_{2,p}^p = \sum_{j=1}^N \|Z^{j \rightarrow}\|_2^p$ ($Z^{j \rightarrow}$ is the vector whose entries form the j^{th} row of $Z = \Psi X$), $\|\cdot\|_F$ denotes the Frobenius norm of the matrix and ε is the variance of noise multiplied by the length of the transform vector and the number of receiver coils (C in our case).

The values of the inner (l_2) and outer (l_p) norms have been suggested in [13]. The choice of such values for the norms can be understood intuitively. The inner l_2 -norm over the rows enforces non-zero values on all the elements of the row vector whereas the outer l_p -norm enforces row-sparsity, *i.e.*, the selection of only a few rows [13].

The aforesaid problem Equation (5) is convex for $p = 1$. However, it has been found better MR image reconstruction results can be obtained if non-convex priors are used.

The analysis prior optimization directly solves for the images. The synthesis prior formulation solves for the transform coefficients. In situations where the sparsifying transform is orthogonal or a tight-frame, the inverse problem Equation (4) can be solved via the following synthesis prior optimization:

$$\min_Z \|Z\|_{2,p}^p \quad \text{subject to} \quad \|Y - F_\Omega \Psi^T Z\|_F^2 \leq \varepsilon, \quad 0 < p \leq 1 \quad (7)$$

where $Z = \Psi X$.

The images are recovered by:

$$X = \Psi^T Z \quad (8)$$

The final image (I) is obtained from the individual coil images by sum-of-squares combination in a fashion similar to GRAPPA and SPIRiT:

$$I = \left(\sum_{i=1}^C x_i^2 \right)^{1/2} \quad (9)$$

The analysis and the synthesis priors yield same results for orthogonal transforms but different results for redundant tight-frames.

2.2. Connection with Previous Works

In a recent work, a method similar to ours has been proposed [14]. The individual coil images were reconstructed by the solving the following optimization problem:

$$\min_X \|Y - F_\Omega X\|_F^2 + \tau \|\Psi X\|_{2,1} \quad (10)$$

This is actually the unconstrained version of our prior analysis problem Equation (6) with $p = 1$. The algorithm proposed in [14] to solve Equation (10) is ad hoc and is not derived from any optimization principle. It formulates an analysis prior problem and then suggests a synthesis prior type algorithm to solve it. Furthermore there is also the issue of choosing parameters ε and τ ; For correct choice of parameters the constrained and the unconstrained versions yield the same results. Unfortunately, no analytical relationship exists between the two. It is easy to estimate ε since it is dependent on the noise variance. But there is no known way to estimate τ given the value of ε . One can only manually try different values of τ and report the best possible results. However, such a technique is not guaranteed to give optimum results in practical scenarios.

There have been other studies that used joint-sparsity models for parallel MRI reconstruction [15–17]. However, they are all modification of the basic SENSE method and require estimates of the coil sensitivities. They require explicit knowledge regarding the sensitivity maps and therefore are not calibration free techniques. The approach proposed here and those in the aforementioned studies are different.

Prior to this work, we proposed a naive version of the CaLM MRI technique [18]. There in, instead of stacking the coil images/transform coefficients as columns of a MMV matrix (as done here), were concatenated to a long vector, *i.e.*, instead of Equation (4) the data acquisition model was expressed as follows:

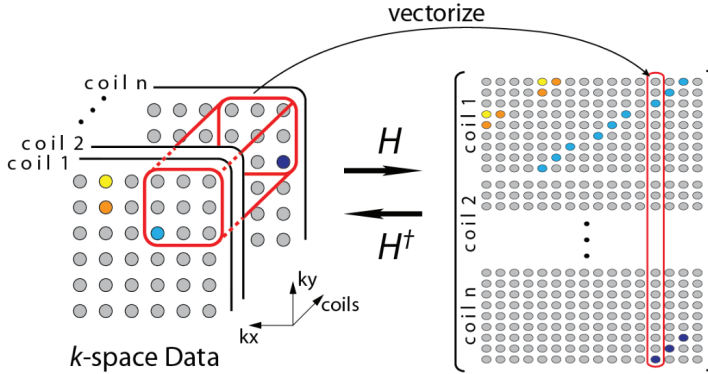
$$y = E_{\Omega}x + \eta \quad (11)$$

$$\text{where: } y = \begin{bmatrix} y_1 \\ \dots \\ y_c \end{bmatrix}, E_{\Omega} = \begin{bmatrix} RF_{\Omega} & 0 & 0 \\ 0 & \dots & 0 \\ 0 & 0 & RF_{\Omega} \end{bmatrix} \text{ and } x = \begin{bmatrix} x_1 \\ \dots \\ x_c \end{bmatrix}$$

In this formulation, the vector x will be group-sparse in transform domain for the same reasons it is row-sparse in the proposed formulation. In [18] a convex group-sparse recovery problem is proposed to recover the coil images. Even though the reconstruction philosophy is the same in [18] and the proposed approach; the approach proposed in this work is more general since we can handle both convex and non-convex formulations. Also the data acquisition model Equation (4) is more natural than Equation (11).

In this work, we also do an in-depth analysis as to why the proposed technique is likely to be successful. None of the previous studies [14,18] have carried out such an analysis. Over all this work is a more generalized, thorough and in-depth extension to the prior studies.

During the review, one of the reviewers pointed out to a few recent studies that do not require a calibration stage [19,20]. The formulation in [19] can be understood from the following diagram (Figure 3)—overlapping blocks from all the channels are vectorized and stacked as columns of a Hankel matrix A .

Figure 3. Formation of low-rank hankel matrix.

The Hankel matrix thus formed is low-rank owing to local correlations. In [18] the low-rank structure is exploited to recover the coil images. This is a good intuitive approach, but the main problem with this approach is that the Hankel matrix thus formed is huge owing to overlap of the blocks. Estimating the low-rank matrix is an iterative process and at each iteration the SVD of this matrix needs to be computed. Computing the SVD for such a large matrix becomes infeasible in practice. This (low-rank) assumption (behind SAKE) follows from intuition but is not very practical for large scale problems especially for 3D volume reconstruction.

SAKE is pegged on the idea that the coil images are correlated spatially; also the various channel images are correlated. Thus, the K-space samples are also correlated (The Fourier transform being orthogonal do not disturb the correlation). To overcome the computational issue of SAKE, the CLEAR technique was proposed in [20]. In CLEAR, a partial Hankel matrix is formed by considering a small section of the K-space. CLEAR assumes that the K-space is correlated locally. However, such an assumption does not follow readily from the mathematics of MRI acquisition—local correlation in the pixel domain does not translate to local correlation in the Fourier frequency domain. Thus, although CLEAR addresses the computational issues of SAKE, it introduces more severe problems—the reconstruction shows heavy artifacts owing to incorrect modeling.

3. Theoretical Understanding of Proposed Approach

A lot of practical CS problems exploit the sparsity of the natural signals in the wavelet basis in order to reconstruct them. The sparsity of the wavelet coefficients arises on account of the piecewise smooth (e.g., piecewise polynomial) structure of such signals, and the vanishing moments of wavelets. A precise way of describing this is that the action of any wavelet $\psi(t)$ can be regarded as a “smoothed” derivative operation [21], namely:

$$\int f(t)\psi(t-t_0)dt = D^{(n)}(f*\phi)(t_0) \quad (12)$$

where the order of differentiation n is precisely the number of vanishing moments of $\psi(t)$. Here $\phi(t)$ is some low-pass function matched with the wavelet $\psi(t)$. As a result, large wavelet coefficients are

obtained in the vicinity of singularities, while a relatively smaller response is obtained in the smooth portions of the signal.

In this sub-section, we make some observations on how the sparsity of the piecewise smooth signal is affected by modulation. To keep it simple, we work with one-dimensional signals. Let $f(t)$ be a piecewise smooth signal that is multiplied by a waveform $m(t)$ to get the modulated signal $g(t) = f(t)m(t)$. A natural question then is whether $g(t)$ is sparse in the wavelet domain, and if so, does it have the same sparsity signature as $f(t)$? By sparsity signature, we simply mean the set of points where the wavelet coefficients are larger than some threshold. The actual size of the response could, however, be very different. Simulation results confirm that this is indeed the case, provided that $m(t)$ and some of its derivatives is non-vanishing. These observations can be explained more precisely.

Note that if $f(t)$ and $g(t)$ are singular at the same set of points, then they clearly have the same sparsity signature. The question then is can the modulation operation create new discontinuities or erase some of the existing ones? It is clear that $g(t)$ cannot have a discontinuity if both $f(t)$ and $m(t)$ are smooth.

Therefore, the only situation of interest is that in which $f(t)$ has a discontinuity and we ask as to under what conditions on $m(t)$ will $g(t)$ exhibit a discontinuity? For the simplest case of *jump discontinuity*, we easily see the following.

Proposition 1 (Jump singularity). Suppose $f(t)$ has a jump discontinuity at $t = t_0$, and $m(t)$ is smooth. Then $g(t)$ has a jump at t_0 if and only if $m(t_0)$ is non-zero (see Figure. 4).

Note that by smooth we mean that $m(t)$ is continuous and has sufficient derivatives. On the other hand, $f(t)$ has a jump at t_0 in the sense that $f(t)$ is smooth away from t_0 , but has different left and right limits at t_0 , that is, $f(t)$ tends to different values as t approaches t_0 from the left and right of t_0 . As a simple example, consider the Heaviside function with a transition at t_0 .

In practice this proposition demands that the sensitivity map (modulation function) should be smooth and non-vanishing. The fact that the sensitivity map is smooth is well known and is the basis of all studies in parallel MRI. But we make the additional demand that the sensitivity map should be non-vanishing as well. Ideally this constraint is satisfied by the design of the scanner—there is no portion of the subject which is completely blind to a particular channel; thus the sensitivity profile for all the channels are non-vanishing.

Note that higher-order singularities can arise when two smooth functions are glued together. For example, consider the function obtained by gluing the zero function and a polynomial:

$$f(t) = \begin{cases} 0 & \text{if } t \leq 0 \\ x^n & \text{if } t > 0 \end{cases} \quad (13)$$

It is clear that $f(t)$ is continuous. In fact, $f(t)$ has n derivatives. However, the n -th derivative $f^{(n)}(t)$ has a jump at t_0 . As a result, the wavelet transform of $f(t)$, obtained using a wavelet with sufficient vanishing moments, is sparse with a large non-zero response around t_0 .

So what is the effect of modulation on the wavelet transform of such signals? Of course, one would expect $g(t)$ to have at most n derivatives. The only way it could have more derivatives is if the corresponding derivatives of $m(t)$ vanish at t_0 .

Proposition 2 (Higher-order singularity). Suppose $f(t)$ has n derivatives at $t = t_0$, but its n -th derivative is discontinuous at t_0 . Then $g(t)$ can have $m > n$ derivatives at t_0 if and only if $m^{(k)}(t_0) = 0$ for $n \leq k \leq m - 1$. Otherwise, the $g(t)$ would have at most n derivatives at t_0 .

Combined with Equation (12), the implication of this observation is that if the wavelet at least n vanishing moments, then the wavelet transforms of both $f(t)$ and $g(t)$ would exhibit a large response around t_0 , unless the n -th and larger derivatives of $m(t)$ are zero at t_0 (see Figures 4 and 5). In summary, if it can be guaranteed that $m(t)$ and its derivatives are always positive (or negative), then the wavelet coefficients of $g(t)$ would have the same sparsity signature as that of $f(t)$.

Figure 4. (Left)—Modulation function $m(t)$; (Middle)—Signal $f(t)$; (Right)—Modulated signal $m(t)f(t)$.

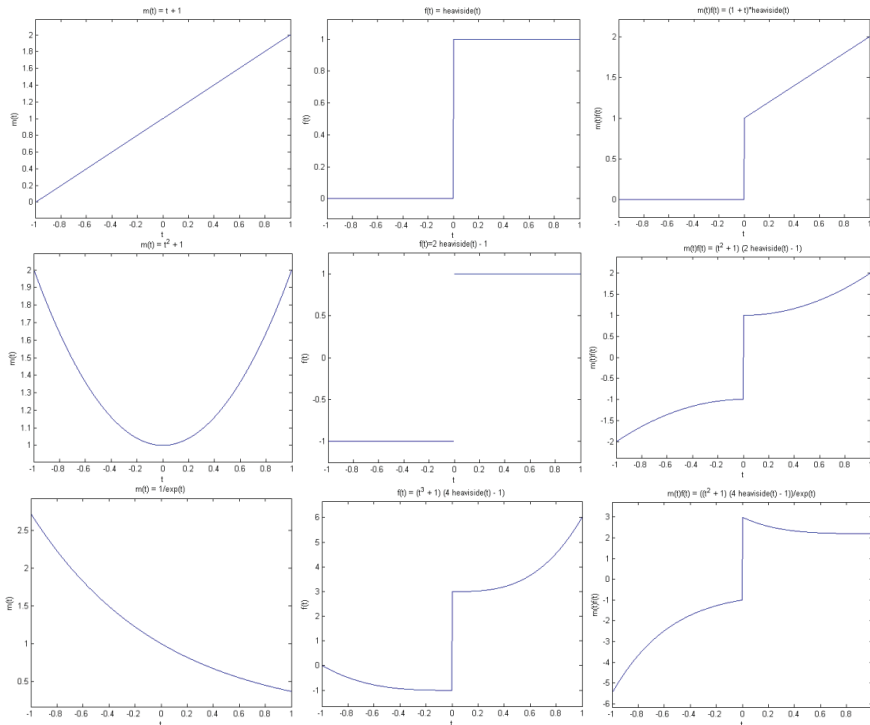
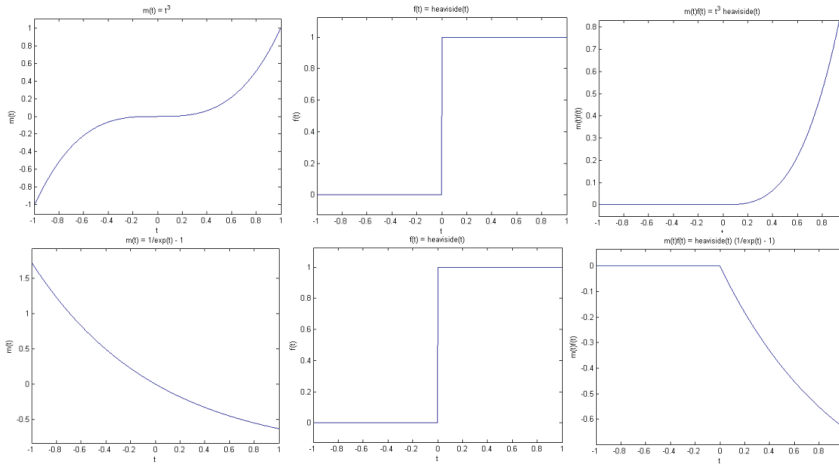


Figure 5. (Left)—Modulation function $m(t)$; (Middle)—Signal $f(t)$; (Right)—Modulated signal $m(t)f(t)$.



For parallel MRI reconstruction, the sensitivity map modulates the underlying signal (MR image). The sensitivity maps are assumed to be smooth and can be modeled as polynomials [22]. The design of the scanner ensures that there are no singularities in the sensitivity maps; physically this ensures that each receiver coil has information about the full image. Based on the discussion in this sub-section, this guarantees that the jump discontinuities in the MR image are preserved after sensitivity encoding. Hence, the positions of the high valued wavelet transform coefficients will remain unchanged before and after sensitivity encoding.

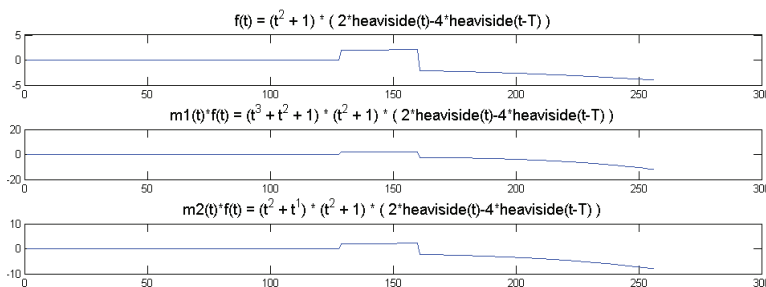
We show a toy example. We considered a function $f(t) = (1 + t^2) (2 \text{heaviside}(t) - 4 \text{heaviside}(t-T))$. Which was modulated by two polynomials of small order; the modulation functions are:

$$m1(t) = t^3 + t^2 + 1$$

$$m2(t) = t^2 + 1$$

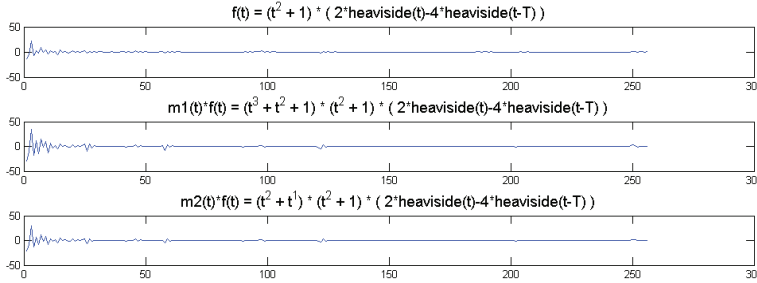
The original function and its modulated versions are shown in Figure 6.

Figure 6. Original and modulated signals. (Top) to (bottom): $f(t)$; $m1(t) \times f(t)$; $m2(t) \times f(t)$.



We compute the wavelet transforms of the original and the modulated signals. These are shown in Figure 7. Daubechies wavelets of order 16 is used and the decomposition scale is 7.

Figure 7. Wavelet transform of original and modulated signals. **(Top)** to **(bottom)**: $f(t)$; $m1(t) \times f(t)$; $m2(t) \times f(t)$.



It can be seen from Figure 6 that the sparsity signatures are exactly the same. The wavelet transform of the original and the modulated signals have high valued coefficients at the same positions; but the actual values at these positions are varying.

4. Optimization Algorithms

The Majorization-Minimization (MM) approach [23] is employed to derive solution to the following problems:

$$\text{Synthesis: } \min_X \|X\|_{2,p}^p \text{ subject to } \|Y - HX\|_F^2 \leq \varepsilon \quad (14a)$$

$$\text{Analysis: } \min_X \|AX\|_{2,p}^p \text{ subject to } \|Y - HX\|_F^2 \leq \varepsilon \quad (14b)$$

For the synthesis prior $X = Z$, $H = F_\Omega \Psi$ and for analysis prior, $A = \Psi$ and $H = F_\Omega$.

Instead of solving the aforesaid constrained problems, we propose solving their unconstrained counterparts,

$$\min_X J_1(X), \text{ where } J_1(X) = \frac{1}{2} \|Y - HX\|_F^2 + \lambda \|X\|_{2,p}^p \quad (15a)$$

$$\min_X J_2(X), \text{ where } J_2(X) = \frac{1}{2} \|Y - HX\|_F^2 + \lambda \|AX\|_{2,p}^p \quad (15b)$$

The constrained and the unconstrained formulations are equivalent for proper choice of the Lagrangian λ . Unfortunately for most practical problems it is not possible to determine λ explicitly by analytical means. Therefore, instead of ‘guessing’ λ , given the value of ε (as in [14]), we will reach the solution of the constrained problem by iteratively solving a series of unconstrained problems with decreasing values of λ . Such cooling techniques are successful since the Pareto curve for the said problem is smooth [24]; similar cooling algorithms have been successfully used in the past for solving Compressed Sensing problems [24–26].

4.1. Solving the Unconstrained Problems

We solve this problem by the Majorization-Minimization (MM) approach [23]. The generic MM algorithm is as follows,

Let $J(x)$ be the (scalar) function to be minimized

1. Set $k = 0$ and initialize x_0 .

Repeat step 2–4 until suitable a stopping criterion is met.

2. Choose $G_k(x)$ such that

a. $G_k(x) \geq J(x)$ for all x .

b. $G_k(x_k) = J(x_k)$.

3. Set x_{k+1} as the minimizer for $G_k(x)$.

4. Set $k = k + 1$, go to step 2.

For this paper, the problems to be solved are Equations (15a) and (15b). They do not have a closed form solution and therefore must be solved iteratively. At each iteration, we chose

$$G_1^{(k)}(x) = (X - X^{(k)})'(\alpha I - H^T H)(X - X^{(k)}) + \|Y - HX\|_F^2 + \lambda \|X\|_{2,p}^p \quad (16a)$$

$$G_2^{(k)}(x) = (X - X^{(k)})'(\alpha I - H^T H)(X - X^{(k)}) + \|Y - HX\|_F^2 + \lambda \|AX\|_{2,p}^p \quad (16b)$$

$G_1^{(k)}(x)$ and $G_2^{(k)}(x)$ satisfies the condition for MM algorithm when $\alpha \geq \max \text{eigvalue}(H^T H)$.

Equations (16a) and (16b) can alternately be expressed as,

$$G_1^{(k)}(x) = \alpha \|X^{(k)} + \frac{1}{\alpha} H^T (Y - HX) - X\|_2^2 + \lambda \|X\|_{2,p}^p + K_1 \quad (17a)$$

$$G_1^{(k)}(x) = \alpha \|X^{(k)} + \frac{1}{\alpha} H^T (Y - HX) - X\|_2^2 + \lambda \|AX\|_{2,p}^p + K_2 \quad (17b)$$

where K_1 and K_2 are terms independent of X .

Minimizing Equations (17a) and (17b) are the same as the following,

$$\min_X G_1^{(k)}(X), \quad G_1^{(k)}(X) = \frac{1}{2} \|B^{(k)} - X\|_F^2 + \frac{\lambda}{\alpha} \|X\|_{2,p} \quad (18a)$$

$$\min_X G_2^{(k)}(X), \quad G_2^{(k)}(X) = \frac{1}{2} \|B^{(k)} - X\|_F^2 + \frac{\lambda}{\alpha} \|AX\|_{2,p} \quad (18b)$$

where $B^{(k)} = X^{(k)} + \frac{1}{\alpha} H^T (Y - HX^{(k)})$.

These updates Equation (18) are known as the Landweber iterations.

For the synthesis prior problem, we need to solve Equation (18a) at each iteration. Taking the derivative of $G_1^{(k)}(X)$ we get,

$$\frac{dG_1^{(k)}(X)}{dX} = X - B^{(k)} + \frac{\lambda}{\alpha} \Lambda \text{signum}(X)$$

where signum is the sign of the components in X , where $\Lambda = \text{diag}(\|X^{(k)j \rightarrow}\|_2^{p-2})|X^{(k)}|$; here $\|X^{(k)j \rightarrow}\|_2^{p-2}$ means that the l_2 -norm of the j^{th} row of X is raised to power $p-2$.

Setting the derivative to zero and re-arranging, we get:

$$B = X + \frac{\lambda}{\alpha} \Lambda \text{signum}(X) \quad (19)$$

This can be solved by the following soft-thresholding:

$$X^{(k+1)} = \text{signum}(B^{(k)}) \max(0, |B^{(k)}| - \frac{\lambda}{\alpha} \Lambda) \quad (20)$$

Equations (18a) and (20) suggest a compact solution for the unconstrained synthesis prior problem. This is given in the following algorithm.

Algorithm 1: Unconstrained Synthesis Prior

Initialize:

$$X^{(0)} = 0$$

Repeat until convergence:

$$B^{(k)} = X^{(k)} + \frac{1}{\alpha} H^T (Y - HX^{(k)})$$

$$X^{(k+1)} = \text{signum}(B^{(k)}) \max(0, |B^{(k)}| - \frac{\lambda}{\alpha} \Lambda)$$

Solving the analysis prior problem requires minimization of Equation (18b) in each iteration. Taking the derivative of $G_2^{(i)}(X)$ $G_2^{(i)}(X)$ we get:

$$\frac{dG_2^{(k)}(X)}{dX} = X - B^{(i)} + \frac{\lambda}{\alpha} A^T \Omega A X \quad (21)$$

where $\Omega = \text{diag}(\|W^{(i)j \rightarrow}\|_2^{p-2})$ $\Omega = \text{diag}(\|W^{(i)j \rightarrow}\|_2^{p-2})$ and $W = AX$.

Setting the gradient to zero we get:

$$(I + \frac{\lambda}{\alpha} A^T \Omega A) X = B^{(k)} \quad (22)$$

It is not possible to solve Equation (22) directly as the sparsifying transform (A) in most cases is available as a fast operator and not as an explicit matrix. To overcome this problem, the matrix inversion lemma is used to simplify it:

$$(I + \frac{\lambda}{\alpha} A^T \Omega A)^{-1} = I - A^T (\frac{\alpha}{\lambda} \Omega^{-1} + AA^T)^{-1} A$$

From Equation (22), we have using the above identity:

$$X = B^{(k)} - A^T (\frac{\alpha}{\lambda} \Omega^{-1} + AA^T)^{-1} AB^{(k)}$$

Adding cz to both sides and subtracting $AA^T z$ from both sides gives the equivalent equation we get:

$$Z^{(k+1)} = \left(\frac{\alpha}{\lambda} \Omega^{-1} + cI\right)^{-1} (cZ^{(k)} + A(B^{(k)} - A^T Z^{(k)})) \quad (23)$$

$$X^{(k+1)} = B^{(k)} - A^T Z^{(k)} \quad (24)$$

where $c \geq \max \text{eigvalue}(A^T A)$.

This leads to the following algorithm for solving the analysis prior joint-sparse optimization problem.

Algorithm 2: Unconstrained Analysis Prior

Initialize:

$$X^{(0)} = 0$$

Repeat until convergence:

$$B^{(i)} = X^{(i)} + \frac{1}{\alpha} H^T (Y - HX^{(i)})$$

$$Z^{(i+1)} = \left(\frac{\alpha}{\lambda} \Omega^{-1} + cI\right)^{-1} (cZ^{(i)} + A(B^{(i)} - A^T Z^{(i)}))$$

$$X^{(i+1)} = B^{(i)} - A^T Z^{(i)}$$

4.2. Solving the Constrained Problem via Cooling

We have derived algorithms to solve the unconstrained problems. As mentioned before, the constrained and the unconstrained forms are equivalent for proper choice of ε and λ . However, there is no analytical relationship between them in general. When faced with a similar situation, we employed the cooling technique following previous studies [24–26].

The cooling technique solves the constrained problem in two loops. The outer loop decreases the value of λ . The inner loop solves the unconstrained problem for a specific value λ . As λ is progressively decreased, the solution of the unconstrained problem reaches the desired solution. Such a cooling technique works because the pareto curve between the objective function and the constraint is smooth. The cooling algorithm for the synthesis and analysis prior are:

Algorithm 3: Synthesis Prior Algorithm

Initialize:

$$X^{(0)} = 0; \lambda < \max(P^T x)$$

Choose a decrease factor (*DecFac*) for cooling λ

Outer Loop: While¹

$$\|y - Hx\|_r^2 \geq \varepsilon$$

Inner Loop: While²

$$\frac{J^{(i)} - J^{(i+1)}}{J^{(i)} + J^{(i+1)}} \geq Tol$$

$$J^{(i)} = \|Y - HX^{(i)}\|_F^2 + \lambda \|X^{(i)}\|_{2,p}^p$$

Compute:

$$B^{(i)} = X^{(i)} + \frac{1}{\alpha} H^T (Y - HX^{(i)})$$

Compute:

$$X^{(i+1)} = \text{signum}(B^{(i)}) \max(0, |B^{(i)}| - \frac{\lambda}{\alpha} \Lambda)$$

$$J^{(i+1)} = \|Y - HX^{(i+1)}\|_F^2 + \lambda \|X^{(i+1)}\|_{2,p}^p$$

End While² (inner loop ends)

$$\lambda = \lambda \times DecFac$$

End While¹ (outer loop ends)

Algorithm 4: Analysis Prior Algorithm

Initialize:

$$X^{(0)} = 0; \lambda < \max(P^T x)$$

Choose a decrease factor (*DecFac*) for cooling λ

Outer Loop: While¹

$$\|y - Hx\|_F^2 \geq \varepsilon$$

Inner Loop: While²

$$\frac{J^{(k)} - J^{(k+1)}}{J^{(k)} + J^{(k+1)}} \geq Tol$$

$$J^{(k)} = \|Y - HX^{(k)}\|_F^2 + \lambda \|AX^{(k)}\|_{2,p}^p$$

Compute:

$$B^{(k)} = X^{(k)} + \frac{1}{\alpha} H^T (Y - HX^{(k)})$$

Update:

$$Z^{(k+1)} = \left(\frac{\alpha}{\lambda} \Omega^{-1} + cI\right)^{-1} (cZ^{(k)} + A(B^{(k)} - A^T Z^{(k)}))$$

Update:

$$X^{(k+1)} = B^{(k)} - A^T Z^{(k)}$$

$$J^{(k+1)} = \|Y - HX^{(k+1)}\|_F^2 + \lambda \|AX^{(k+1)}\|_{2,p}^p$$

End While² (inner loop ends)

$$\lambda = \lambda \times DecFac$$

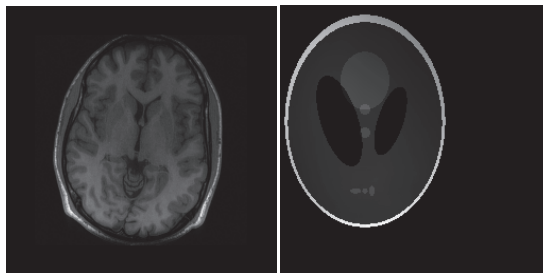
End While¹ (outer loop ends)

In this work, we proposed solving the reconstruction problem via non-convex optimization algorithms. Theoretically one may argue about the convergence of such algorithms to local minima. However, in practice it has never been a problem. In previous studies [9–11,27], non-convexity never posed to be problem for MRI reconstruction.

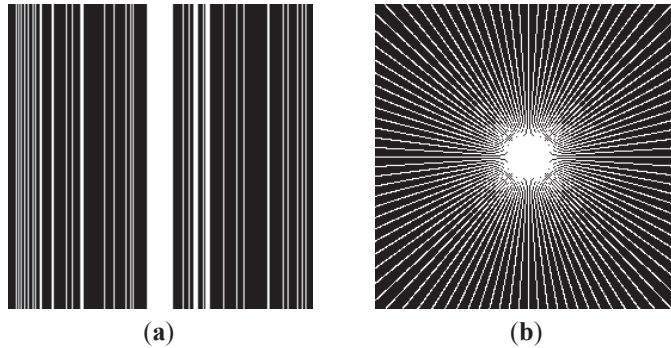
5. Experimental Evaluation

There are two sets of ground-truth data used for our experimental evaluation (Figure 7). The brain data and the Shepp-Logan phantom have been used previously in [4]. The brain data is a fully sampled T1 weighted scan of a healthy volunteer. The volunteer was scanned using Spoiled Gradient Echo sequence with the following parameters—echo time = 8 ms; repetition time = 17.6 ms; flip angle = 20 degrees. The scan was performed on a GE Sigma-Excite 1.5-T scanner, using an eight-channel receiver coil. The 8-channel data for Shepp-Logan phantom was simulated. The ground-truth is formed by sum-of-squares reconstruction of the multi-channel images.

Figure 7. Groundtruth images: Brain and Shepp-Logan Phantom.



In this work, we show results for two different K-space sampling schemes (Figure 8)—Variable Density Random Sampling (Cartesian) and Radial Sampling (non-Cartesian). In VD Random (VDR) Sampling, the center of the K-space is densely sampled, while the rest of the K-space is sparsely sampled by randomly omitting lines in the phase encoding direction. This is widely used sampling method for parallel MRI. Radial sampling is one of the fastest sampling methods [28,29] and has been previously used in parallel MRI [30]. For the brain image, the acceleration factor of 4 is used, for the Shepp-Logan phantom, acceleration factor of 6 is used for both Variable Density random sampling and radial sampling.

Figure 8. (a) VD Random Sampling, (b) Radial sampling.

We compare our proposed method with two state-of-the-art calibrated methods—L1SPIRiT [4] (frequency domain method) and CS SENSE [6] (image domain method) and two calibration free techniques DCS [14] and SAKE [19]. For our proposed method, the mapping from non-Cartesian K-space to the Cartesian image space is the Non-Uniform Fast Fourier Transform (NUFFT) [31,32].

For CS SENSE the sensitivity profiles are estimated in the fashion shown in [30]. A Kaiser-Bessel window at the center of the K-space is densely sampled, from which a low resolution image for each coil is obtained. These images are combined by sum-of-squares. The sensitivity map is computed by dividing the low resolution image of the corresponding coil by the combined sum-of-squares image.

Our proposed method and the DCS based method propounded in [14] do not require any parameter estimation. In [14], the reconstruction is solved via Equation (10). However, as mentioned earlier, it is not possible to determine the parameter τ analytically. For this work, we determine the value of τ as specified in [14]—1/500 of the maximum (in absolute value) of the zero-filled image for the first 50 iterations, and 1/100 of the maximum value for the last 10 iterations. Sixty iterations were used to generate the final image.

For our non-convex formulation, we found that the best results were obtained for $p = 0.5$ (this value of p has also been suggested in [11]). The quantitative reconstruction results are shown in Table 1. Normalized Mean Squared Error (NMSE) is the metric used for evaluation. The best reconstruction (lowest error) results are shown in bold.

Table 1. Comparison of reconstruction accuracies for calibration-free techniques.

Image →	Brain		Phantom	
Type of Sampling →	VDR	Radial	VDR	Radial
L1SPIRiT [4]	0.13	0.07	0.13	0.09
CS SENSE [5]	0.16	0.28	0.14	0.04
DCS reconstruction [13]	0.25	0.19	0.29	0.17
SAKE [19]	0.14	0.14	0.13	0.10
Proposed non-convex synthesis prior	0.08	0.03	0.15	0.01
Proposed non-convex analysis prior	0.06	0.03	0.13	0.00

The DCS reconstruction yields the worse results. This is expected—DCS is an ad hoc algorithm and consequently it fails. Our proposed non-convex analysis prior formulation yields the best results. The synthesis prior formulation is slightly worse off than the analysis prior. The SAKE technique does not yield as good results as our proposed technique. CS SENSE and l1SPIRiT yield better results than SAKE, but they have to be thoroughly calibrated and hence are not robust.

Although NMSE is an often used metric for evaluating the reconstruction accuracy, it does not always reflect the qualitative aspects of reconstruction. For qualitative evaluation we show the reconstructed images in Figure 9. Owing to limitations in space we only show the results for variable density random sampling. The qualitative results more or less corroborate the quantitative results. With 6-fold undersampling, all the methods apart from our proposed analysis prior formulation yields significant reconstruction artifacts.

Figure 9. Reconstruction for Variable Density Random sampling. From Top to Bottom: DCS Reconstruction, l1SPIRiT, CS SENSE, SAKE, Proposed Non-Convex Synthesis Prior, Proposed Non-Convex Analysis Prior.

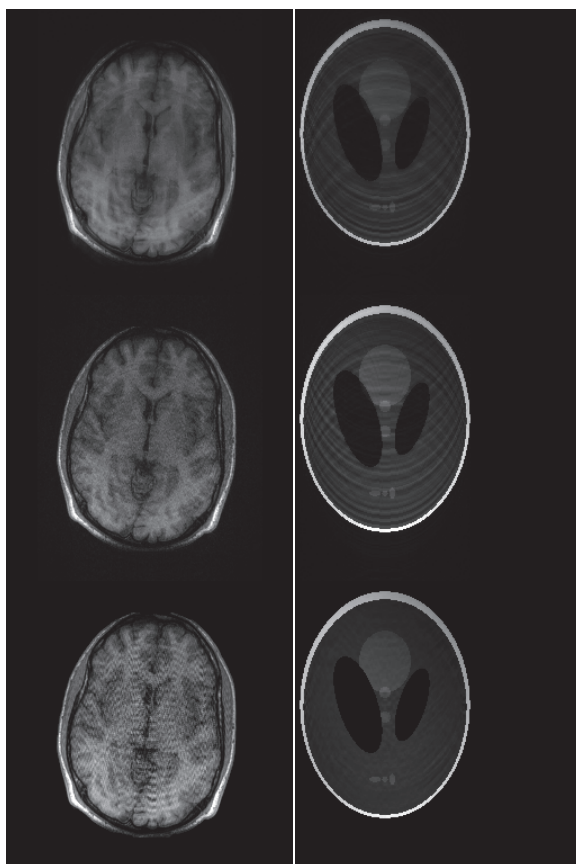
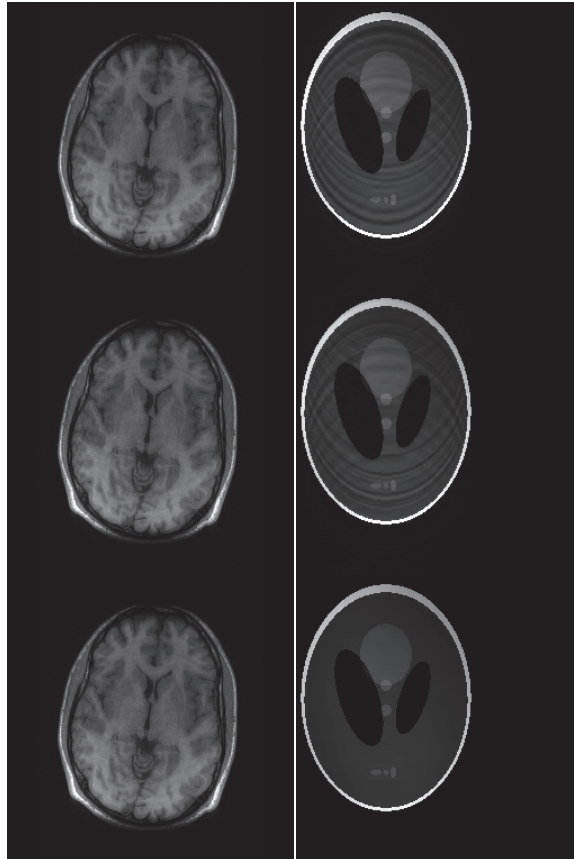
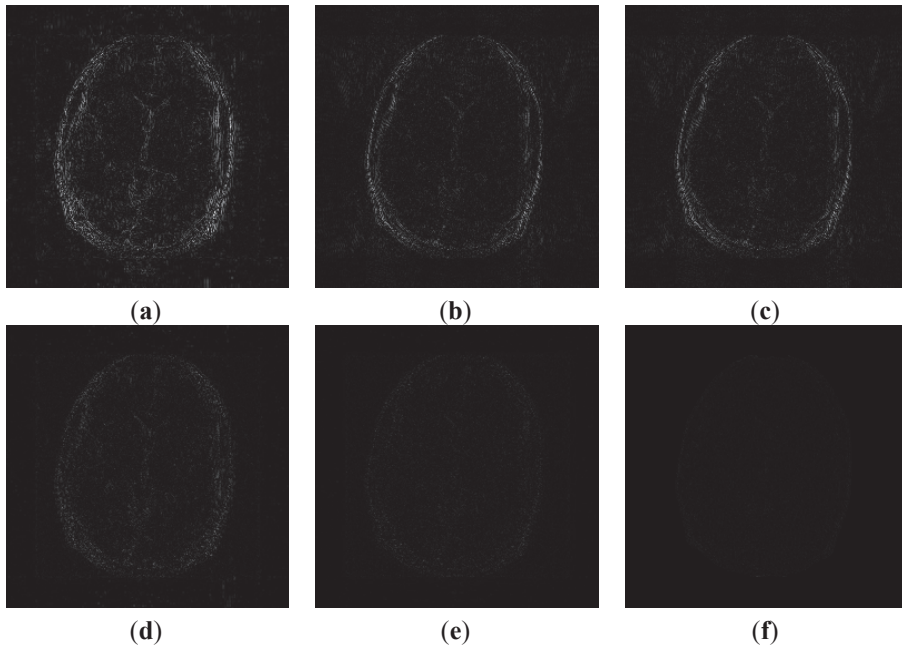


Figure 9. Cont.

In order to elucidate the reconstruction even more, we show the difference (between groundtruth and reconstructed) images for the brain image. The difference images are shown in Figure 10. The contrast of the difference images have been enhanced five times for visual clarity. The difference images corroborate our previous findings. We see that the DCS reconstruction yields the worst results. CS SENSE and SAKE yields almost similar difference images; 11SPIRiT slightly improves upon CS SENSE and SAKE. Our analysis prior formulation yields the best results; the synthesis prior is better than 11SPIRiT but is slightly worse than the analysis prior.

Figure 10. Difference Images. (a) DCS; (b) CS SENSE; (c) SAKE; (d) I1SPIRiT; (e) non-convex synthesis prior; (f) non-convex analysis prior.



6. Conclusions

State-of-the-art parallel MRI techniques either implicitly or explicitly require a calibration stage to estimate the sensitivity maps (for SENSE, SMASH and related techniques) or interpolation weights (for GRAPPA, SPIRiT and related techniques). Thus, all these methods are sensitive to the calibration stage. In recent times there is a concerted effort in developing calibration free reconstruction techniques. In this paper we improve upon a previous technique calibration free reconstruction technique [18].

We compare our proposed technique with other calibrated and calibration free methods. We find that our proposed non-convex analysis prior formulation always yields the best results. However there are two shortcomings with the proposed method. The first one is more of a constraint than a shortcoming. Our technique does not work with uniform periodic undersampling. This is because, our solution approach requires solving an under-determined problem Equation (4) and is based on the tenets of Compressed Sensing; and Compressed Sensing demands that the sampling scheme should be randomized.

The second problem with our work is on the assumption that the modulation function is smooth that does not change the number of discontinuities in the image. However, the function can introduce new discontinuities if the function is zero in certain positions. Ideally this is taken care of during the design of the scanner, the FOV is designed such that no area of the subject is completely blind to the channel. However, if the SNR the modulation function can be effectively zero. This would violate the row-sparsity assumption and our method would fail to produce good results.

Acknowledgments

The authors are thankful to Michael Lustig for multi-channel MRI data and codes for SPIRiT and GRAPPA. This work was supported by NSERC and by Qatar National Research Fund (QNRF) No. NPRP 09-310-1-058.

Conflicts of Interest

The authors declare no conflict of interest.

References

1. Pruessmann, K.P.; Weiger, M.; Scheidegger, M.B.; Boesiger, P. SENSE: Sensitivity encoding for fast MRI. *Magn. Reson. Med.* **1999**, *42*, 952–962.
2. Sodickson, D.K.; Manning, W.J. Simultaneous acquisition of spatial harmonics (SMASH): Fast imaging with radiofrequency coil arrays. *Magn. Reson. Med.* **1997**, *38*, 591–603.
3. Griswold, M.A.; Blaimer, M.; Breuer, F.; Heidemann, R.M.; Mueller, M.M.; Jakob, P.M. Parallel magnetic resonance imaging using the GRAPPA operator formalism. *Magn. Reson. Med.* **2005**, *54*, 1553–1556.
4. Seiberlich, N.; Breuer, F.A.; Blaimer, M.; Barkauskas, K.; Jakob, P.M.; Griswold, M.A. non-cartesian data reconstruction using GRAPPA operator gridding (GROG). *Magn. Reson. Med.* **2007**, *58*, 1257–1265
5. Lustig, M.; Pauly, J.M. SPIRiT: Iterative self-consistent parallel imaging reconstruction from arbitrary K-space. *Magn. Reson. Med.* **2010**, *64*, 457–471.
6. Bauer, S.; Markl, M.; Honal, M.; Jung, B.A. The effect of reconstruction and acquisition parameters for GRAPPA-based parallel imaging on the image quality. *Magn. Reson. Med.* **2011**, *66*, 402–409.
7. Liang, D.; Liu, B.; Wang, J.; Ying, L. Accelerating SENSE using compressed sensing. *Magn. Reson. Med.* **2009**, *62*, 1574–1584.
8. Van den Berg, E.; Friedlander, M.P. Probing the Pareto frontier for basis pursuit solutions. *SIAM J. Sci. Comput.* **2008**, *31*, 890–912.
9. Trzasko, J.; Manduca, A. Highly undersampled magnetic resonance image reconstruction via homotopic l0-minimization. *IEEE Trans. Med. Imaging* **2009**, *28*, 106–121.
10. Majumdar, A.; Ward, R.K. Under-determined non-cartesian MR reconstruction. *MICCAI* **2010**, *13*, 513–520.
11. Chartrand, R. Fast algorithms for nonconvex compressive sensing: MRI reconstruction from very few data. *IEEE Int. Symp. Biomed. Imaging* **2009**, doi:10.1109/ISBI.2009.5193034.
12. Lustig, M.; Donoho, D.L.; Pauly, J.M. Sparse MRI: The application of compressed sensing for rapid MR imaging. *Magn. Reson. Med.* **2007**, *58*, 1182–1195.
13. Cotter, S.F.; Rao, B.D.; Engang, K.; Kreutz-Delgado, K. Sparse solutions to linear inverse problems with multiple measurement vectors. *IEEE Trans. Sig. Proc.* **2005**, *53*, 2477–2488.

14. Akçakaya, M.; Hu, P.; Chuang, M.L.; Hauser, T.H.; Ngo, L.H.; Manning, W.J.; Tarokh, V.; Nezafat, R. Accelerated noncontrast-enhanced pulmonary vein MRA with distributed compressed sensing. *J. Magn. Reson. Imaging* **2011**, *33*, 1248–1255.
15. Otazo, R.; Sodickson, D.K. Distributed Compressed Sensing for Accelerated MRI. In Proceedings of the 17th Annual Meeting of ISMRM, Toronto, ON, Canada, 3–9 May 2008; p. 378.
16. Liang, D.; King, K.F.; Liu, B.; Ying, L. Accelerating SENSE Using Distributed Compressed Sensing. In Proceedings of the 17th Annual Meeting of ISMRM, Toronto, ON, Canada, 3–9 May 2008; p. 377.
17. Otazo, R.; Kim, D.; Axel, L.; Sodickson, D.K. Combination of compressed sensing and parallel imaging for highly accelerated first-pass cardiac perfusion MRI. *Magn. Reson. Med.* **2010**, *64*, 767–776.
18. Majumdar, A.; Ward, R.K. Calibration-less multi-coil MR image reconstruction. *Magn. Reson. Imaging* **2012**, *30*, 1032–1045.
19. Shin, P.J.; Larson, P.E.Z.; Ohliger, M.A.; Elad, M.; Pauly, J.M.; Vigneron, D.B.; Lustig, M. Calibrationless parallel imaging reconstruction based on structured low-rank matrix completion. *Magn. Reson. Med.* **2013**, doi:10.1002/mrm.24997.
20. Trzasko, J.; Manduca, A. Calibrationless parallel MRI using CLEAR. *ISMRM* **2012**, doi:10.1109/ACSSC.2011.6189958.
21. Unser, M.; Blu, T. Wavelet theory demystified. *IEEE Trans. Signal Process.* **2003**, *51*, 470–483.
22. Ying, L.; Sheng, J. Joint image reconstruction and sensitivity estimation in SENSE (JSENSE). *Magn. Reson. Med.* **2007**, *57*, 1196–1202.
23. Selesnick, I.W.; Figueiredo, M.A.T. Signal restoration with overcomplete wavelet transforms: Comparison of analysis and synthesis priors. *Proc. SPIE* **2009**, doi:10.1117/12.826663.
24. Hennenfent, G.; van den Berg, E.; Friedlander, M.P.; Herrmann, F.J. New insights into one-norm solvers from the pareto curve. *Geophysics* **2008**, *73*, A23–A26.
25. Majumdar, A.; Ward, R.K. On the choice of compressed sensing priors: An experimental study. *Signal Process. Image Comm.* **2012**, *27*, 1035–1048.
26. Majumdar, A.; Ward, R.K. Compressive color imaging with group sparsity on analysis prior. *IEEE ICIP* **2010**, doi:10.1109/ICIP.2010.5653685.
27. Majumdar, A.; Ward, R.K. An algorithm for sparse MRI reconstruction by Schatten p-norm minimization. *Magn. Reson. Imaging* **2011**, *29*, 408–417.
28. Zhang, S.; Block, K.T.; Frahm, J. Magnetic resonance imaging in real time: Advances using radial FLASH. *J. Magn. Reson. Imaging* **2010**, *31*, 101–109.
29. Katoh, M.; Spuentrup, E.; Buecker, A.; Manning, W.J.; Günther, R.W.; Botnar, R.M. MR coronary vessel wall imaging: Comparison between radial and spiral K-space sampling. *J. Magn. Reson. Imaging* **2006**, *23*, 757–762.
30. Block, K.T.; Uecker, M.; Frahm, J. Undersampled radial MRI with multiple coils. Iterative image reconstruction using a total variation constraint. *Magn. Reson. Med.* **2007**, *57*, 1086–1098.

31. Fessler, J.A. On NUFFT-based gridding for non-Cartesian MRI. *J. Magn. Reson.* **2007**, *188*, 191–195.
32. Tamhane, A.A.; Anastasio, M.A.; Gui, M.; Arfanakis, K. Iterative image reconstruction for PROPELLER-MRI using the nonuniform fast fourier transform. *J. Magn. Reson. Imaging* **2010**, *32*, 211–217.

MDPI AG

Klybeckstrasse 64

4057 Basel, Switzerland

Tel. +41 61 683 77 34

Fax +41 61 302 89 18

<http://www.mdpi.com/>

Sensors Editorial Office

E-mail: sensors@mdpi.com

<http://www.mdpi.com/journal/sensors>



MDPI • Basel • Beijing • Wuhan • Barcelona
ISBN 978-3-906980-99-7
www.mdpi.com

